DEVELOPMENT OF 3D BIOACTIVE AND ANTIBACTERIAL SILICATE-BASED SCAFFOLDS FOR BONE TISSUE REGENERATION IN LOAD-BEARING APPLICATIONS

By

Adam Christoph Marsh

A DISSERTATION

Submitted to
Michigan State University
in partial fulfillment of the requirements
for the degree of

Materials Science & Engineering – Doctor of Philosophy

2022

ABSTRACT

DEVELOPMENT OF 3D BIOACTIVE AND ANTIBACTERIAL SILICATE-BASED SCAFFOLDS FOR BONE TISSUE REGENERATION IN LOAD-BEARING APPLICATIONS

By

Adam Christoph Marsh

Current gold-standard approaches to addressing the needs of bone defects in load-bearing applications entail the use of either autographs or allographs. Both solutions, however, are imperfect as both autographs and allographs carry the risk of additional trauma, threat of disease transmission, and potential donor rejection respectively. Porous 3D scaffolds are attractive alternatives, illuminating a potential path towards achieving the ideal scaffold for targeting bone tissue regeneration in load-bearing applications, usurping autographs to become the new gold-standard. To unlock the full healing potential of 3D scaffolds, such scaffolds must be multifunctional such that (1) their mechanical performance meets the requisite requirements as dictated by the mechanical performance characteristics of interest for native bone tissue, (2) they stimulate the necessary biological responses for bone tissue regeneration, and (3) they exhibit antibacterial characteristics to combat the threat of infection. To date, no reports document 3D scaffolds exhibiting all three performance characteristics. The aim of this dissertation, therefore, is to deliver 3D scaffolds that are mechanically competent, possess and exhibit inherent and advanced antibacterial characteristics, and are successful at providing the needed biological characteristics for bone tissue regeneration.

To achieve this, this dissertation implements a multidisciplinary approach, utilizing comprehensive structural characterization across a wide range of scales to elucidate process – performance relationships to execute scientifically driven modifications to engineer and deliver a 3D scaffold to successfully target bone tissue regeneration in load-bearing applications. A silver-doped bioactive glass-ceramic (Ag-BG) composition was selected as the material for scaffold synthesis due to its inherent and attractive antibacterial and biological performance characteristics. Two fundamentally different processing approaches were utilized for synthesizing Ag-BG scaffolds: the polymer foam replication technique and fused filament fabrication (FFF). The Ag-BG scaffolds studied herein were

found to exhibit advanced antibacterial performance characteristics against methicillin-resistant Staphylococcus aureus (MRSA), a common pathogen implicated in osteomyelitis development, able to combat MRSA both in planktonic and biofilm forms. Ag-BG scaffolds demonstrated the ability to form an apatite-like layer when immersed in simulated body fluid (SBF), an indicator that Ag-BG scaffolds will induce the necessary mineralization for bone tissue regeneration, in addition to exhibiting attractive cell viability, proliferation, and differentiation characteristics when studied *in vitro*. The mechanical performance of Ag-BG scaffolds reported herein saw progressive improvements in each iteration of Ag-BG scaffold synthesis, achieving desirable mechanical competency and reliability as a result of the multidisciplinary approach formulated.

In addition to the exploration of developing 3D antibacterial and biological silicate-based scaffolds capable of targeting bone tissue regeneration in load-bearing applications, foundational work towards the development of class II hybrid scaffolds comprised of gelatin methacryloyl (GelMA) and Ag-BG for targeting softer tissue regeneration. The novel syntheses applied to the successful molecular coupling of GelMA and Ag-BG presents an attractive class II hydrogel showing great promise as a compatible ink for 3D bioprinting cell-laden scaffolds capable of targeting tissue regeneration of more sophisticated systems.

To the family members taken too soon to witness this monumental accomplishment, Howard Delbert Marsh, Jr. (Peepaw) and Shirley Ann Dorner (Nina).

ACKNOWLEDGEMENTS

First, I would like to extend my sincerest thanks and gratitude to my advisor, Dr. Xanthippi Chatzistavrou for not only accepting me into her research group, but also for molding me into the researcher that I am today. I know deep down within my heart of hearts, I never would have achieved such success without her guidance, assistance, and mentoring. I will never forget the unparalleled kindness and compassion she has shown me during my time as her student, and I strive every day to reflect that in my own life. The trajectory of my life has fundamentally shifted because of this experience and journey, and that is something I cannot thank you for enough. I would also like to extend my deepest thanks and appreciation to my committee: Dr. Martin Crimp, Dr. Aljoscha Roch, Dr. Shiwang Cheng, and Dr. Neal Hammer, whose knowledge and expertise were invaluable to the success of my research and my growth as a researcher. All of you have always made time to meet whether it be to answer questions, give suggestions, or challenge me to approach problems from a different perspective, and for that I am forever grateful.

I would additionally like to extend my thanks to the members of the Biomaterials group: Dr. Natalia Pajares-Chamorro, Mr. Logan Soule, and Ms. Kayla Chuong for their assistance and company during my journey. I also would like to thank the contributions of Dr. Per Askeland, Dr. Nathan Mellott, Dr. Kurt Hankenson, Dr. Yadav Wagley, Ms. Parker Acevedo, Mr. Jeremy Hix, Ms. Melinda Frame, Dr. Alicia Withrow, Mr. Jeffery Daneault, Dr. Haiping Sun, Ms. Sarah Rebolloso, Mr. John Buchweitz, Dr. Ehsanul Hoque Apu, Dr. Nureddin Ashammakhi, Dr. Cristopher Contag, Dr. Anthony Wren, Dr. Yaozhong Zhang, and Ms. Lucrezia Poli towards the work presented in this dissertation.

I would be remised if I did not extend my appreciation for the friends made along this journey: Ms. Madeline Mackinder, Ms. JoAnn Ballor, Mr. Young Kim, Mr. Tom Mittelbrun, Mr. Brad Luzenski, Ms. Rachel Zarger, and Mr. Tom Lindsay. You guys were my rock, keeping me grounded, and supporting me throughout this journey. I never could have done this without you guys.

My deepest gratitude, however, must go to my family. My sister, Ms. Amelia Marsh, who has had to put up with me day in and day out throughout most of this journey though all the best and worst of times. To my parents, Ms. Pamela Marsh and Mr. Terry Marsh, whose unconditional love and support encouraged me to keep going even in the times when all hope seemed lost. To my extended family, who all have supported me during this journey. To my cats, Luna and Louie for keeping me company all these years and to my (parents) dogs, Lucy and Finn for always providing much needed pet therapy when the going got tough.

Last, but certainly not least, I would like to thank you, the reader, for taking the time to explore this dissertation. Your valuable time spent here is unknowably appreciated. Now, let us journey together into the exciting and fantastical world of 3D scaffolds.

TABLE OF CONTENTS

LIST OF TABLES

LIST OF FIGURES

KEY TO ABBREVIATIONS

^{1}H-NMR, Proton NMR

Å, Angstrum

$\widetilde{E}_{\mathbf{HS+}}$, Upper Hashin-Shtrikman bound

$\widetilde{E}_{\mathbf{HS-}}$, Lower Hashin-Shtrikman bound

$\widetilde{E}$, Effective elastic modulus

$\sigma_{\mathbf{0}}$, Characteristic strength

α-MEM, Alpha-minimum essential medium

α-TCP, Alpha-tricalcium phosphate

β-TCP, Beta-tricalcium phosphate

μA, Micro amp

μm, Micron

ACP, Amorphous calcium phosphate

ASTM, American Society for Testing and Materials

ATR, Attenuated total reflectance

Ag-BG, Silver-doped bioactive glass-ceramic

AgNP, Silver nanoparticle

AgNT, Silver nitrate

AlNT, Aluminum nitrate

BET, Brunauer-Emmett-Teller

BG, Bioactive glass

BJ, Binder jetting

CAD, Computer aided design

CDHA, Calcium deficient hydroxyapatite

CFU, Colony forming units

CLSM, Confocal laser scanning microscopy

CaNT, Calcium nitrate

CaP, Calcium phosphate

D_2O, Deuterium oxide

DIW, Direct ink writing

DMEM, Dulbecco's modified eagle media

DMSO, Dimethyl sylfoxide

DS, Degree of substitution

DTA, Differential thermal analysis

E. faecalis, Enterococcus faecalis

E.coli, Eschericha coli

EDS, Energy dispersive spectroscopy

FBS, Fetal bovine serum

FDM, Fused deposition modeling

FFF, Fused filament fabrication

FWHM, Full width half max

G′, Storage modulus

G′′, Loss modulus

GAB, Gelatin methacryloyl - Ag-BG

GPTMS, (3-Glycidyloxypropyl)trimethoxysilane

GelMA, Gelatin methacryloyl

H_2O, Water

HA, Hydroxyapatite

HCA, Hydroxycarbonate apatite

HRTEM, High resolution transmission electron microscopy

HS, Hashin-Shtrikman

HSM, Hot stage microscopy

ICDD, International Centre for Diffraction Data

ICP-OES, Inductively coupled plasma optical emission spectroscopy

IUPAC, International Union of Pure and Applied Chemistry

L. casei, Lactobacillus casei

MAA, Methacrylic anhydride

MAS-NMR, Magic angle spinning-nuclear magnetic resonance

MIC, Minimum inhibitory concentration

MPa, Megapascal

MRSA, Methicillin-resistant *Staphylococcus aureus*

MeOH, Methanol

MurA, UDP-N-acetylglucosamine-3-enolpyruvyltransferase

N, Newton

NMR, Nuclear magnetic resonance

NaNT, Sodium nitrate

PBS, Phsophate-buffered saline

PCL, Polycaprolactone

PDF, Powder diffraction file

PLA, Polylactic acid

PPI, Pores per inch

PVA, Poly(vinyl)alcohol

PsW, Pseudowollastonite

$\mathbf{S_c}$, Sinterability

S. mutans, Streptococcus mutans

SAD, Selected area diffraction

SBF, Simulated body fluid

SEM,Scanning electron microscopy

SENB, Single-edge notched beam

SLS, Selective laser sinteirng

SPR, Surface plasmon resonance

Sol-Gel, Solution-gelation

$\mathbf{T_g}$, Glass transition temperature

$\mathbf{T_{MS}}$, The temperature at which maximum shirnkage is observed

T, Tesla

TCP, Tissue culture plate

TEM, Transmission electron microscopy

TEOS, Tetraethyl orthosilicate

TEP, Triethyl phosphate

TGA, Thermogravimetric analysis

TRIS, Tris(hydroxymethyl)aminomethane

TSA, Tryptic soy agar

TSB, Tryptic soy broth

TTT, Time-temperature-transformation

UV-Vis, Ultraviolet/visible light spectroscopy

VA-086, 2,2'-Azobis[2-methyl-N-(2-hydroxyethyl)propionamide]

$\mathbf{W_0}$, Dry mass

$\mathbf{W_t}$, Hydrated mass

W. 2M, Wollastonite-2M

XRD, X-Ray diffraction

hMSC, Human mesenchymal stem cell

k, Flow consistency index

keV, Kilo electron volt

mV, millivolt

micro-CT, Micro-computerized tomography

n, Flow index behavior

ppm, Parts per million

w/v, weight/volume

w/w, weight/weight

wt%, Weight%

CHAPTER 1

INTRODUCTION

1.1 Current strategies for addressing the needs of bone defects in load-bearing applications

Natural bone tissue is a low-density high strength adaptive nanocomposite primarily comprised of nanosized Ca-deficient hydroxyapatite (HA) crystals (60-70%) mineralized onto collagen molecules on the molecular scale [1, 2]. Such structures are further assembled on increasingly large scales (i.e. micro- and macro-) culminating in the formation of a structural hierarchy (Fig. 1.1.1a) where each subscale serves a specific functionality giving rise to the low-density high strength nature of bone. Figure 1.1.1b demonstrates the various toughening mechanisms natural bone has incorporated at the relevant subscales to achieve this low-density high strength behavior. Additionally, unique to natural bone tissue are its related adaptive and regenerative capabilities. This is possible because as bone tissue is replaced (i.e. 10% annually [3]), it responds to external stimuli in the form of mechanotransduction signals [4] allowing for its mechanical performance to adapt to applied stresses per Wolff's law [5]. Consequently, the continuous formation of new bone tissue additionally imparts bone with unique regenerative properties allowing for defects (i.e. fracture, trauma, infection [6]) below a critical size [7] to be healed without external intervention. The challenge, however, is adequately addressing bone defects once they reach a critical size, especially when located in load-bearing applications.

The gold standard for addressing bone defects in load-bearing applications is autographs [10]. Autographs have remained the gold standard resulting from the excellent osteogenic, osteoconductive, and osteoinductive performance characteristics in addition to their unparalleled mimicry of the natural hierarchal structure of bone [10]. However, the resources needed for autographs are severely limited due to the need to harvest healthy bone from a separate region of the body, thus creating a second painful defected site in addition to introducing unnecessary trauma and the potential risk

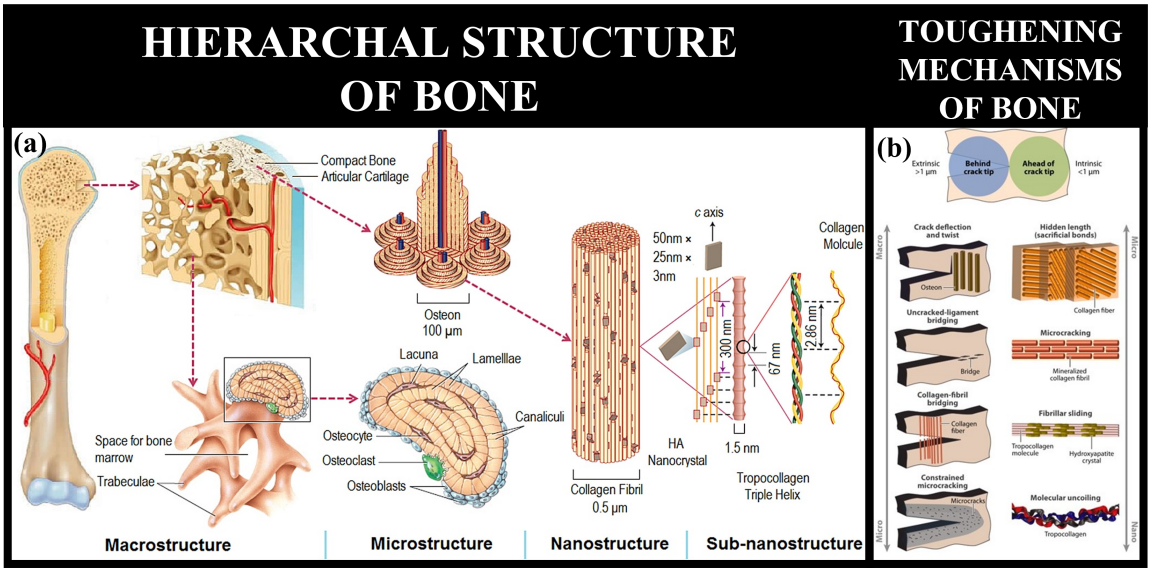

Figure 1.1.1: (a) The hierarchal structure of natural bone tissue visualizing the structural assembly from the atomic to the gross (overall) structure of a femur [8]. (a) This figure is presented unaltered from Figure 2 of Wang et al. entitled "Topological design and additive manufacturing of porous metals for bone scaffolds and orthopaedic implants: A review" [8]. (b) Schematic of the inherent toughening mechanisms present within natural bone from the nano- to macroscale demonstrating how bone exhibits its low-density high strength behavior [9]. (b) This schematic is presented unaltered from Figure 3 of Launey et al. entitled "On the Mechanistic Origins of Toughness in Bone" [9].

for infection [10–12]. Allographs, while addressing the resource limitations of autographs through harvesting of viable cadaver bone tissue, however introduce the risk of disease transmission and immunological rejection, thus presenting allographs as an imperfect solution [10–12], thus signaling the need for alternative approaches.

1.2 Significance of alternative approaches

Porous 3D scaffolds are attractive candidates for their promise in providing an ideal solution for addressing the needs required to successfully heal bone defects in load-bearing applications. The porous 3D structure allows for the simultaneous support of physiological load [13, 14] while aiding in the regeneration of bone [2, 15] by providing a template for the bone remodeling process. To achieve the full healing potential of scaffolds for addressing bone defects in load-bearing applications, the scaffolds must be multifunctional such that (1) their mechanical properties reflect the specific type of native bone present (Table 1.1.1), (2) stimulate biological responses necessary

for bone regeneration, and (3) exhibit antibacterial properties to combat the risk of infection.

Table 1.2.1: The mechanical properties of interest for cancellous and cortical bone [16–18].

Property	Cancellous bone	Cortical bone
Porosity(%)	40-95	5-15
Compressive strength (MPa)	0.2-12	100-200
Young's modulus (GPa)	0.05-0.5	7-30
Flexural strength (MPa)	10-20	135-193
Fracture toughness ($MPa \cdot m^{1/2}$)	0.1-0.8	2-6

The greatest need currently is developing a scaffold that satisfies all the above criteria for use in addressing the needs of bone defects in load-bearing applications. To date, no reports have detailed a scaffold capable of satisfying the mechanical, antibacterial, and biological performance requirements for targeting bone tissue regeneration in load-bearing applications. For example, metallic scaffolds have demonstrated their capabilities in achieving the requisite mechanical properties [13, 19, 20] at the expense of antibacterial and biological performance, while bioceramic and bioactive glass/glass-ceramic scaffolds display adequate antibacterial and biological performance [21–24], however, their intrinsically brittle behavior is not well-suited for targeting bone defects in load-bearing applications [25, 26].

1.3 Dissertation—Objectives & structure

This dissertation aims to develop a scaffold capable of satisfying the mechanical, antibacterial, and biological requirements for bone tissue regeneration that specifically address the requirements for targeting bone defects in load-bearing applications. To accomplish this, a multidisciplinary approach shall be implemented utilizing in-depth multiscale characterization to bridge the gap between process and performance (Fig. 1.3.1) to identify and execute advantageous, scientifically driven process modifications to not only deliver but also bring to the biomaterials field the needed knowledge to transform bioactive materials into porous scaffolds capable of adequately addressing the needs imposed by targeting bone tissue regeneration in load-bearing applications. Furthermore, following this approach will be critical to the successful development of class II bioactive glass

containing hybrid materials targeting softer tissue regenerative applications.

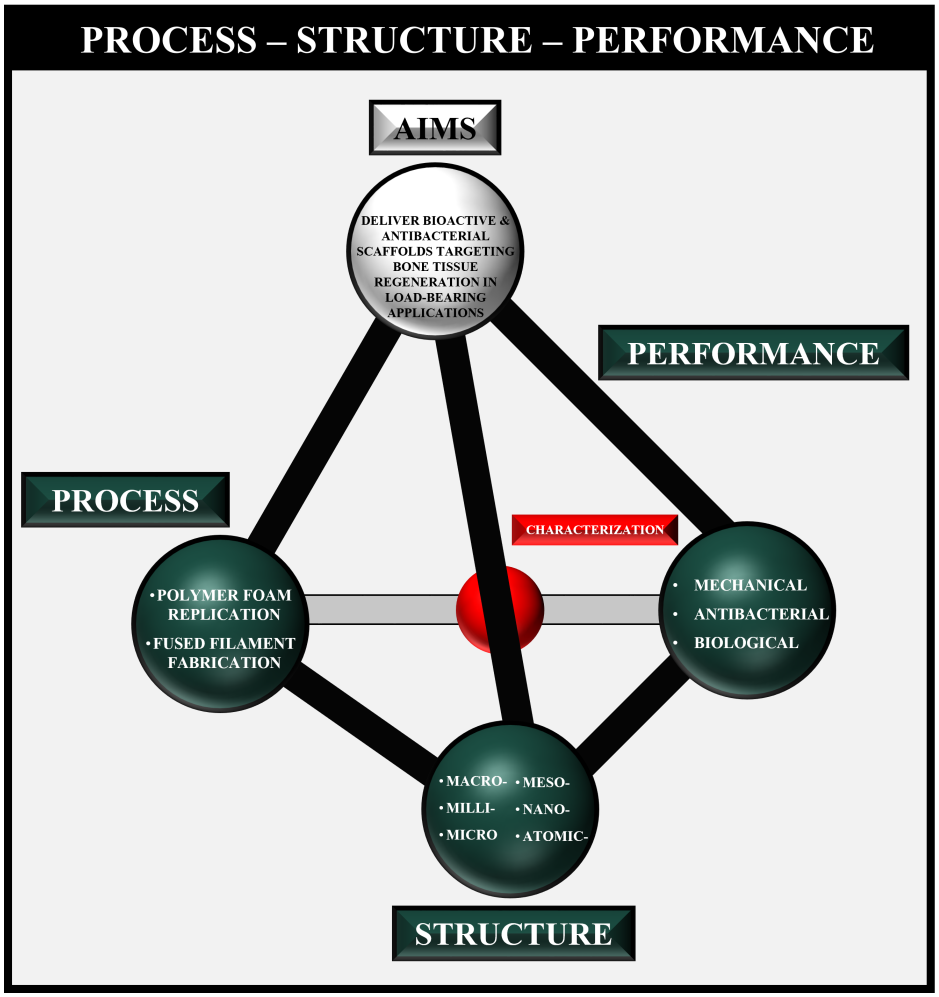

Figure 1.3.1: The process – structure – performance tetrahedron, visualizing the multidisciplinary approach used to deliver Ag-BG scaffolds capable of meeting the needs described in the "Aims" sphere.

CHAPTER 2

BACKGROUND

2.1 Bioactive glasses, glass-ceramics, & bioceramics

2.1.1 Genesis of bioactive ceramics

54 years ago, back in 1967, a researcher by the name of Larry Hench attended a United States Army Materials Research Conference to present his findings on the attractive radiation resistance of vanadium phosphate glasses [27, 28]. One fateful day, as Hench bussed to the conference, he spoke with an army colonel, Colonel Klinker, who had recently returned from the Vietnam war about the work he was presenting. During these discussions, Colonel Klinker asked Hench a simple question: "If you can make a material that will survive exposure to high energy radiation can you make a material that will survive exposure to the human body" [27]. The answer to this question would forever transform the biomaterials field.

In 1968, the United States Army Medical R and D command provided a year of funding for Hench to explore the following hypothesis: "The human body rejects metallic and synthetic polymeric materials by forming scar tissue because living tissues are not composed of such materials. Bone contains a hydrated calcium phosphate component, hydroxyapatite [HA] and therefore if a material is able to form a HA layer *in vivo* it may not be rejected by the body" [27]. One year later, in 1969, Hench demonstrated the remarkable bone-bonding ability of a glass composition in the system $45SiO_2$ – $24.5CaO$ – $24.5Na_2O$ – $6P_2O_5$ (wt%), later known by its registered trademark name 45S5 Bioglass, observing *in vivo* that his glass had bonded so well to the bone that the only way to remove the material was to break the bone [27, 28]. This marked the genesis of bioactive ceramics, opening an entirely new class of biomaterials for exploration.

2.1.2 Overall structures—Advantages & disadvantages

Bioactive glasses (BGs) are oxide-based glasses that are most commonly synthesized using silica as the primary network former. Silica is an attractive network former for synthesizing bioactive materials targeting bone tissue regeneration given the advantageous role Si atoms play in stimulating new bone growth [22, 29]. In silicate-based oxide glasses, Si atoms will form tetrahedral structures with 4 O atoms (i.e. SiO_4). In pure silica glasses, all the O atoms have Q^4 speciation, meaning all 4 O atoms bonded to the central Si atom in the tetrahedron are also bonded to other Si atoms, creating Si-O-Si linkages with the O atoms classified as a bridging O. The addition of network modifying atoms such as Ca, Na, and K act to perturb the silicate network by bonding with an O atom on a silica tetrahedron, thus creating what is known as a non-bridging oxygen. In terms of Q speciation, Q^3 species represent a silica tetrahedron having 3 bridging oxygens and 1 non-bridging oxygen, Q^2 species are comprised of a silica tetrahedron having 2 bonding oxygens and 2 non-bridging oxygens, Q^1 species contain 1 bridging oxygen and 3 non-bridging oxygens, and Q^0 species describes a silica tetrahedron having zero bridging oxygens and 4 non-bridging oxygens.

Examination of the Q speciation of a silicate-based oxide glass provides some insight into the rate of dissolution the glass might experience when immersed in an aqueous solution. This is because each addition of a non-bridging oxygen introduces more disorder into the glass network resulting in an increase in free volume that translates to a faster rate of dissolution. Therefore, the dissolution rates can be generalized by the following rankings from fastest to slowest dissolution rate: $Q^0 > Q^1 > Q^2 > Q^3 > Q^4$ [30]. Bioactive glasses such as 45S5 possess low Q speciation due to the large number of network modifiers present allowing them to degrade quicker and stimulate the necessary mineralization for bone bonding [30].

An additional advantage to the use of silicate-based bioactive glasses for targeting bone tissue regeneration is the ease at which network modifying ions can be incorporated, as eluded to previously. As a result, silicate-based bioactive glasses possess remarkable versatility in which their composition can be specifically tailored to tune their performance characteristics to deliver

an "ideal" material for targeting bone tissue regeneration. There has been strong interest in doping these silicate-based bioactive glasses with Ag to impart inherent antibacterial capabilities. The final form of Ag for most of these compositions is found in the form of particles, as Ag has a stronger propensity to bond with itself rather than be incorporated into the silicate network like other modifying atoms such as Ca or Na. While Ag particles are known to exhibit some antibacterial properties, Ag^+ ions are known to be a more potent antibacterial agent. Thus, to maintain Ag^+ in its ionic form, Chatzistavrou et al. identified a viable process for synthesizing an Ag-doped bioactive glass composition engineered specifically to preserve Ag^+ ions. For this reason, in addition to the well-documented biocompatibility and simultaneous delivery of therapeutic agents capable of addressing the needs of diseased and damaged bone [31–41], was the motivation behind selecting this specific Ag-doped bioactive glass-ceramic composition for developing 3D bioactive glass-ceramics.

Specifically, the first reported use of Ag-BG was in 2012, where Chatzistavrou et al. designed a bioactive glass-ceramic composition to be synthesized by the solution-gelation (sol-gel) process, modeled after the well-documented sol-gel derived 58S ($58SiO_2 - 33CaO - 9P_2O_5$ (wt%)) bioactive glass composition [42–50], and modified to take into account the findings by Kawashita et al., whose work demonstrated the viability of incorporating and stabilizing Ag^+ ions in sol-gel derived silica compositions containing Al to deliver materials with controlled and potent antibacterial properties [51–53]. The incorporation of Al in combination with the sol-gel process, theoretically, generated the conditions required to allow for the formation of $[AlO_4]^-$ molecules [51], thus presenting negatively charged species that can be electrically neutralized by the presence of cations such as Ag^+ ions. This hypothesis was reportedly verified in 2014 [32] through the use of ^{27}Al magic angle spinning – nuclear magnetic resonance (MAS-NMR) performed by Chatzistavrou et al. confirming the predominant status of Al to be $[AlO_4]^-$ charge compensated by Ag^+ ions.

The delivery of therapeutic concentrations of an antibacterial agent such as Ag^+ ions required a controllable and sustainable release of Ag^+ ions at a concentration between 0.1 ppm and 1.6 ppm [32] to (1) effectively destroy bacteria without (2) causing cytotoxicity for eukaryotic cells. Satisfaction

of these two criteria was achieved when an Al/Ag molar ratio of ~4.5 was used, demonstrating effective antibacterial capabilities for combating *Staphylococcus aureus* (S. aureus) bacteria whilst preventing cytotoxic effects on human gingival fibroblasts [33]. Further studies found that Ag-BG was effective at combating *Escherichia coli* (E. coli) [31, 32, 35], *Enterococcus faecalis* (E. faecalis) [31, 32], *Streptococcus mutans* (S. mutans) [31, 34–36, 54], and *Lactobacillus casei* (L. casei) [36, 54], thus presenting a strong case for the selection of the Ag-BG composition to develop 3D scaffolds capable of treating infection-induced bone damage [37, 55] while simultaneously facilitating bone tissue regeneration.

While many advantages to the use of bioactive glasses in the development of 3D scaffolds for bone tissue regeneration have previously been described, their most pronounced disadvantage is their mechanical performance. Glasses, glass-ceramics, and bioceramics, while possessing the greatest stiffness amongst the different classes of materials (i.e. metals, polymers, and composites) due to the ionic bonding between atoms, are inherently brittle, exhibiting catastrophic failure without warning [56]. Creating porous 3D scaffolds out of glasses, glass-ceramics, and bioceramics further extubates this disadvantage, as the introduction of porosity significantly weakens their mechanical performance compared to their bulk counterparts [57]. Overcoming these challenges to unite reliable and satisfactory mechanical performance with the attractive biological (and antibacterial) of bioactive glasses, glass-ceramics, and bioceramics will be key in delivering the ideal 3D scaffold for targeting bone tissue regeneration in load-bearing applications.

2.1.3 Influence of composition on thermal behavior

The composition of bioactive glasses is known to play a large role in the thermal behavior exhibited during heat treatment, dictating whether the glass will undergo viscous flow and deliver an amorphous (i.e. a material lacking long-range order) or undergo densification through crystallization delivering either a glass-ceramic or ceramic structure. For example, take the 45S5 bioactive glass composition, reported above in Section 2.1.1, and 13-93 bioactive glass in the system $53SiO_2$ – $12K_2O$ – $6Na_2O$ – $5MgO$ – $4P_2O_5$ – CaO (wt%). Synthesizing 3D scaffolds using the same

processing technique delivering scaffolds of comparable porosity, the mechanical performance for 13-93 bioactive glass surpassed that of 45S5 by a margin greater than 2,500% [58]. This stark difference was correlated to the ability of 13-93 bioactive glass to exhibit viscous flow during heat treatment, allowing for the struts to fully densify, whereas, for 45S5 bioactive glass, its composition exhibits minimal viscous flow characteristics, leading to partial strut densification as a result of the crystallization that takes place during heat treatment [59]. Compositionally, the increase in silica concentration provides a sufficient amount of network formers that in conjunction with the 4-fold reduction in Na2O provides suppresses the tendency of the 45S5 BG system to crystallize into combeite ($Na_2Ca_2Si_3O_9$) [25, 60]. It should be noted as well that the presence of Mg and K in the 13-93 BG composition plays a large role in eliciting viscous flow at temperatures below the onset of crystallization [61–66]. The addition of Mg has been demonstrated to decrease the glass transition temperature and dilatometric softening point, thus helping to increase the temperature range for sintering as a result of the comparatively weak Mg-O bonds to Si-O bonds [66, 67]. The presence of K meanwhile helps to lower the required sintering temperature, with reports detailing K-containing BG having the ability to undergo sufficient viscous flow at temperatures as low as 750ºC [62], thus preventing the need to use temperatures known to induce crystallization making it an attractive composition for 3D BG scaffold synthesis [59, 63].

2.1.3.1 Sintering mechanisms

As previously eluded to, sintering of glasses, glass-ceramics, and ceramics can either occur by way of viscous flow or by undergoing densification after crystallization. For glasses able to undergo viscous flow, once they reach temperatures above their glass transition temperature, the glass is soft enough to allow sufficient flow of the material, allowing for densification to occur if the viscosity is sufficiently low and the surface tension sufficiently high [68–71].

If, however, the surface tension is sufficiently low and the viscosity sufficiently high, BG systems have a propensity to undergo crystallization, transforming them from a bioactive glass to a bioceramic, where 6 different sintering mechanisms can occur (Fig. 2.1.1). Examination of the

diffusion rates of the main diffusion mechanisms occurring (i.e. surface diffusion, grain boundary diffusion, and lattice diffusion) can be generalized by the following ranking: surface diffusion > grain boundary diffusion > lattice diffusion [72]. Surface diffusion shows the highest rate of diffusion out of the three main groups previously described as a result of the increased free energy due to the dangling bonds present, thus providing a driving force for the atoms to reconfigure into a lower energy state [72]. Grain boundary diffusion occurs at a slower rate than surface diffusion as the driving force for the atoms to rearrange into lower-energy configurations is lessened as dangling bonds are less plentiful, only existing due to the vacancies present at the grain boundaries [72]. Lattice diffusion has the lowest rate amongst surface and grain boundary diffusion as diffusion can only occur through vacancy mobility, which does not become appreciable until there are sufficient vacancies generated through the increased activity of phonons [72].

Examining Figure 2.1.1 in more detail, there is a balance of forces at play that will dictate whether densification will occur during sintering. At lower sintering temperatures, atomic diffusion is faster on the surface than within the lattice given the greater concentrations of vacancies on the surface as opposed to the lattice. This results in increased compressive sintering stress being applied compared to the tensile sintering stress from lattice and grain boundary diffusion [70, 72]. At higher sintering temperatures, the balance between compressive and tensile sintering stresses changes due to the increased vacancy concentration inside the lattice providing a stronger driving force for atomic diffusion from the interior to the neck of the particle, causing neck growth as grain boundary and lattice diffusion to become dominant resulting in densification [70, 72]. These phenomena are explored further in Section 4.1.1. It is important to note that while sintering through plastic flow is a sintering mechanism presented in Figure 2.1.1, this mechanism is not explored for ceramics and is thus assumed to be negligible.

2.1.3.2 Kinetics

Kinetically, a time-temperature-transformation (TTT) curve excellently illustrates the competition between nucleation and grain growth allowing for careful selection of the applied heat treatment

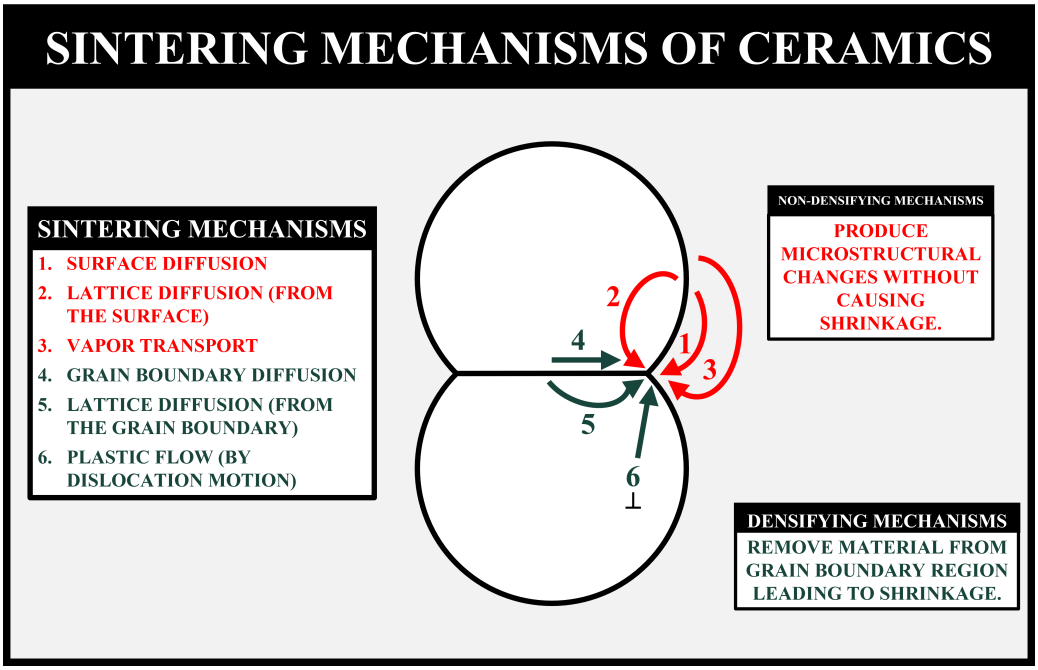

Figure 2.1.1: The six different known sintering mechanisms for ceramics. Figure reproduced from figure 4.1.1 from Chapter 4 in the text entitled, "Handbook of Advanced Ceramics" written by Lutgard C. De Jonghe and Mohamad N. Rahaman [70].

and providing a method for microstructural design. For BGs, the closest analog to a relevant TTT curve was the one reported for the eutectic apatite – wollastonite (i.e. $40Ca_3(PO_4)_2$ – $60CaSiO_3$) glass composition by Magallanes-Perdomo et al. [73]. The TTT curve elucidated by Magallanes-Perdomo et al. (Fig. 2.1.2). From this TTT curve, a basic understanding of the potential phases that may form during heat treatment of Ag-BG scaffolds can be obtained. The semi-transparent yellow rectangle in Figure 2.1.2 represents the ranges of sintering temperatures and durations used in the synthesis of Ag-BG scaffolds. Although the figure reported by Magallanes-Perdomo et al., as shown in Figure 2.1.2, should have reported time on a logarithmic rather than linear scale, it is minorly useful in that it provides some insight into the phases and phase transformations that may occur during sintering of Ag-BG scaffolds. A detailed description of the transformations occurring in Ag-BG during sintering can be found in Section 5.1.2.

2.1.4 BG synthesis methods

There are two fundamentally different pathways to process BGs: the melt-derived and solution-

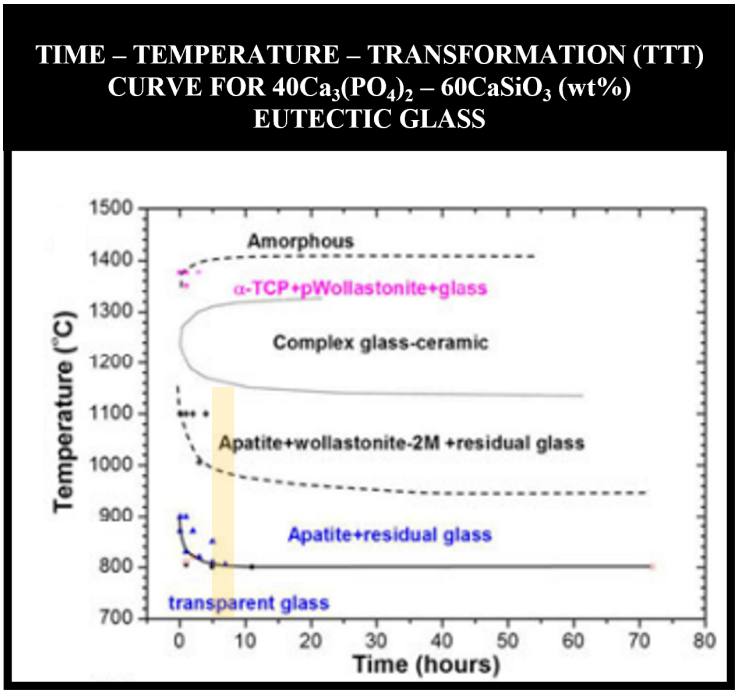

Figure 2.1.2: Time – Temperature – Transformation (TTT) curve for the eutectic apatite – wollastonite (i.e. $40Ca_3(PO_4)_2$ - $60CaSiO_3$ glass composition. This figure was reproduced from figure 3a in Magallanes-Perdomo et al. entitled "Structural changes during crystallization of apatite and wollastonite in the eutectic glass of $Ca_3(PO_4)_2$ - $CaSiO_3$" [73]. The semi-transparent yellow rectangle annotated onto this figure represents the times and temperatures applied for Ag-BG scaffold synthesis.

gelation (sol-gel) techniques. Their methods, advantages, and disadvantages will be explored herein.

2.1.4.1 Techniques

Melt-derived BGs are synthesized through the melting of the desired reagents, where sufficient time is given to the reagent melts so that homogenization of the elements can occur. The melt is then quenched, solidifying the melt quickly enough to prevent crystallization, forming an amorphous BG that should lead to preferential biological performance characteristics. Disadvantageous to the melt-derived technique, however, is the low surface area (i.e. $\sim$1 m^2 g^{-1}) delivered, which limits the concentration of silica to a maximum of 60 mol% of silica before bone-bonding behavior is no longer observed [49, 50].

The sol-gel technique, however, instead of preparing BG through a quenching process, starts

under ambient temperatures and pressures, where the temperature is carefully raised in stages in an attempt to deliver an amorphous BG. During this process, as volatiles are evaporated, micro-, meso-, and nanosized pores are formed, allowing for surface areas exceeding 100 m^2 g^{-1} [49, 50] to be achieved, thus allowing bone-bonding behavior to be exhibited in glass systems containing a maximum 90 mol% of silica.

In detail, the synthesis of sol-gel BGs involves the dissolution of precursors in an aqueous environment before a low-temperature (T~700°C) heat treatment. Metal alkoxides [74] (e.g. tetraethyl orthosilicate (TEOS) and triethyl phosphate (TEP)) are typical network forming precursors and nitrate-based salts typically used as the network modifying precursors. The production of BGs is accomplished under acid catalysis to promote the hydrolysis of the network forming precursors. Hydrolysis of TEOS (Eq. 2.1.1) [75] promotes the formation of silanols that will subsequently go through a condensation reaction (Eq. 2.1.2) [75] that over time produces a silicate network.

$$Si(C_2H_5O)_4 + 4H_2O \rightarrow Si(OH)_4 + 4C_2O_5OH \tag{2.1.1}$$

$$2Si(OH)_4 \rightarrow 2(Si\text{-}O\text{-}Si) + 4H_2O \tag{2.1.2}$$

As the reactions proceed, the network modifying ions (i.e. Na^+, K^+, etc.) begin to be trapped within the silicate network. Once solution homogenization is achieved, the sol undergoes an aging process (~60°C) to promote the condensation reactions to favor nucleation and growth of silicate-based colloids that will coalesce into a gel [76]. It is important to note that during aging, the reaction conditions do not favor the entrapment of Ca^{2+} ions in the network and instead see their segregation into the pore liquor as calcium nitrate (CaNT) [77]. The aged gel is then dried (T<180°C) to remove the remaining water, and at this stage, CaNT is found to surround the silicate-based particles [78]. To remove toxic byproducts and converge the strength and hardness of the silicate-based material towards glass-like behavior, calcination is required and is typically performed at ~600°C [79]. During this process, as temperatures exceed 400°C, Ca^{2+} ions begin to diffuse and modify the

silicate network [15]. After calcination, silicate-based BGs undergo a thermal stabilization process (T=700°C) [80], which can be used to alter the physical and textural properties of the final product.

2.1.4.2 Mechanism of bioactivity

The mechanism by which BGs bond to bone is a process that has been well-established in the literature [81–84] with the first five stages explored herein. To start, the first stage is a preferential ion-exchange corrosion process whereby network modifying ions (i.e. Na^+, Ca^{2+}) are leached into the solution and exchanged with H^+ ions leading to a local increase in basicity. This promotes hydroxyl ions (OH^-) to attack the silica network resulting in both the release of soluble silica in the form of silicic acid ($Si(OH)_4$) and the formation of silanols (SiOH), representing the second stage. In the third stage, the silanols polymerize forming a silica-rich gel leading up to the fourth stage that sees the adsorption of Ca and P containing species forming an amorphous calcium phosphate (ACP) layer. CO_3^- are additionally adsorbed, and over time, the fifth stage sees the ACP layer crystallize into a hydroxycarbonate apatite (HCA) layer. The remaining stages concern the biological reactions occurring *in vivo* [82, 83] resulting in the formation of new bone tissue.

2.2 Cellular solids

2.2.1 Ideal 3D scaffold for bone tissue regeneration

2.2.1.1 Hard tissue applications

The following criteria should be satisfied when developing an ideal scaffold for targeting bone tissue regeneration in load-bearing applications: (1) observable osteoconduction and osteoinduction, (2) support physiological loads, (3) controllable macro- to nanostructure, (4) degradation rate matching new bone tissue formation, (5) provide a bactericidal environment during tissue regeneration to prevent infection-related failure, (6) interconnected highly porous 3D structure, and (7) mean pore diameter >300 μm to promote sufficient delivery of nutrients to the interior of the scaffold [4, 13, 17, 26, 32, 85–87].

2.2.1.2 Soft tissue applications

BG-containing hybrid scaffolds are becoming an area of increased focus within the biomaterials field for their ability to target softer tissue regeneration and allow for more complex tissue systems to be targeted [4, 88–91]. The high stiffness of BGs, while attractive for targeting hard tissue regeneration such as bone, are not suitable for the softer mechanical requirements for targeting regeneration at, for example, the osteochondral interface [88–90]. To overcome this, it has been of great interest to combine BGs with biocompatible polymers (i.e. polycaprolactone (PCL), polylactic acid (PLA), poly(vinyl) alcohol (PVA) etc.) to combine the tissue regenerative abilities of BGs with the softness of biocompatible polymers.

The conventional approach applied to target softer tissue regeneration has been in the synthesis of composites, and more specifically nanocomposites, to homogenize the materials characteristics down to the mesoscale [5, 92–145]. However, this approach fails to unlock the full potential of combining a biocompatible polymer with BGs and limiting scaffold synthesis to spatial control.

To overcome the previously mentioned limitations, reports within the last 10 to 15 years have detailed investigations on methods to combine bioceramics and biocompatible polymers at the finest possible scale [15]. From this work, five different classes of hybrid materials have been developed, as shown in Figure 2.2.1.

In Figure 2.2.1, a class I hybrid material is formed through the entanglement of the biocompatible polymer (organic) within a BG (inorganic) network. The organic and inorganic networks are bonded together by intermolecular forces [28, 146, 147]. A class II hybrid material (Fig. 2.2.1) is similar to a class I hybrid material in that the organic network is entangled within the inorganic network, yet dissimilar in that a coupling agent is used to mediate the bonding between the organic and inorganic networks, allowing for covalent bonds to serve as the connections. This allows for a greater homogenization of the materials exhibited by the class II hybrid compared to a class I hybrid [28, 146, 147]. In class III hybrid materials (Fig. 2.2.1), instead of the organic network becoming entangled with the inorganic network, both organic and inorganic networks are found to be mutually penetrating with intermolecular forces bonding said networks [15]. A class IV hybrid

material (Fig. 2.2.1) is similar to a class III hybrid material in that both organic and inorganic networks are mutually interpenetrating, yet dissimilar in that covalent bonds are used to connect the organic and inorganic networks [15]. Important to note about class IV hybrids is that this mutual interpenetrating covalent bonding scheme is only possible when both the organic and inorganic networks are formed in situ [15, 146]. Lastly, class V hybrid materials describe a non-shrinking sol-gel composite [15].

Since the use of biocompatible polymers restricts the maximum processing temperature that can be applied, this presents a particular challenge for successful incorporation of a BG system given that temperatures exceeding 400ºC are required for successful Ca incorporation into a silicate network, as previously described. Different inorganic (i.e. CaNT [148, 149], $CaCl_2$ [148, 150]) and organic precursors (i.e. $Ca(OH)_2$ [148], $C_6H_{14}CaO_4$ [148, 149], $C_4H_{10}CaO_2$ [148], $Ca_3(C_6H_5O_7)_2$ [148], and $Ca_4H_6CaO_4$ [148]) have all claimied successful incorporation. It should be noted, however, that such reports of successful Ca incorporation into hybrid materials fail to report supporting visual evidence using energy dispersive spectroscpy (EDS) in either scanning electron microscopy (SEM) or transmission electron microscopy (TEM), thus convoluting claims of successful Ca incorporation [148–150]. This will be explored further starting in Section 3.2.4.

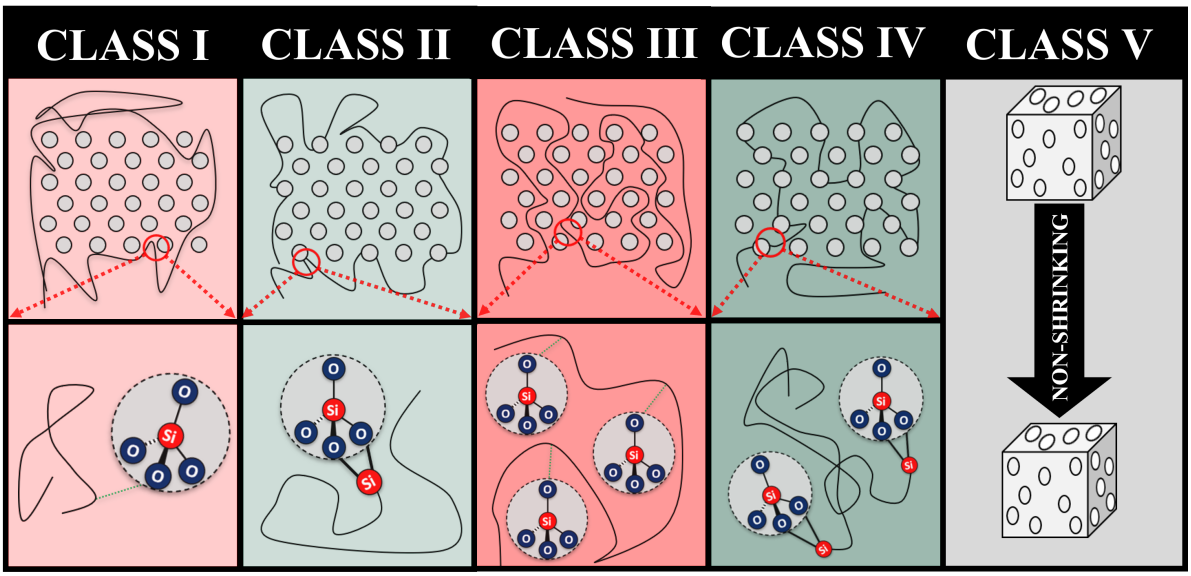

Figure 2.2.1: The five different classes of polymeric – silicate-based hybrid materials [28, 146, 147].

2.3 3D scaffold synthesis approaches

2.3.1 Polymer foam replication technique

In 1963, Schwartzwalder and Somers patented a method for delivering porous ceramic material, using an open-celled polymeric foam as a sacrificial template [151]. Given its genesis was before the conception of BGs, it is not surprising that this became a well-studied technique for delivering BG scaffolds [16, 25, 57, 58, 152–159]. In brief, the polymer foam replication technique is most well-known for using a slurry of ceramic particles in combination with a polymeric binder to adhere the ceramic particles to the sacrificial open-cell polymeric foam template [151]. During heat treatment, the slurry-coated foams are vaporized, and ceramic particles sintered together, delivering a 3D porous structure with potential for targeting bone tissue regeneration at the expense of delivering hollow internal structures. It should be noted, however, that while less well-known, the polymer foam replication technique is compatible with the sol-gel process, using the sol to coat the sacrificial template rather than particles, termed as the solution technique [154–156, 158, 159]. As a result, greater control over the delivered microstructures is possible. Both solution (Section 3.2.1.1) and slurry-based (Section 3.2.1.2) polymer foam replication processes will be explored herein, elucidating the advantages and disadvantages to each technique in Section 4.2.

2.3.2 Additive manufacturing

In recent years, the biomaterials field has gravitated towards utilizing additive manufacturing (i.e. 3D printing) techniques for the fabrication of bioactive bioceramic scaffolds for bone tissue regeneration [160–165]. Additive manufacturing has the advantage of being able to precisely control pore geometry, strut thickness, and consequently porosity [166], while also eliminating processing defects (i.e. internal porosity) known to occur when using the polymer foam replication technique. Control over these structural characteristics help to achieve improved mechanical performance to deliver reliable and mechanically competent 3D scaffolds for targeting bone tissue regeneration in load-bearing applications. Dispensing-based 3D printing techniques, such as direct

ink writing (DIW), have gained popularity for 3D printing bioceramic scaffolds [167–170] given their capability of creating different printable pastes from a wide range of materials (e.g. micro- or nanosized calcium phosphates (CaP), hydroxyapatite (HA), β-tricalcium phosphate (β-TCP), carbonated Ca-deficient hydroxyapatite (CDHA), bioactive glasses, etc.). Successful fabrication of 3D scaffolds using the DIW requires, however, precise control over the rheological properties during the printing process, an understanding of the rheological properties of the ink, and ensuring a rapid ink-to-gel transition that is capable of sustaining the applied forces from subsequently printed layers [160, 171, 172]. Furthermore, precise control over the surrounding environment is advantageous as temperature and pH modulations can affect the stability and fluid-gel transition, thus affecting the quality of the resulting 3D scaffold [160]. Such optimization over the ink can be time-consuming and tedious, warranting exploration of the benefits of other additive manufacturing techniques.

Other 3D printing techniques such as selective laser sintering (SLS) or binder jetting (BJ) are powder bed processing approaches [173]. First, a homogenous powder bed surface is created by spreading fine powder particles using a set of rollers [174]. The flowability of the powder is critical for successful processing, depending on particle size, shape, and surface roughness [173, 175]. The size of said powder granules determines the smoothness and resolution of the final printed construct. Here, the use of a finer powder allows a thinner print layer and better print resolution [176]. However, fine powders tend to agglomerate due to van der Waals forces [177], resulting in poor flowability, compaction, and unacceptable powder bed recoating. Hence, relatively large particles of 50-150 μm are usually used, limiting the resolution and surface finish. Additionally, said techniques are not only costly but the powder bed concept also makes it challenging to remove powder from clogging the pores of the printed scaffold.

An additional 3D printing technique, fused filament fabrication (FFF), has received increasing attention as a potentially viable processing approach for delivering 3D scaffolds for targeting bone tissue regeneration. Rather than using pastes or inks, a biocompatible thermoplastic is used as feedstock for 3D printing pure biocompatible polymer and biocompatible polymer–particle

composite scaffolds. The most popular implementation of the FFF technique for synthesizing bioceramic (i.e. < 20 wt% of bioceramic particles) scaffolds has primarily focused on producing biocompatible thermoplastic-based (i.e. polycaprolactone (PCL), polylactic acid (PLA), polyvinyl alcohol (PVA), etc.) biocompatible polymer (> 80 wt%) composite scaffolds to improve degradation and impart regenerative capabilities to the scaffolds [95, 108, 178–180].

2.3.2.1 Processing fundamentals for fused filament fabrication

In 1988, Scott Crump created the technology for the FFF technique under the trademarked name fused deposition modeling (FDM), with Stratasys Inc., USA commercializing the technology in 1992 [181, 182]. Since then, the FFF technique has become a widely popular 3D printing technique for the low-cost of entry for the technology, benchtop compatibility, ability to fabricate 3D objects in a support-free manner, and ease of utilizing multiple materials [172, 181, 183, 184].

Successful synthesis of highly filled composite filaments requires investigation into the printability of the as-prepared filament, the viscosity of the filament melt during the 3D printing process, achieving adequate interaction between the components within the filament, and ensuring the components within the filament exhibit a homogenous distribution [185, 186]. Optimization of these characteristics is accomplished by studying the thermal, mechanical, and rheological behavior of the filament with additional investigations into the effect of particle loading, particle shape, and particle size distribution determine printability.

Advantages of the FFF technique include the ease of process application in addition to a variety of different parameters that can be manipulated to optimize the printed scaffold [184]. Additionally, this technique has the ability to 3D print free-standing objects along with the capacity to print multi-material objects [172, 183]. The applicability of the FFF technique for targeting bone tissue regeneration, however, is challenged by the incorporation of appropriate amounds of bioceramic particles without compromising the printability of the filament [185].

Utilization of the FFF process for 3D printing requires the preparation of a filament composed primarily of thermoplastic(s), and if applicable, the addition of filler particles. The composite

filaments are typically prepared by compounding processes using, for example, a twin-screw extruder for preparing pellets containing homogeneously distributed particles in the polymer matrix for subsequent extrusion using a single screw extruder to extrude a filament having a precise and consistent diameter. For the 3D printing process itself, the filament is fed from a spool into the liquefier at a constant speed where the filament is melted at a preset temperature to prepare it for extrusion through the print nozzle, thus limiting print resolution to the diameter of the print nozzle. The as-deposited filament melt will bond to its adjacent layer as it solidifies, thus resulting in the formation of the next layer in the printing sequence. This process will repeat itself until the 3D printed object has been fully constructed.

2.3.2.1.1 Filament printability

Assessing the printability of an as-prepared filament can be accomplished following the analytical approach described in equation 2.3.1 [99, 187–189], where E describes the compressive modulus of the filament, η_a represents the apparent viscosity of the filament melt, Q describes the volumetric flow rate of the filament melt through the print nozzle, L represents the length of the print nozzle, l describes the distance the filament has to travel from the rollers to the top of the liquefier, r represents the radius of the filament, and R describes the radius of the print nozzle.

$$\frac{E}{\eta_a} > \frac{2QL(\frac{l}{r})^2}{\pi^3 R^4} \tag{2.3.1}$$

To successfully implement equation 2.3.1, the thermal behavior of the filament should be characterized to determine the working temperature range. The working temperature range is dependent on the material selection of the as-prepared filament (i.e. the thermoplastic) that is modified through the addition of filler particles (e.g. bioceramic particles). The effect of the print temperature on the mechanical performance of PVA/β-TCP (80/20 wt%) composites was elucidated by Chen et al. identifying a dependency correlated to different interfacial bonding strengths between print layers [99].

It is important to note that the equation describing the printability of an as-prepared filament

(Eq. 2.3.1) derives from the combination of Euler's buckling analysis (Eq. 2.3.2) [187–189] of the filament and the Hagen-Poiseuille equation (Eq. 2.3.3) [187–190]. Euler's bucking analysis (Eq. 2.3.2) describes the stress experienced by the filament as it travels from the rollers to the top of the liquefier and can be used to evaluate whether the stress on the filament has exceeded a critical threshold. The inequality in equation 2.3.2 describes this, and the satisfaction of said inequality will result in the filament buckling as it enters the liquefier disrupting the printing process.

$$\sigma_{cr} < \frac{4\pi E}{(\frac{l}{r})^2} \tag{2.3.2}$$

Euler's buckling analysis is limited to describing the stress at the entrance of the liquefier, thus a description of the forces as the filament melt exits the print nozzle is required. The Hagen-Poiseuille equation (Eq. 2.3.3) serves this function by describing the pressure drop as the filament melt is extruded through the print nozzle and is dependent on the viscosity of the melt (characterized via a capillary rheometer), the volumetric flow rate (empirical), and the geometry of the print nozzle (fixed).

$$\Delta P = \frac{8\eta_a Q L}{\pi R^4} \tag{2.3.3}$$

The empirical evidence collected coupled with the unity of equations 2.3.2 and 2.3.3 allows for the printability equation (Eq. 2.3.1) to be derived, which can be further extrapolated to show how the printability of the filament varies as a function of viscosity and shear rate as was demonstrated by Chen et al. who elucidated the printable-unprintable boundary as a function of melt viscosity and shear rate for PVA—β-TCP composites containing 5-20 wt% β-TCP [99].

2.3.2.1.2 Viscosity of filament

When as-prepared filament melts are evaluated for their rheological behavior, they behave as a non-Newtonian fluid exhibiting shear-thinning behavior [99] allowing for the viscosity of the filament melt to decrease at increasing shear rates. This relationship can be inferred from the printability plot in Figure 2.3.1, and assuming the compressive modulus of the filament is constant

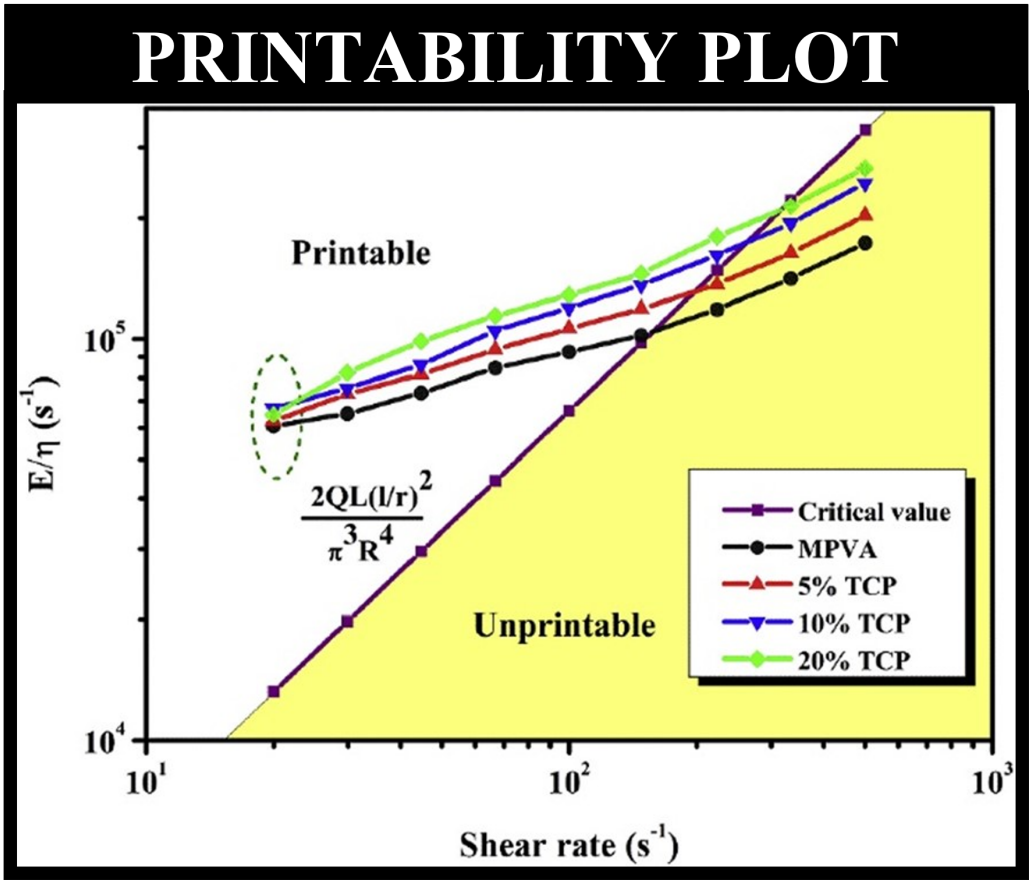

Figure 2.3.1: The printability plot, as reported by Chen et al., shows the ratio of compressive modulus to apparent viscosity as a function of shear rate for PVA — β-TCP ranging from a β-TCP concentration (wt%) from 5-20% [99].

and can be negated, the printability plot becomes the inverse filament melt viscosity as a function of shear rate, thus confirming the pseudoplastic nature of the filament melt. Characterization of the viscosity of the filament melt is typically performed through the use of a capillary rheometer evaluating shear rates from 10-1000 s^{-1} as these conditions best replicate the FFF printing process [99, 163, 188].

When the printing temperature is assumed to be fixed, the rheological behavior of the as-prepared filament is dependent on the filament composition, filler particle concentration, and particle size distribution. The materials selection for non-sinterable filaments is limited to thermoplastics and filler particles limited typically to 20 vol% or lower as increased concentrations run a significant risk of compromising the FFF printing process (i.e. melting temperature exceedingly high, detrimental

embrittlement). Therefore, there is limited flexibility when attempting to modify the viscosity of the filament melt through a compositional approach and the impact of the filler particles used thus becomes of great interest.

To start, the use of a unimodal distribution of coarse filler particles is known to have a straightforward effect on the viscosity of the filament melt. As the concentration of filler particles increases, so will the viscosity of the filament melt. The maximum concentration of filler particles is thus limited based on the packing efficiency of said coarse particles. For random spherical, loosely packed particles result in maximum incorporations of 55 vol%, whereas compact packaging allows for maximum achievable incorporations of approximately 63.4 vol% [191]. Consider now a bimodal distribution of filler particles created by combining the concentrations of coarse and fine filler particles using an arbitrarily defined ratio. The fine particles serve to occupy the vacant spaces created by the coarse particles resulting in an improvement in the overall packing efficiency of the filler particles. Based on this, when the overall filler particle concentration is fixed, the bimodal distribution of filler particles will exhibit a lower viscosity compared to a unimodal distribution due to the improved packing efficiency [191]. This relationship thus allows for the increased filler particle concentrations within the filament without causing significant deviations in the viscosity of the filament melt [192] that theoretically can achieve a loading of 72.5 - 75 vol% [192].

Mathematically, the model developed by Farris was formulated to describe the relationship of viscosity to particle size distribution with further extrapolation of said model to describe the lower bound of viscosity for a multimodal suspension (i.e. filament melt) [192]. Equations 2.3.4 and 2.3.5 describe how to quantify the overall filler particle concentration of a multimodal system (Eq. 2.3.4) and how to quantify the relative viscosity of each filler particle component.

$$\ln(1 - \Phi_r) = \sum_{i=1}^{N} \ln(1 - \Phi_i) \tag{2.3.4}$$

$$\ln(\eta_r) = \sum_{i=1}^{N} \ln(H(\Phi_i)) \tag{2.3.5}$$

In Equation 2.3.4, Φ_r represents the overall filler particle concentration, Φ_i describes the filler particle concentration of an individual particle size distribution, and N represents the nth filler particle mode being considered. In Equation 2.3.5, η_r describes the overall relative viscosity of the suspension (defined as the quantity of the filler particle-polymer viscosity over the viscosity of the polymer alone), and $H(\Phi_i)$ represents the relative viscosity when considering an individual filler particle mode as a function of its concentration.

Additionally, Farris demonstrated a mathematical method to optimize the ratios of a multimodal filler particle suspension to compute the lower bound of viscosity through differentiation of the relative viscosity with respect to filler particle concentration, and the result is shown as equation 2.3.6 [192].

$$0 = \sum_{i=1}^{N-1} [\frac{\partial \ln(H(\Phi_i))}{\partial \Phi_i} - (\frac{1-\Phi_N}{1-\Phi_i})\frac{\partial \ln(H(\Phi_N))}{\partial \Phi_i}] d\Phi_i \tag{2.3.6}$$

In equation 2.3.6, Φ_n represents the concentration of the nth mode being considered, and $H(\Phi_N)$ describes the viscosity of the next largest particle size distribution as a function of concentration [192]. Advantageous of utilizing the model developed by Farris is that it can be extrapolated to an infinite modal filler particle suspension providing versatility. It is important to note, however, that the model created by Farris assumes that all filler particles are spherical and the net particle-particle interaction is zero. The model, nevertheless, is useful in approximating the viscosity that the filament melt may exhibit. There are ongoing efforts however in the field of rheology working towards developing an ideal model that can best describe the viscosity of a multimodal suspension [193–198].

2.3.2.2 Bioprinting

Within the biomaterials field, 3D bioprinting has recently become a viable and attractive processing method for delivering cell-laden 3D scaffolds for targeting more sophisticated tissue engineering applications, allowing for biomimetics to be engineered into the printed scaffolds, this increasing their customizability to meet patient-specific needs [199]. Just as the adaptation of 3D

printing techniques was a disruptive technology, 3D bioprinting is expected to have an even greater disruptive effect on the biomaterials and biomedical engineering fields, allowing for customizable medicine to come to fruition [200, 201].

To create a printable bioink, a liquid matrix capable of undergoing rapid solidification post-printing is needed in addition to providing a suitable environment for cell incorporation [202, 203]. Successful 3D bioprinting relies on the use of extrusion-based printing techniques known to reduce cell viability due to the shear forces introduced during the extrusion process. Typically, bioinks used for 3D bioprinting of scaffolds aimed at bone tissue engineering applications incorporate osteo-promotive elements [204] such as Ca-based bioceramics [205, 206] or silicate-based biomaterials [207, 208] in the form of either micro-sized [208] or nano-sized particles [202, 205, 207, 209, 210]. The particles are introduced into the cell-laden polymer matrix through mixing allowing for a bioink compatible with 3D bioprinting [211]. For example, nanoparticles (NPs) of silicate glasses have been combined with gelatin methacryloyl (GelMA) forming nanocomposites [212]. Such nanocomposite bioinks are limited to the degree of homogeneity they can achieve not only by the size of the particles incorporated but also by the degree of agglomeration of said particles [209, 213]. This was evidenced by the increase in dead osteoblasts after 3D bioprinting of BG containing cell-laden bioinks as a result of the increased shear forces [209] introduced by the BG particles [209]. Therefore, it is imperative that alternative strategies for incorporating such osteopromotive elements be investigated to overcome the current limitations.

An innovative approach to overcoming said limitations is to chemically link the osteopromotive component(s) to the polymer matrix. Currently, there have been few reported instances where this approach has been investigated, emphasizing its novelty. It is expected that the chemical bonding of the osteopromotive component(s) and polymer matrix will result in a stable structure minimizing the agglomeration of the incorporated osteopromotive component(s). Furthermore, to achieve the greatest degree of homogenization between the osteopromotive component(s) and the polymer matrix will ideally implement an *in situ* synthesis method. Both factors combined are expected to deliver cell-laden 3D bioprinted scaffolds with the individual components rendered invisible,

from the perspective of the body, allowing for advanced materials characteristics to be achieved that could not otherwise have been realized following the composites approach.

CHAPTER 3

EXPERIMENTAL METHODS

3.1 Ag-doped bioactive glass-ceramic synthesis

The synthesis process for the delivery of Ag-BG uses a two-system sol-gel approach. Table 3.1.1 presents the compositions of the two systems used for the synthesis while Table 3.1.2 describes the resulting Ag-BG composition.

Table 3.1.1: The nominal compositions (wt%) used to synthesize Ag-BG.

Oxide	SiO_2	CaO	P_2O_5	Al_2O_3	Ag_2O	Na_2O
System 1 (wt%)	60	11	3	14	7	5
System 2 (wt%)	58	33	9	0	0	0

Table 3.1.2: The nominal composition (wt%) of Ag-BG used for the synthesis of 3D scaffolds.

Oxide	Wt% Oxide	Mol% Oxide	Element	Atomic %
SiO_2	58.6	62.1	O	62.5
CaO	26.4	30.0	Si	21.5
P_2O_5	7.2	3.23	Ca	10.4
Al_2O_3	4.2	2.62	P	2.24
Ag_2O	2.1	0.58	Al	1.82
Na_2O	1.5	1.54	Ag	0.40
			Na	1.07

To synthesize the Ag-BG, analytical grade tetraethyl orthosilicate (TEOS; $SiC_8H_2OO_4$), triethyl phosphate (TEP; $C_6H_{15}O_4P$), aluminum nitrate nonahydrate (AlNT; $Al(NO_3)_3{\cdot}9H_2O$), silver nitrate (AgNT; $AgNO_3$), calcium nitrate tetrahydrate (CaNT; $Ca(NO_3)_2{\cdot}4H_2O$), and sodium nitrate (NaNT; $NaNO_3$) were all purchased from Millipore Sigma (United States) and used without further purification.

Using two beakers (system 1, system 2) comprised of polytetrafluoroethylene (Teflon; $(C_2F_4)_n$), 28.30 mL of distilled water and 4.72 mL of 2N nitric acid (HNO_3) were added to system 1 and

stirred using a magnetic stir bar and a hot plate set to achieve a stirring rate of 500 RPM for 5 minutes to perform subsequent reactions under acid catalysis. For all subsequent reagents added, a waiting period of 30 minutes was observed to allow sufficient time for the next reagent to be properly dissolved. To this end, 40.14 mL of TEOS was added and the stir rate increased to 600 RPM to ensure its rapid hydrolysis. The stir rate was reduced to 500 RPM before adding 1.29 mL of TEP. 18.54 g of AlNT, 1.85 g of AgNT (pulverized using a mortar and pestle), 8.34 g of CaNT, and 2.47 g of NaNT (pulverized using a mortar and pestle) were the remaining reagents added in order.

For system 2, 69.84 mL of distilled water and 11.64 mL of 2N nitric acid were added and stirred at the same rate as system 1 for 5 minutes. 90.53 mL of TEOS, 9.00 mL of TEP, and 58.37 g of CaNT were the reagent amounts added to system 2 following the same procedures as described for system 1.

For system 1 and system 2, both syntheses occurred inside a fume hood with a layer of Parafilm used to cover the open portion of the beakers and a layer of aluminum foil placed on top to protect the photosensitive components present. After the addition of NaNT for system 1 and CaNT for system 2, a fresh covering was used for each beaker. This entailed creating a tri-layer of Parafilm-Al foil-Parafilm was used to cover the open portion of the beaker, while Parafilm was used to cover the sides of the beaker. This setup provided robust protection for each system as they underwent 17 h of stirring at 500 RPM to ensure solution homogeneity. After system 2 was added to system 1 and the robust covering technique applied as previously described while the combined solution underwent a subsequent 17 h of stirring at 500 RPM. To deliver the final Ag-BG composition described in Table 3.1.2, a heat treatment was applied following the scheme presented in Figure 3.1.1.

3.2 Processing of 3D scaffolds

The assessment of the 3D scaffolds to address the needs for targeting critical-sized bone defects in load-bearing applications explored three distinct processing iterations: (1) the polymer foam replication technique, (2) 3D printing using fused filament fabrication technologies, and (3) the

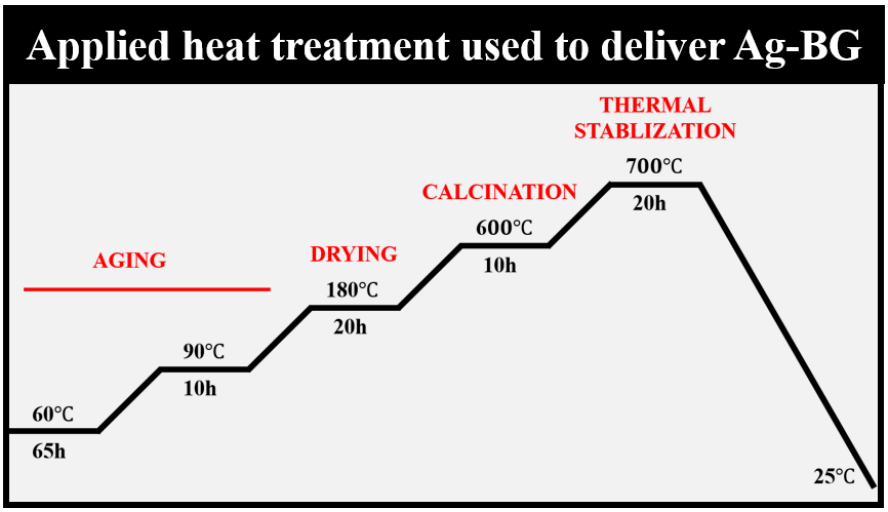

Figure 3.1.1: The applied heat treatment used to deliver Ag-BG in the composition prescribed in Table 3.1.2.

development of organic-inorganic hybrid scaffolds by way of ink extrusion-based 3D printing technologies. All processing avenues explored centered on the transformation of an Ag-doped bioactive glass-ceramic (Ag-BG) composition from its conventional particle-form to novel 3D scaffolds that deliver therapeutic and regenerative properties for bone defects in load-bearing applications.

3.2.1 Polymer foam replication

The polymer foam replication technique, entailing the sacrificial use of a polyurethane template, is a well-known technique [16, 25, 57, 58, 152–154, 157–159, 214, 215] for fabricating 3D bioactive glass-ceramic scaffolds for its ability to produce highly porous scaffolds, where the structure can be modified on multiple scales to deliver a scaffold possessing similar characteristics to that of native bone tissue. The sol-gel process is highly compatible with the polymer foam replication technique, where this process can either be used during the sol-gel process, termed the solution technique (Section 3.2.1.1), or after heat treatment using sol-gel derived particles, termed the slurry technique (Section 3.2.1.1). Both the solution and slurry techniques offer unique advantages, which will be explored in Section 4.2.

3.2.1.1 Solution technique

The solution technique [154, 157, 159, 214] for the fabrication of 3D Ag-BG scaffolds was investigated for its single-step approach, where the Ag-BG undergoes a single heat treatment whilst maintaining the large surface area [158, 215] afforded by the use of the sol-gel technique to amplify the ensuing antibacterial and biological responses.

To this end, 12.5 mm x 12.5 mm x 12.5 mm polyurethane foam (United Plastics) cubes having 45 pores per inch (PPI; 569±63.6 μm) were prepared, cleaned ultrasonically for 15 minutes in ethanol (Koptek; 200 proof), and dried at 60°C for 15 minutes before use. The Ag-BG solution used for scaffold fabrication was the combined system 1- system 2 solution after 17 h of stirring, prepared as previously described in Section 3.1.

The cleaned polyurethane foam cubes were immersed in the Ag-BG solution for ~60 seconds before removal. Excess solution was removed through the manual application of compressive forces to achieve ~50% compression for each principle axis for 5 seconds to minimize the blockage of the pores in the polyurethane foam cubes. The single-coating of Ag-BG solution on the polyurethane foam cubes were placed in an oven set at 60°C for 24 h to allow the Ag-BG solution to dry and prepare the coated polyurethane foam cubes for additional soakings. This soaking process was repeated six times to increase the thickness of the Ag-BG coating applied to the polyurethane foam cubes. The Ag-BG sol-coated polyurethane foam cubes were then allowed to dry at 60°C before applying the heat treatment following the prescribed conditions detailed in Table 3.2.1. Figure 3.2.1 is shown to provide a visual schematic of the process applied to deliver Ag-BG scaffolds fabricated using the solution technique (Section 3.2.1.1).

3.2.1.2 Slurry technique

The slurry technique [16, 25, 57, 58, 152, 153] for the fabrication of Ag-BG scaffolds was investigated, given it is a well-documented process that is compatible with bioactive glasses (BGs) fabricated using the melt-derived technique. It is important to note the slurry technique utilizes previously synthesized BGs that are ball-milled and sieved to deliver BG particles within a pre-

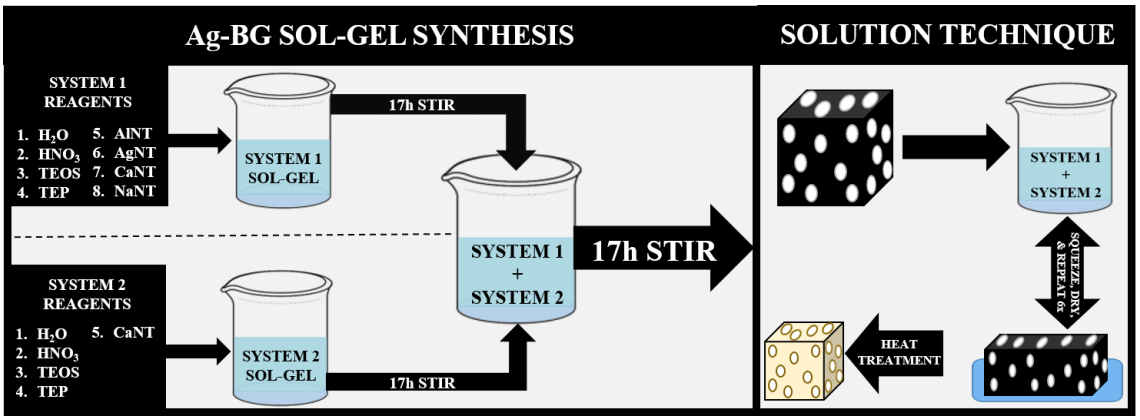

Figure 3.2.1: Figure of the applied process to deliver Ag-BG scaffolds fabricated by the solution technique.

Table 3.2.1: The applied heat treatment to deliver Ag-BG scaffolds using the solution technique.

Temperature (°C)	Rate (°C min^{-1})	Duration (minutes)	Rationale
25→400	2	60	Allows the polyurethane to vaporize without catastrophic failure
400→700	2	300	Transform Ag-BG into its final glass-ceramic form
700→25	5	—	—

determined range of particle sizes. Given this, the high sintering temperatures (T > 800°C) required to achieve notable sintering significantly increase the probability that the BG particles will undergo crystallization due to the BGs experiencing a second heat treatment. The BG scaffolds synthesized by the slurry technique commonly delivered scaffolds having a surface area of roughly 2 m^2 g^{-1}. These factors are expected to slow the rate of dissolution of 3D BG-based scaffolds synthesized by the slurry technique leading to a potential reduction in antibacterial potency and a slower rate of formation of an apatite (CaP)-like layer during subsequent studies.

The synthesis of Ag-BG scaffolds using the slurry technique entailed the use of polyurethane foam cubes of the same geometry, PPI, and cleaning procedures, as described previously in Section 3.1.2.1. A slurry consisting of distilled water, poly(vinyl) alcohol (PVA) to act as a binder, and Ag-BG micro-sized particles ball-milled (i.e. ZrO_2 jar, beads) and sieved to achieve an Ag-BG particle size below 38 μm was prepared, combining the reagents at a ratio 1.67:0.167:1 respectively (Fig. 3.2.2).

In detail, distilled water was heated to 80°C in a Teflon beaker with the PVA added once the temperature achieved equilibrium. The distilled water – PVA mixture was stirred by use of a magnetic stir bar for 60 minutes at 400 RPM. The Teflon beaker containing the distilled water – PVA mixture was then transferred to a second hot plate to achieve ambient temperatures before the addition of the Ag-BG micro-sized particles. 60 minutes was the duration used to homogenize the Ag-BG micro-sized particles with the distilled water – PVA mixture. Using the prepared slurry, polyurethane foam cubes were immersed for a duration of ~60 seconds before removal. The excess slurry was removed from the slurry-coated polyurethane foam cubes using the manual compression method, previously described in Section 3.2.1.1. The slurry-coated polyurethane foam cubes were then dried under ambient conditions before applying a heat treatment following the conditions detailed in Table 3.2.2.

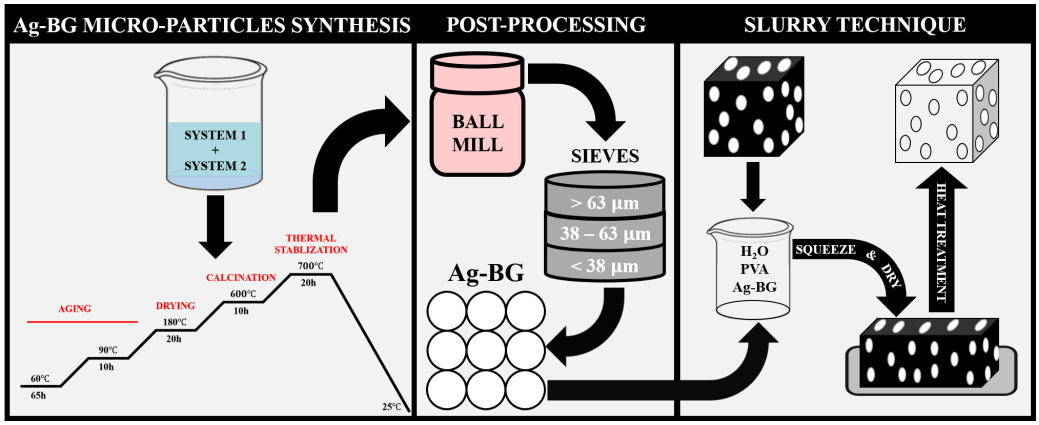

Figure 3.2.2: Figure of the applied process to deliver Ag-BG scaffolds fabricated by the slurry technique.

Table 3.2.2: The applied heat treatment to deliver Ag-BG scaffolds using the slurry technique.

Temperature (°C)	Rate (°C min^{-1})	Duration (minutes)	Rationale
25→400	2	60	Allows the polyurethane to vaporize without catastrophic failure
400→1000	10	300	Allow for the Ag-BG particles to sinter, creating a durable 3D scaffold
1000→25	5	—	—

3.2.2 Fused filament fabrication

3.2.2.1 Filament synthesis

Synthesis of a filament compatible with the fused filament fabrication (FFF) technique entails the creation of an Ag-BG-filled polymeric binder system satisfying the flexibility and durability requirements to successfully wind the filament onto an FFF-compatible spool. These criteria were achieved through the formulation of a multi-component binder system. The binder system was comprised of polyolefins (binder), thermoplastic elastomer (backbone), and stearic acid to act as a surfactant and improve homogenization between Ag-BG and polyolefins. The sizes of the micro-sized Ag-BG particles used during the synthesis of FFF-compatible filaments were following the parameters detailed in Table 3.2.3.

Table 3.2.3: The parameters of micro-sized Ag-BG particles used in the synthesis of FFF-compatible filaments.

Ag-BG particle size-distribution	Ag-BG particle size(s) (μm)	Concentration (vol%)
Unimodal	20-38	46-49
Bimodal	Mode 1: 20-38 (29±5) Mode 2: < 20 (13±3)	40

Specifically, the synthesis of the filament started with drying the Ag-BG micro-sized particles and polymeric components at 40°C for 60 minutes to remove excess moisture before being fed into a modified-twin extruder. The barrel of the modified-twin extruder was kept between 170°C and 210°C with the mixing velocity set to 50 RPM. The extruded Ag-BG filament was 1.75 mm in diameter and spooled immediately for 3D printing.

3.2.2.2 Shaping—Debinding—Sintering for delivery of pristine 3D silicate-based bioceramic scaffolds

To 3D print, Ag-BG scaffolds using the FFF technique, a shaping, debinding, and sintering process was applied to deliver pristine Ag-BG scaffolds. To start, the spooled Ag-BG containing

FFF-compatible filament was properly placed into a Renkforce RF-1000 3D printer. A 3D computerized CAD model (Fig. 3.2.3) comprised of an interconnected porous simple cubic lattice was used to 3D print Ag-BG green body (i.e. 3D printed as-received) scaffolds. The parameters used to 3D print the green-body Ag-BG scaffolds were in accordance with Table 3.2.4.

To remove the soluble, polyolefin binder from the green body Ag-BG scaffolds, said 3D scaffolds were immersed for 18 hours in acetone. This post-processing step allowed for the generation of vacant channels that will provide avenues for thermoplastic elastomer (backbone) vapors during thermal debinding, thus eliminating concerns regarding structural deformation during the applied heat treatment.

The parameters used for thermal debinding were in accordance with Table 3.2.5 for Ag-BG scaffolds 3D printed using an FFF-compatible filament comprised using a unimodal Ag-BG particle size distribution (Table 3.2.3), and in accordance with Table 3.2.6 for Ag-BG scaffolds, 3D printed using an FFF-compatible filament comprised using a bimodal particle-size distribution of Ag-BG (Table 3.2.3). After thermal debinding, the Ag-BG scaffolds are classified as brown-bodies, as shown in Figure 3.2.3. To sinter, the brown-body Ag-BG scaffolds, the maximum temperature used was either 900°C (Table 3.2.5) or 1150°C (Table 3.2.6) when either a unimodal particle size distribution or a bimodal particle size distribution of Ag-BG particles was used (Table 3.2.3), respectively, in the creation of an Ag-BG containing FFF-compatible filament. After sintering, pristine Ag-BG scaffolds were obtained (Fig. 3.2.3).

Table 3.2.4: The printing parameters used to 3D print green-body Ag-BG scaffolds using the FFF technique.

Parameter	Quantity
Extruder Temperature (°C)	180
Nozzle Diameter (mm)	0.40
Print Velocity (mm min^{-1})	1000

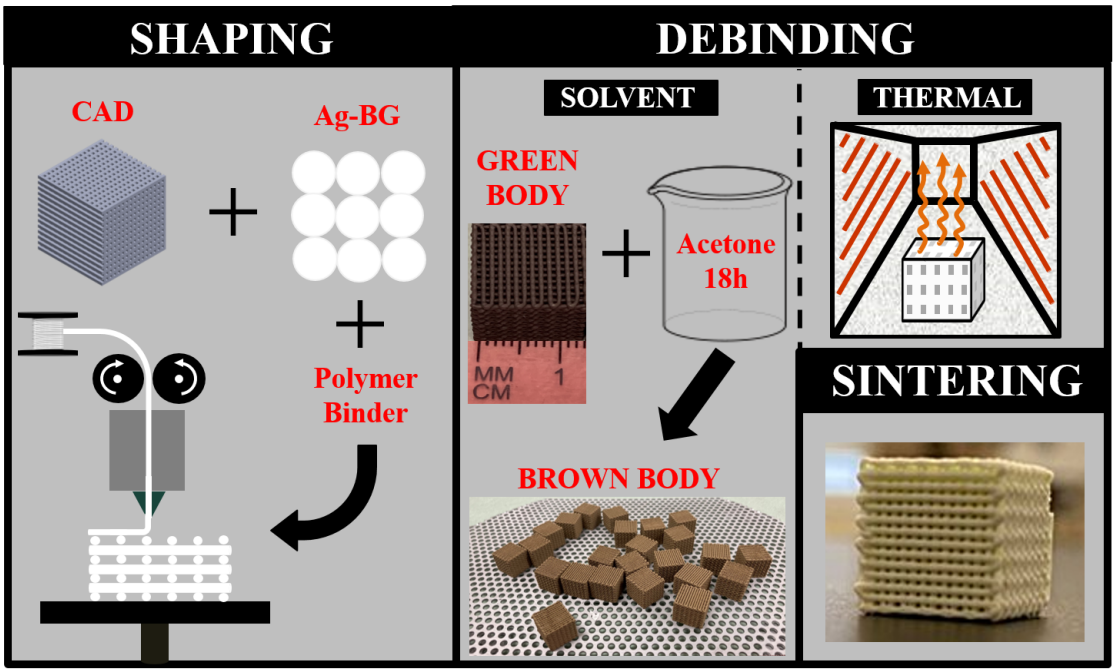

Figure 3.2.3: Figure of the shaping, debinding, and sintering processes applied to deliver pristine Ag-BG scaffolds using the fused filament fabrication technique.

Table 3.2.5: The thermal debinding and sintering profiles used to deliver pristine Ag-BG scaffolds 3D printed using an FFF-compatible filament synthesized using a unimodal particle-size distribution of Ag-BG micro-sized particles.

Condition	Step	Temperature (°C)	Rate (°C min^{-1})	Duration (minutes)
Thermal Debinding	1	200	5	0
	2	390	2	30
	3	500	1	60
Sintering	4	900	2	120
	5	25	5	0

3.2.3 Hybrid synthesis

3.2.3.1 Synthesis of gelatin methacryloyl

The synthesis of gelatin methacryloyl (GelMA) required the dissolution of type A gelatin (300 bloom; 10% (w/v)) into warm (i.e. 50°C) dimethyl sulfoxide (DMSO) at a stirring velocity of 500 RPM (Fig. 3.2.4). To transform type A gelatin (Fig. 3.2.4) into its methacrylic derivative, capable of photopolymerization, methacrylic anhydride (MAA; Fig. 3.2.4) was used. The amount of MAA required was calculated through fixation of the ratio between MAA and lysine present

Table 3.2.6: The thermal debinding and sintering profiles used to deliver pristine Ag-BG scaffolds 3D printed using an FFF-compatible filament synthesized using a bimodal particle-size distribution of Ag-BG micro-sized particles.

Condition	Step	Temperature (°C)	Rate (°C min^{-1})	Duration (minutes)
Solvent Debinding	1	—	—	1,080
Thermal Debinding	2	260	5	0
	3	600	5	0
Sintering	4	1150	5	480
	5	25	5	0

in type A gelatin at 2.20 [216, 217]. MAA was added to the dissolved type A gelatin in DMSO in 30-minute increments for 180 minutes [217]. The now photopolymerizable gelatin derivative, termed gelatin methacryloyl (GelMA; Fig. 3.2.4), was extracted with the addition of three times the reaction volume of toluene [218]. The use of toluene was recently reported to be an effective precipitating agent for GelMA [218], where the small dielectric constant for toluene allowed for the attractive forces between the electrically disparate charges present in GelMA molecules, creating insoluble agglomerates viable for extraction through decantation after 24 hours under ambient conditions. The extracted GelMA was washed thrice with distilled water to remove residual solvent before dissolution in distilled water at 50°C having a stir velocity of 500 RPM. After dissolution of GelMA in distilled water, the solution was placed at 37°C for 24 hours to maintain the dissolution of GelMA whilst allowing sufficient time for any residual toluene to volatilize. The GelMA solution was then frozen and lyophilized before storage.

3.2.3.2 Compatible synthesis of Ag-doped bioactive glass

Synthesis of an Ag-BG sol compatible with organic-inorganic hybrid synthesis required the use of an alcohol-based (i.e. methanol (MeOH)) solvent, adapted as required from previous reports [219]. In detail, a Teflon beaker containing a magnetic stir bar was used and reagents added following the molar ratios detailed in Table 3.2.7. MeOH, TEOS, and TEP were all added to the Teflon beaker, the stirring velocity set to 500 RPM, and all components left to homogenize for 24h under ambient conditions. For the addition of AlNT, AgNT (crushed using a mortar and pestle),

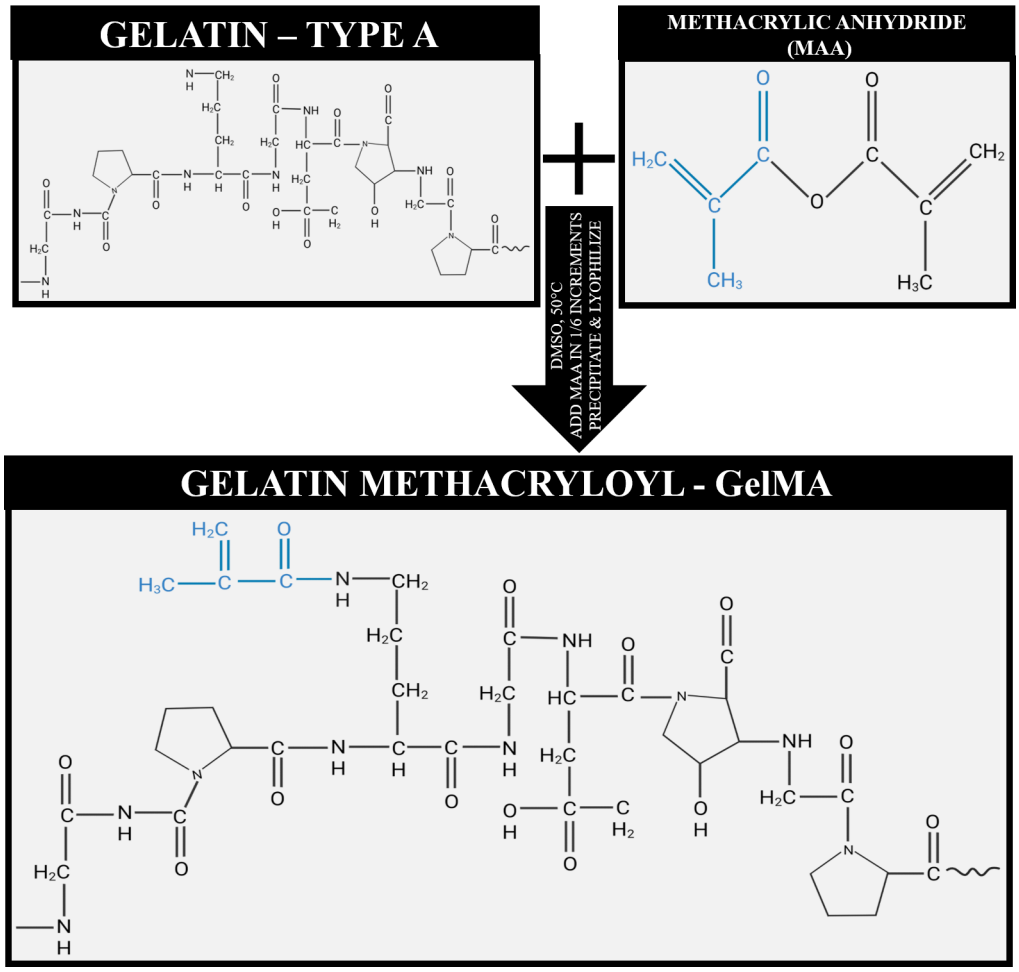

Figure 3.2.4: Figure of the synthesis method applied to deliver gelatin methacryloyl (GelMA).

and CaNT were added sequentially in 24-hour increments. It is important to note that a robust covering was applied to the Teflon beaker to protect the photosensitive Ag-BG sol following the procedures detailed in Section 3.1.

Table 3.2.7: The molar ratios used in the successful synthesis of a compatible Ag-BG sol for subsequent organic – inorganic class II hybrid fabrication.

Row / Column	MeOH	TEOS	TEP	AlNT	AgNT	CaNT	H_2O
MeOH	1.00	40.60	366.00	333.00	1,565.93	86.19	13.62
TEOS	0.03	1.00	9.02	8.20	38.57	2.12	0.34
TEP	0.003	0.11	1.00	0.91	4.28	0.24	0.04
AlNT	0.003	0.12	1.10	1.00	4.70	0.26	0.04
AgNT	0.001	0.026	0.23	0.21	1.00	0.06	0.01
CaNT	0.01	0.47	4.25	3.86	18.17	1.00	0.16
H_2O	0.07	2.98	26.88	24.46	115.00	6.33	1.00

3.2.3.3 Class II hybrids synthesis

The formation of an organic-inorganic class II hybrid material commonly requires the use of a coupling agent to act as an intermediary between the organic and inorganic component(s) [28, 91, 146, 147]. Here, GelMA and Ag-BG are the organic and inorganic components respectively. The coupling agent selected for class II hybrid synthesis was (3-Glycidyloxypropyl)trimethoxysilane (GPTMS) for its ability to react both with GelMA and Ag-BG.

The previously lyophilized GelMA (Section 3.2.4.1) was dissolved in warm (50°C) DMSO at a concentration of 10% (w/v) by way of a magnetic stir bar containing Teflon beaker, whose stir velocity was set at 500 RPM. GPTMS was added to the GelMA solution so that the molar ratio between the sum total of the amino acids hydroxylysine, lysine, and arginine present to GPTMS was two. GPTMS was allowed to react for 24 h with GelMA (Fig. 3.2.5), providing sufficient time to allow for the epoxy ring-opening reaction to occur whilst preventing hydrolysis of the trimethoxysilane group of GPTMS through the use of the non-aqueous solvent, DMSO. The previously prepared Ag-BG sol (Section 3.2.4.2) was added to the GelMA – GPTMS solution at a concentration of 3% (w/w). To ensure adequate hydrolysis between Ag-BG and the trimethoxysilane group of GPTMS, 12.7 M of distilled water was added to the Ag-BG sol before addition in the GelMA – GPTMS solution. The resulting GelMA – GPTMS – Ag-BG solution was allowed to homogenize for 24 h (Fig. 3.2.5). Extraction, washing, and lyophilization of the GelMA – GPTMS – Ag-BG class II hybrid (GAB; Fig. 3.2.5) material from solution followed identical procedures to those previously described in Section 3.2.4.1. Transformation of the lyophilized materials (i.e. GelMA, GAB) into viable hydrogels suitable for 3D printing required the dissolution of the lyophilized material in warm (50°C) phosphate-buffered saline (PBS) using a concentration of 10% (w/v) and a stir velocity of 500 RPM. After complete dissolution of the lyophilized material, 1.5% (w/v) of 2,2'-Azobis[2-methyl-N-(2-hydroxyethyl)propionamide] (VA-086) was added to initiate the photopolymerization reaction when exposed to near-ultraviolet radiation. Here, the photocrosslinking was applied for 120 seconds at 385 nm, producing the (GAB) hydrogels shown in Figure 3.2.5.

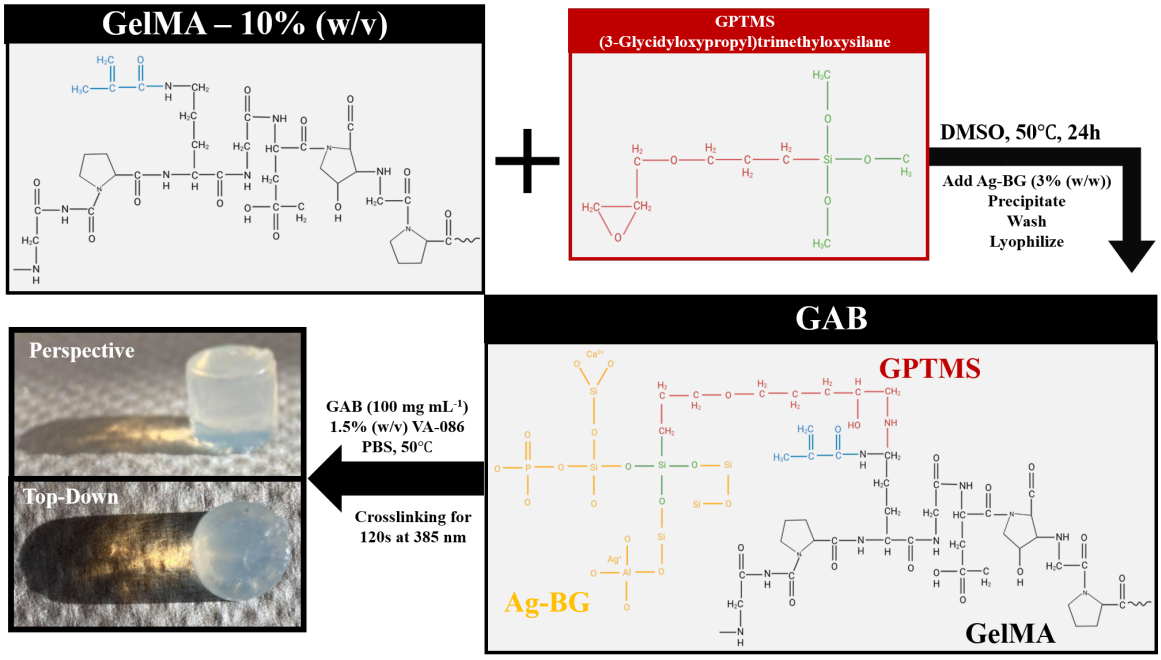

Figure 3.2.5: Figure of the applied processes used to deliver GelMA-Ag-BG class II hybrid (GAB) hydrogels.

3.2.3.4 Extrusion-based 3D printing of hydrogel inks

An extrusion-based 3D printer (Allevi 3) was used in the 3D printing of lattice-like constructs using hydrogels synthesized following the procedures described previously in Section 3.2.4.3. Specifically, the 3D printer was equipped for pneumatic extrusion, where an air compressor was used to provide controlled pressure.

To this end, hydrogels 8 mm in diameter having 1.5 mm of thickness were used for 3D printing. A single hydrogel was added to a 5 mL syringe (fitted with a 27-gauge metal tapered tip), whose rubber stopper and plunger was removed prior. Replacement of the rubber stopper then occurred, minimizing angular distortion through the use of the displaced plunger. The syringe-containing hydrogel was placed into the center of the three possible extruder positions available for use by Allevi 3 secured in place through proper placement of the cylindrical rubber extension used for the delivery of pneumatic pressure. The temperature of the extruder was set to 37°C to allow the hydrogel to undergo a thermally reversible state of matter change, allowing for any residual air pockets to be removed for 15 minutes. The extruder temperature was subsequently lowered to

27°C for 15 minutes to solidify the contents of the syringe and achieve thermal equilibrium. The parameters applied for 3D printing using the hydrogel inks were in accordance with the parameters specified in Table 3.2.8.

Table 3.2.8: The quantities of the printing parameters used in the pneumatic 3D printing of hydrogel inks by way of Allevi 3.

Parameter	Quantity
Layer height (mm)	0.5
Print speed (mm s^{-1})	4
Extruder temperature (°C)	27
Print bed temperature (°C)	23
Pneumatic pressure (psi)	12
Photo crosslinking time (s)	120
Nozzle gauge	27

3.3 Structural characterization

The Ag-BG scaffolds synthesized by way of the processes described in Section 3.1 deliver interconnected porous three-dimensional constructs presenting hierarchal multiscale structures. Structure is the indispensable bridge connecting scaffold processing with scaffold performance driving innovation in the expedition to successfully deliver 3D Ag-BG scaffolds suitable for targeting critical-sized bone defects in load-bearing applications. Therefore, the terms defined in Table 3.2.1 will be the prefix nomenclature used to describe structures on the spatial-multiscale.

Table 3.3.1: The prefix nomenclature used to describe the resulting hierarchical multiscale structures studied for Ag-BG scaffolds.

Prefix	Scale Range
Macro-	> 1 mm
Milli-	> 0.1 mm - 1 mm
Micro-	> 1 μm - 100 μm
Meso-	> 100 nm - 1000 nm
Nano-	> 10 nm - 100 nm
Atomic-	< 10 nm

3.3.1 Thermal analysis

3.3.1.1 Thermogravimetric analysis

Thermogravimetric analysis (TGA) is a characterization technique that elucidates the thermal behavior of a material through measurements of mass change as a function of temperature [220]. Phenomena that TGA can detect include evaporation of volatile species, thermal stability/decomposition, and adsorption/desorption of gaseous species [220]. TGA is compatible with a diverse set of atmospheric conditions such as N_2, O_2, Ar, He, and CO_2 [220].

As TGA is a thermal analysis technique reliant on gravimetric measurements, a buoyancy correction is required to account for the temperature dependence observed with the density of gaseous species [220]. Mathematically, the buoyancy force, F, exerted by the material being studied having a volume, V, can be calculated through rearrangement of Sir Isaac Newton's second law of motion, as shown in equation 3.3.1 [220]. In equation 3.3.1, ρ_0 represents the density of the atmospheric gas being used at a reference temperature, T_0, equating to a temperature of 298 K while g is defined by the acceleration of gravity, 9.81 kg m^{-1} s^{-2} [220]. In practice, the buoyancy force is determined through measurement of a blank, which is considered to be the crucible without any material, and studied under the exact conditions to be applied when evaluating a material by TGA means. This allows for the mass changes from the TGA study with the material of interest and crucible together to be subtracted from the mass changes from the TGA study performed on the crucible alone to elucidate the mass changes occurring with the material of interest. This approach, however, is limited by the failure to account for volumetric buoyancy changes [220].

$$F = V \cdot (\rho_0 \frac{T_0}{T}) \cdot g \qquad \text{(3.3.1 [206])}$$

Herein, TGA was utilized to elucidate the thermal behavior of the Ag-BG containing filament(s) used in the fused filament fabrication printing of 3D Ag-BG scaffolds to optimize the thermal debinding treatment(s) applied (Table 3.2.5 and Table 3.2.6). The TGA measurements on the FFF-compatible Ag-BG containing filament(s) were conducted in an N_2 atmosphere with the inflow

of N_2 gas set to 50 mL min^{-1} [221]. The TGA study was performed using the dynamic analysis mode using a temperature range of 25°C to 600°C, where the dynamic analysis mode allowed the instrument to automatically adjust the heating rate in accordance with the mass losses recorded [221]. From temperatures ranging from 150°C to 300°C, a variable heating rate between 2°C min-1 and 6°C min^{-1} were used as no significant mass loss (i.e. < 3%) was detected. In temperatures ranging from 300°C to 340°C, the heating rate applied varied from 0.5°C min^{-1} to 1°C min^{-1} as notable mass loss was detected within this temperature region, as shown in Figure 4.1.1.

3.3.1.2 Differential thermal analysis

Differential thermal analysis (DTA) is similar to TGA in that measurements are collected as a function of temperature, yet differs as DTA measures the temperature differential between the expected (programmed) temperature and the actual temperature of the sample as a function of sample temperature [222]. It was Henri Louis Le Chatelier that demonstrated that the temperature differentials represented endothermic and exothermic processes occurring within the sample [222] allowing for phenomena such as state of matter changes, crystallization events, and transition temperatures to be observed and quantified.

Ag-BG micro-sized particles sieved below 38 μm were placed in a sapphire alumina pan, where the mass of the Ag-BG micro-sized particles used was 9.85 mg. An inert atmosphere containing N_2 gas was generated using an inflow rate of 100 mL min^{-1}. A reference study was performed using the sapphire alumina pan alone so that temperature differentials related to the sapphire alumina pan could be subtracted from the Ag-BG micro-sized particle-containing DTA study. A constant heating rate of 10°C min^{-1} was applied from ambient temperatures (25°C) up to 1500°C with these specified conditions used for all DTA studies. The data collected were expressed and reported as heat flow (mV) as a function of temperature to elucidate the glass-transition temperature of the Ag-BG micro-sized particles in addition to identifying crystallization events or phase changes that occurred within the Ag-BG micro-sized particles throughout the DTA study (Fig. 4.1.1) [223].

3.3.2 Microscopy techniques

Underneath the umbrella of microscopy is a plethora of characterization techniques that can be utilized to evaluate structures ranging from the milli-scale (Table 3.3.1) down to the atomic scale (Table 3.3.1) and can be performed either in ex-situ or in-situ conditions with the appropriate setup. Ag-BG micro-sized particles and Ag-BG scaffolds were structurally observed using hot stage microscopy (Ag-BG micro-sized particles; Section 3.3.2.1), optical microscopy (Ag-BG scaffolds; Section 3.3.2.2), scanning electron microscopy (SEM; all Ag-BG containing samples; Section 3.3.2.3.1), transmission electron microscopy (TEM; Ag-BG scaffolds; Section 3.2.2.3.2), and confocal scanning laser microscopy (CSLM; Ag-BG scaffolds; Section 3.3.2.4).

3.3.2.1 Hot stage microscopy

Hot stage microscopy (HSM) is a microscopy technique that commonly utilizes a compatible optical microscope to observe morphological changes of a material as a function of time and temperature [224]. From this, changes in the area of the material can be quantified to elucidate the shrinkage of the material as a function of increasing temperature providing a metric with which the % of sintering can be realized.

Ag-BG micro-sized powder sieved below 38 μm were placed into the sample holder of the Misura 3.32 hot stage microscope for HSM. The source of illumination was found perpendicular to and above the Ag-BG micro-sized particles to form a two-dimensional shadow projection below the sample stage. The shadow projections of the Ag-BG micro-sized particles were recorded from 400°C to 1500°C through the use of videography and a heating rate of 10.01±0.06°C min^{-1} applied. The changes in the area of the shadow projection created by the Ag-BG micro-sized particles were recorded in increments of 7°C, with the change in the area reported relative to the initial area (i.e. 100%) of the shadow projection of the Ag-BG micro-sized particles. Images were captured at various points of interest from the videograph, as determined by the behavior of the shrinkage as a function of temperature. Superimposed onto these images was the shadow projection of the Ag-BG

micro-sized particles recorded at the initial temperature of the HSM study set at 70% transparency to provide a visual reference at each temperature of interest.

3.3.2.2 Visible light microscopy

Conventional visible light microscopy (Keyence VHX-600E Digital Microscope) was used herein to elucidate the surface morphology and variations in color intensity of Ag-BG scaffolds on the milli-scale [221, 223, 225]. Specifically, Ag-BG scaffolds were manually sectioned into two halves for observation of the Ag-BG scaffolds from a top-down perspective and a cross-sectional perspective. Given the three-dimensional nature of the Ag-BG scaffolds, the images were collected using the focus stacking mode available on the microscope, which is an image processing method by which images captured at varying focal points are combined providing a composite image with increased depth of field relative to the individual images used.

3.3.2.3 Electron microscopy

The advent of electron microscopy provided the means to break through the limitations in resolution when using a visible light source, as dictated by the Rayleigh criterion, shown in equation 3.3.2 [226].

$$\delta = \frac{0.61\lambda}{\mu \sin\beta} \qquad \text{(3.3.2 [226])}$$

In equation 3.3.2, λ represents the wavelength of the radiation source being used, μ is the refractive index of the viewing medium, and β, which describes the semi-angle of collection for the magnifying lens [226]. A visible light microscope using a wavelength of 550 nm can resolve features as small as 300 nm, however, this limit of 300 nm cannot resolve features on the nano-scale (Table 3.3.1), preventing elucidation of important characteristics needed to fully control the properties of materials [226].

When discussing resolution, it is important to note that in the context of microscopy, resolution is thought of as the ability to resolve two incoherent point sources [226]. These two incoherent

point sources, or Airy disks, can be individually resolved when, under the Rayleigh conditions, the loss in intensity in between the Airy disks is greater than 20% relative to the maximum intensity of the individual Airy disk.

The use of electrons as the illumination source results in multiple different signals being generated when an incident electron beam interacts with a (thin) specimen, as shown in Figure 3.3.1 [226]. The signals displayed in Figure 3.3.1 will be described as they are used in the context of scanning electron microscopy (SEM; Section 3.3.2.3.1) and transmission electron microscopy (TEM; Section 3.3.2.3.2).

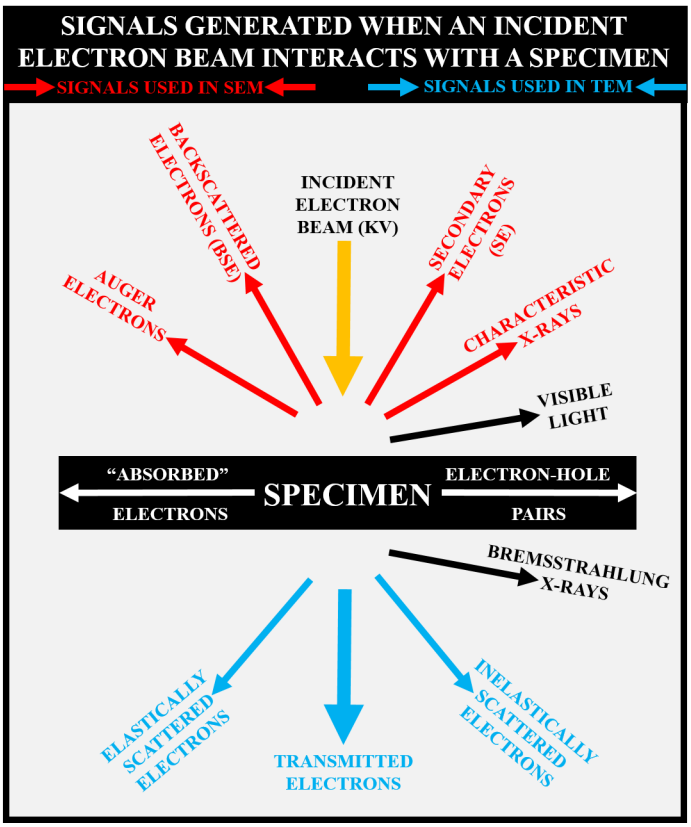

Figure 3.3.1: Figure of the different signals generated when an incident electron beam interacts with a specimen [226]. Red denotes the signals used in scanning electron microscopy (SEM) and blue represents the signals used in transmission electron microscopy (TEM). This schematic was adapted from Figure 1.3 as presented in chapter 1 of the textbook written by David B. Williams and C. Barry Carter titled, "Transmission Electron Microscopy A Textbook for Materials Science" [226].

3.3.2.3.1 Scanning electron microscopy

Scanning electron microscopy (SEM) utilizes an electron beam focused using a series of electromagnetic lenses as the source of illumination, where the energy of the electrons used is between 1 and 30 keV corresponding to a maximum spatial resolution of ~4 nm [227]. This range of electron energy is not sufficiently high to result in electrons being transmitted through the sample, thus the signals used for imaging are generated from the elastic and inelastic interactions between the electron beam and the specimen. Figure 3.3.2 shows the interaction volume generated when an incident electron beam interacts with a specimen during SEM observation in addition to showing the different signals generated as a function of distance from the top surface of the specimen.

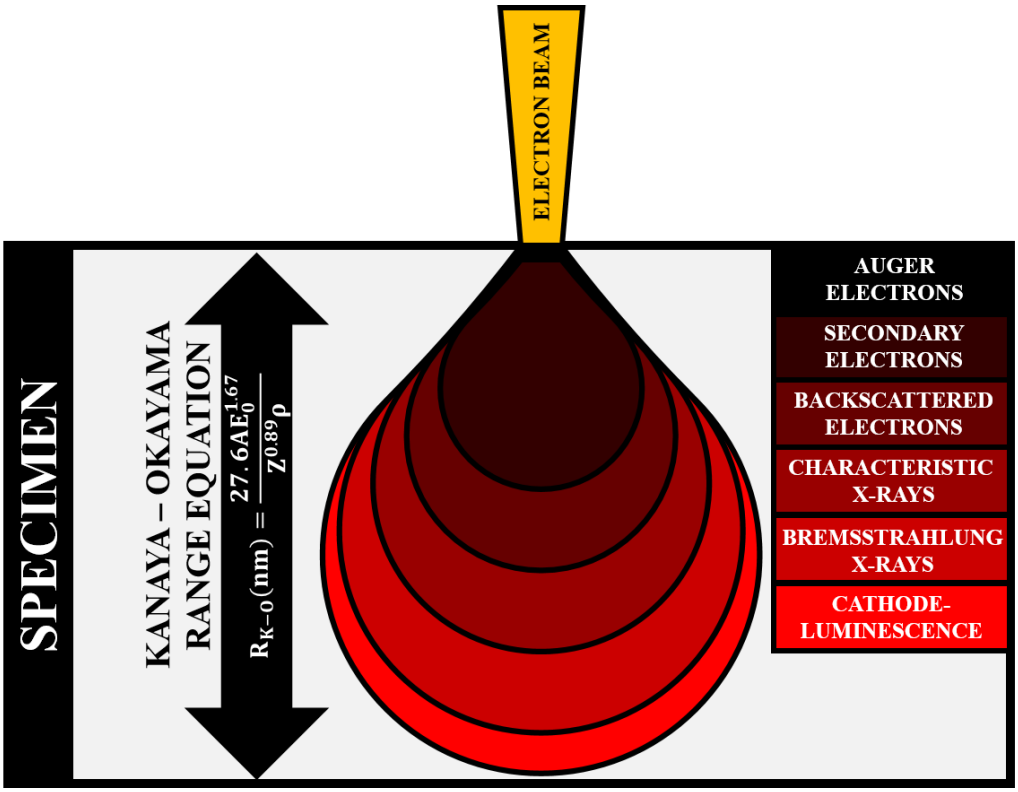

Figure 3.3.2: The interaction volume for a scanning electron microscope when the electron beam interacts with the specimen. The signals generated in relation to depth are additionally shown. The Kanaya – Okayama range equation presented describes the total penetration distance of an incident electron beam perpendicular to the specimen surface; where A represents the atomic weight of the specimen (g mol^{-1}), Z describes the atomic number of the specimen, ρ represents the density of the specimen (g cm^{-3}), and E_0 describes the energy of the incident electron beam (keV) [228].

Herein, 3D Ag-BG scaffolds were observed using SEM to elucidate their morphological and topological characteristics whilst energy dispersive spectroscopy (Section 3.3.3.4.1) was used for

elemental analysis. To prepare specimens for SEM observation, all Ag-BG scaffolds were mounted on Al-based specimen stubs adhered using C-tape. The insulating nature of the Ag-BG scaffolds demanded metallization before SEM observation to minimize the buildup of negative charge on the specimen surface and prevent the formation of charging-based artifacts. The metallization processes applied used either (a) Pt or (b) Os to metalize the surface of the Ag-BG scaffolds for either (a) 60 seconds or (b) 15 seconds. The instruments used to observe the Ag-BG scaffolds were either a Tescan MIRA or a JEOL 6610LV. The morphological and topological characteristics of the Ag-BG scaffolds were observed at an incident electron beam energy of 5 keV.

3.3.2.3.2 Transmission electron microscopy

When the energy of the electron beam is sufficiently high (i.e. > 80 keV) and the specimen amply thin (i.e. < 100 nm), the electrons from the incident beam contain enough energy to allow for electron transmission. The signals generated from these conditions are shown in Figure 3.3.1 and able to achieve a minimum spatial resolution of ~0.2 nm when using an incident electron beam energies between 100 keV and 300 keV and focused onto the specimen through the use of electromagnetic lenses [229].

Depending on the signals used, images can be generated containing different information allowing greater nanostructural (Table 3.3.1) information to be obtained. For example, phase-contrast images are generated using signals generated from both the transmitted and the scattered electrons (Fig. S1). Bright-field TEM images are formed using only the transmitted beam by filtering out the signals generated by scattered electrons (Fig. S2) generating images having a bright background with the specimen appearing as dark given the decrease in electron transmission due to the increased mass and thickness created by the specimen. Axial dark-field TEM images (Fig. S3), useful for identifying specific phases within a specimen, are generated using only scattered electrons with all other electrons being filtered out. Important to note for dark-field TEM imaging, it is ideal to align the diffracted electron spot in the selected area diffraction pattern in the center, where the transmitted beam appears so that the scattered electron signals are aligned along the optic

axis of the instrument, thus minimizing spherical aberrations.

Regarding selected area diffraction in TEM, amorphous materials appear as a diffuse ring centered around the transmitted spot, whereas crystalline materials will present SAD patterns either as spots (for single crystals present within the region being analyzed) or concentric rings (for polycrystalline materials present within the region being analyzed) [229]. Mathematically, the relation between the transmitted spot and the diffracted spots can be used to determine the interplanar spacing using Bragg's law that can then be used for phase identification through comparison with phases reported in the International Centre for Diffraction Data (ICDD). Equations 3.3.3 and 3.3.4 describe Bragg's law and the mathematical relation that exists between the transmitted spot and the diffracted spots, where n represents an integer and assumed to be 1 in all cases herein, d describes the interplanar spacing between atoms, θ_B represents the Bragg angle, λ describes the wavelength of the incident electron beam, L represents the camera length, and R describes the distance between the transmitted spot and the diffracted spot of interest [229].

$$n\lambda = 2d\sin\theta_B \qquad \text{(3.3.3 [229])}$$

$$d = \frac{\lambda L}{R} \qquad \text{(3.3.4 [229])}$$

All Ag-BG scaffolds imaged using TEM were prepared by first pulverizing the sample with a mortar and pestle. The powdered Ag-BG scaffolds were suspended in isopropanol, transferred to an Eppendorf, and ultrasonicated for 30 minutes to generate a homogenous suspension of particles. The pulverized Ag-BG scaffolds were then dispersed onto 200 mesh copper grids with carbon support film (Electron Microscopy Sciences; CF200-CU) and imaged using either a JEOL 100CX TEM/JEOL 1400 Flash TEM at an incident electron beam energy of 120 keV or a JEOL 2010F AEM TEM with an incident electron beam energy of 200 keV.

3.3.2.4 Confocal laser-scanning microscopy

Confocal scanning laser microscopy (CLSM) utilizes lasers as the source of illumination com-

pared to using either a non-monochromatic light source (visible light microscopy) or electrons. The high degree of monochromaticity, polarization, coherence, and intensity allows for thin optical planes to be imaged whilst preventing out-of-focus fluorescence presenting CLSM as an optical imaging method for biological samples [230].

CLSM was employed to image methicillin-resistant Staphylococcus aureus (MRSA) biofilms after exposure to 3D Ag-BG scaffolds and live/dead staining applied (Live/Dead Baclight Bacterial Viability Kit; ThermoFisher Scientific). The experimental setup and sample preparation will be discussed in detail in Section 3.4.3.3. The imaging was performed using a Nikon C2 CLSM, where the living MRSA was imaged using a 488 nm diode laser to excite the carboxyfluorescence diacetate (live component of the live/dead stain) with green fluorescence emission detected using a 500-550 nm bandpass filter. Propidium iodide, the dead component of the live/dead stain, was excited using a 560 nm diode laser with red fluorescence detected using a 575-625 bandpass filter to image the MRSA killed by the Ag-BG scaffolds.

3.3.3 Electromagnetic radiation-based characterization techniques

The use of electromagnetic radiation for materials characterization can provide a plethora of information about structures of interest depending on both the setup and the wavelength of radiation used. Figure 3.3.3 shows the different quantum changes that are observed for various wavelengths of electromagnetic radiation. Herein, nuclear magnetic resonance (NMR; Section 3.3.3.1), infrared (FTIR; Section 3.3.3.2), visible and ultraviolet light (Section 3.3.3.3), and X-Ray (Section 3.3.3.4) characterization techniques were used and will be explored further.

3.3.3.1 Nuclear magnetic resonance

Nuclear magnetic resonance (NMR) can be either performed in a liquid state or a solid state, allowing for flexibility in the types of samples that can be analyzed. The process of performing NMR entails exposing the sample to an oscillating radio-frequency electromagnetic field in combination with a strong (i.e. > 1 T) external magnetic field excites the nuclei present in the sample causing a

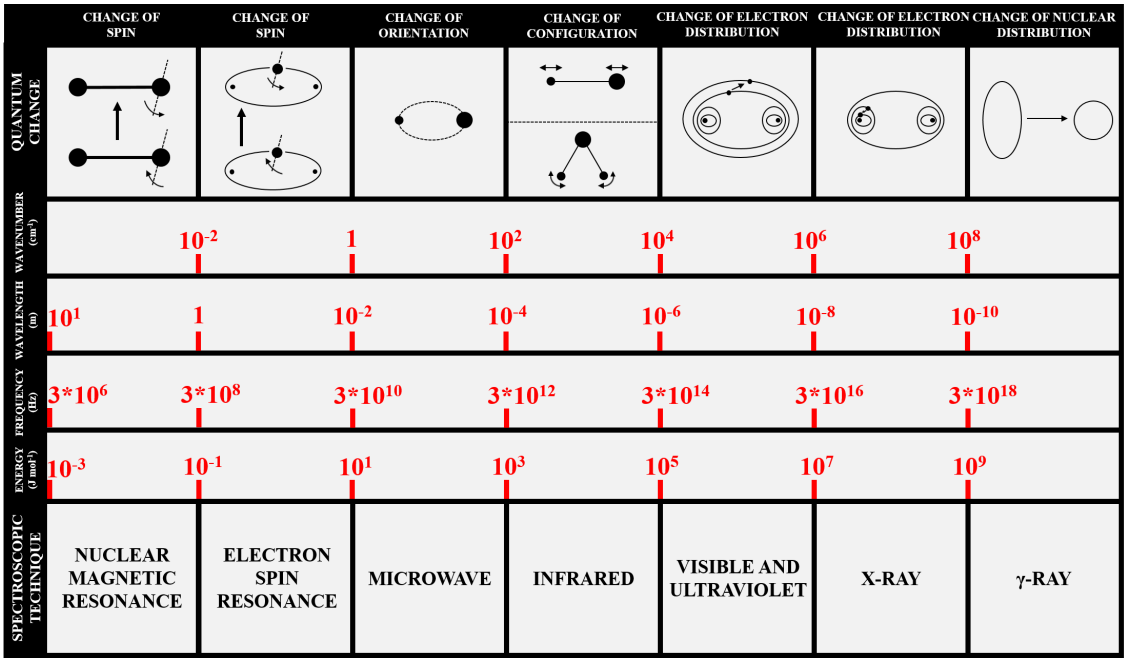

Figure 3.3.3: Chart depicting the various types of electromagnetic radiation used in materials characterization. This figure was adapted from Figure 1.4 as presented in chapter 1 of the textbook written by C. N. Banwell titled, "Fundamentals of Molecular Spectroscopy" [231].

change in the nuclear spin, as shown in Figure 3.3.3 [232]. The change in nuclear spin is measured by measuring the energy released when the nuclei return to equilibrium from an excited state. The energy released during the return to equilibrium induces currents that resonant at specific frequencies that are correlated to the degree of electron shielding around the nuclei providing useful information about the local environments of the nuclei. NMR can be performed either in a liquid state or a solid state, where both techniques were used herein.

3.3.3.1.1 Liquid nuclear magnetic resonance

Herein, proton nuclear magnetic resonance (^{1}H-NMR) was used for determining the degree of methacrylation (substitution) that occurred during the synthesis of GelMA for later use in developing GelMA-AgBG hybrid hydrogels for targeting bioprinting applications [233]. The 1D spectra were collected using an Agilent DirectDrive 2 500 MHz NMR spectrometer, where a sample concentration of 50 mg mL^{-1} in deuterium oxide (D_2O) was used for all measurements. The degree of substitution (DS) was calculated using the lysine integral method, where the integral of the lysine

methylene signals of the gelatin as received was compared to the integral of the lysine methylene signals in GelMA, as described in equation 3.3.5 [234].

$$DS_{Lysine} = (1 - \frac{\int \text{Lysine GelMA}}{\int \text{Lysine Gelatin}}) \cdot 100 \qquad \text{(3.3.5 [234])}$$

3.3.3.1.2 Magic angle spinning—nucelar magnetic resonance

Magic angle spinning – nuclear magnetic resonance (MAS-NMR) is utilized to apply NMR characterization to solid (powder) samples. Performing solid-state NMR can lead to large peak broadening or featureless spectral lines, so to overcome this limitation and achieve better resolution, the samples are spun at 54.74° respective to the applied magnetic field [232]. This angle is considered the "magic" angle as this angle leads to a vanishing of the dipolar interactions, thus removing this from contributing to peak broadening.

Herein, ^{27}Al MAS-NMR was performed on powdered Ag-BG scaffolds to determine the coordination of the Al atoms present within the scaffold structure. All spectra were collected using a Varian Infinity – Plus 400 NMR spectrometer using a 6 mm probe and a spin speed of 4 kHz. For ^{27}Al MAS-NMR spectra, one pulse at 104.16 MHz was applied for 1 μs with a delay time of 0.2 s. Peak deconvolution was performed assuming a Gaussian profile with the peak position, full-width half-max (FWHM), and intensity (area) allowed to vary separately and in combination to minimize the residuals maximizing the correlation coefficient.

3.3.3.2 Fourier-transformed infrared spectroscopy

Fourier-transformed infrared spectroscopy (FTIR) utilizes infrared radiation at varying wavelengths to elucidate both inorganic and organic components within the sample being measured. As shown in Figure 3.3.3, the infrared radiation changes the configuration of the molecules present by exciting the dipole moments present [235]. At specific wavelengths, these bonds are excited, and the infrared radiation is absorbed and converted to vibrational energy (wavenumber, cm^{-1}) [235]. The vibrational energy is correlated to different types of bonds (e.g. Si-O bonds stretching

or bending, P-O bonds stretching or bending) [235]. Given that different atoms and different bonds absorb infrared radiation at specific wavelengths, the "fingerprint" of the molecules present can be identified.

Herein, Ag-BG scaffolds were pulverized, where the powdered Ag-BG scaffold was placed on top of a diamond crystal and compressive forces applied at 10,000 psi to ensure good contact between the powder and the crystal. This configuration allowed for the instrument to be operated in the attenuated total reflectance (ATR) mode. All samples were measured using a wavenumber range of 4000-400 cm^{-1} at a resolution of 2 cm^{-1}.

3.3.3.3 Ultraviolet & visible light spectroscopy

Ultraviolet and visible light spectroscopy (UV-Vis; Fig. 3.3.3) entails applying radiation in the visible and ultraviolet wavelength range, where absorbance is measured as a function of wavelength. As this technique utilizes radiation in the visible light spectrum, this allows for a chromatic correlation with different statuses of a particular element.

Herein, Ag-BG scaffolds were pulverized, and the UV-Vis spectra collected using the solid-state mode of the instrument (Lambda 900). Spectra were collected from 350 nm to 600 nm to determine and support other experimental evidence of the status of Ag within the Ag-BG scaffolds. This was achieved, as Ag, when in metallic form, is known to undergo surface plasmon resonance, whereby the electrons on the surface of Ag begin to resonate leading to specific absorption peaks that can be correlated to the specific size and shape of the Ag present within the Ag-BG scaffolds [236].

3.3.3.4 X-Ray based characterization techniques

X-Ray-based radiation (Fig. 3.3.3) for materials characterization is commonly utilized given the versatility in the different X-Ray-based characterization techniques that can be performed. Such X-Ray-based characterization techniques can elucidate elemental distribution (energy dispersive spectroscopy; EDS), crystallographic information (XRD), and the overall gross structure (micro-CT) of a material.

3.3.3.4.1 Energy dispersive spectroscopy

Energy dispersive spectroscopy (EDS) is utilized in conjunction with SEM. When the incident electron beam interacts with the specimen, the electrons can collide with the electrons present in the shells surrounding the atoms, creating a vacancy in one of the inner electron shells. To fill this vacancy, an electron from a higher shell will drop down, releasing the excess energy in the form of X-Rays.

Interestingly, there is a unique characteristic X-Ray energy not only for all the elements but also for each shell (i.e. the X-Ray energy detected when an electron drops down from the L-shell to the K-shell is different than the X-Ray energy detected when an electron drops from the M-shell to the K-shell). As a result, the characteristic X-Ray energies can be used to elucidate either the elements present at a specific point, the elements present within a line (useful when studying the elemental distribution across an interface), or the elements within a specific region (generating EDS X-Ray maps).

Herein, EDS X-Ray maps were collected for all samples to evaluate the elemental homogeneity of elements present down to the micron level. EDS is limited to a spatial resolution in the micron range due to the interaction volume created by the incident electron beam (Fig. 3.3.2) with the spatial distribution of the interaction volume calculated using the Kanaya-Okayama range equation [228]. It should be noted that this spatial resolution limitation can be overcome utilizing the thin-foil effect [228], where the spatial resolution can be mediated by the thickness of the specimen.

All EDS X-Ray maps were collected using an incident electron beam energy of less than or equal to 21 keV with a spectra resolution of 126.2 eV. EDS was additionally used to collect point spectra to evaluate the Ca/P ratio after immersion in SBF to determine if the appropriate apatite-like layer (Ca/P ratio of 1.7) is forming.

3.3.3.4.2 X-Ray diffraction

X-Ray diffraction (XRD) is an X-Ray-based characterization technique that can elucidate the crystallographic nature of the material being analyzed. Such crystallographic characteristics that

can be revealed are the degree of crystallinity, the specific crystalline phases present, texture, lattice parameters, and crystallite size [237].

XRD is performed using a monochromatic source of X-Ray radiation, with monochromatic X-Rays generated from the interaction between an incident electron beam and the target, which most commonly is Cu [237]. Similar to EDS, this interaction causes characteristic X-Rays to be emitted, with Cu K_α radiation at a wavelength (λ) of 1.5406 Å used to irradiate the sample.

As shown in Figure 3.3.4, the incident X-Ray beam is elastically scattered by the atoms present in the specimen. This elastic scattering creates both constructive and destructive interference depending on the geometry of the incident X-Ray beam and the lattice spacing (d-spacing) of the atomic planes present [237]. This geometric relation is the foundation of Bragg's Law [237], as shown in equation 3.3.3, thus allowing for specific crystalline phases to be identified within the sample through comparison within the ICDD database. XRD can provide additional crystallographic information beyond diffraction peak indexing of crystalline materials, where the lattice parameters of a crystalline material can be elucidated given the sensitivity of this characterization technique to different atoms and different crystal structures. Furthermore, XRD can reveal crystallite size through application of Scherrer's equation (eq. 3.3.6) [237], where λ describes the wavelength of the incident X-Rays (i.e. 1.5406 Å), B represents the breadth, for full-width half-max (FWHM) of the diffraction peak being examined, and θ describes the angle at which the diffraction peak of interest occurred [237]. For Scherrer's equation, it is important to note that it is limited to calculating the crystallite size of meso- to nanosized crystallites, whereas other quantification techniques are required when crystallites are micron-sized and greater [237].

$$t = \frac{0.9\lambda}{B\cos\theta} \qquad \text{(3.3.6 [237])}$$

Herein, all Ag-BG scaffolds were pulverized to utilize the powder diffraction principles within the Bragg-Brentano configuration of the Rigaku Smartlab X-Ray Diffraction System. The powdered Ag-BG scaffolds were placed onto the sample holder, where the powder was flattened and smoothed using a previously cleaned glass slide to minimize Z-height contributions. Cu K_α radiation was used

at 40 kV and 44 mA with diffraction patterns obtained from 10° to 90° 2θ. The background was fitted to a B-spline function, where peak positions were refined using a shift axial displacement function to correct for zero-sum error, axial divergence, and eccentricity effects. Rietveld analysis was performed to quantify the weight fraction of the phases present within the Ag-BG scaffolds, where the peak shape was calculated using a split pseudo-Voight function [238], and all crystallographic parameters allowed to vary to minimize the residuals between the experimental and calculated diffraction patterns. Preferred orientation was assessed using the March-Dollase function [239] and manually adjusted to identify any preferred crystallographic orientations.

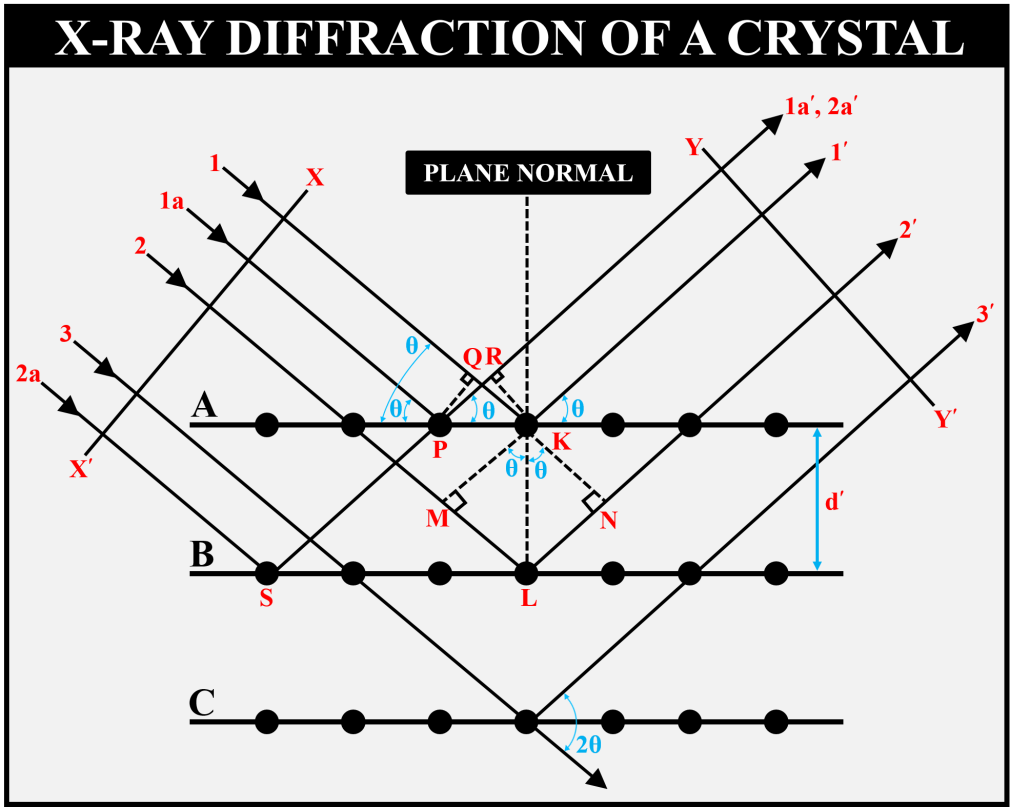

Figure 3.3.4: A geometric figure of how X-Rays diffract when going through a crystal. This schematic was adapted from Figure 3-2 as presented in chapter 3 of the textbook written by B. D. Cullity titled, "Elements of X-RAY DIFFRACTION" [237].

3.3.3.4.3 Micro-computerized tomography

Micro-CT is a non-destructive characterization technique that utilizes the highest X-Ray beam energies out of all the X-Ray based characterization techniques described herein. Higher X-Ray

beam energies are required as micro-CT is an X-Ray transmission characterization technique, thus high energy is required for X-Ray transmission. Micro-CT is performed by adhering the sample to a sample holder, where the sample is rotated 360° so that the X-Ray projections that are detected can be computed into 2D cross-sections having a thickness dependent on the voxel size used [240]. These 2D cross-sections can be reconstructed to generate a 3D reconstruction of the sample [240]. Contrast differences are interpreted as density fluctuations given density affects the attenuation of the incident X-Ray beam [240].

Ag-BG scaffolds were characterized using a Rigaku Quantum GX micro-CT instrument to evaluate the overall macrostructure of the Ag-BG scaffolds. Images were collected using the parameters described in Table 3.3.2. The acquired micro-CT images were analyzed using MicroView (Parallax Innovations, ON, Canada) to determine porosity (%), strut thickness (μm) of the Ag-BG scaffolds, pore diameter (μm), and specific scaffold density (g cm^{-3}).

Table 3.3.2: The parameters used during micro-CT characterization of Ag-BG scaffolds.

Parameter	Value
Scan mode	High resolution
Gantry rotation time (min.)	57
Power (kV_p/μA)	90/88
Field of view (mm)	5
Number of slices	512
Slice thickness (μm)	10
Voxel resolution (μm^3)	10

3.3.4 Nitrogen adsorption & desorption

N_2 adsorption and desorption measurements allow for characterization of the surface area, porosity, and pore size distributions of a material when interpreted using the Brunauer-Emmett-Teller (BET) theory [241]. To determine the specific surface area of the material, the specimen is cooled to cryogenic temperatures using liquid nitrogen, where N_2 gas is introduced with pressure and volumetric changes measured as a function of N_2 adsorption. The isotherms produced when the volume of N_2 adsorption is a function of pressure, where the shape of the isotherm curve is classified

as one of the six isotherm adsorption curves as presented and maintained by the International Union of Pure and Applied Chemistry (IUPAC) [242].

Herein, Ag-BG scaffolds were pulverized and degassed at 80°C for 6 h under vacuum pressure before measurement using an ASAP 2020 Micromeritics instrument. The amount of N_2 adsorbed was measured volumetrically at cryogenic temperatures (i.e. -196°C using liquid N_2) once thermal equilibrium was achieved.

3.3.5 Nitrogen pycnometry

N_2 pycnometry utilizes Boyle's law to measure the volume of a solid material by measuring the volume displacement of the gas used [243]. By knowing the volume of the displaced gas and the mass of the material being studied, the density of the material can be established.

Herein, N2 pycnometry (AccuPyc II 1340) was employed to determine the density of the Ag-BG powder used for the synthesis of the Ag-BG scaffolds. The mass of the Ag-BG powder was measured before placing the powder inside the chamber. The chamber was purged 5 times using N_2 gas. 20 measurements were recorded for the Ag-BG powder, where N_2 gas was added to the chamber at a rate of 0.1 psig min^{-1} and the measurements averaged to determine the density of the Ag-BG powder.

3.4 Performance characterization

3.4.1 Degradation behavior

The study of the degradation behavior of the Ag-BG scaffolds presented herein provides useful correlative information regarding the antibacterial and biological behavior of the Ag-BG scaffolds. Additionally, the study of the degradation behavior allows for predictions to be made on the approximate time it takes for the Ag-BG scaffolds to fully degrade to give a rough estimate on the time it should take for the Ag-BG scaffolds to degrade in vivo. Herein, the degradation behavior was studied by examining the mass loss and pH behavior of the Ag-BG scaffolds immersed in the

medium as a function of time. At each time point, extracts were collected to perform inductively coupled plasma optical emission spectroscopy (ICP-OES) to determine the concentrations of ions released at each time point.

3.4.1.1 Mass loss, pH, & inductively coupled plasma—optical emission spectroscopy

The degradation behavior of the printed Ag-BG scaffolds was elucidated through immersion of the Ag-BG scaffolds in 0.05 M tris(hydroxymethyl)aminomethane (TRIS; $C_4H_{11}NO_3$) buffer prepared to have a pH of 7.25 at 37.5°C. The mass to volume ratio used was 3.33 with the Ag-BG scaffolds kept at 37.5°C under 174 RPM of shaking for the duration of the study. The pH and mass loss of the Ag-BG scaffolds was measured in triplicate every 3 d for up to 30 d, where extracts (in triplicate) were collected at each time point for inductively coupled plasma – optical emission spectrometer (ICP-OES) to quantify the concentration of ions present to support the findings from antibacterial and biological studies.

For the hydrogel samples used for creating a compatible bioink for 3D bioprinting scaffolds, their degradation behavior was elucidated by immersing samples in 1X phosphate-buffered saline (PBS) at 37°C under an agitation rate of 175 RPM. The pH and mass loss were recorded at 1, 3, 5, and 7 days.

Characterization of hydrogels additionally requires a study of their swelling behavior, as hydrogels can absorb great quantities of the medium. This allowed for the elucidation of the effect the status and form of Ag-BG have on the swelling ratio when incorporated into GelMA. Hydrogels were lyophilized to determine their dry mass before hydration using 1X PBS, where samples 8 mm in diameter and 1.5 mm in thickness were immersed for 24 h. The hydrogels were removed from the medium, gently blotted dry to remove excess moisture, and their mass measured. The dry (W_0) and hydrated (W_t) masses were used to determine the swelling ratio as described by equation 3.4.1.

$$\frac{W_t\text{-}W_0}{W_0} \tag{3.4.1}$$

3.4.2 Mechanical performance

The study of the mechanical performance of the synthesized Ag-BG scaffolds is critical to determining the success of delivering Ag-BG scaffolds capable of targeting load-bearing applications for bone tissue regeneration. American Society for Testing and Materials (ASTM) standards were utilized, when possible, for consistency and accuracy of the measurements obtained for the different mechanical behaviors examined herein.

3.4.2.1 Compressive behavior

The compressive strength (MPa) of the Ag-BG scaffolds were evaluated using either a Rheometric Solids Analyzer (RSA-III) instrument using a load cell of 2 kg and a crosshead speed of 0.5 mm min^{-1} for fragile Ag-BG scaffolds (i.e. solution scaffolds) or a United SFM electromechanical series universal testing machine with a 4.45 kN load cell. All Ag-BG scaffolds had dimensions of 10 x 10 x 10 mm and were subjected to compressive forces that were maintained using a constant crosshead speed of 0.5 mm min^{-1}. The engineering compressive strength was calculated using equation 3.4.2, where F was the force (N) applied to the Ag-BG scaffold, and A was the initial cross-sectional area of the Ag-BG scaffolds (m^2).

$$\sigma_c = \frac{F}{A_0} \tag{3.4.2}$$

The average strut strength (MPa) for the Ag-BG scaffolds was computed from their compressive strengths using equation 3.4.3 as derived by Gibson-Ashby [57], where σ_{bulk} is the strut strength (MPa), $\sigma_{scaffold}$ is the compressive strength of the Ag-BG scaffold (MPa), and ρ_R being the relative density of the Ag-BG scaffold, defined as 1 - porosity.

$$\sigma_{bulk} = \frac{\sigma_{scaffold}}{0.65(\rho_R)^{1.5}} \tag{3.4.3}$$

3.4.2.2 Flexural behavior

Four-point flexural testing of the Ag-BG scaffolds having dimensions of 23.9 x 5.4 x 3.1 mm was performed on a fully articulated fixture having an outer and inner span of 20 mm and 10 mm, respectively and in accordance with ASTM C1674-16 [244] using a United SFM electromechanical series universal testing machine with a 0.445 kN load cell. Forces were applied along the z-axis at a constant crosshead speed of 0.2 mm min^{-1}. The flexural strength (MPa) of the Ag-BG scaffolds was determined using equation 3.4.4, where P was the maximum force (N) applied at failure, L was the outer span of the fully articulated fixture used, and b and d were the width and thickness of the Ag-BG scaffold, respectively.

$$\sigma_{flex} = \frac{3PL}{4bd^2} \tag{3.4.4}$$

3.4.2.3 Fracture toughness

The fracture toughness of the Ag-BG scaffolds having dimensions of 23.9 x 5.4 x 3.1 mm was measured using the single-edge notched beam (SENB) technique on a fully articulated fixture setup in the four-point configuration, where the outer and inner span was 20 mm and 10 mm, respectively. A 1.5 mm notch having a thickness below 100 μm was introduced to the Ag-BG scaffolds at their midpoint to satisfy the conditions for the application of linear elastic fracture mechanics following ASTM C1421-18 guidelines [245]. The fracture toughness was calculated using equation 3.4.5, where K_{Ic} was the fracture toughness ($MPa{\cdot}m^{1/2}$), f was a function of the ratio $\frac{a}{W}$ for the four-point configuration, P_{max} was the maximum force (N) applied, S_0 was the outer span of the four-point configuration, S_i was the inner span of the four-point configuration, B was the length of the Ag-BG scaffold perpendicular to the depth of the notch, W was the length of the Ag-BG scaffold parallel to the depth of the notch, and a was the length of the introduced notch.

$$K_{Ic} = [\frac{P_{max}(S_0 - S_1)10^{-6}}{BW^{3/2}}][\frac{3(\frac{a}{W})^{1/3}}{2(1-\frac{a}{W})^{3/2}}] \tag{3.4.5}$$

3.4.2.4 Rheology

Rheology was employed to elucidate the mechanical performance of hydrogel samples used for developing and determining if the hydrogel will be compatible with 3D bioprinting. The viscoelastic behavior of the samples was evaluated through measurement of the storage (G') and loss (G'') moduli as a function of temperature from ambient conditions to 40°C. The viscosity of the hydrogels was measured at 37°C (i.e. physiological temperatures) using a shear rate from 0.1 to 100 s^{-1}. Equation 3.4.6 was subsequently used to compute the flow consistency index (K) and flow index behavior (n) for hydrogel samples using the linear region of viscosity (Pa·s) as a function of shear rate (s^{-1}) [246].

$$\eta_{app} = K\dot{\gamma}^{(n-1)} \tag{3.4.6}$$

3.4.3 Antibacterial performance

All characterization of the antibacterial properties of the Ag-BG scaffolds was performed using laboratory-derived methicillin-resistant Staphylococcus aureus (MRSA) USA300JE2 [247] as MRSA is a commonly identified pathogen in bone infection(s) [37, 55]. To prepare the MRSA cultures for all the antibacterial studies, MRSA cells were obtained from a frozen stock stored at -78°C, streaked onto tryptic soy agar (TSA), and cultured at 37°C for 24 h to prepare for isolation. 5 mL of sterile tryptic soy broth (TSB) was used to culture a single isolated MRSA colony at 37°C for 24 h under 225 RPM of shaking. 1 mL aliquots of planktonic MRSA were prepared in sterile phosphate-buffered saline (PBS) and normalized to an optical density (OD600) of 1, where the MRSA concentration equated to 10^8 colony forming units (CFU) mL^{-1}. All Ag-BG scaffolds were preconditioned using Dulbecco's modified eagle media (DMEM) to prevent the osmotic effect [248, 249] from confounding their antibacterial behavior and UV sterilized for 1 h.

3.4.3.1 Combating planktonic MRSA

The ability of the Ag-BG scaffolds to combat planktonic MRSA was assessed up to 48h under growth-arrested conditions with CFUs enumerated every 24 h. To accomplish this, 11 mg mL^{-1} of the polymer foam replication scaffolds and FFF printed Ag-BG scaffolds using a unimodal distribution of Ag-BG particles were used in addition to a 100 mg mL^{-1} concentration for FFF printed Ag-BG scaffolds using a bimodal distribution of Ag-BG particles. All Ag-BG scaffolds were inoculated with MRSA and cultured at 37℃ and accompanied by controls for each time point that were prepared using a MRSA to PBS (sterile) ratio of 1:1.

To enumerate CFUs, the Ag-BG scaffolds having a concentration of 11 mg mL^{-1} were pulverized and homogenized to perform ten-fold serial dilutions. The Ag-BG scaffolds having a concentration of 100 mg mL^{-1} required transfer to a sterile Eppendorfs at the respective time points, where 0.5 mL of sterile trypsin was introduced, and samples incubated for 5 minutes to detach the MRSA from the Ag-BG scaffolds, given such scaffolds were too strong to pulverize utilizing the technique described above. To neutralize the trypsin, 0.5 mL of sterile TSB was added, the Ag-BG scaffold removed from the Eppendorf, and the trypsin-TSB aliquots spun down for 10 minutes at 12 g. After, the trypsin-TSB was discarded and replaced with sterile PBS. The PBS aliquots were spun down twice more, replacing the medium each time to wash the MRSA cells before combination with PBS at a 1:1 ratio with the original PBS aliquot that housed the Ag-BG scaffolds. Aliquots were homogenized, ten-fold serial dilutions performed, and dilutions plated onto tryptic soy agar (TSA) before culturing at 37°C for 24 h.

3.4.3.1.1 Combating antibiotic resistance with Ag-BG scaffolds

To elucidate whether the Ag-BG scaffolds could restore the efficacy of antibiotics MRSA is known to resist, 11 mg mL^{-1} of the Ag-BG slurry scaffolds were combined with either 0.2 μg mL^{-1} of Fosfomycin or 2 mg mL^{-1} of Vancomycin [250]. The antibiotics were dissolved in PBS, the Ag-BG slurry scaffolds were inserted into the Eppendorfs and combined with the MRSA in PBS solution at a 1:1 ratio. The CFUs were enumerated as previously described.

Further investigation entailed examining the effect the status of the microstructure and overall morphology had on the potency of the Ag-BG scaffolds to destroy MRSA, providing additional evidence to support whether the Ag-BG scaffolds are capable of restoring antibiotics MRSA is known to resist. To this end, Ag-BG slurry scaffolds were pulverized, sieved so that their particle size was below 20 μm, and the anti-MRSA effect compared to the Ag-BG slurry scaffolds themselves and Ag-BG powder as-received, and CFUs enumerated after 24 h under growth-arrested conditions, as previously described.

3.4.3.2 Combating MRSA biofilms

To assess the ability of Ag-BG scaffolds to combat a previously formed MRSA biofilm, aliquots of MRSA in sterile TSB at a concentration of 10^8 CFUs mL^{-1} were prepared and placed into a 6-well tissue culture plate (TCP) containing a glass coverslip having an area of ~78 mm^2 and incubated for 48 h at 37°C to allow a MRSA biofilm to grow. The glass coverslips containing the MRSA biofilm were then transferred to a fresh 6-well TCP containing sterile TSB and 100 mg mL^{-1} of the Ag-BG scaffolds ensuring that the Ag-BG scaffold did not directly interact with the glass coverslip containing the MRSA biofilm when added. The Ag-BG scaffolds and glass coverslips containing the MRSA biofilm were incubated for 72 h at 37°C. Wells containing sterile TSB alone and wells having sterile TSB and the glass coverslip with the MRSA biofilm were additionally prepared to serve as the negative and positive controls respectfully.

To quantify the biomass present after the MRSA biofilms on the glass coverslips after the 72 h of incubation at 37°C, the Ag-BG scaffolds were removed and the glass coverslips containing the MRSA biofilms were transferred to a new 6-well TCP and gently washed thrice with sterile PBS. The MRSA biofilms were then fixed using 100% ethanol (Koptec; 200 proof) with immediate aspiration before drying at ambient conditions for 10 min. 0.5 mL of a 1% solution of crystal violet stain were added to the relevant wells and allowed to incubate for 5 min. at ambient conditions. The crystal violet stain was then aspirated, and the relevant wells were washed thrice with sterile PBS and the TCP incubated at 37°C for 24 h to allow sufficient time for the wells to dry. The crystal

violet stain was eluted using 100% ethanol and 0.1 mL aspirated and transferred to a 96 well TCP for OD absorbance measurements at a wavelength of 595 nm.

Live/Dead staining was additionally performed in parallel, where after treating the MRSA biofilms on the glass coverslips with the Ag-BG scaffolds for 72 h at 37°C, the Ag-BG scaffolds were removed, and MRSA biofilms were transferred to a new 6-well TCP and gently washed thrice using sterile 0.85% NaCl distilled water. The MRSA biofilms were stained using the Live/Dead Baclight Bacterial Viability Kit and allowed to incubate for 15 min. at ambient conditions in the absence of light. The live/dead stain was aspirated, and samples were fixed using 4% glutaraldehyde in 0.1M PBS and allowed to incubate for 30 min in ambient conditions before aspiration of the fixative. The MRSA biofilms were washed thrice using sterile 0.85% NaCl distilled water and immediately imaged using a Nikon C2 confocal laser scanning microscope (CLSM). The carboxyfluorescence diacetate was excited using a 488 nm diode laser, with green fluorescence emission detected using a 500-550 nm bandpass filter to image the live MRSA. The propidium iodide was excited using a 560 nm diode laser, with red fluorescence emission detected using a 575-625 bandpass filter to image the dead MRSA. The live and dead MRSA were quantified using Fiji is just ImageJ [251] with values expressed as a percentage.

3.4.4 Biological performance

Both in vitro and in vivo study of the Ag-BG scaffolds is imperative to evaluate the biocompatibility of the Ag-BG scaffolds. Various acellular and cellular characterization techniques were utilized to assess the biocompatibility of the Ag-BG scaffolds and explained hereafter.

3.4.4.1 Acellular conditions—assessing apatite-forming ability

Simulated body fluid (SBF) was prepared with the following ionic concentrations: 142.0Na^{+}, 5.0K^{+}, 2.5Ca^{2+}, 1.5Mg^{2+}, 148.8Cl^{-}, 1.0$HPO_4{}^{-}$, 4.2$HCO_3{}^{-}$, and 0.5$SO_4{}^{2-}$ (mmol dm^3) as previously described by Kokubo et. al [252, 253] to study the capability of the Ag-BG scaffolds to form an apatite-like layer. A mass to volume ratio of 3.33 was used for all Ag-BG scaffolds with

SBF replacement occurring every 48 h. The Ag-BG scaffolds were immersed for up to 21 d kept at 37.5℃ under 174 RPM of agitation. The formation of an apatite-like layer was assessed using SEM-EDS to observe any distinct surface morphological changes along with FTIR-ATR and XRD to detect any molecular or crystallographic changes.

3.4.4.2 Cellular conditions—in vitro

3.4.4.2.1 Cell viability & proliferation

The biocompatibility of the Ag-BG scaffolds (V = 24 mm^3) was assessed indirectly, placing Ag-BG scaffolds in transwells ensuring that the scaffolds were immersed in the medium. Human mesenchymal stem cells (hMSCs) were used and obtained from Tulane University Center for Gene Therapy, where hMSCs were harvested from a 28-year-old male (7043L) and used at passage 6. To evaluate hMSC viability and proliferation, hMSCs were seeded at a concentration of $2.0 \cdot 10^4$ hMSCs mL^{-1} in 24-well TCPs using standard growth media (α-MEM supplemented with 16% fetal bovine serum (FBS), 1% antimycotic (Gibco 15,240,062), and 1% L-glutamine), and the WST-8 (ab228554) assay applied after 2, 5, and 8 d of indirect exposure to Ag-BG scaffolds with ODs measured at 460 nm. Optical images (Lionheart FX automated microscope; BioTek) were additionally captured at each time point to observe hMSC morphology.

3.4.4.2.2 Cell differentiation

To assess the ability of the Ag-BG scaffolds to induce hMSC mineralization, hMSCs were seeded at a concentration of $2.0 \cdot 10^4$ hMSCs mL^{-1} in 24-well TCPs using osteogenic differentiation media (α-MEM supplemented with 8% fetal bovine serum (FBS), 1% antimycotic (Gibco 15,240,062), 1% L-glutamine, 25 μg mL^{-1} ascorbic acid 2-phosphate, 250 μL of β-glycerophosphate, and 100 μM of dexamethasone). The mineralization of hMSCs was quantified after 17 d of indirect exposure to Ag-BG scaffolds using the Alizarin red stain (ARS; Sigma Aldrich) assay to identify Ca-containing osteocytes. In short, 40 mM of ARS solution in distilled water was mixed with hMSCs for 0.5 h, aspirated, and the TCP allowed to dry under ambient conditions. After drying,

optical images were captured of the stained wells and %ARS quantified using Fiji is just ImageJ [251, 254].

3.5 Statistical analysis

3.5.1 Overall statistical methods

The data were expressed in terms of means and standard deviations (error bars). Statistical significance was assessed using the paired Student's t-test and indicated if $p < 0.05$.

3.5.2 Weibuill statistics for mechanical performance

To assess the reliability of the compressive behavior of the FFF printed Ag-BG scaffolds, Weibull statistics following ASTM C1239-13 [255] were computed, where the Weibull modulus (m) was evaluated fitting the compressive strengths of each FFF printed Ag-BG scaffold using equation 3.5.1, where P_f is the probability of failure at stress, σ, having a Weibull scale parameter of σ_0. P_f was calculated using equation 3.5.2, where n is the total number of scaffolds evaluated and i is the rank of the scaffold in ascending order of failure stresses.

$$\ln\ln\left(\frac{1}{1-P_f}\right) = m\ln\left(\frac{\sigma}{\sigma_0}\right) \tag{3.5.1}$$

$$P_f = \frac{i-0.5}{n} \tag{3.5.2}$$

CHAPTER 4

RESULTS

4.1 Characteristics of Ag-BG

The work presented in Section 4.1 has previously been published by Marsh et al., as described by the following citation:

- Journal of the European Ceramic Society, Vol 41, Adam C. Marsh, Nathan P. Mellott, Martin Crimp, Anthony Wren, Neal Hammer, Xanthippi Chatzistavrou, Ag-doped Bioactive Glass-Ceramic 3D Scaffolds: Microstructural, Antibacterial, and Biological properties, 3717-3730, Copyright Elsevier (2021) [223].

4.1.1 Thermal behavior & structural evolution of as-received Ag-BG

Obtaining Ag-BG scaffolds that can elicit both an antibacterial and biological response in addition to possessing satisfactory mechanical performance for targeting load-bearing applications for bone tissue regeneration required first evaluating the thermal behavior of as-received Ag-BG as a function of temperature to determine advantageous structural changes for sintering optimization. To accomplish this, as-received Ag-BG particles were studied using DTA/TGA and HSM characterization techniques (Section 3.3.2.1) to elucidate the glass-transition temperature (T_g) crystallization onset temperature and melting temperatures (T_m). Understanding these thermal transitions allows for control over the microstructure delivered in the Ag-BG scaffolds, thus allowing for preferential microstructures to be delivered. Literature defines the "ideal" processing window for delivering scaffolds having bone tissue regenerative characteristics as the region between T_g and the onset of crystallization [15]. This rationale was aimed at preserving the amorphous structure of the material to promote dissolution enhancing antibacterial and biological responses while maintaining the

required mechanical performance of scaffolds targeting bone tissue regeneration in load-bearing applications.

As shown in Figure 4.1.1a, the DTA plot of the as-received Ag-BG particles exhibited a small endothermic peak at ~450℃ correlated to the glass-transition temperature of the Ag-BG. Beyond T_g, minimal changes in heat flow were observed until ~700℃, at which point the heat flow was observed to steadily increase, demonstrating that exothermic processes are occurring. This event was correlated to the temperature of the onset of crystallization with relevant Ag-BG XRD patterns supporting correlation [33, 223]. Given this, the "ideal" processing window for synthesizing Ag-BG scaffolds was 450°C to 700°C; however, HSM investigations on the Ag-BG particles (Fig. 4.1.1c) identified that notable shrinkage does not occur until temperatures exceeding 800°C are achieved. Thus, the HSM findings are inconsistent with the criteria previously defined for the "ideal" scaffold processing window.

To reconcile this disagreement between DTA and HSM data, the glass formability, or Hrubý coefficient [68, 256–259], of the as-received Ag-BG was quantified using equation 4.1.1, where T_x is the onset of crystallization, Tg is the glass transition temperature, and Tm is the melting temperature [258] This computation has been widely used as a result of the ability of the Hrubý coefficient to quantify the densification competition that arises between viscous flow and crystallization within glassy systems.

$$K_H = \frac{T_x - T_g}{T_m - T_x} \tag{4.1.1}$$

The values for T_x, T_g, and T_m were derived from the DTA plot shown in Figure 4.1.1, where T_x was defined at 701℃, T_g at 450℃, and T_m at 1450℃, where complete melting of the Ag-BG was thought to occur. The resulting Hrubý coefficient for as-received Ag-BG was 0.34, which can be interpreted to state that the as-received Ag-BG possesses modest glass stability. This finding would suggest that the as-received Ag-BG should have the ability to undergo viscous sintering avoiding significant crystallization. Given the mismatch between this interpretation for the Hrubý coefficient for the as-received Ag-BG and the experimental evidence presented in Figure 4.1.1,

it was concluded that the use of the Hrubý coefficient was inadequate to accurately describe the thermal behavior of as-received Ag-BG.

Investigating methods for achieving agreement between experimental evidence and computation, Lara et al. expanded on the Hrubý coefficient to derive an approach to calculate the sinterability (S_c) of silicate-based-glass systems beyond the sinterability of bioactive glass systems as demonstrated by Baino et. al [68, 71]. The sinterability calculation attempts to quantify the independence between viscous sintering and crystallization, where positive values demonstrate independence between viscous sintering and crystallization mechanisms and negative values, meaning the two aforementioned densification mechanisms are dependent. Equation 4.1.2 describes the sinterability calculation, where T_x is the onset of crystallization (T1, 701°C; Fig. 4.1.1b) and T_{MS} (1093°C; Fig. 4.1.1b) is the temperature at which maximum shrinkage was observed during HSM investigations.

$$S_c = T_x - T_{MS} \tag{4.1.2}$$

From this, the as-received Ag-BG was found to possess a largely negative sinterability, where viscous sintering and crystallization are highly dependent events [68]. Further extrapolation from the results computed using equation 4.1.2 infers that as-received Ag-BG exhibits low surface tension and high viscosity at elevated temperatures given that these conditions are known to lead to densification via crystallization [68, 71]. Given the agreement between the sinterability parameter and experimental evidence (Fig. 4.1.1) collected for as-received Ag-BG, it was concluded that the sinterability parameter provides the most accurate description of the thermal behavior of as-received Ag-BG.

Additionally, the highlighted temperatures shown in the DTA plot (i.e. $T_1 - T_5$; Fig. 4.1.1a) for as-received Ag-BG were used to investigate how the various thermal events correlated to shrinkage. To this end, the temperature where notable shrinkage was first observed (T_3 - 764°C; Fig. 4.1.1b) corresponded to the low end (T_1 - 770°C; Fig. 4.1.1a) of the broad exothermic peak spanning from ~700°C to 1000°C. At the peak of the broad exothermic event (T3 - 917°C; Fig. 4.1.1a), shrinkage of as-received Ag-BG demonstrated a linear increase, with the rate of shrinkage plateauing at T_6

(964°C; Fig. 4.1.1b).

Interestingly, the shrinkage remained relatively stable at ~42% within the ~1000°C to ~1200°C temperature range. XRD patterns demonstrated that the concentration of wollastonite-2M is increasingly diminished in favor of its high-temperature polymorph, pseudowollastonite [223]. Given that the volume of the pseudowollastonite unit cell volume is approximately 400% greater than wollastonite-2M, an expansion of as-received Ag-BG would have been expected; however, this is not the case. To remedy this discrepancy, it was hypothesized that the expected volume increase was counterbalanced by increased densification of Ag-BG as received.

Important to note that within the stable shrinkage temperature region for as-received Ag-BG (Fig. 4.1.1b), a calcium phosphate phase transformation occurs. To start, at temperatures below 1000°C, literature has shown that bioactive glass systems such as Ag-BG develop a Ca-deficient hydroxyapatite phase [260]. Starting ~1050°C, the Ca-deficient hydroxyapatite thought to be present in as-received Ag-BG is reported to undergo phase transformation to β-tricalcium phosphate (β-TCP) [261, 262]. Examination of the respective unit cell volumes for Ca-deficient hydroxyapatite and β-TCP while additionally taking into account the number of atoms per unit cell finds that there is minimal volume change during this phase transformation, providing additional evidence to describe the stable shrinkage that was observed in HSM for as-received Ag-BG (Fig. 4.1.1b).

As temperatures began to exceed 1200°C, as-received Ag-BG was found to expand culminating at ~1268°C, interestingly correlating to the development of the endothermic peak observed in DTA (Fig. 4.1.1a) of as-received Ag-BG. At these temperatures, β-TCP is reported to undergo a phase transformation to α-tricalcium phosphate (α-TCP) [263, 264], where α-TCP is associated with increased disorder and decreased packing of the atoms leading to an increase in the free volume [263]. This increase in free volume between CaP polymorphs was hypothesized to be the cause of the expansion observed in HSM of as-received Ag-BG (Fig. 4.1.1b) assuming complete densification of as-received Ag-BG was achieved before the β-TCP→α-TCP phase transformation.

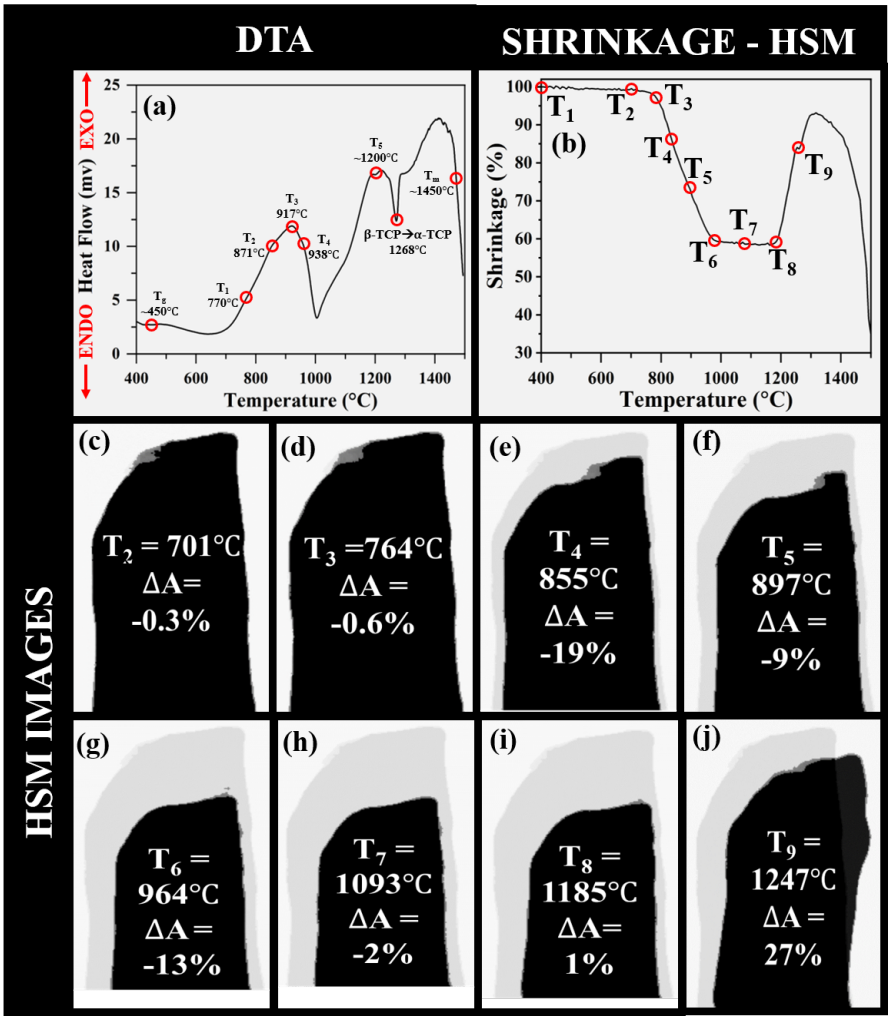

Figure 4.1.1: (a) Shows the DTA/TGA behavior of Ag-BG particles, (b) presents the shrinkage behavior of the Ag-BG particles as a function of temperature derived from HSM, and (c) are images of the Ag-BG at different temperatures during HSM. ΔA represents the area change between each temperature shown in (c), computed using image analysis.

4.2 Ag-BG scaffolds synthesized using the polymer foam replication technique

The thermal information derived from the DTA and HSM characterization of as-received Ag-BG were utilized to help determine the sintering conditions that were applied for Ag-BG scaffolds synthesized using the polymer foam replication technique.

The work presented in Section 4.2 has previously been published by Marsh et al., as described by the following citations respectively:

- Bioactive Materials, Vol 4, Adam C. Marsh, Nathan P. Mellott, Natalia Pajares-Chamorro, Martin Crimp, Anthony Wren, Neal D. Hammer, Xanthippi Chatzistavrou, Fabrication and multiscale characterization of 3D silver containing bioactive glass-ceramic scaffolds, 215-223, Copyright Elsevier (2020) [225].

- Journal of the European Ceramic Society, Vol 41, Adam C. Marsh, Nathan P. Mellott, Martin Crimp, Anthony Wren, Neal Hammer, Xanthippi Chatzistavrou, Ag-doped Bioactive Glass-Ceramic 3D Scaffolds: Microstructural, Antibacterial, and Biological properties, 3717-3730, Copyright Elsevier (2021) [223].

4.2.1 Structural characteristics

4.2.1.1 Macro- & milli- structure

Ag-BG scaffolds synthesized by the solution (Section 3.2.1.1) and slurry (Section 3.2.1.2) techniques were successful in delivering highly porous (Table 4.2.1) scaffolds patterned after the PU foam template used. Optical microscopy of solution and slurry Ag-BG scaffolds demonstrated that the scaffold synthesis processes had a chromatic effect on the delivered Ag-BG scaffolds, as shown in Figure 4.2.1a, b. Ag-BG scaffolds delivered using the solution technique presented with a random distribution of yellow/brown dark coloration interspersed with regions having a vitreous sheen. This observed dark coloration (Fig. 4.2.1a, b) suggested the possibility that the solution technique was unable to fully maintain the Al-tetrahedron mechanism utilized to stabilize Ag^{+} ions warranting further investigation into the microstructural and nanostructural characteristics of the Ag-BG scaffolds synthesized by the solution technique. Conversely, this dark coloration phenomenon was not observed for Ag-BG scaffolds synthesized by the slurry technique (Fig. 4.2.1c, d), whose coloration was found to be primarily white with an opaque nature. Given the contrasting chromatic nature between solution and slurry Ag-BG scaffolds, it was hypothesized that the vitreous sheen observed for solution scaffolds was optical evidence that the amorphous component of Ag-BG in solution scaffolds was preserved to an extent leading to improved antibacterial and biological

responses [265].

SEM images of Ag-BG solution scaffolds (Fig. 4.2.1e, f) revealed prominent fracturing across the entire scaffold surface and expected to have a deleterious effect on mechanical performance when characterized. Ag-BG slurry scaffolds showed fewer surface fractures (Fig. 4.2.1g, h) on the scaffold surface comparatively; however, the surface fractures were observed to be concentrated at the interfaces, where the scaffold material is found to change angular orientation (Fig. 4.2.1h), thus weakening the expected mechanical performance for Ag-BG slurry scaffolds.

Examination of the Ag-BG solution scaffolds at higher magnification resolution (Fig. 4.2.1f) revealed a porous microscopic surface morphology, demonstrating that the solution polymer foam replication synthesis process can preserve the inherent porosity known to be introduced when using the sol-gel process. Ag-BG slurry scaffolds, however, presented a rough microscopic surface morphology (Fig. 4.2.1h), where Ag-BG particles appear to be sintered together. Interestingly, strut cross-section appears comparatively more pronounced for the Ag-BG slurry scaffolds; however, for both solution and slurry Ag-BG scaffolds, the strut cross-sections revealed a hollow internal structure generated from the sacrifice of the polyurethane foam during heat treatment. These findings provide additional evidence to support the weak mechanical performance hypothesis.

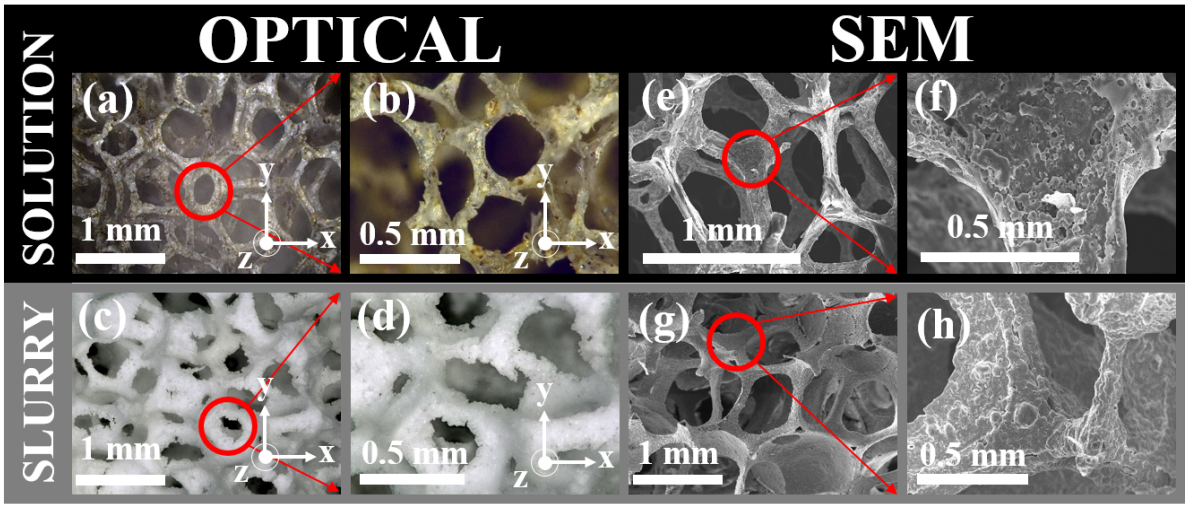

Figure 4.2.1: Optical images of Ag-BG scaffolds synthesized by the (a-b) solution and the (c-d) slurry technique. SEM images respective of Ag-BG scaffolds synthesized by the (e-f) solution technique and (g-h) slurry technique.

The macro- and milli- structural characteristics of interest (i.e. porosity, pore size, strut thickness, and apparent density) for Ag-BG solution and slurry scaffolds are summarized in Table 4.2.1 and calculated based on both optical and micro-CT characterization. Optically, the porosity (%) was calculated using equation 4.2.1 [225], where V_{AIR} describes the total empty volume of the scaffold and V_{TOTAL} defines the overall volume of the scaffold. Pore size was measured from optical images and analyzed using Fiji is just ImageJ [251] and adjusted through the application of a correction factor (1.67; [266]) to account for the dimensional difference created by measuring a 3D quantity in 2D space.

$$\%\text{Porosity} = \frac{V_{AIR}}{V_{TOTAL}} \cdot 100 \tag{4.2.1}$$

Table 4.2.1: Macro- and milli-structural characteristics of Ag-BG scaffolds synthesized by the polymer foam replication technique.

	Foam Characteristics	Solution-Optical	Solution-Micro-CT	Slurry-Optical	Slurry-Micro-CT
Porosity (%)	98.4±0.21	98.4±0.4	95.4	88.2±3.6	92.4
Apparent Density (g cm^{-1})	0.04	0.05±0.01	0.05	0.25±0.08	0.08
Pore Size (μm)	569±63.6	842±126	896±48.3	698±157	722±29.4
Strut Thickness (μm)	99.4±16.7	85±16	43.3±2.33	808±36.3	59.6±2.43

Characterization of the overall gross Ag-BG scaffold in addition to elucidation of their internal characteristics was achieved using micro-CT. Examining the gross structure of solution and slurry Ag-BG scaffolds (Fig. 4.2.2a, d), the respective 3D reconstructions identify that the solution technique was more successful at maintaining the open porous network of the polyurethane foam template used as fewer blocked pores were observed. This observation was correlated to the viscosity differences during the solution and slurry processes respectively, with the higher viscosity of Ag-BG slurry increasing the challenge of maintaining the open porous network desired.

4.2.1.2 Microstructure

As previously shown in Section 4.2.1.1, the macro- and milli structure of the Ag-BG scaffolds are expected to deleteriously influence the resulting mechanical performance due to their hollow interior; however, it is hypothesized that examining the finer structures (i.e. micro-, meso-, and

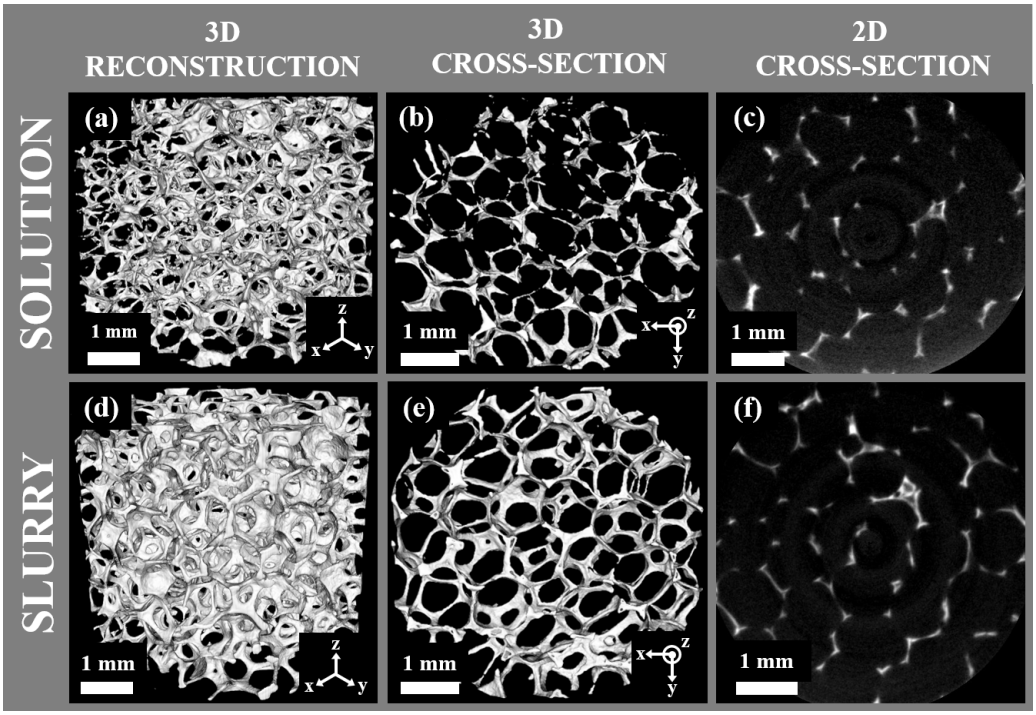

Figure 4.2.2: Complete 3D reconstructions of Ag-BG (a) solution and (d) slurry scaffolds. 3D reconstructions having a thickness of 1 mm are additionally presented for Ag-BG (b) solution and (e) slurry scaffolds to better show the porous structure of each scaffold type. Representative 2D cross-sections for Ag-BG (c) solution and (f) slurry scaffolds are shown to give a 2D perspective of the open porous structure for both scaffold types.

nano-) of the Ag-BG scaffolds will elucidate the expected correlations between structure and antibacterial and biological performance. Evidence supporting this hypothesis will be explored herein.

Moving from macro- and millistructural characterization of the Ag-BG solution and slurry scaffolds to microstructural characterization utilized XRD, FTIR, and SEM-EDS techniques. From the XRD patterns collected for Ag-BG solution and slurry scaffolds, the solution scaffolds (Fig. 4.2.3a) presented partial crystallization interpreted to state that the solution scaffolds possess a glass-ceramic nature. Examining the XRD pattern in closer detail revealed crystalline phases consisting of hydroxyapatite (HA; $Ca_{10}(PO_4)_6(OH)_2$), cristobalite (C; SiO_2), and Ag as determined through examination of relevant powder diffraction files (PDF) housed within the ICDD database. Underneath the diffraction peaks for the XRD pattern of Ag-BG solution scaffolds (Fig. 4.2.3a) was a broad peak spanning a width greater than 5° 2θ correlated to the presence of an amorphous

component. This amorphous contribution in the XRD pattern correlates with the vitreous sheen that was observed in the optical images (Fig. 4.2.3a, b) for the Ag-BG solution scaffolds. Interestingly, out of the three crystalline phases observed in the XRD pattern of Ag-BG solution scaffolds (Fig. 4.2.3a), only the presence of Ag in the form of particles is known to possess chromatic characteristics consistent with the yellow/brown dark coloration observed in their optical images (Fig. 4.2.3a, b). EDS characterization on Ag-BG solution scaffolds is expected to detect evidence of Ag particles only if their size is greater than the interaction volume generated by the incident electron beam. The XRD pattern for Ag-BG slurry scaffolds (Fig. 4.2.3a), a highly crystalline structure was observed that lacked evidence of the presence of an amorphous component. Five crystalline phases were identified in the XRD pattern for Ag-BG slurry scaffolds (Fig. 4.2.3a) that were cristobalite, HA, wollastonite-2M (W. 2M; $CaSiO_3$), pseudowollastonite (PsW; $Ca_3Si_3O_3$), and Ag. The highly crystalline nature of Ag-BG slurry scaffolds is hypothesized to slow their dissolution during antibacterial and biological performance characterization, leading to a slower formation of an apatite-like layer and a weaker anti-MRSA response compared to the glass-ceramic nature of Ag-BG solution scaffolds.

The respective FTIR spectra for Ag-BG solution and slurry scaffolds (Fig. 4.2.3b) revealed the glass-ceramic nature of Ag-BG solution scaffolds was evidenced complementing the findings from the XRD pattern of the Ag-BG solution scaffolds. Interestingly, the highly crystalline nature of Ag-BG slurry scaffolds was reflected in their respective FTIR spectra (Fig. 4.2.3b) by the presence of sharp, well-defined peaks. Given this, the bonds identified in the FTIR spectrum (Fig. 4.2.3b) could be correlated to the crystalline phases identified in the XRD pattern (Fig. 4.2.3a), thus providing supporting evidence for the phases previously noted.

From low wavenumber to high wavenumber, Si-O bending peaks were observed at ~450 cm^{-1} and ~800 cm^{-1}, where the peak at ~450 cm^{-1} is a characteristic peak of silicate-based glass systems while the peak at ~800 cm^{-1} was correlated to the presence of cristobalite [45, 265]. Si-O bending peaks at ~650 cm^{-1} and ~720 cm^{-1} were solely observed in the FTIR spectrum for Ag-BG slurry scaffolds (Fig. 4.2.3b) and correlated to the presence of cristobalite and PsW respectively

[235, 267, 268]. Regarding Si-O stretching peaks, the peaks observed at ~900 cm^{-1} and ~1005 cm^{-1} were correlated to the presence of W. 2M [235, 268, 269] while the Si-O stretching peaks at ~930 cm^{-1} and ~990 cm^{-1} were correlated to the presence of PsW [235, 267, 268]. The Si-O stretching peak noted at ~1200 cm^{-1} was correlated to the presence of cristobalite [45, 265]. Given that the only phosphate-containing phase was hydroxyapatite for both Ag-BG solution and slurry scaffolds, the relevant P-O bending peaks observed at ~570 cm^{-1} and ~620 cm^{-1} and P-O stretching peaks noted at ~1000 cm^{-1} and ~1070 cm^{-1} were all correlated to the presence of hydroxyapatite [235].

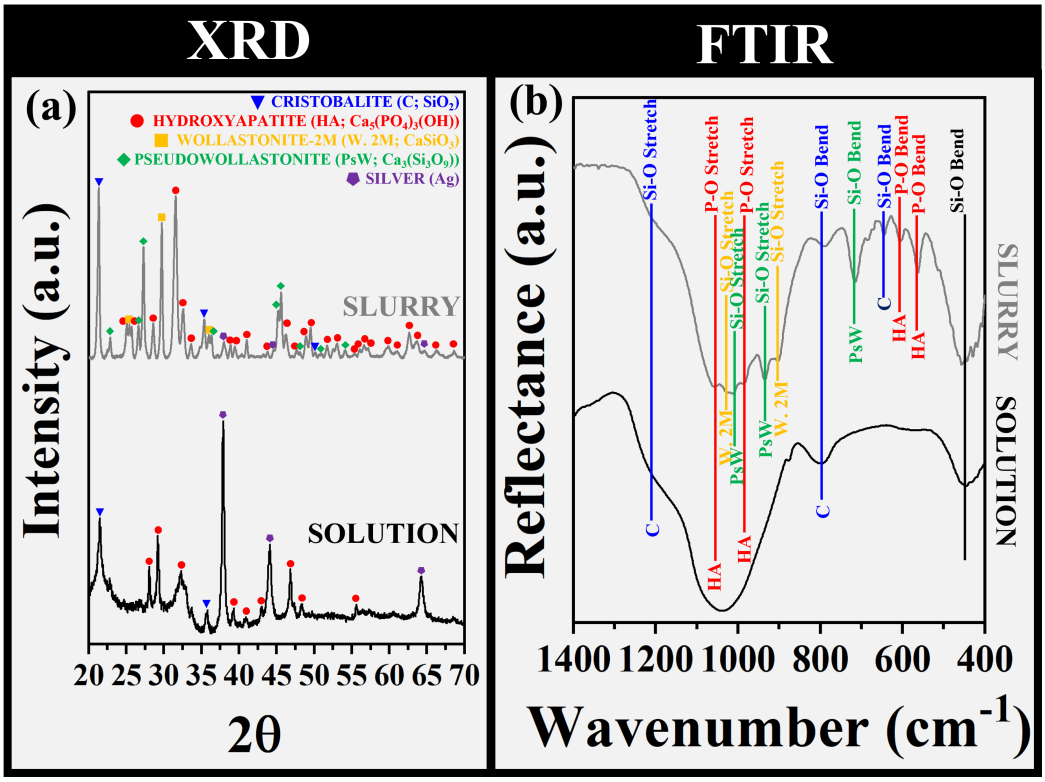

Figure 4.2.3: Representative (a) XRD patterns for powdered Ag-BG solution and slurry scaffolds in addition to the (b) complementary FTIR spectra for both Ag-BG solution and slurry scaffolds.

Investigation of the Ag particle hypothesis described previously was studied using SEM-EDS characterization. SEM showed (Figure 4.2.4a, b) that both Ag-BG solution and slurry scaffolds had relatively smooth surface morphologies down to the micron level, where the meso-sized pores observed for Ag-BG solution scaffolds was correlated to the use of the sol-gel process as was

previously noted in Figure 4.2.4f, while the meso sized-pores for Ag-BG slurry scaffolds was correlated to the development of vacancies during the sintering process of the Ag-BG particles during Ag-BG slurry scaffold synthesis. EDS mapping analysis of both Ag-BG solution (Fig. 4.2.4c-h) and slurry scaffolds (Fig. 4.2.4i-n) revealed all elements were homogeneously distributed down to the micron level. While elemental homogeneity down to the micron level is expected to produce a homogenous response when Ag-BG solution and slurry scaffolds are characterized for their antibacterial and biological performance, the lack of elemental heterogeneity for Ag suggested that Ag particles were either meso- or nano-sized given the presence of Ag diffraction peaks in the XRD patterns (Fig. 4.2.4a) for both Ag-BG solution and slurry scaffolds, thus requiring the use of additional characterization techniques to prove/disprove the Ag particle hypothesis.

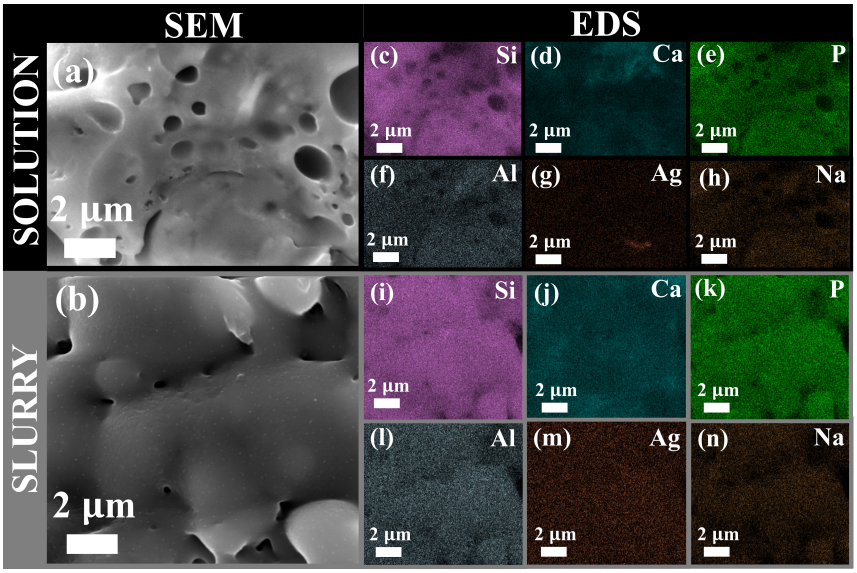

Figure 4.2.4: Representative (a) XRD patterns for powdered Ag-BG solution and slurry scaffolds in addition to the (b) complementary FTIR spectra for both Ag-BG solution and slurry scaffolds.

Further, the XRD pattern of Ag-BG slurry scaffolds (Fig. 4.2.3a), given its pentaphasic highly crystalline nature and the expected dissolution delay for antibacterial and biological performance, it was advantageous to explore methods at modifying the weight concentrations of the phases present as an approach to improving antibacterial and biological performance. To achieve this, additional Ag-BG slurry scaffolds were sintered at 900°C for the same duration as what was performed for the synthesis of Ag-BG slurry scaffolds sintered at 1000°C (Table 3.2.2) to elicit the formation

of cristobalite, HA, and Ag in similar concentrations while suppressing the high-temperature polymorph of W. 2M, PsW [267, 270]. Table 4.2.2 shows the phase concentrations for both types of Ag-BG slurry scaffolds demonstrating that this approach was successful at modifying the W. 2M and PsW phase concentrations while keeping the phase concentrations of cristobalite, HA, and elemental Ag relatively consistent between sintering temperatures. The impact of this phase concentration modification will be explored further in Sections 4.2.2.2 and 4.2.2.3.

Table 4.2.2: The phase concentrations for Ag-BG slurry scaffolds sintered at 900°C and 1000°C as computed through Rietveld analysis.

Phases	Sintering at 900°C	Sintering at 1000°C
Cristobalite	10%	9%
HA	39%	36%
W. 2M	25%	16%
PsW	25%	38%
Elemental Ag	< 1%	< 1%

4.2.1.3 Meso- & nano- structure

Elucidation of the meso- and nanostructure of both Ag-BG solution and slurry scaffolds was achieved using TEM, UV-Vis, and MAS-NMR characterization techniques, whose results will be explored herein. The representative bright-field TEM image for powdered Ag-BG solution scaffolds (Fig. 4.2.5a) revealed the presence of circular features < 50 nm in size allowing minimal electron transmission compared to other features located within the meso-sized particle being examined. The powdered Ag-BG solution scaffold (Fig. 4.2.5a) was additionally studied using selected area diffraction (SAD; Fig. 4.2.5b) to determine what phases (if any) were present in the analysis region (Fig. 4.2.5a). Both HA and elemental Ag were identified in the SAD pattern consistent with the phases identified during XRD (Fig. 4.2.5a) and FTIR (Fig. 4.2.5b) characterization. Given the presence of Ag in the SAD pattern of the powdered Ag-BG solution scaffold (Fig. 4.2.5b) coupled with the minimal electron transmission of the < 50 nm sized particles, it was hypothesized that these were Ag nanoparticles (AgNPs) given that Z for Ag is 27 units greater than the next highest Z

element in the Ag-BG composition (i.e. Ca). This difference in Z results in a greater atomic nuclei size for Ag compared to all other elements present in the Ag-BG composition, resulting in a greater probability that electrons will be scattered by the Ag atomic nuclei rather than be transmitted, thus leading to a low degree of electron transparency providing further evidence to support the presence of AgNPs. To provide further verification, UV-Vis (Fig. 4.2.5c) was performed on powdered Ag-BG solution scaffolds, where an absorbance peak of 428 nm was observed. This absorbance peak is within the region expected in the presence of AgNPs exhibiting surface plasmon resonance (SPR) [271–273] excited by the visible light that is additionally chromatically expressed as yellow hues, thus providing supporting evidence to describe the yellow/brown dark coloration observed for the Ag-BG solution scaffolds optically (Fig. 4.2.5a, b).

Examining powdered Ag-BG slurry scaffolds by way of TEM, the bright-field TEM image presented in Figure 4.2.5d shows meso-sized particles having variable electron transmission due to overlapping of the individual meso-sized particles. Additionally, a random distribution of nanosized particles (< 50 nm) having minimal electron transparency similar to those observed in the bright-field image for the powdered Ag-BG solution scaffold (Fig. 4.2.5a) and hypothesized to be AgNPs. Examination of one of these features (Fig. 4.2.5e) resolved lattice fringes, where the lattice fringe spacing was measured at 0.236 consistent with the inter-planar spacing of the (1 1 1) planes of Ag and validating the AgNP hypothesis for Ag-BG slurry scaffolds. The SAD pattern for the powdered Ag-BG slurry scaffold (Fig. 4.2.5f) presented a complex spot pattern, where cristobalite, HA, W. 2M, PsW, and Ag were all identified supporting the peak indexing performed on the respective XRD pattern (Fig. 4.2.5a). Additional indexing, however, was not possible given the pentaphasic nature of Ag-BG slurry scaffolds further convoluted by the overlapping of the meso-sized particles resulting in double diffraction making indexing exponentially more complicated [274].

The micro-, meso-, and nanostructural features observed for Ag-BG solution and slurry scaffolds clearly show that the use of the polymer foam replication technique disrupts the ability of $[AlO_4]^-$ to stabilize Ag^+ ions given the presence of AgNPs for both types of polymer foam replication scaffolds explored herein. Had the polymer foam replication technique caused a reduction of all

Ag^+ ions into Ag^0 in the form of AgNPs, the Rietveld analysis should have detected a greater concentration of Ag than what was reported in Table 4.2.2. Therefore, there may be a mix of Ag^+ ions and AgNPs within the polymer foam replication scaffolds.

To determine whether a mix of Ag^+ ions and AgNPs are present, powdered Ag-BG slurry scaffolds were characterized using ^{27}Al MAS-NMR (Fig. 4.2.5g). Previous reports by Chatzistavrou et al. [32] have demonstrated that the addition of Ag in the presence of Al within the Ag-BG composition increases the signal of five-fold coordinated Al as a result of the bond formed between $[AlO4]^-$ and Ag^+. For Ag-BG slurry scaffolds, an asymmetric peak observed around +50.0 ppm in the ^{27}Al MAS-NMR spectrum (Fig. 4.2.5g) that when deconvoluted produced two peaks: the first at (+)42.0 ppm correlated to the presence of aluminum in five-fold coordination [275, 276] and the second at (+)52.4 ppm correlated to Al in four-fold coordination [32, 276]. This provides evidence supporting the hypothesis that Ag is likely present as both Ag^+ and Ag^0, thus reconciling the Rietveld analysis (Table 4.2.2) with the TEM observations (Fig. 4.2.5) previously described.

4.2.2 Performance characteristics

4.2.2.1 Mechanical perforamnce

Characterization of the mechanical performance for Ag-BG solution and slurry scaffolds was conducted following the procedures detailed in Section 3.4.2. For Ag-BG solution scaffolds, the compressive strength and elastic modulus (Fig. 4.2.6a) were measured at $4.4{\cdot}10^{-3}{\pm}2.5{\cdot}10^{-3}$ MPa and $3.2{\cdot}10^{-4}{\pm}7.0{\cdot}10^{-5}$ GPa. It is important to note that the compressive strength and elastic modulus for Ag-BG solution scaffolds are only 2.2% and 0.64% respectively required to meet the minimum requirements for targeting bone tissue regeneration in load-bearing applications [16–18]. Regarding Ag-BG slurry scaffolds, their compressive strength and elastic modulus (Fig. 4.2.6b) were measured at 0.15±0.06 MPa and 0.027±0.003 GPa respectively and consistent with values reported for other silicate-based scaffolds [25, 57]. The compressive strength and elastic modulus were found to be at 75% and 54.6% of the minimum requirements for targeting bone

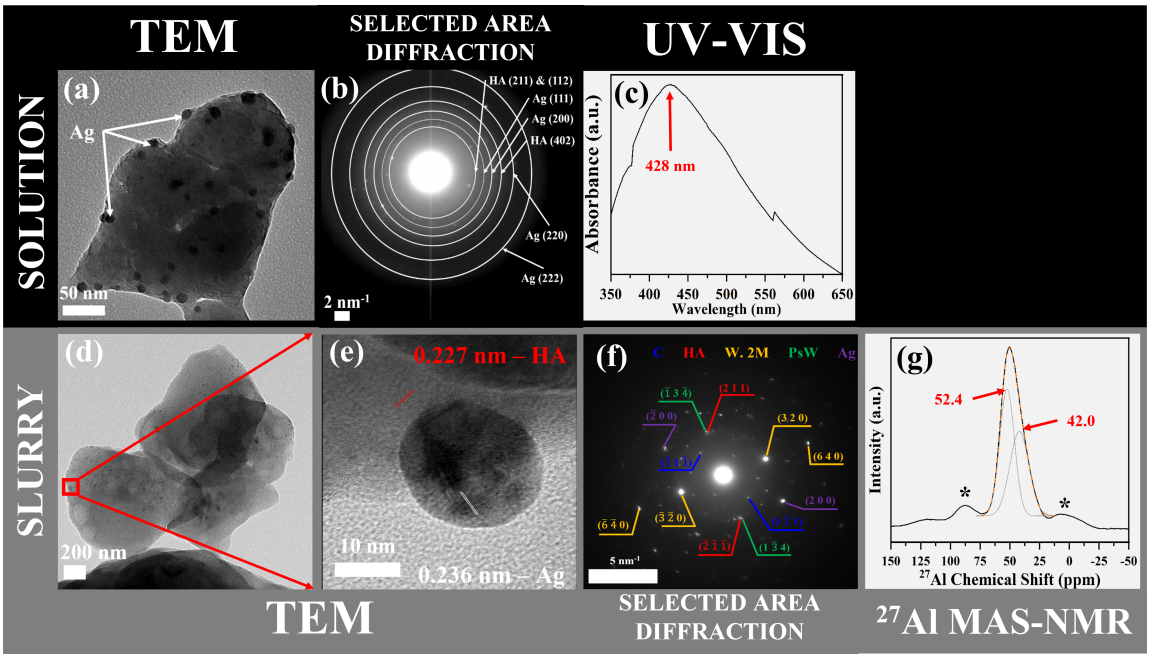

Figure 4.2.5: (a) Representative TEM bright-field image and (b) respective SAD pattern for powdered Ag-BG solution scaffolds in addition to the relevant (c) UV-Vis spectrum. (d-e) Representative bright-field TEM images of powdered Ag-BG slurry scaffolds in addition to the relevant (f) SAD pattern. (g) ^{27}Al MAS-NMR spectrum of powdered Ag-BG slurry scaffolds used to determine the coordination number(s) of Al. (*) Denotes magic angle spinning sidebands and the yellow dashed line represents the cumulative fitting from peak deconvolution.

tissue regeneration in load-bearing applications [16–18]. While the Ag-BG slurry scaffolds fell just short of the mechanical performance requirements needed, it should be noted that the compressive strength and elastic modulus are consistent with reported values for other silicate-based slurry scaffolds.

To investigate the effect of the observed structural defects in more detail for Ag-BG polymer foam replication scaffolds (Fig. 4.2.1 and Fig. 4.2.2), the Hashin-Shtrikman (HS) bounds [277] were calculated and transformed using the theory of elasticity [278] to determine the effective elastic modulus ($\widetilde{E}$; Fig. 4.2.6c) to describe the elastic modulus as a function of porosity. This mathematical treatment is consistent with previous reports for other porous and scaffold-like constructs [279–281]. Regardless of the increased loading of Ag-BG during the synthesis of Ag-BG slurry scaffolds compared to Ag-BG solution scaffolds, both scaffold types were near the lower HS bound demonstrating the deleterious effects of the structural defects observed in Figures 4.2.1 and

4.2.2 had on mechanical performance, as previously hypothesized.

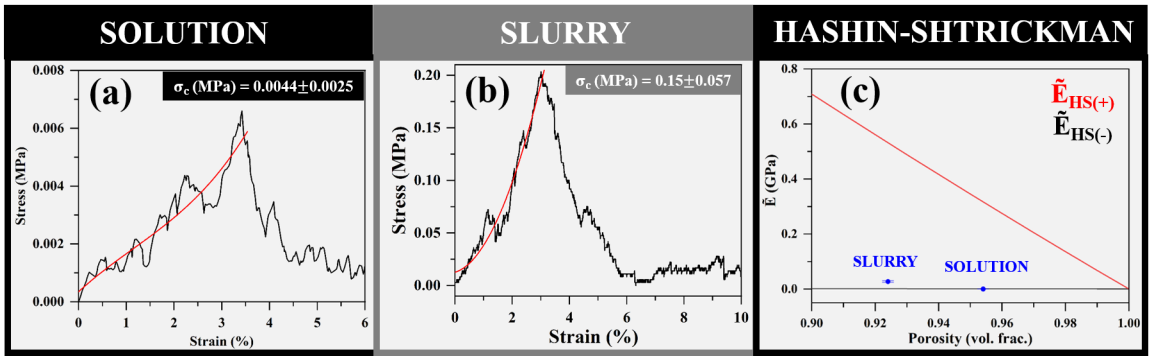

Figure 4.2.6: Representative stress-strain curves for the compressive behavior of Ag-BG (a) solution and (b) slurry scaffolds. The (c) Hashin-Shtrikman (HS) bounds for the effective elastic modulus ($\widetilde{E}$) show both where the Ag-BG solution and slurry scaffolds are on the plot. $\widetilde{E}$ and denote the upper and lower bounds respectively. $\widetilde{E}_{\text{HS+}}$ and $\widetilde{E}_{\text{HS-}}$ denote the upper and lower bounds respectively.

4.2.2.2 Antibacterial performance

The antibacterial performance for both Ag-BG solution and slurry scaffolds was assessed through the exposure of both scaffold types to MRSA for 24 h and application of the CFU assay. While both Ag-BG solution and slurry scaffolds were capable of significant MRSA inhibition after 24 h of exposure when compared to the untreated control, the Ag-BG solution scaffolds were more effective at inhibiting MRSA; however, this difference was statistically insignificant (Fig. 4.2.7a). It was previously hypothesized that the glass-ceramic nature of the Ag-BG solution scaffolds would elicit a significant decrease in CFUs compared to Ag-BG slurry scaffolds due to an increased rate of dissolution. This, however, was not the case given the insignificant difference in CFUs between scaffold types.

Previous reports have demonstrated the bactericidal capabilities of as-received Ag-BG when used as micro-particles [37], which was not observed for the polymer foam replication scaffolds. Given that microstructural differences were found to have an insignificant effect on MRSA inhibition, the effect of the overall morphology (i.e. particle versus scaffold) of Ag-BG was assessed. When Ag-BG slurry scaffolds were pulverized and particles < 20 μm were used and compared to

as-received Ag-BG (< 20 μm in size), both Ag-BG slurry scaffold and as-received Ag-BG particles elicited bactericidal behavior against MRSA after 24 h of exposure.

To further expand on the impact of morphology on antibacterial performance, BET was used to quantify the surface area of both Ag-BG as received and Ag-BG slurry scaffolds. The surface area measurements revealed as-received Ag-BG had a surface area of 90.4±0.6 m^2 g^{-1} while Ag-BG slurry scaffolds had a surface area of 0.44±0.01 m^2 g^{-1}. This stark difference in the surface area has a significant impact on the surface area to volume ratio, where low surface area to volume ratios is expected to slow the rate of dissolution and thus slow the rate of ion release leading to less effective anti-MRSA properties. These pieces of evidence, therefore, conclusively demonstrate that the overall morphology of Ag-BG is the predominant structural factor dictating antibacterial performance.

Previous reports for micro-sized Ag-BG particles have additionally demonstrated the remarkable ability to reactivate the efficacy of antibiotics MRSA is known to resist, thus identifying a novel pathway to combat antibiotic resistance [37]. Given the insignificant difference in MRSA inhibition between Ag-BG solution and slurry scaffolds and improved mechanical performance of slurry scaffolds over solution scaffolds, Ag-BG slurry scaffolds were used to investigate whether Ag-BG scaffolds would also exhibit this remarkable reactivation ability. Fosfomycin and vancomycin were used given their previous study with Ag-BG micro-sized particles [37] and different mechanisms of MRSA inhibition. Fosfomycin inhibits bacterial growth by targeting peptidoglycan and cell wall synthesis by inhibiting UDP-N-acetylglucosamine-3-enolpyruvyltransferase (MurA) and previously reported to strongly synergize with Ag-BG micro-sized particles [37] while vancomycin inhibits bacterial growth by disrupting the transport of cell wall precursors from cytoplasm to peptidoglycan [282].

After 24 h of MRSA exposure to the combination of Ag-BG slurry scaffold and either fosfomycin (Fig. 4.2.7b) or vancomycin (Fig. 4.2.7c), a significant reduction in CFUs was observed for both antibiotics showing the potential for further CFU reduction when exposed to MRSA for 48 h. Interestingly, while significant inhibition of MRSA was observed comparing the performance of

Ag-BG slurry scaffolds after 24 h and 48 h of exposure to MRSA, only an insignificant reduction in CFUs was observed when examining the combined performance at equivalent time points. Not only was the reduction in CFUs insignificant when Ag-BG slurry scaffolds were combined with the antibiotics, but the CFUs after 48 h of exposure to MRSA for the scaffold-antibiotic combination were approximately equal to the CFUs of Ag-BG slurry scaffolds alone. Given the surface area to volume ratio findings described previously, it was concluded that the low surface area to volume ratio for Ag-BG slurry scaffolds is the dominant structural characteristic limiting the anti-MRSA and synergistic effect of the Ag-BG polymer foam replication scaffolds.

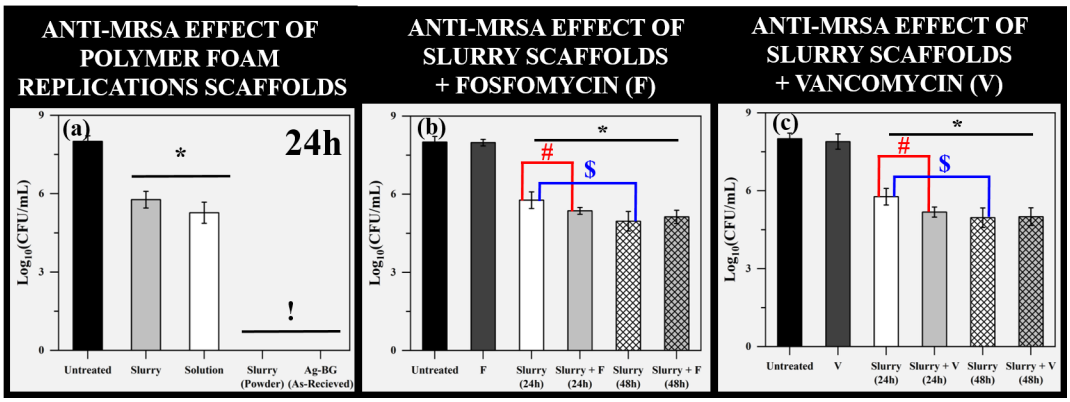

Figure 4.2.7: (a) The anti-MRSA effect of Ag-BG solution and slurry scaffolds in addition to the anti-MRSA effect of as-received Ag-BG and pulverized Ag-BG slurry scaffolds after exposure to planktonic MRSA for 24 h. (b) Shows the anti-MRSA effect of Ag-BG slurry scaffolds alone and in combination with 0.2 μg mL^{-1} of Fosfomycin (F) after 24 h and 48 h of exposure. (c) Shows the anti-MRSA effect of Ag-BG slurry scaffolds alone and in combination with 2 mg mL^{-1} of vancomycin (V). (*) indicates $p < 0.05$ against the untreated and antibiotic controls, (!) represents $p < 0.05$ of pulverized Ag-BG slurry scaffolds and as-received Ag-BG, (#) denotes $p < 0.05$ of Ag-BG slurry scaffold-antibiotic combination compared to Ag-BG slurry scaffolds alone after 24 h of MRSA exposure, and ($) indicates $p < 0.05$ of the anti-MRSA response of Ag-BG slurry scaffolds after 48 h of exposure compared to 24 h of exposure.

4.2.2.3 Biological performance

The biological performance of both Ag-BG solution and slurry scaffolds were evaluated through immersion in SBF for 14 d. Structural changes were observed in the FTIR spectra (Fig. 4.2.8a, b) and XRD patterns (Fig. 4.2.8c, d) for powdered Ag-BG solution and slurry scaffolds after 14 d of immersion in SBF. To start, the FTIR spectrum of Ag-BG solution scaffolds (Fig. 4.2.8a) after 14 d

of immersion in SBF saw the development of two P-O bending peaks at ~570 cm^{-1} and ~610 cm^{-1} [235] correlated to the development of an apatite-like layer, as expected after SBF immersions. The complementary XRD pattern (Fig. 4.2.8c) saw an increase in relative intensity for the main diffraction peaks for hydroxyapatite (i.e. ~30° to ~35° 2θ) providing supporting evidence that Ag-BG solution scaffolds could form an apatite-like layer after 14 d of immersion in SBF.

For Ag-BG slurry scaffolds, structural changes were less noticeable than what was observed for Ag-BG solution scaffolds resulting from the highly crystalline nature of the Ag-BG slurry scaffolds. While somewhat notable changes in the P-O bending peaks in the FTIR spectra for Ag-BG slurry scaffolds (Fig. 4.2.8b) were observed, these peak changes do not conclusively demonstrate whether Ag-BG slurry scaffolds could form an apatite-like layer after 14 d of immersion in SBF. Other spectroscopic changes, however, were more notable, specifically in the 900 cm^{-1} to 1100 cm^{-1} wavenumber range. After 14 d of immersion in SBF, the small well-defined peaks that were observed before SBF immersion was replaced with a broad peak indicating that an apatite-like phase could have formed. Structural changes were more evident when examining the XRD patterns of Ag-BG slurry scaffolds (Fig. 4.2.8d), where the diffraction peaks previously indexed to W. 2M and PsW (Fig. 4.2.8a) were found to both have decreased in relative intensity and undergone mild peak broadening that could be resultant from both the dissolution of W. 2M and PsW during immersion in SBF in conjunction with the formation of an apatite-like layer. Regardless, SEM-EDS investigations were required to conclude if Ag-BG solution and slurry scaffolds formed an apatite-like layer during 14 d of immersion in SBF.

SEM-EDS of Ag-BG solution (Fig. 4.2.8e) and slurry (Fig. 4.2.8f) both presented globular-like surface features consistent with morphologies indicative of an apatite-like layer [283] with needle-like morphologies observed within the globular features for Ag-BG slurry scaffolds (Fig. 4.2.8f). Using EDS spot analysis, the Ca/P ratio for Ag-BG solution and slurry scaffolds after 14 d of SBF was ~1.7 and > 2 respectively. The Ca/P ratio of ~1.7 for Ag-BG solution scaffolds is close to the expected stoichiometric ratio of 1.67, while Ag-BG slurry scaffolds after 14 d of immersion had not yet converged towards the expected 1.67 value. Examining the depth of the interaction volume

using the Kanaya – Okayama range equation (Fig. 3.3.2) generated by the incident electron beam was found to have a maximum penetration depth of 3.78 μm. Given the higher than expected Ca/P ratio for Ag-BG slurry scaffolds, it was hypothesized that the thickness of the apatite-like layer did not exceed the maximum penetration depth of the interaction volume and that the Ca/P ratio was likely the result of a combination of the Ca/P ratio of the deposited apatite-like layer on the surface of Ag-BG slurry scaffolds and the underlying scaffold substrate.

Additional biological performance testing was performed on Ag-BG slurry scaffolds sintered at 900°C that were used during Rietveld analysis to investigate the influence W. 2M and PsW had on the rate of formation of an apatite-like layer. After 14 d of immersion in SBF, the apatite-like layer that was observed had a similar globular-like morphology as Ag-BG slurry scaffolds sintered at 1000°C, however, the needle-like morphologies observed inside the globular-like features were found to be less defined. Furthermore, the Ca/P ratio failed to appreciably converge towards the expected 1.67 value unlike Ag-BG slurry scaffolds sintered at 1000°C. This difference was correlated to the increased phase concentration of PsW for Ag-BG slurry scaffolds sintered at 1000°C (i.e. 37%) compared to the PsW phase concentration present when slurry scaffolds were sintered at 900°C (i.e. 25%). Previous reports by Sainz et al. [284] and Magallenes-Perdomo et al. [285] investigated thermodynamically the difference in dissolution rates between PsW and W. 2M supporting both their experimental evidence and agreeing with the experimental evidence reported herein.

4.2.3 Addressing observed challenges and limitations

Through the utilization of the polymer foam replication technique to synthesize Ag-BG solution and slurry scaffolds, the effect of each process on mechanical, antibacterial, and biological performance was elucidated using a multistructural comprehensive materials characterization approach, where structural differences were able to account for the differences in performances observed. While both Ag-BG solution and slurry scaffolds demonstrated satisfactory antibacterial and biological performance, their mechanical performance was unacceptable for targeting bone

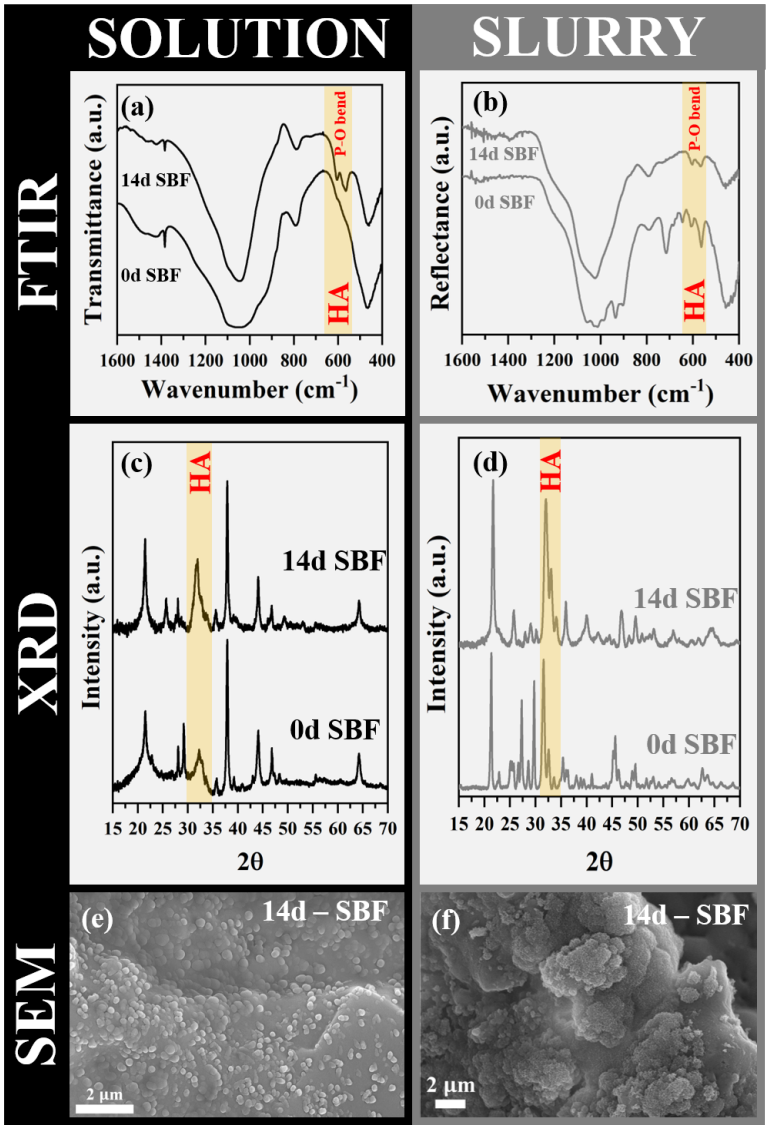

Figure 4.2.8: (a) FTIR spectra and (c) XRD patterns of powdered Ag-BG solution scaffolds after 0 d and 14 d of immersion in SBF, where (e) shows a representative SEM image of the surface morphology of Ag-BG solution scaffolds after 14 d of immersion in SBF. (b) FTIR spectra and (d) XRD patterns of powdered Ag-BG slurry scaffolds after 0 d and 14 d of immersion in SBF, where (e) shows a representative SEM image of the surface morphology of Ag-BG slurry scaffolds after 14 d of immersion in SBF.

tissue regeneration in load-bearing applications. Delivering Ag-BG scaffolds that possess adequate mechanical, antibacterial, and biological performance will likely require pioneering an innovative approach for scaffold processing. The application and effect of this novel approach shall be explored herein.

4.3 Fused filament fabrication

Herein, we demonstrate that our novel and innovative approach to FFF printing is capable of synthesizing pristine silicate-based scaffolds targeting bone tissue regeneration in load-bearing applications.

The work presented in Section 4.3 has previously been published by Marsh et al., as described by the following citation:

- Materials Science and Engineering: C, Vol 118, Adam C. Marsh, Yaozhong Zhang, Lucrezia Poli, Neal Hammer, Aljoscha Roch, Martin Crimp, Xanthippi Chatzistavrou, 3D printed bioactive and antibacterial silicate glass-ceramic scaffold by fused filament fabrication, 111516, Copyright Elsevier (2020) [221].

4.3.1 FFF printing of 3D silicate-based scaffolds

The computer-aided design (CAD) model shown in Figure 4.3.1a shows the 3D scaffold design that was used for FFF printing pristine Ag-BG scaffolds. The scaffold design selected for FFF printed Ag-BG scaffolds consisted of a simple cubic lattice having an interconnected porous network. Figure 4.3.1b shows both green body and sintered FFF printed Ag-BG scaffolds, where the term "green body" references the status of FFF printed Ag-BG scaffolds immediately after being 3D printed. As shown, while FFF-printed Ag-BG scaffolds underwent significant shrinkage during the thermal debinding and sintering processes, the overall porous structure of FFF printed Ag-BG scaffolds was maintained, showing minimal evidence of gross structural deformation during post-processing.

To optimize the thermal debinding conditions to be applied that minimizes gross structural deformation, the thermal behavior of FFF-compatible Ag-BG containing filaments was studied using TGA (Fig. 4.3.1c). In the first stage of notable mass loss (i.e. 300°C to 350°C), the surfactants and low molecular weight flow additives that assist in the 3D printing process undergo decomposition. During the second stage of notable mass loss (i.e. 390°C to 450°C), the higher molecular

weight polyolefins (i.e. thermoplastics and elastomers) present within the FFF-compatible Ag-BG containing filament undergo decomposition (Fig. 4.3.1c). Critical to the success of removing the polyolefin components while maintaining a high degree of structural integrity was the removal of the fatty acid groups during the first stage of notable mass loss (Fig. 4.3.1c). This removal created pores that could then serve as channels providing an escape route for the vaporized thermoplastics and elastomers, thus avoiding catastrophic structural deformation such as bloating. As temperatures reached 600°C, the mass loss recorded by TGA (Fig. 4.3.1c) plateaued at ~70% of the original mass, signifying that the polymeric binder used for the synthesis of FFF-compatible Ag-BG containing filaments was fully decomposed. Above 600°C, only Ag-BG particles remain requiring sintering at temperatures as high as 900°C for solidification and densification delivering mechanically robust (i.e. σ_c > 1 MPa) and pristine Ag-BG scaffolds.

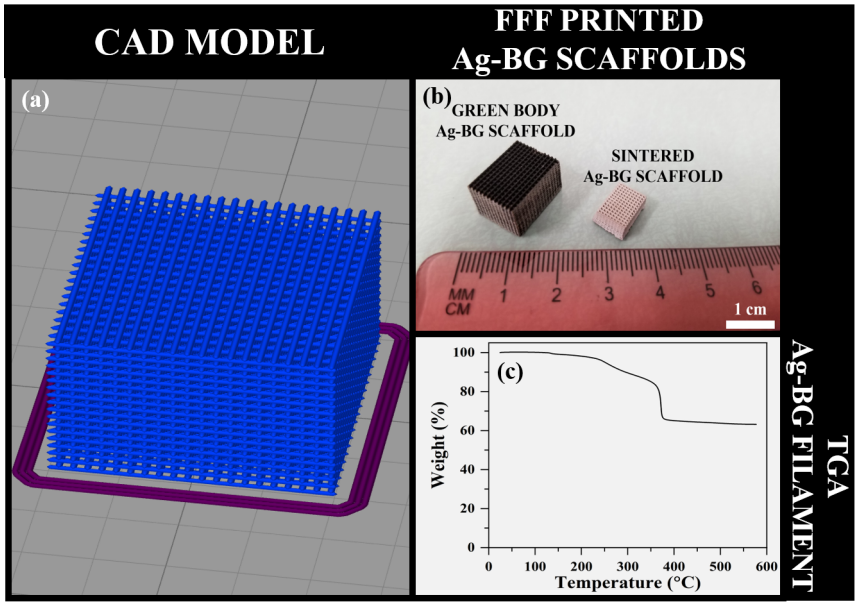

Figure 4.3.1: The (a) CAD model used for 3D printing, (b) green body and pristine Ag-BG scaffolds synthesized using FFF technology, and (c) thermogravimetric analysis (TGA) of the Ag-BG containing filament.

4.3.2 Structural characteristics

4.3.2.1 Macro- & milli- structure

Optical microscopy of FFF printed Ag-BG scaffolds (Fig. 4.3.2) was performed examining the FFF printed Ag-BG scaffolds from both a top-down (Fig. 4.3.2a, b) and cross-sectional (Fig. 4.3.2c, d) perspectives. The FFF printed Ag-BG scaffolds, from a top-down perspective (Fig. 4.3.2a, b) showed well-defined cubic pores demonstrating that the thermal debinding and sintering conditions applied were successful at maintaining the simple-cubic lattice structure from the CAD model (Fig. 4.3.1a). Additionally, the optical images (Fig. 4.3.2a, b) from the top-down perspective displayed no evidence to suggest that the presence of vacancies, unlike what was observed for Ag-BG solution and slurry scaffolds synthesized by the polymer foam replication technique (Fig. 4.2.1a-d).

Investigations into the optical characteristics of the FFF printed Ag-BG scaffolds from a cross-sectional perspective (Fig. 4.3.2c, d), however, presented evidence contradicting the claim that FFF printed Ag-BG scaffolds were fully dense. This evidence was identified by the observation of micro-sized concentric pores in the centers of many of the struts (Fig. 4.3.2c). Additionally, the cross-sectional perspectives (Fig. 4.3.2c, d) showed signs of deformation along the z-axis evidenced by the observation of rectangular rather than cubic pore geometry and correlated to the vaporization of organic components during thermal debinding. To investigate how widespread these phenomena were, micro-CT was used in addition to quantifying porosity, apparent scaffold density, and pore size.

Micro-CT of FFF printed Ag-BG scaffolds (Fig. 4.3.3) revealed an interconnected porous network, as expected given the CAD model (Fig. 4.3.3a) used. The quantitative characteristics of FFF-printed Ag-BG scaffolds found a porosity of 70±5 %, an apparent scaffold density of 0.3 g cm^{-3}, and an average pore size of 622±139 μm. The porosity of FFF printed Ag-BG scaffolds is within the middle to upper range for trabecular human bone (i.e. 40% to 95%; [16–18]). The large pore size observed is expected to be well-suited for cell migration and spreading given that these characteristics start to become inhibited once pore sizes are below 300 μm [87].

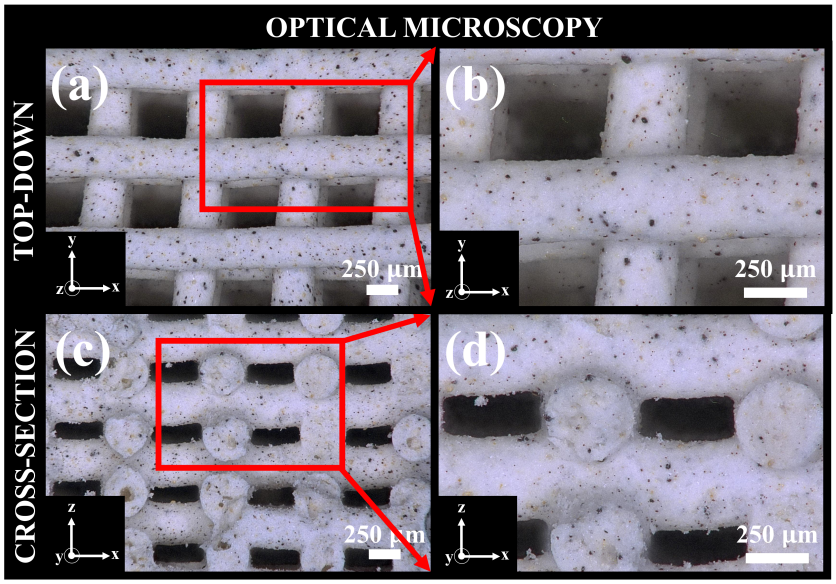

Figure 4.3.2: Optical images of FFF printed Ag-BG scaffolds from (a-b) top-down and (c-d) cross-sectional perspectives.

Interestingly, in all 3D reconstructions shown for FFF printed Ag-BG scaffolds (Fig. 4.3.3a-d, f-h) milli and micro-sized pores and voids are observed randomly distributed across the entire scaffold structure. The presence of such pores and voids is expected to limit the mechanical performance of FFF printed Ag-BG scaffolds similar to what was previously shown for Ag-BG solution and slurry scaffolds synthesized by the polymer foam replication technique. It was hypothesized that the use of a unimodal distribution of Ag-BG particles (i.e. 20 µm to 38 µm in size) induced the formation of these structural defects as a result of Ag-BG particles sintering together, but failing to achieve full densification leading to pore coalescence [286]. The representative 2D cross-section, presented in Figure 4.3.3e, shows how severe and pervasive this phenomenon was, thus presenting a processing challenge to overcome (explored in Section 4.4).

Additional examination of 2D cross-sections for FFF printed Ag-BG scaffolds (Fig. 4.3.3e) saw small circular-like features of high X-Ray attenuation (white arrows; Fig. 4.3.3e) randomly dispersed throughout the scaffold structure. These spots were correlated to the presence of Ag particles, as their compact face-centered (FCC) crystal structure along with the comparatively high Z value of Ag is expected to have a higher density compared to the other crystalline phases indexed in the respective XRD pattern (Fig. 4.3.3b) given the proportionality between density and X-Ray

attenuation.

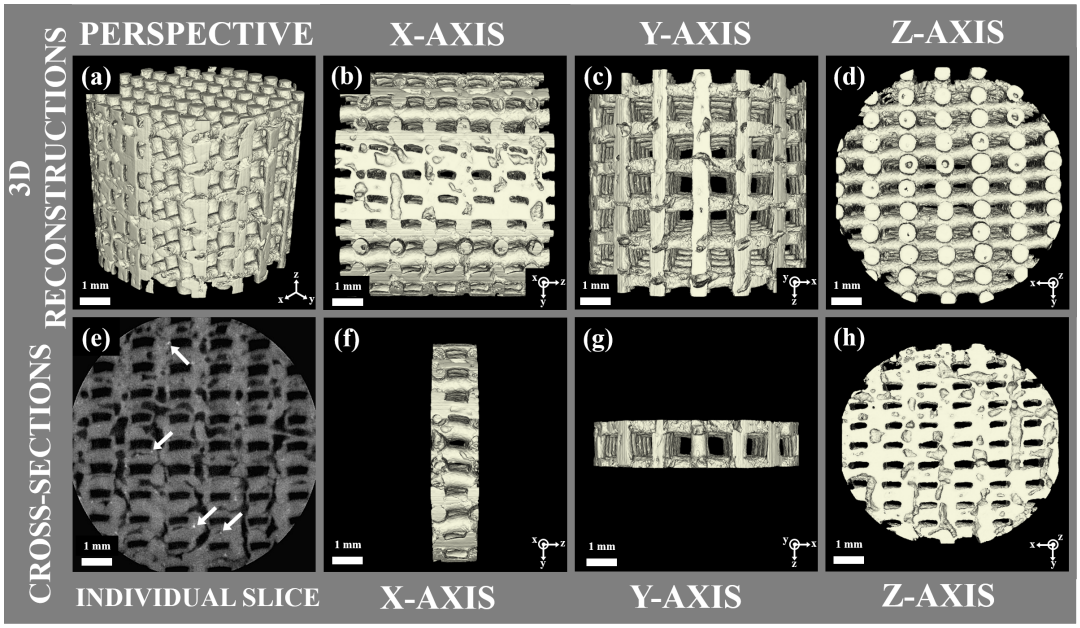

Figure 4.3.3: 3D reconstructions from micro-CT imaging applied to an FFF printed Ag-BG scaffold, where (a) presents an overall 3D perspective of the FFF printed Ag-BG scaffold in addition to 3D perspectives along the (b-d) x-, y-, and z-axes respectively. (e) Representative 2D cross-section of the FFF printed Ag-BG scaffold, where the white arrows denote local regions of high X-Ray attenuation. (f-g) Present 1 mm thick 3D reconstructions consisting of two-print layers as viewed along the x-, y-, and z-axes respectively.

4.3.2.2 Microstructure

To study the crystallographic and microscopic characteristics of FFF printed Ag-BG scaffolds, FTIR and XRD (Fig. 4.3.4) were applied using powdered FFF printed Ag-BG scaffolds, while SEM-EDS was utilized to observe surface morphological features and assess elemental homogeneity down to the micron level.

The respective FTIR spectrum (Fig. 4.3.4a) of powdered FFF printed Ag-BG scaffolds show multiple well-defined peaks indicating the FFF printed Ag-BG scaffolds likely are highly crystalline. The XRD pattern shown in Figure 4.3.4b provides supporting evidence given the presence of sharp, well-defined diffraction peaks with showing minimal evidence of an amorphous component. Diffraction peak indexing for FFF printed Ag-BG scaffolds found that FFF printed Ag-BG scaffolds

were pentaphasic consisting of cristobalite, HA, W. 2M, PsW, and Ag, as what was observed for Ag-BG slurry scaffolds synthesized by the polymer foam replication technique (Fig. 4.3.4a).

The highly crystalline nature of FFF printed Ag-BG scaffolds allowed for correlation between FTIR peaks and respective phases indexed in the XRD pattern. To start, the characteristic Si-O bending peak (Fig. 4.3.4a) known to be present in silicate-based glass systems was observed around ~450 cm^{-1} known to be present in silicate-based glass systems [45, 235]. Additional Si-O bending peaks (Fig. 4.3.4a) were noted at ~650 cm^{-1} and ~800 cm^{-1} correlated to cristobalite [45, 265] and ~700 cm^{-1} (Fig. 4.3.4a) correlated to PsW [235, 267, 268]. Si-O stretching peaks observed at ~900 cm^{-1} and ~1020 cm^{-1} (Fig. 4.3.4a) were correlated to the presence of W. 2M [235, 268, 269], the peaks noted at ~930 cm^{-1} and ~1000 cm^{-1} (Fig. 4.3.4a) were correlated to PsW [235, 267, 268], with the last Si-O stretching peak at ~1200 cm^{-1} (Fig. 4.3.4a) being correlated to cristobalite [45, 265]. The P-O bending peaks at ~570 cm^{-1} and ~610 cm^{-1} (Fig. 4.3.4a) and P-O stretching peaks observed at ~1030 cm^{-1} and ~1080 cm^{-1} (Fig. 4.3.4a) were all correlated to the presence of HA within powdered FFF printed Ag-BG scaffolds [235].

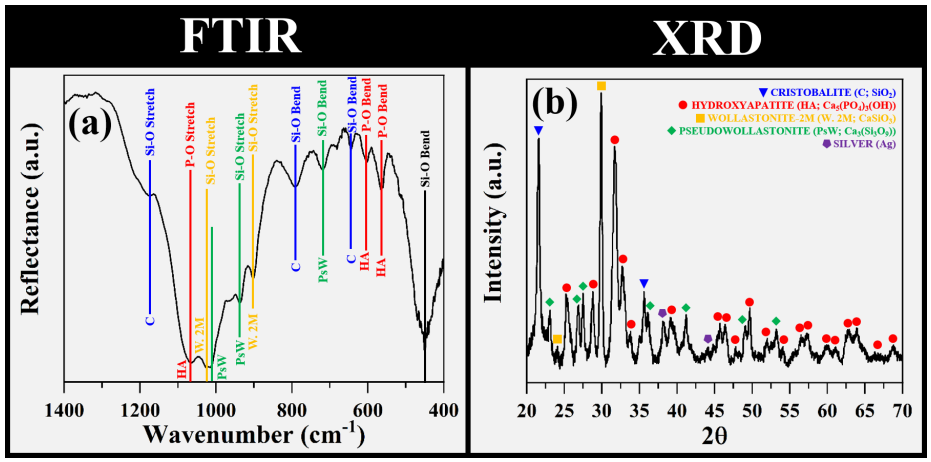

Figure 4.3.4: Respective (a) FTIR and (b) XRD pattern of powdered FFF printed Ag-BG scaffolds.

SEM-EDS investigations (Fig. 4.3.5) for FFF printed Ag-BG scaffolds elucidated both their surface morphological characteristics and elemental homogeneity down to the micron level. To start, the milliscale SEM images (Fig. 4.3.5a, b) of FFF printed Ag-BG scaffolds show evidence of a rough surface morphology that was confirmed during micro-scale investigations (Fig. 4.3.5c).

SEM examination of FFF printed Ag-BG scaffolds from a top-down perspective at the milliscale (Fig. 4.3.5a) show the presence of surface micro-cracks that, while not observed during optical microscopy (Fig. 4.3.5a, b), were noted during micro-CT characterization (Fig. 4.3.3), thus the SEM image in question (Fig. 4.3.5a) supports previous observations. From a cross-sectional perspective (Fig. 4.3.5b), while surface micro-cracks were not apparent, concentric pore-like features were observed in the center of some of the struts, supporting previous optical (Fig. 4.3.2) and micro-CT (Fig. 4.3.3) investigations.

EDS X-Ray mapping was performed on the SEM region imaged in Figure 4.3.5c), where all elements (Fig. 4.3.5d-i) present in FFF printed Ag-BG scaffolds were homogenously distributed down to the micron-level and accompanied with the relevant EDS spectrum generated during EDS X-Ray mapping. Given the homogenous distribution of elements down to the micron level, FFF printed Ag-BG scaffolds are expected to exhibit homogenous performances when studied for their antibacterial and biological characteristics.

4.3.2.3 Meso- & nano- structure

TEM investigations of FFF printed Ag-BG scaffolds (Fig. 4.3.6) were employed to elucidate their meso- and nanostructure. Phase-contrast imaging (Fig. 4.3.6a) of an individual micron-sized FFF printed Ag-BG scaffold particle revealed variable electron transmission, where a clear boundary was observed between the interior and exterior of the particle indicating that this region could be multiphasic, warranting further investigation. Bright-field imaging (Fig. 4.3.6c) showed that the isolated micron-sized FFF printed Ag-BG particle exhibited minimal electron transparency throughout, indicating that this region is possibly highly crystalline. Indeed, when this region was examined using SAD (Fig. 4.3.6b), a clear spot pattern was revealed with no evidence of an amorphous halo, supporting that this region is, in fact, highly crystalline, as hypothesized. Indexing of the SAD pattern (Fig. 4.3.6b) identified W. 2M and HA as the constituent phases comprising this analytical region, supporting the XRD diffraction peak indexing shown in Figure 4.3.4b. Further evidence was collected when implementing axial dark-field imaging (Fig. 4.3.6d) of the (2 0 0)

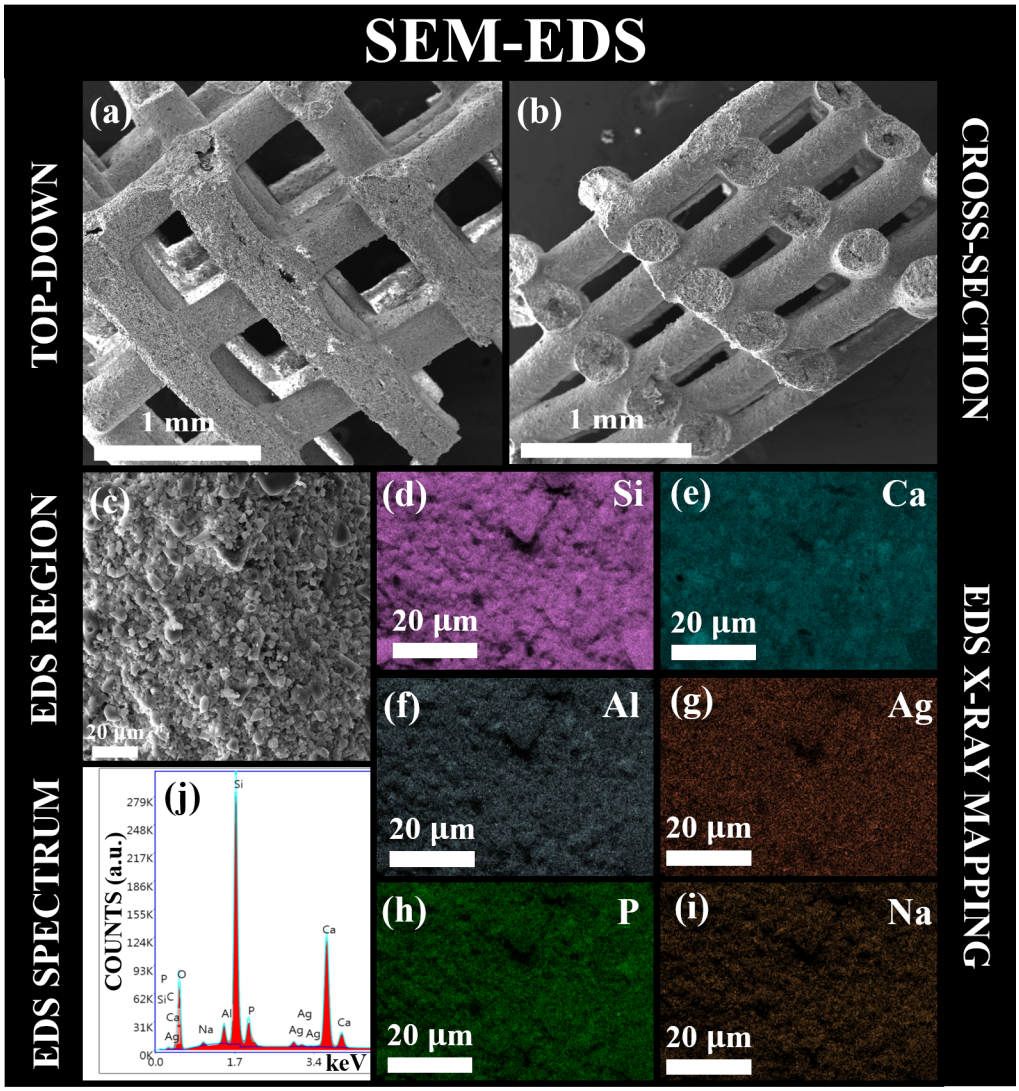

Figure 4.3.5: (a-b) Milliscopic SEM images of an FFF printed Ag-BG scaffold from both a top-down and cross-sectional perspective respectively. (c) Presents the region that was used for (d-i) EDS X-Ray mapping to assess elemental homogeneity down to the micron level accompanied by the respective (j) EDS spectrum.

planes of W. 2M demonstrated widespread electron transmission agreeing with XRD observations (Fig. 4.3.4b).

In the XRD pattern of powdered FFF printed Ag-BG scaffolds (Fig. 4.3.4b), Ag diffraction peaks were indexed disagreeing with the elemental homogeneity of Ag observed during EDS (Fig. 4.3.5g) investigations. To bring these results into agreement, UV-Vis (Fig. 4.3.6e) was performed on powdered FFF printed Ag-BG scaffolds to observe if any surface plasmon resonance from Ag

particles was occurring, as previously demonstrated in (Fig. 4.2.5). An absorbance peak at 415 nm supports the presence of nano-sized Ag particles, however, this should be paired with visible evidence from TEM imaging. Indeed, when performing HRTEM (Fig. 4.3.6f), the phase contrast image revealed an ovoid-like feature ~15 nm to ~20 nm in diameter of locally decreased electron transmission with lattice fringes observed inside. Measurement of the lattice fringes found the d-spacing to be 0.233 nm that was correlated to the (1 1 1) atomic planes of Ag. The surface plasmon resonance peak (Fig. 4.3.6e) coupled with the visual evidence of AgNPs during HRTEM investigations (Fig. 4.3.6f) provided sufficient evidence to support the Ag diffraction peak indexing in the XRD pattern (Fig. 4.3.4b).

4.3.3 Performance characteristics

4.3.3.1 Mechanical performance

The mechanical performance of FFF printed Ag-BG scaffolds was assessed by compression testing (Fig. 4.3.7), where the compressive strength and elastic modulus were measured at 2.84±0.75 MPa and 0.11±0.06 GPa respectively. Both values surpassed the minimum required criteria for targeting bone tissue engineering in load-bearing applications [16–18]. The representative stress-strain curve, shown in Figure 4.3.7a, of the compressive behavior of FFF-printed Ag-BG scaffolds, presented non-uniformity in the linear behavior within the elastic region. While the compressive behavior of FFF printed Ag-BG scaffolds conforms more closely to the expected linear rise in stress as a function of strain observed within the elastic region before catastrophic failure for fully dense ceramic materials [56], local regions of decreasing stress as a function of strain were observed, similar to what was observed in the compressive behavior of Ag-BG solution and slurry scaffolds but to a milder degree resulting from the improved strut density observed during optical (Fig. 4.3.2) and micro-CT investigations (Fig. 4.3.3).

To evaluate how severely the structural defects, shown in Figures 4.3.2 and 4.3.3, impacted the mechanical performance of FFF printed Ag-BG scaffolds in addition to providing a consistent

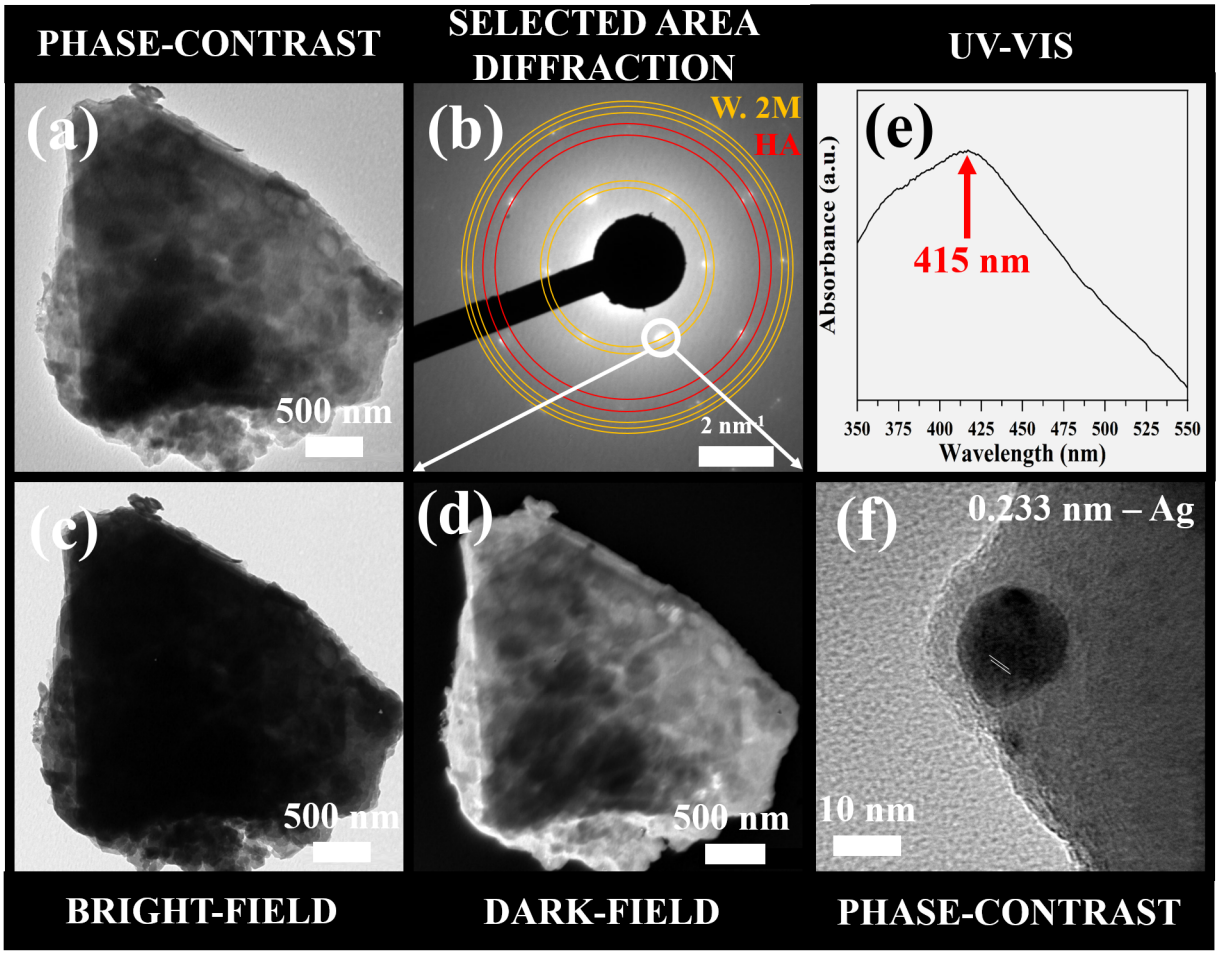

Figure 4.3.6: (a) Phase-contrast TEM image of an isolated micron-sized FFF printed Ag-BG particle. The respective (b) SAD pattern revealed diffraction spots indexed to W. 2M and HA. The (c) bright-field image presents with minimal electron transmission suggesting a high degree of crystallinity. The (d) axial dark-field image was generated using the electrons diffracting from (2 0 0) atomic planes of W. 2M. The (e) UV-Vis spectrum presented with an absorbance peak at 415 nm suggesting the possibility of surface plasmon resonance of AgNPs that was (f) visually confirmed in the HRTEM image.

method of comparing the mechanical performance of all Ag-BG scaffolds, the Hashin-Shtrikman bounds were calculated and presented in Figure 4.3.7b. The elastic modulus of FFF printed Ag-BG scaffolds while having a higher modulus compared to Ag-BG solution or slurry scaffolds, was still found to be near the lower Hashin-Shtrikman bound indicating that the structural defects severely compromised mechanical performance. Based on this, the decrease in porosity for FFF printed Ag-BG scaffolds likely contributed heavily to the improvements in compressive strength and elastic modulus observed.

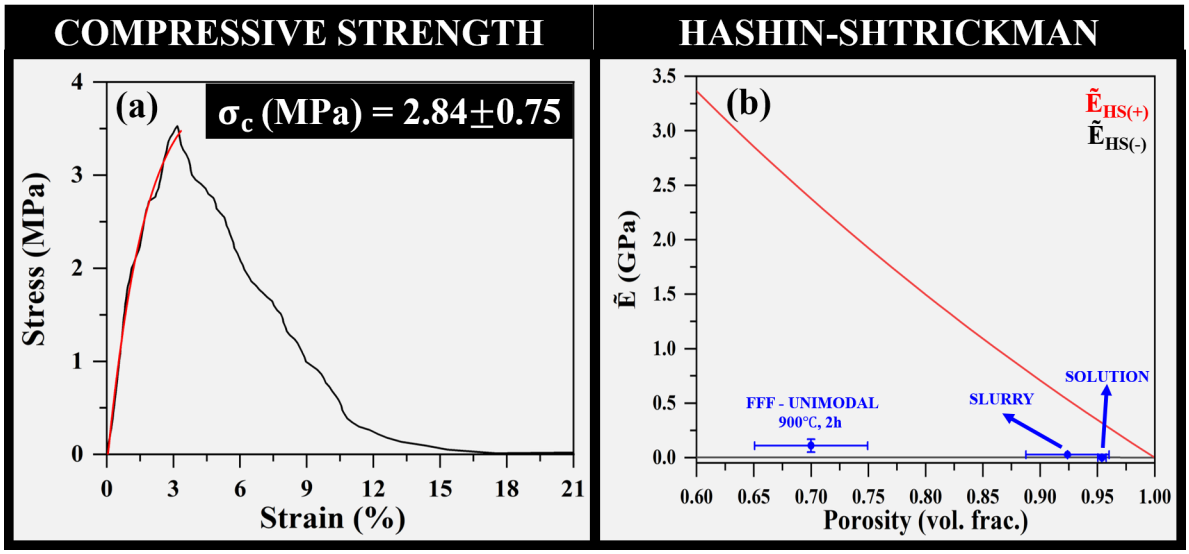

Figure 4.3.7: (a) Representative stress-strain curve of the compressive behavior of FFF printed Ag-BG scaffolds with the red line denoting a guide-to-the-eye. (b) The Hashin-Shtrikman bounds were computed for Ag-BG to evaluate the impact of structural defects on mechanical performance.

4.3.3.2 Antibacterial performance

Characterization of the antibacterial performance of FFF printed Ag-BG scaffolds using the CFU assay found that FFF printed Ag-BG scaffolds were capable of significantly inhibiting planktonic MRSA after 24 h of exposure (Fig. 4.3.8). Doubling the MRSA exposure time to 48 h saw an approximately 10-fold reduction in CFUs compared to 24 h of exposure that was found to be statistically significant. This demonstrates that the anti-MRSA effect of the FFF printed Ag-BG scaffolds is a time-dependent process related to their rate of dissolution and respective ion-release profiles.

4.3.3.3 Biological performance

The biological performance of FFF printed Ag-BG scaffolds was evaluated through immersion in SBF for 14 d and 28 d, similar to how the biological performance of Ag-BG solution and slurry scaffolds (Fig. 4.2.8) was evaluated. After 14 d of immersion in SBF, FFF printed Ag-BG scaffolds presented with patchy surface morphological characteristics consistent with the formation of an apatite-like layer [283] when observed in SEM (Fig. 4.3.9c, d). EDS X-Ray spot analysis of

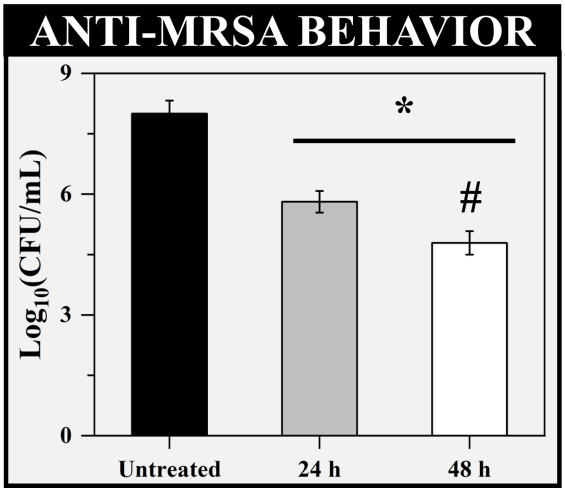

Figure 4.3.8: Anti-MRSA behavior of FFF printed Ag-BG scaffolds after exposure to planktonic MRSA after 24 h and 48 h, as elucidated through the application of the CFU assay. (*) Denotes statistical significance compared to the untreated control, and (#) notes statistical significance between 24 h and 48 h of MRSA exposure.

the characteristic surface morphological features of a deposited apatite-like layer was performed, finding that the Ca/P ratio in these regions was ~2.16. Given the Ca/P ratio after 14 d of immersion in SBF failed to converge to the expected 1.67 value coupled with the patchy depositions observed in SEM demonstrate that the thickness of the apatite-like layer that has formed is less than 5 μm when the interaction volume depth was computed using the Kayana-Okayama range equation (Fig. 3.3.2). The FTIR spectrum (Fig. 4.3.9a) and XRD pattern (Fig. 4.3.9b) of powdered FFF printed Ag-BG scaffolds after 14 d of immersion in SBF displayed minimal changes to the respective FTIR spectrum and XRD pattern shown in Figure 4.3.9 before SBF immersions. Given this, the FTIR and XRD peaks were indexed, as previously described in Section 4.3.2.1.2.

Doubling the SBF immersion time to 28 d, the SEM images presented in Figure 4.3.9e, f show again a patchy network of needle-like surface morphological features with EDS X-Ray spot analysis revealing a Ca/P ratio of ~2.04 due to the thin (i.e. < 5 μm thick) deposits of the expected apatite-like phase. The corresponding FTIR spectrum (Fig. 4.3.9a) and XRD pattern (Fig. 4.3.9b) for powdered FFF printed Ag-BG scaffolds after 28 d of immersion in SBF, did, however, display evidence that structural changes occurred between 14 d and 28 d of immersion in SBF. Specifically, the weak peaks observed from ~650 cm^{-1} to ~750 cm^{-1} and ~900 cm^{-1} to ~1100 cm^{-1} were

hardly noticeable, presenting as weak shoulders rather than clearly defined peaks. The relative intensity of the main HA diffraction peaks (i.e. ~30° to ~35° 2θ) was found to have increased significantly in relation to the cristobalite, W. 2M, and PsW diffraction peaks, indicating that an apatite-like phase has formed during immersions in SBF. While EDS X-Ray spot analysis failed to deliver conclusive evidence that the deposited phase is an apatite-like phase, the combination of FTIR, XRD, and SEM data provide sufficient evidence in support of this.

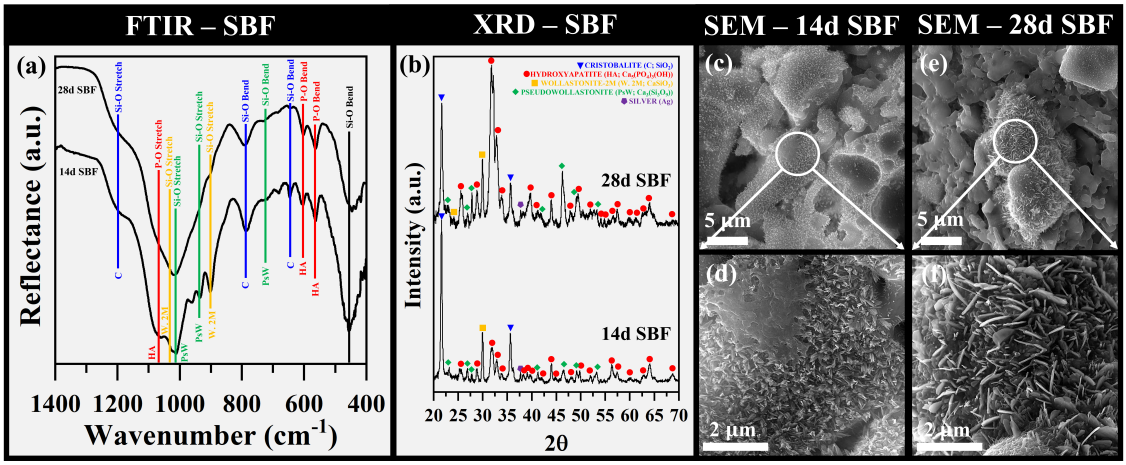

Figure 4.3.9: (a) FTIR spectra and (b) XRD patterns of powdered FFF printed Ag-BG scaffolds after 14 d and 28 d of immersion in SBF. Complementary SEM images present the surface morphology of the FFF printed Ag-BG scaffolds after (c-d) 14 d and (e-f) 28 d of immersion in SBF.

4.3.4 Need for improvement strategies

While many advantageous structural and performance characteristics were identified for the maiden implementation of successfully 3D printing Ag-BG scaffolds using FFF technology, the structural defects observed (Fig. 4.3.2 and Fig. 4.3.3) in conjunction with the proximity of the measured elastic modulus remaining close to the lower Hashin-Shtrikman bound for FFF printed Ag-BG scaffolds, demonstrating the need for improvement in the processes applied. As previously conjectured in Section 4.3.2.1.1, the generation of structural defects was likely the result of insufficient packing of Ag-BG particles during filament synthesis due to the limited size range of particles used (i.e. 20 µm to 38 µm). Therefore, it was hypothesized that using a bimodal distribution of Ag-BG particles (i.e. 20 µm to 38 µm and < 20 µm) will significantly decrease

structural defects leading to vast improvements in mechanical performance. This hypothesis is explored further in Section 4.4.

4.4 Advancements in FFF printing of 3D silicate-based scaffolds

The work presented in Section 4.4 is currently under submission and described by the following citation:

- Materials Science and Engineering: C, Under Submission, Adam C. Marsh, Yaozhong Zhang, Yadav Wagley, Martin A. Crimp, Aldo Boccaccini, Kurt Hankenson, Neal D. Hammer, Aljoscha Roch, Xanthippi Chatzistavrou, 3D printing Ag-Doped Bioceramic Scaffolds for Bone Tissue Engineering Using Fused Filament Fabrication (FFF) Technology [287].

4.4.1 Structural characteristics

Moving to the use of a bimodal distribution of Ag-BG particles (i.e. 20 μm to 38 μm and < 20 μm) during filament synthesis allowed for much greater sintering conditions to be applied that was not possible when using a unimodal distribution of Ag-BG particles (i.e. 20 μm to 38 μm) was used due to the large number of structural defects observed in Figure 4.3.2 compromising the structural integrity of FFF printed Ag-BG scaffolds during sintering. Given this, the optical images presented in Figure 4.4.1 explored three different sintering conditions with the optimal sintering conditions applied throughout the rest of Section 4.4.

4.4.1.1 Macro- & milli- structure

The three different sintering conditions that were explored all used a maximum sintering temperature of 1150°C with the holding time varied from 3 h to 6 h to 8 h. Determination of the optimal sintering conditions was conducted studying the FFF printed Ag-BG scaffolds with optical microscopy and SEM characterization techniques (Fig. 4.4.1). Regardless of the sintering conditions applied, the optical image inserts (Fig. 4.4.1) demonstrated minimal variation in color

intensity, with all FFF printed Ag-BG scaffolds appearing relatively white and opaque. Additionally, the optical image inserts (Fig. 4.4.1) presented minimal structural deformation as evidenced by the absence of collapsed pores.

For the first set of sintering conditions applied (i.e. 1150°C, 3 h) to FFF printed Ag-BG scaffolds, SEM imaging (Fig. 4.4.1a, b) revealed a rough overall surface morphology on the milli-scale (Fig. 4.4.1a) with clearly defined individual particle-like features observed down to the micro-scale (Fig. 4.4.1b). Had significant densification occurred under the applied sintering conditions, the surface morphology would be expected to be relatively smooth, indicating that further improvements in the sintering conditions were possible.

When the sintering time was doubled (i.e. 1150°C, 6 h), SEM (Fig. 4.4.1c, d) revealed an increase in surface roughness compared to FFF-printed Ag-BG scaffolds sintered for 3 h (Fig. 4.4.1a, b). This unexpected increase in surface roughness was correlated to the phase transformation of Ca-deficient HA to β-TCP known to occur under the applied sintering conditions used [223, 261, 262]. Interestingly, when examining the FFF printed Ag-BG scaffolds at the milli-scale (Fig. 4.4.1c), local regions having a smoother surface morphology were observed interspersed between the regions of rough surface morphology. This was indicative that high-quality densification of Ag-BG particles was beginning to be achieved. Given this, the last set of sintering conditions increased the hold time from 6 h to 8 h rather than doubling the sintering time.

After a holding time of 8 h at 1150°C was applied for sintering FFF printed Ag-BG scaffolds, a smooth surface morphology was observed both at the milli- and micro-scales (Fig. 4.4.1.e, f) with no discernable particle-like features noted. The dramatic change in surface morphology when the sintering hold time was increased by 2 h from 6 h to 8 h, was thought to be the result of the phase transformation previously described, where significant densification was achieved once the phase transformation was complete. Interestingly, microscopic pores were observed randomly dispersed throughout the FFF-printed Ag-BG scaffolds. While the presence of these microscopic pores was expected to increase the surface area of FFF printed Ag-BG scaffolds and lead to improved antibacterial and biological performance compared to FFF printed Ag-BG

scaffolds lacking such microscopic pores. While the presence of internal microscopic pores will hurt mechanical performance, the high degree of densification achieved is expected to help move the elastic modulus closer to the upper Hashin-Shtrikman bound.

Through the application of three different sintering conditions, the optical and SEM observations (Fig. 4.4.1) identified sintering at 1150°C for 8 h were the optimal conditions to be applied for FFF printed Ag-BG scaffolds.

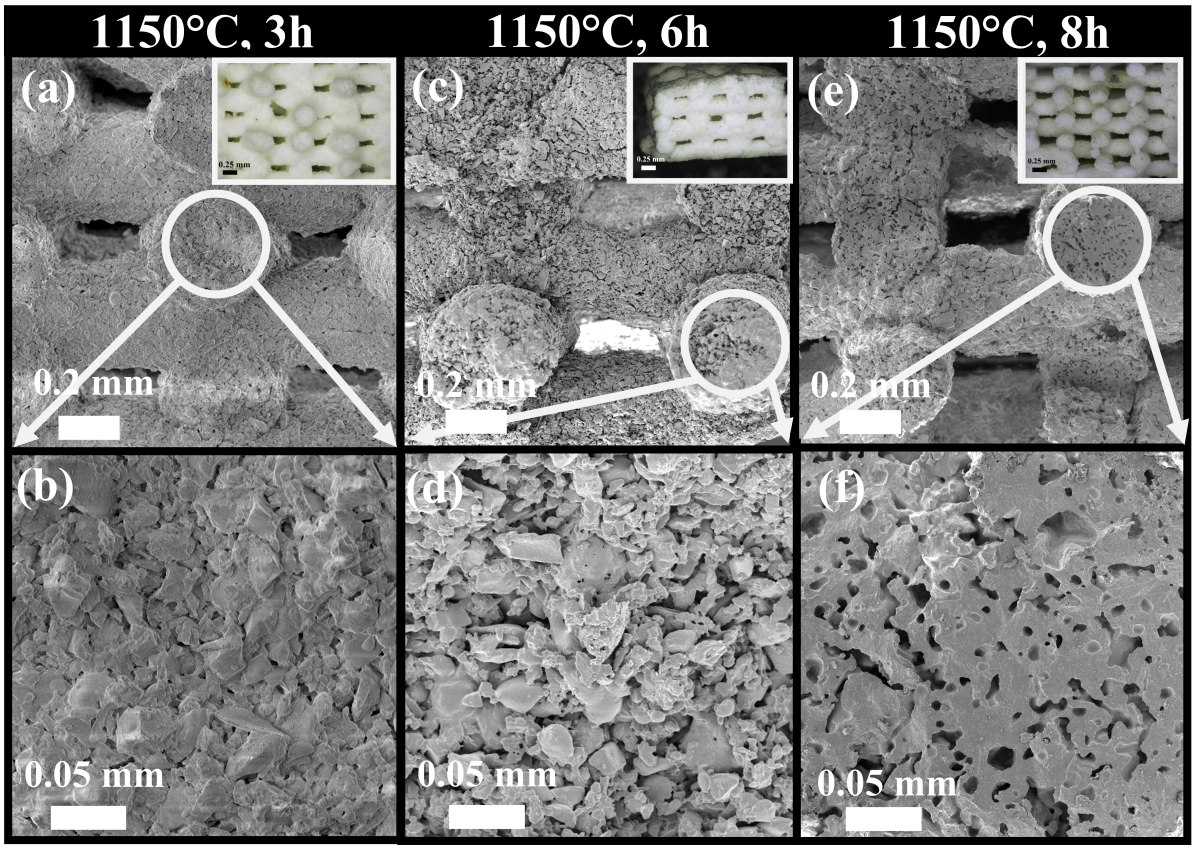

Figure 4.4.1: SEM images of FFF printed Ag-BG scaffolds sintered at, (a-b) 1150°C for 3 h, (c-d) 1150°C for 6 h, and (e-f) 1150°C for 8 h with inserts of relevant optical images of the FFF printed Ag-BG scaffolds under each of the applied sintering conditions.

Micro-CT of FFF printed Ag-BG scaffolds was performed on those sintered under the optimal conditions described previously and presented in Figure 4.4.2 for a comprehensive examination of the macro- and millistructures in both two- and three-dimensions. The perspective 3D reconstruction of a representative FFF printed Ag-BG scaffold, shown in Figure 4.4.2a, presents a well densified gross structure with minimal evidence suggesting detrimental structural deformation dur-

ing thermal debinding and sintering, demonstrating the success of pairing the use of a bimodal distribution of Ag-BG particles with the appropriate shaping, debinding, and sintering processes. This was further evidenced when examining the 3D reconstructed FFF printed Ag-BG scaffold along the x-, y-, and z-axes (Fig. 4.4.2b, d).

Quantification of the porosity, pore size, and strut thickness of the FFF printed Ag-BG scaffold revealed a porosity of ~60% having a pore size and strut thickness of 297±35 μm and 199±23 μm. The porosity of these FFF printed Ag-BG scaffolds was within the range reported for cancellous bone [16–18], and the pore size acceptably large, where any inhibition in cell migration is expected to be negligible [87].

Intriguingly, the representative 2D cross-sectional image of the FFF printed Ag-BG scaffold (Fig. 4.4.2e) displayed random fluctuations in radiopacity indicative of density fluctuations present within its internal structure. Closer examination revealed microscopic, localized regions of minimal radiopacity in the 2D cross-sectional image (Fig. 4.4.2e) that were infrequently observed suggesting that their appearance is not a pervasive feature present throughout the internal gross structure of the FFF printed Ag-BG scaffold. The localized regions of minimal radiopacity were hypothesized to be microscopic pores greater than 10 μm in diameter. This was supported by the observation of a pore in the 1 mm thick 3D reconstruction of the FFF printed Ag-BG scaffold along the z-axis (Fig. 4.4.2h).

The 1 mm thick 3D reconstructions, presented in Figure 4.4.2f-h and viewed along the x-, y-, and z-axes respectively, show minor buckling of the struts. These mild structural defects are likely induced by the presence of microscopic pores during sintering leading the struts to be unable to perfectly maintain their shape while Ag-BG is in its softened state.

4.4.1.2 Microstructure

With the modifications to the application of FFF technology to 3D print Ag-BG scaffolds using a bimodal distribution of Ag-BG particles, as previously described in Section 4.4.1, in addition to the superior sintering conditions applied comparatively, FTIR, XRD, and SEM-EDS were needed

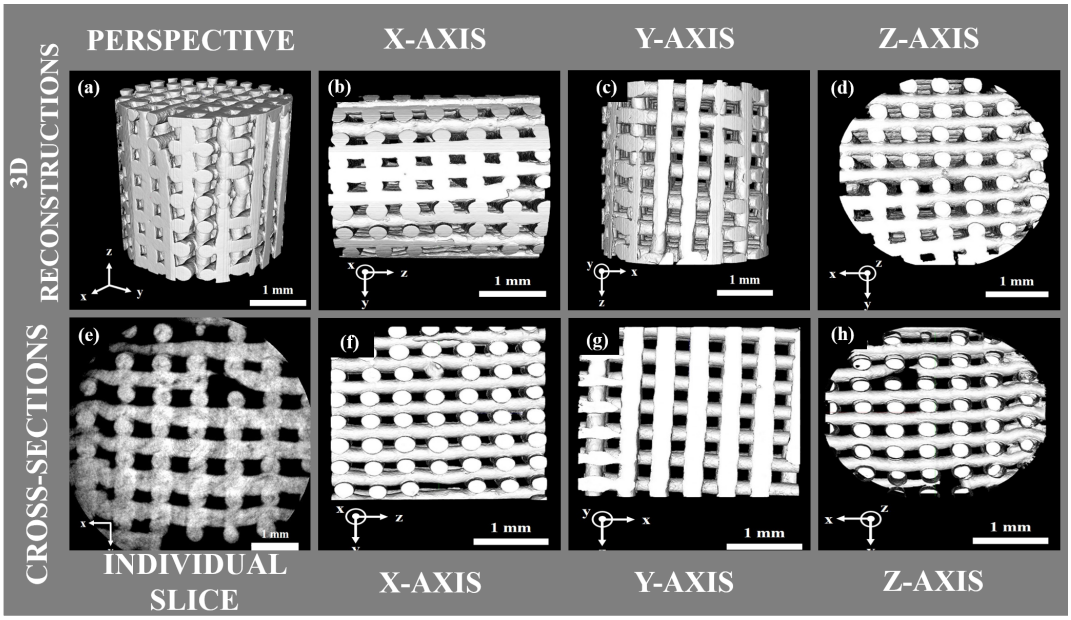

Figure 4.4.2: Representative micro-CT images of an FFF printed Ag-BG scaffold sintered at 1150°C for 8 h, where (a) shows a 3D reconstruction from a perspective point of view in addition to 3D reconstructions along the (b) x-, (c) y-, and (d) z-axes. A (e) representative 2D cross-section showing a well-sintered layer with minimal defects. (f-h) Show 1 mm thick 3D reconstructions of the FFF printed Ag-BG scaffold along the x- y- and z-axis respectively.

to elucidate their crystallographic and molecular structures.

The FTIR spectrum of powdered FFF printed Ag-BG scaffolds synthesized using a bimodal distribution of Ag-BG particles (Fig. 4.4.3a) presented with sharp, well-defined peaks indicative that these FFF printed Ag-BG scaffolds are highly crystalline, as expected. The correlation of these peaks to their respective phases necessitated the use of XRD to index the diffraction peaks present (Fig. 4.4.3b). Interestingly, the XRD pattern of powdered FFF printed Ag-BG scaffolds (Fig. 4.4.3b) was found to be triphasic consisting of cristobalite, W. 2M, and β-TCP compared to the pentaphasic XRD patterns shown previously for both Ag-BG slurry scaffolds and FFF printed Ag-BG scaffolds 3D printed using a unimodal distribution of Ag-BG particles. This decrease in the number of constituent phases is hypothesized to result predominately from the modification to the sintering conditions applied; however, it cannot be ruled out that the minimization of porous structural defects, as shown in Figures 4.4.1 and 4.4.2, allowed for a greater percentage of bulk crystallization to occur during sintering, rather than surface crystallization. Rietveld analysis was

performed on the XRD pattern shown in Figure 4.4.3b to quantify not only the concentrations of each phase indexed, but also to compare how similar the experimental phase concentrations were to the theoretical phase concentrations expected. These findings are described in Table 4.4.1. The phase concentrations elucidated by Rietveld analysis were found to differ from their theoretical phase concentrations by less than approximately 1%, demonstrating agreement providing evidence to support the validity of the experimental values obtained. Unlike all other XRD patterns of powdered Ag-BG scaffolds previously shown thus far, these FFF printed Ag-BG scaffolds contained a significant amount of cristobalite, known to be bioinert, that could hurt antibacterial and biological performance. Additionally, the Rietveld analysis (Table 4.4.1) elucidated the lattice parameters for all phases indexed in the XRD pattern (Fig. 4.4.3b) finding that the experimental lattice parameters differed from their theoretical values by ~4 pm, thus bolstering the validity of the diffraction peak indexing performed.

Table 4.4.1: The concentrations (wt%) of the phases present in the FFF printed Ag-BG scaffolds as calculated by Rietveld analysis and their theoretical maximum in addition to the lattice parameters as calculated by Rietveld analysis along with the lattice parameters from the PDF cards used. Δ was calculated by subtracting the theoretical values from the values determined by Rietveld analysis.

Phase	Rietveld (wt%)	Theoretical (wt%)	Lattice Parameters Rietveld (Å)	Lattice Parameters Theoretical (Å)
			a = 15.4125	a = 15.4240
W. 2M ($CaSiO_3$)	41.2±1.2	42.3	b = 7.3178	b = 7.3240
			c = 7.0638	c = 7.0692
			a = 10.3737	a = 10.3633
β-TCP ($Ca_3(PO_4)_2$)	13.0±0.4	13.1	b = 10.3737	b = 10.3633
			c = 37.2953	c = 37.2581
			a = 7.1004	a = 7.1264
Cristobalite (SiO_2)	45.7 ±1.4	44.7	b = 7.1004	b = 7.1264
			c = 7.1004	c = 7.1264

With the verification of the diffraction peak indexing performed on the XRD pattern shown in Figure 4.4.3b, the sharp well-defined FTIR peaks (Fig. 4.4.3a) previously described could now be correlated to the phases present in powdered FFF printed Ag-BG scaffolds. As demonstrated

by previous FTIR spectra, the characteristic Si-O bending peak for silicate-based glass systems was present at ~450 cm^{-1} [45, 235, 265]. Si-O bending peaks observed at ~630 cm^{-1} and ~800 cm^{-1} were correlated to the presence of cristobalite [235] while the Si-O bending peak noted at ~700 cm^{-1} was correlated to the presence of W. 2M [268, 269]. Regarding the Si-O stretching peaks observed, the presence of W. 2M was correlated to peaks noted at ~900 cm^{-1}, 1005 cm^{-1}, and 1070 cm^{-1} [268, 269]. The remaining Si-O stretching peak at ~1200 cm^{-1} was correlated to the presence of cristobalite [235], as noted previously in the FTIR spectra of Ag-BG solution and slurry scaffold along with FFF printed Ag-BG scaffolds 3D printed using a unimodal distribution of Ag-BG particles. The remaining FTIR spectrum peaks present (Fig. 4.4.3a) were correlated to the presence of β-TCP, with two P-O bending peaks assigned at ~570 cm^{-1} and ~610 cm^{-1} respectively and one P-O stretching peak assigned at ~920 cm^{-1} [235].

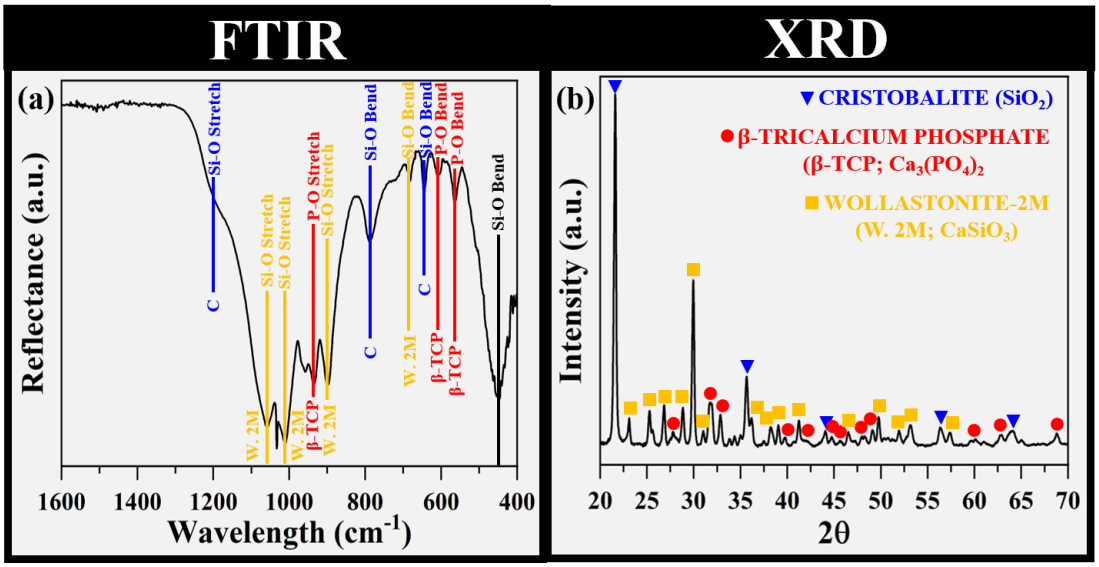

Figure 4.4.3: (a) XRD pattern and (b) FTIR-ATR spectrum of a powdered FFF printed Ag-BG scaffold showing the applied sintering conditions yield a highly crystalline microstructure, where cristobalite, wollastonite-2M, and β-tricalcium phosphate were the crystalline phases identified.

Assessment of elemental homogeneity was elucidated using SEM-EDS characterization techniques (Fig. 4.4.4) found a homogenous distribution of all elements down to the micron-level (Fig. 4.4.4c-h) when the strut cross-section (Fig. 4.4.4b) was used for EDS X-Ray mapping. This demonstrates that while the improved sintering conditions applied for these FFF printed Ag-BG

scaffolds led to the development of different phases than what was previously shown for previous Ag-BG scaffolds, elemental homogeneity down to the micron-level was preserved, indicating that the crystallites formed during the applied heat treatment are, at a minimum, meso-sized. Application of Scherrer's equation (eq. 3.3.6) revealed the crystallite sizes of the diffraction peaks indexed in Figure 4.4.4b are < 50 nm, meaning TEM characterization would be needed for FFF printed Ag-BG scaffolds 3D printed using a bimodal distribution of Ag-BG particles to elucidate evidence of elemental heterogeneity.

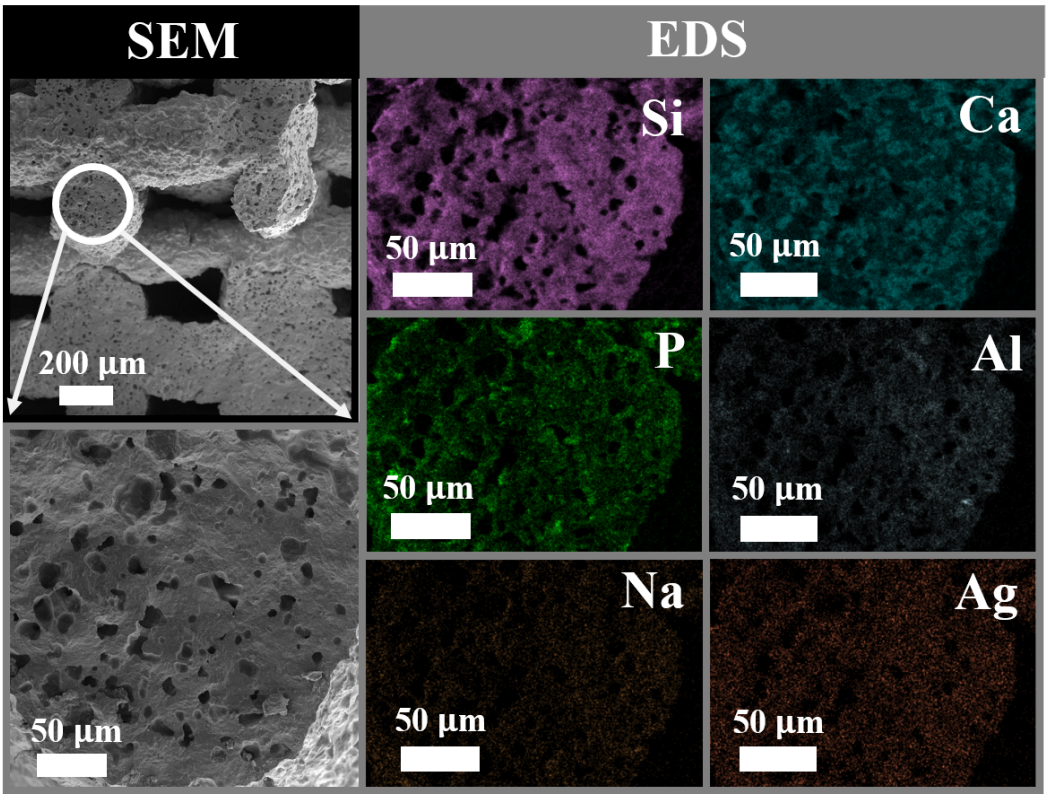

Figure 4.4.4: (a) An SEM image of a cross-section of an FFF printed Ag-BG scaffold, where a (b) strut cross-section was used for EDS X-Ray mapping showing that (c) Si, (d) Ca, (e) P, (f) Al, (g) Na, and (h) Ag are homogenously distributed down to the micron level.

4.4.1.3 Meso- & nano- structure

Powdered FFF Ag-BG scaffolds 3D printed using a bimodal distribution of Ag-BG particles were employed to both identify any heterogeneity at the nanoscale and provide further validation

of the diffraction peak indexing previously described in Section 4.4.1.2. The phase-contrast image presented in Figure 4.4.5a revealed an isolated meso-sized aggregate of powdered FFF printed Ag-BG scaffolds with well-defined geometric features being observed in their interior. The respective SAD pattern (Fig. 4.4.5b) of the observed aggregate in Figure 4.4.5a identified the presence of both W. 2M and β-TCP through indexation of the spots presented. To examine the spatial distribution of the two phases identified, axial dark-field imaging was employed using the spot indexed to the (0 0 2) atomic planes of W. 2M (Fig. 4.4.5c), and the spot indexed to the (0 2 $\bar{2}$) atomic planes of β-TCP (Fig. 4.4.5d). W. 2M was found to be present in the analyzed powdered FFF printed Ag-BG scaffold aggregate in a greater quantity than β-TCP as evidenced by the qualitative increase in bright spots comparatively, consistent with their respective phase concentrations noted from Rietveld analysis (Table 4.4.1).

TEM was utilized to characterize the nanoscale structure of powdered FFF printed Ag-BG scaffolds to identify the presence of nanoscale heterogeneity, and additionally to validate the crystalline phases noted in their respective XRD pattern (Fig. 4.4.3a) and FTIR-ATR spectrum (Fig. 4.4.3b). The broader view of an aggregate of FFF printed Ag-BG particles shown in the phase-contrast image (Fig. 4.4.5a) revealed distinct well-defined geometric features of relatively minimal electron transparency suggesting the presence of crystalline features. W. 2M and β-TCP were identified in the SAD pattern (Fig. 4.4.5b) of the powdered FFF printed Ag-BG scaffold aggregate consistent with the phases identified in both the XRD pattern (Fig. 4.4.5a) and FTIR-ATR spectrum (Fig. 4.4.5b). Axial darkfield imaging using (0 0 2) spot for W. 2M (Fig. 4.4.5c) and (0 2 $\bar{2}$) spot for β-TCP (Fig. 4.4.5d) showed W. 2M was more prevalent than β-TCP given a larger quantity of bright spots were observed in the powdered FFF printed Ag-BG scaffold aggregate and in agreement with the phase concentrations elucidated by the Rietveld analysis (Table 4.4.1).

When examining a partial meso-sized aggregate of the powdered FFF printed Ag-BG scaffold (Fig. 4.4.5e), the phase-contrast image revealed both well-defined rod-like features and meso-sized particle-like features having comparatively minimum electron transmission locally that were hypothesized to be single crystals. Evaluation of this hypothesis entailed collecting the respective

SAD pattern (Fig. 4.4.5f) and using the (3 2 0) atomic planes indexed to W. 2M (Fig. 4.4.5g) and (1 1 0) atomic planes indexed to β-TCP (Fig. 4.4.5h) for axial dark-field imaging. The use of the (3 2 0) atomic planes of W. 2M revealed two large bright regions having well-defined geometry within a dark matrix. The first bright region was pseudo-hexagonal in shape and thought to be a faceted view of a W. 2M monoclinic single crystal along its a-, c-axis that can arise in monoclinic crystal systems [56]. Measurements along the six sides revealed lengths ranging from ~60 nm to ~105 nm. The second bright region observed had a rod-like geometry thought to be a faceted view of a W. 2M monoclinic single crystal along its b-axis consistent with a monoclinic crystal system [56]. The length of this bright rod-like feature was found to be within the mesoscale, while its width was within the nanoscale. It is worth noting that the b-axis facet view of the (3 2 0) W. 2M single crystal is comprised of mono-dimensional silica tetrahedrons with Ca atoms populating the interlayer space along the a- c-axes. Interestingly, the axial dark-field image formed using the (1 1 0) atomic planes of β-TCP (Fig. 4.4.5h) generated a bright matrix interspersing the dark well-defined geometric features previously described. This was indicative that the (1 1 0) atomic planes of β-TCP are more diffuse compared to the (3 2 0) atomic planes of W. 2M, as further evidenced by the minimal presentation of any well-defined geometric features.

Curiously, the phase contrast image shown in Figure 4.4.5e additionally revealed small atomic scale (Table 3.3.1) particle-like features (< 10 nm) locally having significantly less electron transmission compared to the surrounding matrix. These atomic-scale particle-like features could be AgNPs given the detection of cristobalite in the respective SAD pattern (Fig. 4.4.5f) given previous reports demonstrating the plausibility of AgNPs embedded in a cristobalite matrix [288, 289]. The validity of this hypothesis will be explored in more detail in Section 5.1.

4.4.2 Performance characteristics

4.4.2.1 Mechanical performance

Given the superior structural characteristics observed for FFF Ag-BG scaffolds, 3D printed

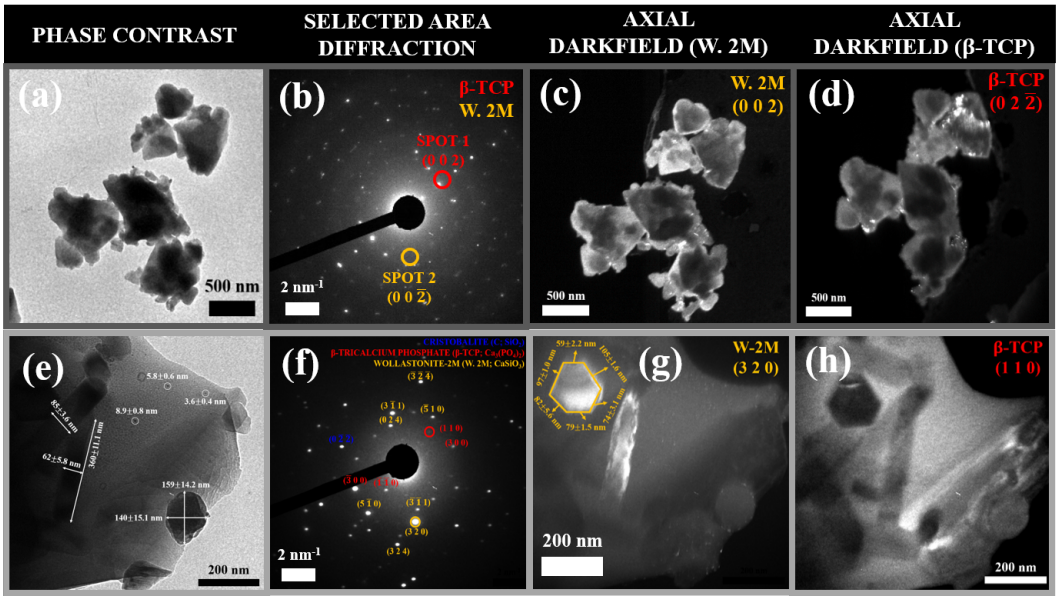

Figure 4.4.5: (a) Phase-contrast image of a powdered FFF printed Ag-BG scaffold of an isolated aggregate of FFF printed Ag-BG particles with (b) presenting the respective SAD pattern. Axial darkfield images were captured using the (c) (0 0 2) and (d) (0 2 $\bar{2}$) atomic planes of W. 2M and β-TCP respectively presenting evidence of nanoscale heterogeneity. (e) Phase-contrast image of a partial powdered FFF printed Ag-BG scaffold aggregate having well-defined geometric features in the interior of the aggregate with (f) elucidating the respective SAD pattern, where the (g) (3 2 0) indexed atomic planes of W. 2M and (h) (1 1 0) indexed atomic planes for β-TCP were correlated to the well-defined geometric features and matrix respectively.

using a bimodal distribution compared to the previously studied Ag-BG scaffolds (Sections 4.2.1, 4.3.2, and 4.4.1) warranted in-depth investigations into their mechanical performance. This was achieved using N=25 samples for compression and flexural testing to not only elucidate their mechanical strength but also to evaluate the reliability of their mechanical performance through the use of Weibull statistics [56]. The fracture toughness of FFF printed Ag-BG scaffolds were additionally characterized to determine if fracture toughness in addition to the compression and flexural strengths revealed satisfy the mechanical performance requirements for targeting bone tissue regeneration in load-bearing applications.

To start, the average compressive strength for FFF Ag-BG scaffolds 3D printed using a bimodal distribution of Ag-BG particles was 19.8±1.7 MPa having a porosity of 59.8±0.8%. This increase in compressive strength compared to FFF Ag-BG scaffolds 3D printed using a unimodal distribution of Ag-BG particles was found to be ~600% greater, signifying significant improvement when using

a bimodal distribution of Ag-BG particles. Using the linear elastic regions of FFF printed Ag-BG stress-strain curves found these FFF printed Ag-BG scaffolds to have an elastic modulus of 0.6±0.1 GPa. Both the compressive strength and elastic modulus for FFF printed Ag-BG scaffolds surpassed the maximum mechanical performance requirements for targeting bone tissue engineering in load-bearing applications by 64% and 20% respectively while maintaining an acceptable porosity (i.e. 40-95%) [16–18].

The elastic modulus previously reported for FFF printed Ag-BG scaffolds were compared to the elastic moduli reported for previously described Ag-BG scaffolds using the Hashin-Shtrikman plot (Fig. 4.4.6i). As observed, FFF Ag-BG scaffolds 3D printed using a bimodal distribution of Ag-BG particles were found to have moved away from the lower Hashin-Shtrikman bound indicating that the applied modifications to FFF printing Ag-BG scaffolds were successful at starting to unlock the full mechanical performance potential of these scaffolds.

Further extrapolation from the compressive behavior of FFF printed Ag-BG scaffolds was possible through the application of Equation 3.4.2 as derived by Gibson-Ashby [57] for computation of the bulk compressive behavior of these FFF printed Ag-BG scaffolds. Equation 3.4.3 assumes that the bulk compressive behavior is for materials having 0% porosity. This, however, was not the case for FFF Ag-BG scaffolds 3D printed using a bimodal distribution of Ag-BG particles, as evidenced by the structural porous defects observed in Figures 4.4.1, 4.4.2, 4.4.4a-b, and 4.4.4g-h. Given the inversely proportional relationship between porosity and mechanical performance, demonstrated herein, suggests that the bulk compressive strength calculated using Equation 3.4.3 will underestimate the actual bulk compressive strength for FFF printed Ag-BG scaffolds. Following this, image analysis was performed post-fracture of FFF printed Ag-BG scaffolds (Fig. 4.4.6g, h) assuming that fracture occurred on the planes containing the highest concentration of internal porous structural defects to estimate the upper bound of porosity that existed internally. The image analysis revealed an average porosity of 7±2% while Equation 3.4.3 revealed a bulk compressive strength of 119±10 MPa for FFF printed Ag-BG scaffolds. These findings are significant considering the porosity range and compressive strength for cortical bone are 5-15% and 100-200 MPa respectively [16–18]

demonstrating the potential for FFF Ag-BG scaffolds 3D printed using a bimodal distribution of Ag-BG particles to be mechanically competent for targeting bone tissue regeneration in cortical bone. In a broader context, this would signify that proper application of FFF technology for 3D printing scaffolds has the potential to be the first scaffold processing technique identified within the biomaterials community to deliver the elusive trifecta of appropriate mechanical, antibacterial, and biological performances to successfully target bone tissue regeneration in cortical bone.

For assessment in the reliability of the compressive behavior of FFF printed Ag-BG scaffolds, a Weibull plot (Fig. 4.4.6b) generated using Equations 3.5.1 and 3.5.2 elucidated a Weibull modulus (m) of 13.6±0.9 associated with a correlation coefficient of 0.9. Importantly, the computed Weibull modulus for FFF printed Ag-BG scaffolds was found to exceed other reported Weibull moduli reported for other bioceramic and bioactive glass scaffolds [59, 169, 290, 291] signifying that the approach applied to FFF printing of Ag-BG scaffolds is capable of synthesizing scaffolds having greater reliability in compressive behavior. Additionally, ASTM standard C1239-13 [255] states that the characteristic strength (σ_0) is determined at a probability of failure (Fig. 4.4.6c) of 63.2%, which was found for the FFF printed Ag-BG scaffolds presented here to be 20.2 MPa, which is in excellent agreement with the average compressive strength previously reported.

Characterization of the flexural strength for FFF printed Ag-BG scaffolds using N=25 samples and computed using Equation 3.4.5 was elucidated at 11.1±1.8 MPa for scaffolds having an average porosity of 55.8±3.0%. Additionally, the flexural strength for FFF printed Ag-BG scaffolds was evaluated through the use of the four-point bending scheme, as described in ASTM 1674-16 [244], to ensure failure was achieved in pure bending rather and avoid mixed modes of failure, known to be present when the three-point bending scheme is used. Figure 4.4.6d presents a representative stress-displacement curve for FFF printed Ag-BG scaffolds showing a strong linear increase in stress as a function of displacement before catastrophic failure.

Application of Weibull statistics on the flexural strengths generated through mechanical performance characterization found that the Weibull modulus for FFF printed Ag-BG scaffolds was 7.3±0.3 and associated with a correlation coefficient of 0.82 (Fig. 4.4.6e). The computed Weibull

modulus reported here for FFF printed Ag-BG scaffolds was found to exist at the upper range for other bioceramic and bioactive glass scaffolds demonstrating highly competitive reliability in flexural strength comparatively scaffolds [59, 169, 290, 291]. The estimated characteristic flexural strength for FFF printed Ag-BG scaffolds (Fig. 4.4.6f) was computed at 11.6 MPa and in excellent agreement with the average flexural strength previously reported.

The fracture toughness for FFF printed Ag-BG scaffolds were characterized following ASTM C1428-18 guidelines [245] and calculated using Equation 3.4.6 elucidating a K_{Ic} value of 0.7±0.1 MPa·$m^{1/2}$ when FFF printed Ag-BG scaffolds had an average porosity of 57.2±1.9%. The computed fracture toughness previously reported was found to be within the range of fracture toughness values reported for cancellous bone (i.e. K_{Ic} = 0.1-0.8 MPa·$m^{1/2}$) [16–18]. Furthermore, the reported fracture toughness for FFF printed Ag-BG scaffolds was within the range reported for other bioceramic and bioactive glass scaffolds [59, 169, 290, 291].

4.4.2.2 Degradation behavior

The degradation behavior for FFF printed Ag-BG scaffolds was elucidated following the procedures previously detailed in Section 3.4.1. For FFF printed Ag-BG scaffolds immersed in TRIS-buffer prepared to have a pH of 7.25 at 37ºC for consistency with FFF printed Ag-BG scaffolds immersed in SBF for apatite-forming ability characterization. The pH (Fig. 4.4.7a) of TRIS-buffer was found to increase when FFF printed Ag-BG scaffolds were immersed up to 15 d, where the most alkaline pH was measured at ~7.72. The pH behavior of FFF printed Ag-BG scaffolds from 18 d of immersion to 30 d of immersion in TRIS-buffer was found to stabilize around a value of ~7.65. Overall, the pH measurements recorded from 3 d of immersion to 30 d immersion of FFF printed Ag-BG scaffolds in TRIS-buffer were all found to deviate no more than 0.2 units suggesting a weak osmotic effect indicative that ions are being released in a controlled and sustained manner. Furthermore, when FFF printed Ag-BG scaffolds are characterized for their cellular biological performance, it is expected that the local medium will not become more than twice as alkaline and thus should not negatively impact antibacterial or biological performance.

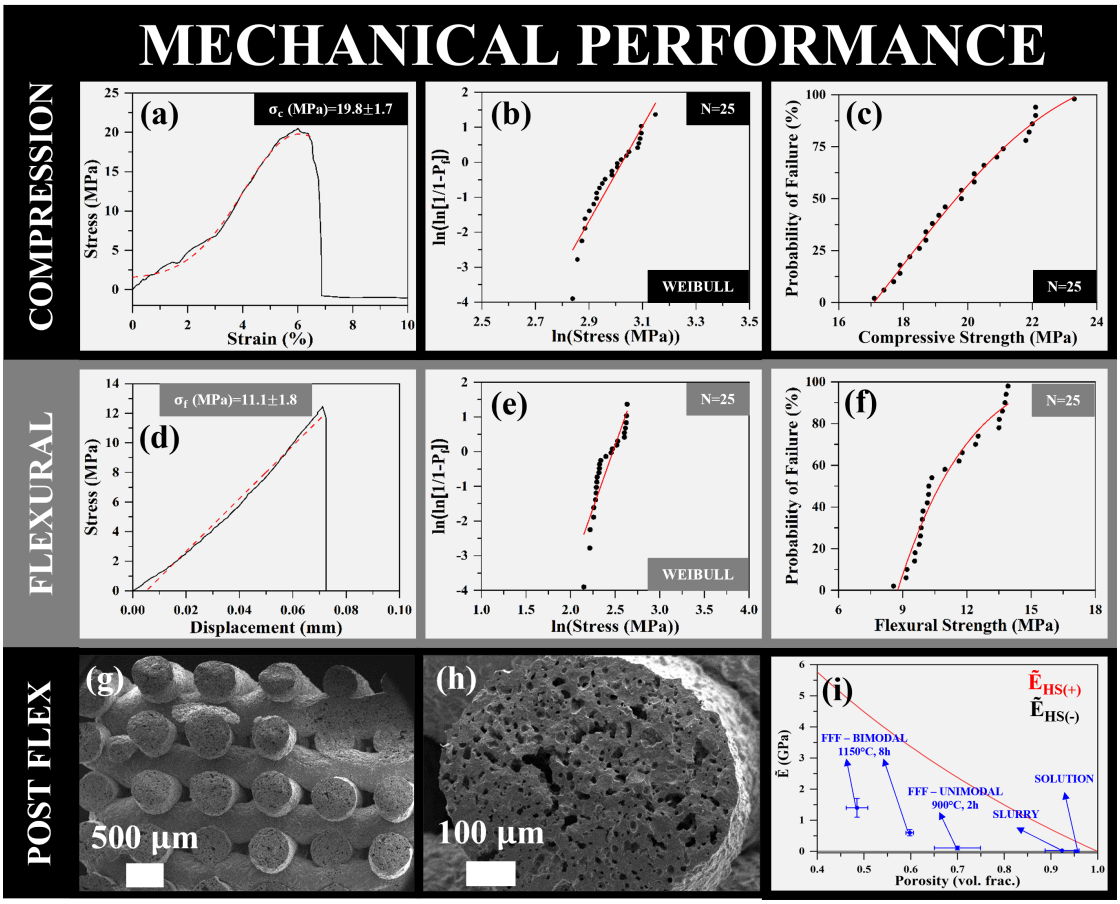

Figure 4.4.6: (a) Representative stress-strain plot of the compressive behavior of FFF printed Ag-BG scaffolds. (b) Weibull plot of the compressive behavior of N=25 FFF printed Ag-BG scaffolds, where a Weibull modulus of 13.6 was elucidated, demonstrating that the FFF technique can produce scaffolds with reliable compressive behavior. (c) Shows the probability of failure for the compressive behavior of N=25 FFF printed Ag-BG scaffolds as a function of compressive strength. (d) Representative stress-displacement plot of the flexural behavior of FFF printed Ag-BG scaffolds as determined using the 4-point bending scheme. (e) The Weibull plot of the flexural behavior of N=25 FFF printed Ag-BG scaffolds, where a Weibull modulus of 7.3 was computed. (f) The probability of failure of FFF printed Ag-BG scaffolds as a function of flexural strength. The red lines are guides-to-the-eye. (g-h) SEM images representative of the fracture surface of FFF printed Ag-BG scaffolds after flexural testing. (i) The Hashin-Shtrikman (HS) bounds for the elastic moduli of all Ag-BG scaffolds presented herein with the red and black lines denoting the upper and lower HS bounds respectively.

The mass loss for FFF printed Ag-BG scaffolds was additionally recorded up to 30 d of immersion in TRIS-buffer (Fig. 4.4.7b) elucidating a maximum mass loss of ~15% after 30 d. Further extrapolation predicts complete mass loss will occur after around 102 days of immersion (i.e. ~14.6 weeks or 3.4 months) hypothesized to provide sufficient structural support for an acceptable

amount of time for targeting bone tissue regeneration in load-bearing applications. Overall, the mass loss for FFF printed Ag-BG scaffolds (Fig. 4.4.7b) was minimal up to 9 d of immersion in TRIS-buffer. From 9 d up to 30 d of immersion (Fig. 4.4.7b), FFF printed Ag-BG scaffolds exhibited a pseudo-linear behavior in mass loss suggesting a steady rate of mass loss indicative that degradation is occurring in a controlled and sustained manner, and in agreement with the elucidation of the pH behavior of FFF printed Ag-BG scaffolds previously described. It must be noted, however, that mass loss for FFF printed Ag-BG scaffolds is expected to be accelerated when studied under load-bearing conditions due to the experienced compressive forces.

ICP-OES (Fig. 4.4.7c-f) of TRIS-buffered extracts collected at consistent time points found the ion release profiles to be within the therapeutic ranges needed for bone tissue regeneration [29, 292, 293] and in agreement with the pH (Fig. 4.4.7a) and mass loss (Fig. 4.4.7b) values recorded. Given this, it is expected, therefore, that FFF-printed Ag-BG scaffolds will exhibit anti-MRSA properties and promote cell viability, proliferation, and differentiation when studied in vitro.

4.4.2.3 Antibacterial performance

Antibacterial performance was characterized for FFF Ag-BG scaffolds 3D printed using a bimodal distribution of Ag-BG particles at a scaffold concentration of 100 mg mL-1. This approximate ten-fold increase in scaffold concentration compared to previous antibacterial performance characterization for other Ag-BG scaffolds previously studied to evaluate scaffold concentrations more comparable to expected concentrations when targeting bone tissue regeneration in load-bearing applications. As performed previously for FFF Ag-BG scaffolds printed using a unimodal distribution of Ag-BG particles (Fig. 4.3.8), the anti-MRSA effect was elucidated using planktonic MRSA under growth-arrested conditions and the CFU assay after 24 h and 48 h of exposure respectively (Fig. 4.4.8a). A significant reduction in CFUs was noted for FFF printed Ag-BG scaffolds (Fig. 4.4.8a) compared to untreated controls after 24 h of exposure to MRSA. After 48 h of MRSA exposure, a significant increase in MRSA inhibition was observed when the exposure

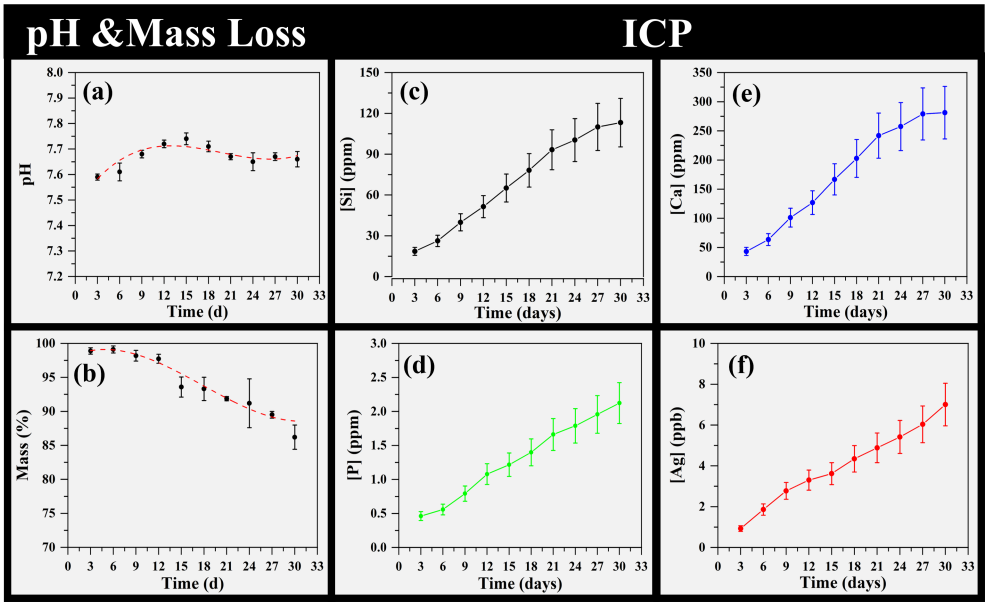

Figure 4.4.7: (a) pH values for FFF printed Ag-BG scaffolds were recorded every 3 d for 30 d when immersed in TRIS buffer. The (b) mass loss (%) for FFF printed Ag-BG scaffolds was similarly recorded every 3 d for 30 d after drying, where 100% represents the initial mass of FFF printed Ag-BG scaffolds. Extracts were collected at consistent time points to elucidate the concentrations of (c) Si, (d) P, (e) Ca, and (f) Ag respectively as measured by ICP-OES. The red-dashed lines in (a) and (b) represent guides-to-the-eye.

time to FFF printed Ag-BG scaffolds was doubled (Fig. 4.4.8a) and found to be consistent with the anti-MRSA effect observed for FFF Ag-BG scaffolds 3D printed using a unimodal distribution of Ag-BG particles, as previously described in Section 4.3.2.2.2. Furthermore, the anti-MRSA effect observed is consistent with the Ag ion concentration elucidated through ICP-OES measurements (Fig. 4.4.7f).

To further expand on the antibacterial performance characteristics exhibited by FFF printed Ag-BG scaffolds entailed exposure to MRSA biofilms. FFF printed AG-BG scaffolds at a concentration of 100 mg mL^{-1} were exposed to previously formed MRSA biofilms for 72 h under growth-assisted conditions. This experimental design was chosen given the increased difficulty in combating an already present biofilm compared to studying the ability of FFF printed Ag-BG scaffolds to prevent MRSA biofilm formation [294].

Crystal violet staining (Fig. 4.4.8b) was performed after exposing FFF printed Ag-BG scaffolds to MRSA biofilms for 72 h under growth-assisted conditions to quantify the amount of MRSA

biomass present. From this, a statistically significant reduction in MRSA biomass was observed when MRSA biofilms were treated with FFF printed Ag-BG scaffolds for 72 h, given the untreated controls and treated biofilms had a normalized OD value of 1.0±0.15 and 0.45±0.12 respectively (Fig. 4.4.8b). Complimentary Live/Dead staining (Fig. 4.4.8c-e) was additionally applied to visualize using CLSM and quantify the amount of living versus dead MRSA. The representative superimposed Live/Dead staining CLSM images for untreated (Fig. 4.4.8d) and treated (Fig. 4.4.8e) MRSA biofilms with FFF printed Ag-BG scaffolds observed 12% and 51% MRSA eradication (Fig. 4.4.8c) for untreated (Fig. 4.4.8d) and treated (Fig. 4.4.8e) MRSA biofilms respectively and found to agree with the crystal violet staining shown in Figure 4.4.8b. These pieces of evidence demonstrate that FFF-printed Ag-BG scaffolds are potential candidates for targeting bone tissue regeneration in bone defects located in load-bearing regions formed by the presence of bacteria such as MRSA.

4.4.2.4 Biological performance

As performed for other Ag-BG scaffolds previously described (Sections 4.2.2.3 and 4.3.3.3), FFF Ag-BG scaffolds 3D printed using a bimodal distribution of Ag-BG particles were immersed in SBF for 7 d, 14 d, and 21 d to characterize their ability to form an apatite-like layer elucidated by FTIR (Fig. 4.4.9d) and XRD (Fig. 4.4.9e) to identify any molecular or crystallographic structural changes that may have occurred, and SEM-EDS (Fig. 4.4.9a-c) to elucidate surface morphology and Ca/P ratios for deposited surface features noted.

Up to 21 d of immersion in SBF, the molecular (Fig. 4.4.9d) and crystallographic (Fig. 4.4.9e) structural characteristics showed minimal changes for powdered FFF printed Ag-BG scaffolds. The FTIR spectra, shown in Figure 4.4.9d, did not present a similar decrease in peak intensity from ~650 cm^{-1} to ~1200 cm^{-1} save for the mild peak broadening observed from ~1000 cm^{-1} to ~1100 cm^{-1} for powdered FFF printed Ag-BG scaffolds after 14 d and 21 d of immersion in SBF respectively. Crystallographically, the strongest change observed for powdered FFF printed Ag-BG scaffolds was the indexing of Ca-deficient HA diffraction peaks (Fig. 4.4.9e) starting at 7 d of immersion in SBF. The breadth of the diffraction peaks for the indexed Ca-P phases was noted

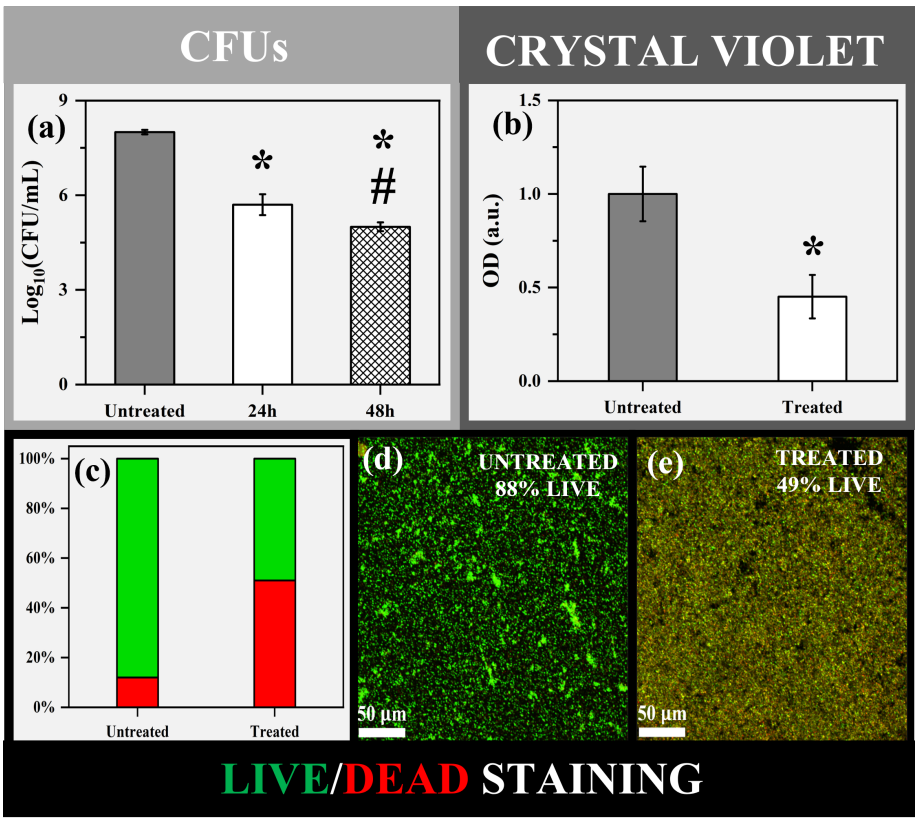

Figure 4.4.8: (a) The anti-MRSA behavior of FFF printed Ag-BG scaffolds after being exposed to MRSA for 24 h and 48 h under growth-arrested conditions. (b) Crystal violet staining of FFF printed Ag-BG scaffolds after exposure to a MRSA biofilm under growth-assisted conditions for 3 d, where FFF printed Ag-BG scaffolds demonstrated a significant reduction in biomass elucidated by normalized OD measurements compared to the untreated controls. (c) Quantification of the Live/Dead staining shown in (e) and (f) demonstrates that FFF printed Ag-BG scaffolds could combat the presence of a previously formed MRSA biofilm.

to undergo a minor reduction after 14 d and 21 d of immersion in SBF for FFF printed Ag-BG scaffolds in addition to a minor up-shift in 2θ for the observed diffraction peaks consistent with the minor d-spacing reduction noted between the three principle diffraction peaks for β-TCP and Ca-deficient HA respectively.

The observed surface morphological changes for FFF printed Ag-BG scaffolds immersed in SBF for up to 21 d provide conclusive evidence that an apatite-like layer formed unlike the respective FTIR spectra (Fig. 4.4.9d) and XRD patterns (Fig. 4.4.9e) previously described. After 7 d of immersion in SBF, FFF printed Ag-BG scaffolds presented minimal evidence of surface morphological features consistent with deposition of an apatite-like layer [283]. EDS spot analysis

revealed a Ca/P ratio of 5.9 (Fig. 4.4.9c), which is approximate to the Ca/P ratio for the used Ag-BG system and further evidence that SBF immersion for 7 d was insufficient time for an apatite-like layer to form. FFF printed Ag-BG scaffolds immersed in SBF for 14 d (Fig. 4.4.9b) presented with bright surface morphological features consistent with the expected surface morphological features for a deposited apatite-like layer [283] having a Ca/P ratio of 1.9. This signified that the apatite-like layer that formed is likely ~5 μm thick given the proximity of the measured Ca/P ratio to the expected stoichiometric Ca/P ratio of 1.67. 21 d of immersion of FFF printed Ag-BG scaffolds in SBF (Fig. 4.4.9) presented with a greater area of depositions on their surfaces compared to 14 d of immersion in SBF. The Ca/P ratio of these depositions was measured at 1.8 after FFF printed Ag-BG scaffolds were immersed in SBF for 21 d having a thickness of at least 5 μm thick given the measured Ca/P ratio is 0.13 units greater than the expected stoichiometric Ca/P ratio of 1.67. Interestingly, the surface morphological features observed (Fig. 4.4.9a), while consistent with the expected surface morphological features [283], displayed cracking creating clear boundaries of micro-sized depositions of an apatite-like layer. Given this, FFF-printed Ag-BG scaffolds would be expected to exhibit bone-bonding behavior *in vivo*, an attractive biological performance characteristic for targeting bone tissue regeneration in load-bearing applications.

The attractive degradation behavior, antibacterial performance, and biological performance studied through immersion in SBF of FFF printed Ag-BG scaffolds warrant further biological performance characterization in vitro, exposing human mesenchymal stem cells (hMSCs) indirectly to FFF printed Ag-BG scaffolds to determine their effect on cell viability (Fig. 4.4.10a), proliferation (Fig. 4.4.10b), and mineralization (Fig. 4.4.10l).

Optical images (Fig. 4.4.10c, d) were captured at time point zero for both hMSCs treated with FFF printed Ag-BG scaffolds (Fig. 4.4.10d) and untreated hMSCs (Fig. 4.4.10c) presenting similar hMSC morphology, where hMSCs appeared compact having short filopodia indicative that hMSCs are dissatisfied with their environment and expected given the handling performed during experimental setup. After 2 d of treatment with FFF printed Ag-BG scaffolds (Fig. 4.4.10f), hMSCs appear satisfied with their environment given the elongation of filopodia and observed interactions

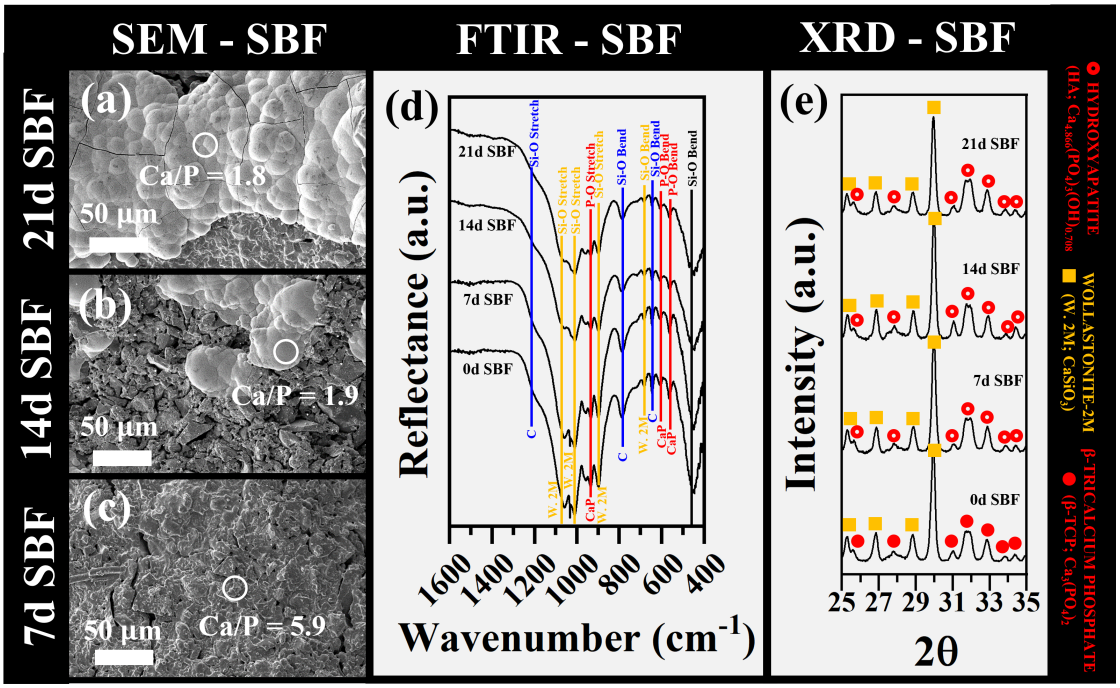

Figure 4.4.9: SEM images after (a) 21 d, (b) 14 d, and (c) 7 d of immersion of FFF printed Ag-BG scaffolds in SBF showing progressive mineralization of an apatite-like layer consistent with the expected surface morphological features. (d) Shows the FTIR spectra and (e) XRD patterns respectively of powdered FFF printed Ag-BG scaffolds after 0, 7, 14, and 21 days of immersion in SBF.

with surrounding hMSCs that provides supporting evidence of cell spreading. For untreated hMSCs after 2 d (Fig. 4.4.10e) displayed similar morphology when examined using optical microscopy to hMSCs treated with FFF printed Ag-BG scaffolds after 2 d (Fig. 4.4.10f). hMSCs treated indirectly with FFF printed Ag-BG scaffolds (Fig. 4.4.10h) displayed confluency given the lack of appearance of the TCP, unlike treated and untreated hMSCs after 0 d and 2 d of incubation (Fig. 4.4.10c-f). Qualitative analysis of Figures 4.4.10g, h identified fewer individual hMSCs when treated with FFF printed Ag-BG scaffolds indicative that the presence of FFF printed Ag-BG scaffolds led hMSCs to reach confluency faster and should be supported by the OD measurements quantifying hMSC viability (Fig. 4.4.10a) and proliferation (Fig. 4.4.10b). After 8 d of treatment with FFF printed Ag-BG scaffolds (Fig. 4.4.10j) displayed similar confluency to untreated hMSCs (Fig. 4.4.10i) after 8 d of incubation.

OD measurements elucidated through the use of the WST-8 assay revealed that after 2 d of treatment with FFF printed Ag-BG scaffolds (Fig. 4.4.10a) had an insignificant improvement on

hMSC viability compared to untreated hMSCs. Starting after 5 d of treatment (Fig. 4.4.10a) and continuing with 8 d of treatment with FFF printed Ag-BG scaffolds (Fig. 4.4.10a) found hMSCs viability was significantly compared to untreated hMSCs. Regarding hMSC proliferation, the respective OD values for treated and untreated hMSCs (Fig. 4.4.10b) as a function of time elucidated a proliferation rate of 0.443 OD day^{-1} for hMSCs treated with FFF printed Ag-BG scaffolds while the proliferation rate for untreated hMSCs was noted at 0.309 OD day^{-1}. The proliferation for hMSCs treated with FFF printed Ag-BG scaffolds, therefore, was found to be 1.43 times more prolific compared to untreated hMSCs.

Further *in vitro* cellular biological performance characterization entailed treating hMSCs in differentiation media with FFF printed Ag-BG scaffolds to compare the mineralization ability exhibited by the present osteoclasts to untreated hMSCs and elucidated through the application of the ARS assay (Fig. 4.4.10l-n). Treatment of hMSCs with FFF printed Ag-BG scaffolds identified a three order of magnitude increase in ARS stain demonstrating a greater than 1,000% increase in mineralization compared to untreated hMSCs. This observation was further corroborated with the representative optical image, shown in Figure 4.4.10m, n, where the surface of the confluent hMSC layer presented stronger evidence of morphological features consistent with mineralization for hMSCs treated with FFF printed Ag-BG scaffolds compared to untreated hMSCs. The optical image inserts, shown for hMSCs treated (Fig. 4.4.10n) with FFF printed Ag-BG scaffolds and untreated hMSCs (Fig. 4.4.10m) reflect this finding as evidenced by the strong intensity of red (Fig. 4.4.10n) indicative of mineralization compared to the weakly intense red (Fig. 4.4.10m) for untreated hMSCs chromatically demonstrating weak mineralization respectively.

4.5 3D printing gelatin—silicate-containing hybrid scaffolds

The work presented in Section 4.5 has previously been published to the preprint server, bioRxiv, by Marsh et al. and is described by the following citation:

- bioRxiv, Adam C. Marsh, Ehsanul Hoque Apu, Marcus Bunn, Christopher H. Contag, Nureddin Ashammakhi, Xanthippi Chatzistavrou, A New Bioink for Improved 3D Bioprinting of

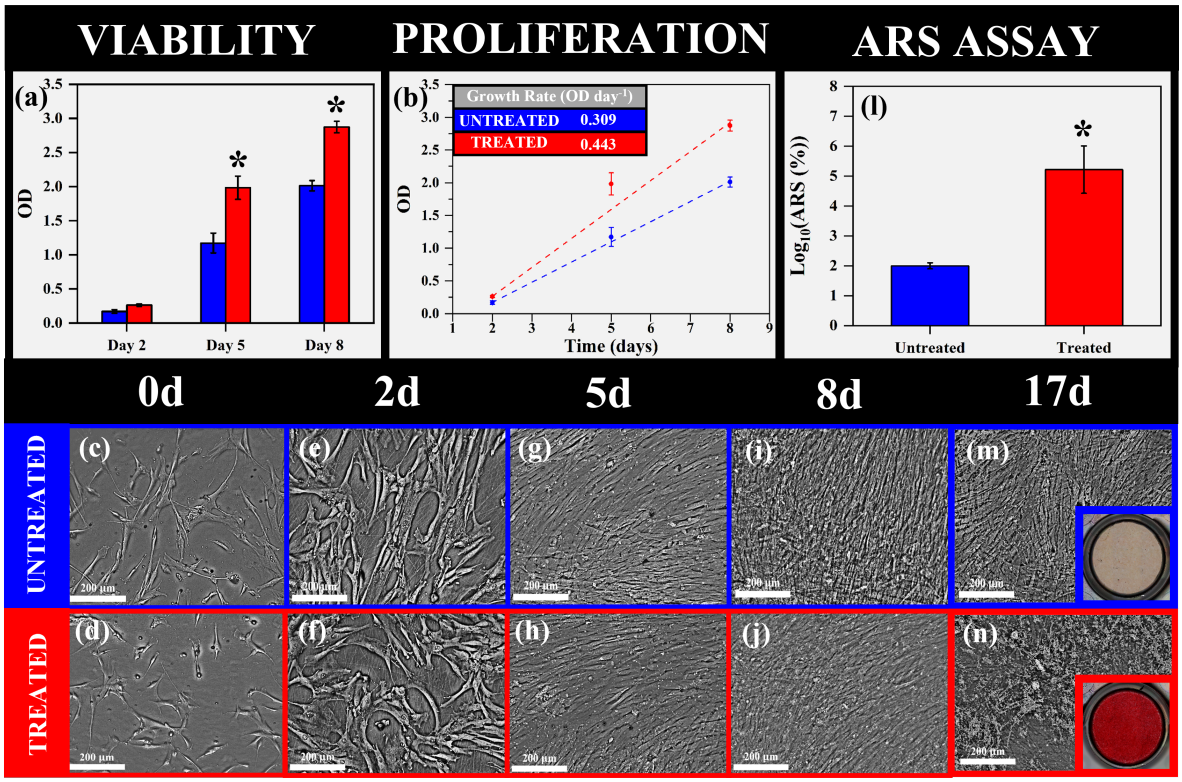

Figure 4.4.10: ODs for the (a) viability and (b) proliferation of hMSCs in standard growth media elucidated using the WST-8 assay after 2, 5, and 8 d of indirect exposure to FFF printed Ag-BG scaffolds. At each time point for the WST-8 assay, (c-j) optical images were captured to compare hMSC morphology between sample groups. Mineralization of osteoclasts was elucidated through the application of the Alizarin Red S (ARS) assay for both sample groups after 17 d of treatment in differentiation media. (m, n) Optical images were additionally captured to observe hMSC morphology with optical image inserts of the respective treated and untreated ARS-stained wells. (*) Denotes $p < 0.05$, when compared to both untreated and treated hMSCs at the respective time points, described previously.

Bone-Like Constructs, 2021 [295].

4.5.1 Structural characteristics

Structurally, the effectiveness of the applied non-aqueous synthesis conditions described in Section 3.2.4.1 was evaluated through the use of ^{1}H-NMR (Fig. 4.5.1a) to quantify the degree of methacryloyl substitution that occurred at the lysine groups present in gelatin as-receive using equation 3.3.5 [234]. The characteristic lysine peak observed between (+) 2.75 ppm and (+) 3.00 ppm chemical shift for gelatin as-received (Fig. 4.5.1a) was found to disappear after functionaliza-

tion with methacrylic anhydride (Fig. 4.5.1a) indicating a high degree of substitution. When the characteristic lysine peak for gelatin as received was integrated in addition to the remaining lysine peak after methacrylic anhydride functionalization, a ~100% degree of substitution (eq. 3.3.5) was elucidated, demonstrating that the applied non-aqueous GelMA synthesis was more effective at substitution compared to traditional aqueous-based (i.e. PBS) synthesis methods, known to achieve a maximum degree of substitution of 85% [296] increasing batch-to-batch variations. Furthermore, when GelMA-Ag-BG (GAB) hybrid hydrogels were characterized using ^{1}H-NMR (Fig. 4.5.1), the degree of substitution was found to be similar to the degree of substitution identified for GelMA (Fig. 4.5.1), as expected.

As previously described in Section 3.2.4.1, toluene was used to precipitate the synthesized GelMA and FTIR spectra (Fig. 4.5.1b) collected for gelatin, GelMA, and GAB and presented with the relevant FTIR spectra (Fig. 4.5.1b) for the reagents used during GelMA and GAB synthesis to evaluate the effectiveness of the toluene precipitation approach in removing the unwanted and cytotoxic reagents used. For the GelMA FTIR spectrum (Fig. 4.5.1b), characteristic amide I, II, and III groups were observed at ~1650 cm^{-1}, ~1500 cm^{-1}, and ~1450 cm^{-1} respectively [235]. Furthermore, FTIR peaks characteristic of methacrylic anhydride (MAA) and dimethyl sulfoxide (DMSO) were not observed for both GelMA and GAB, suggesting that the toluene precipitation approach was successful in extracting GelMA and GAB and preventing MAA and DMSO contamination. For GAB, the respective FTIR spectrum (Fig. 4.5.1b) did not present peaks characteristic to methanol (MeOH) or (3-Glycidyloxypropyl)trimethoxysilane (GPTMS), providing supporting evidence at the effectiveness of the toluene precipitation approach for removal of the cytotoxic reagents used. The FTIR spectrum of the Ag-BG sol (Fig. 4.5.1b) used during GAB synthesis presented with a stronger characteristic Si-O stretching peak ~1000 cm^{-1} [235] compared to GAB; however, this difference was expected given Ag-BG sol was molecularly coupled with GelMA as mediated by the coupling agent, GPTMS, at 3 weight percent. Interestingly, GAB presented with a broad spectroscopic peak from ~650 cm^{-1} to ~900 cm^{-1} (Fig. 4.5.1b) indicative of a characteristic Si-O bending peak [235] characteristic of amorphous Ag-BG providing additional

evidence to support the success achieved when using the toluene precipitation approach.

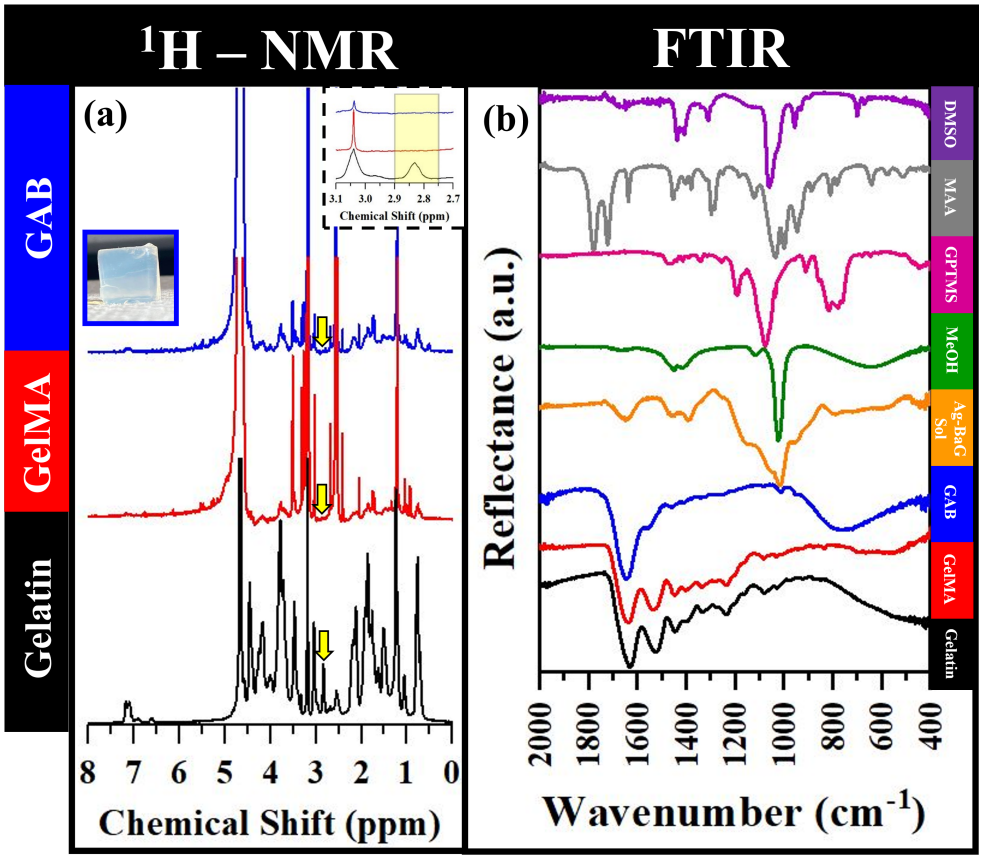

Figure 4.5.1: (a) ^{1}H – NMR spectra of gelatin (as-received), GelMA, and GAB. An optical image insert is additionally included to show the status of GAB hydrogels post-synthesis. The yellow arrows denote the characteristic lysine methylene signals used to determine the degree of methacrylation. Zoomed-in spectra insert is additionally shown from (+) 2.7 ppm to (+) 3.3 ppm for clarity. (b) FTIR spectra of the gelatin (as-received), GelMA, GAB, Ag-BG sol used during GAB synthesis, methanol (MeOH), the coupling agent (3-Glycidyloxypropyl)trimethoxysilane (GPTMS), methacrylic anhydride (MAA) used for the methacrylation of as-received gelatin, and dimethyl sulfoxide (DMSO) used as the solvent for the synthesis of GelMA and GAB.

SEM-EDS (Fig. 4.5.2) was performed for GelMA and GAB hydrogels to study their respective surface morphologies (Fig. 4.5.2a-b, g-h) and to assess elemental homogeneity (Figs. 4.5.2c-f and 4.5.2i-q. While both GelMA (Fig. 4.5.2b) and GAB (Fig. 4.5.2f) displayed evidence of a mesoscopic porous structure, both the pores and GelMA fibers were meso-sized, while GAB showed micro- and meso-sized pores and GAB fibers, where the GAB fibers (Fig. 4.5.2f) were found to be thicker compared to the GelMA fibers (Fig. 4.5.2h) observed. EDS X-Ray mapping for both GelMA (Fig. 4.5.2c-f) and GAB (Fig. 4.5.2i-q) revealed homogeneity of all expected elements

down to the micron-level. Important to note is that the application of the performed EDS X-Ray mapping is not commonly reported for GelMA or GelMA silicate-containing hydrogels, therefore the EDS X-Ray mapping presented in Figures 4.5.2c-d and 4.5.2i-q provides more comprehensive structural information down to the micron-scale, thus providing novel conclusive evidence that the synthesis approaches applied here was successful at maintaining elemental homogeneity down to the micron-level, thus both GelMA and GAB should respond homogenously when performance-based characterization is performed.

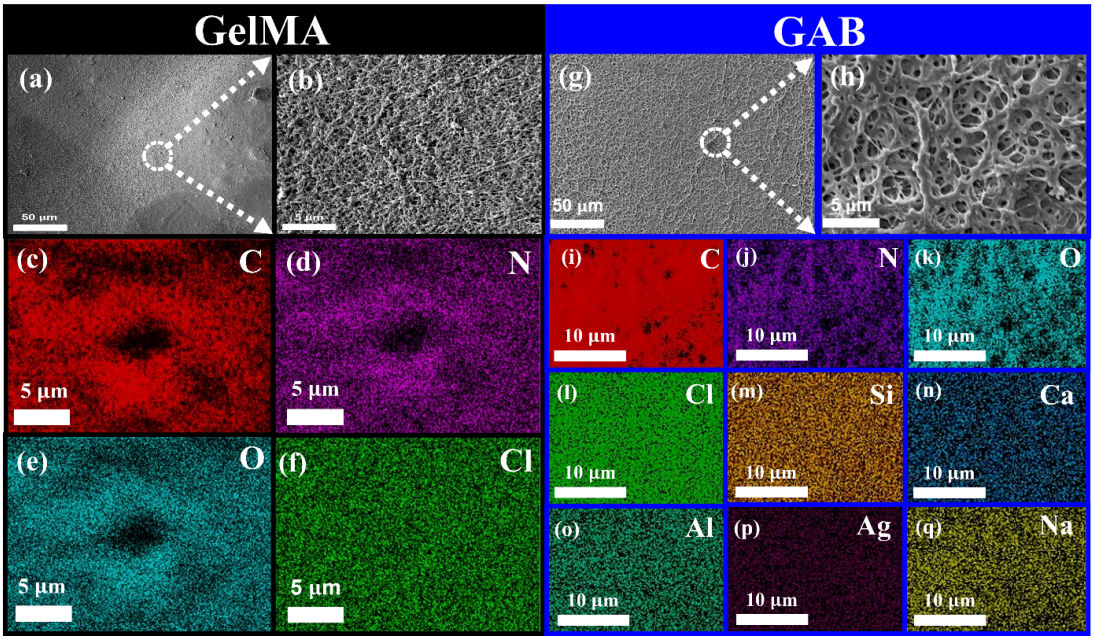

Figure 4.5.2: SEM images of (a, b) GelMA in addition to its respective EDS X-ray mapping, where (c) C, (d) N, (e) O, and (f) Cl were all observed to be homogenously distributed down to the micron level. Additionally, SEM images of (g, h) GAB and corresponding EDS X-Ray mapping showing that (i) C, (j) N, (k) O, (l) Cl, (m) Si, (n) Ca, (o) Al, (p) Ag, and (q) Na are also all homogenously distributed down to the micron-level.

4.5.2 Performance characteristics

Given the hydrogel characteristics of GelMA and GAB samples, it was necessary to study their swelling, pH, and mass loss behavior as a function of time evaluated up to 7 d of immersion in PBS (Fig. 4.5.3). Additionally, the performance characteristics of GelMA-Ag-BG nanocomposite hydrogels were evaluated to highlight their comparative differences with GAB. The swelling ratio

(Fig. 4.5.3a) was found to be inhibited for GelMA-Ag-BG nanocomposites and GAB hydrogels by a statistically significant margin when compared to the swelling ratio of GelMA hydrogels. The pH behavior of GelMA, GelMA-Ag-BG nanocomposite, and GAB hydrogels (Fig. 4.5.3b) was found to reach a maximum of ~7.7 and ~7.9 for GelMA and GAB hydrogels respectively after 1 d of immersion in PBS, whereas GelMA-Ag-BG nanocomposite hydrogels achieved a maximum pH of ~8.8 after 3 d of immersion in PBS. This difference in pH behavior between GelMA-Ag-BG nanocomposite and GAB hydrogels was correlated to the different incorporation processes applied. Furthermore, the mass loss for GelMA, GelMA-Ag-BG nanocomposite, and GAB hydrogels (Fig. 4.5.3c) was elucidated up to 7 d of immersion in PBS finding that the greatest mass loss was observed for GelMA hydrogels, while GAB hydrogels exhibited the least amount of mass loss when evaluated at consistent time points. The mass loss was found to be greater for GelMA-Ag-BG nanocomposite hydrogels compared to GAB hydrogels correlated to the different in Ag-BG incorporation methods applied.

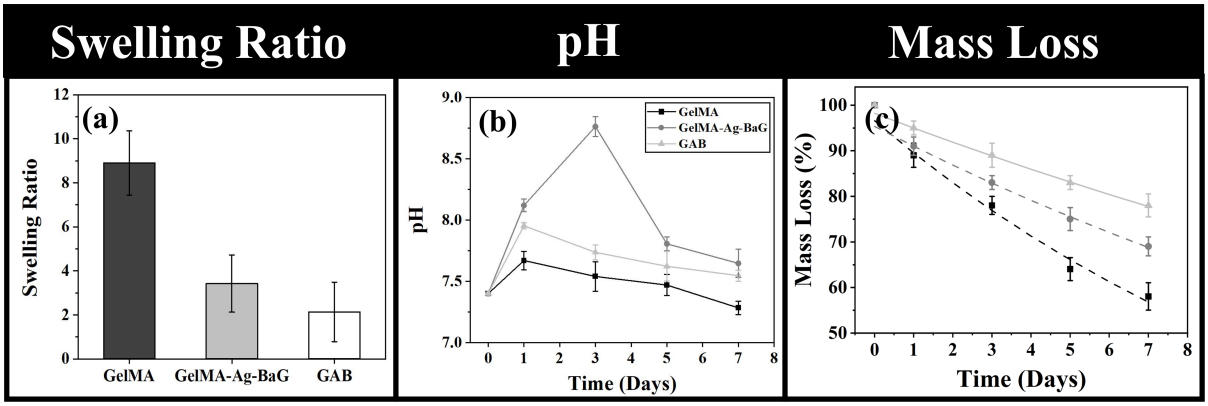

Figure 4.5.3: (a) The swelling ratio of GelMA, GelMA-Ag-BG nanocomposite, and GAB hydrogels. (b) The pH evolution of GelMA, GelMA-Ag-BG nanocomposite, and GAB hydrogels was evaluated after 1 d, 3 d, 5 d, and 7 d of immersion in PBS. (c) Presents the corresponding (c) mass loss for each time point characterized.

In terms of the antibacterial and biological performance of both GelMA and GAB (Fig. 4.5.4), the anti-MRSA effect of GAB was observed to expectedly elicit more potent anti-MRSA capabilities as the mass to volume ratio was increased (Fig. 4.5.4g). Additionally, GelMA was found to possess zero anti-MRSA capabilities, further demonstrating that the toluene precipitation approach was

successful at removing cytotoxic reagents used during synthesis. When examining fibroblast (3T3) viability after 72 h of incubation with either GelMA or GAB (Fig. 4.5.4a), either seeded on top of the hydrogel or homogenously distributed (embedded) within the hydrogel demonstrated an insignificant reduction in viability compared to the 2D untreated culture. This further supports the success of synthesizing both GelMA and GAB, using the toluene precipitation approach to remove the cytotoxic reagents being used. Optical images of embedded 3T3s in GAB (Fig. 4.5.4b-f) captured every 24 h supports the viability findings given that the population of 3T3s appears to increase at each time point. Furthermore, the observed mitosis of 3T3s and agglomeration into spheroid-like shapes suggest 3T3s are mobile and satisfied with the environment they were exposed to.

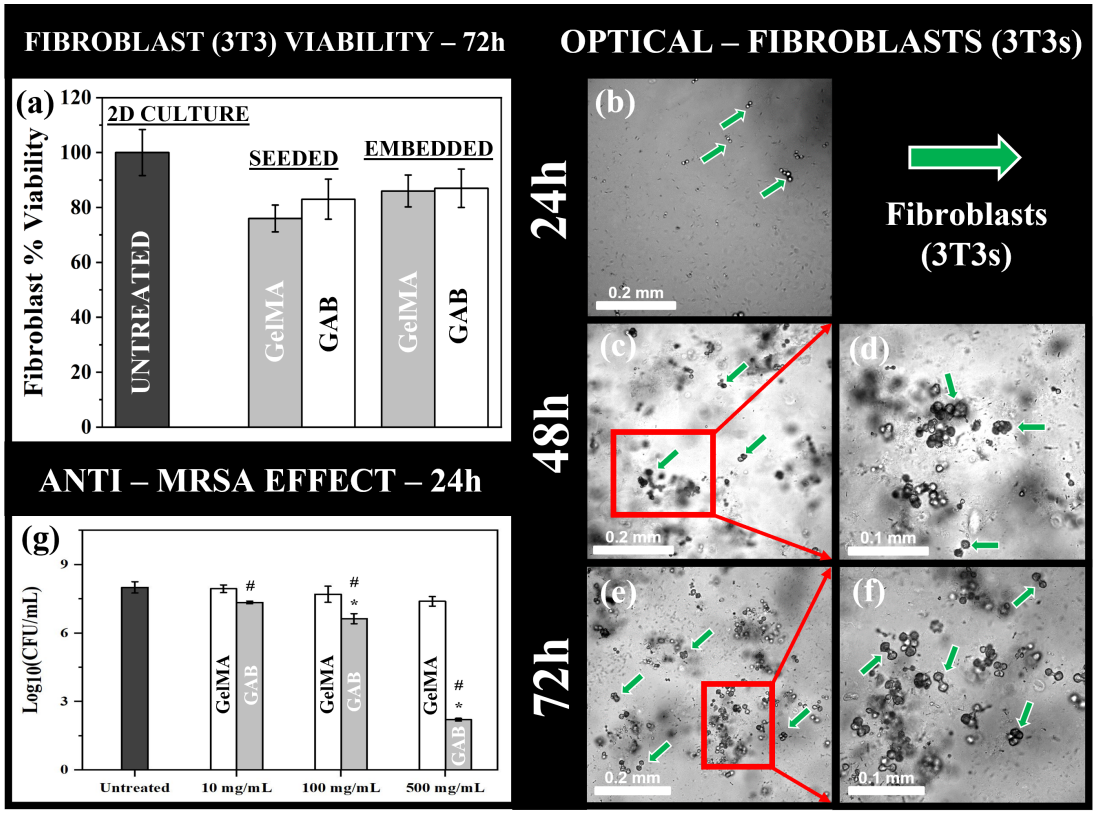

Figure 4.5.4: (a) Fibroblast (3T3s) viability on GelMA and GAB after 72 h of incubation, where 3T3s were either seeded on top or embedded (i.e. 3D homogenous distribution of 3T3s) for hydrogels. After (b) 24 h, (c-d) 48 h, and (e-f) 72 h of incubation, optical images of hydrogels embedded with 3T3s are shown. (g) The anti-MRSA effect of GelMA and GAB, where GelMA exhibited no anti-MRSA effects (as expected) while GAB exhibited increasingly potent anti-MRSA capabilities with increasing GAB concentration.

Rheological performance characterization, following the procedures detailed in Section 3.4.2.4, was performed to elucidate the storage (G′) and loss (G″) moduli in addition to evaluation of viscosity as a function of shear rate to determine whether the formed hydrogels would be compatible with 3D bioprinting. To start, the storage modulus (G′) describes the ability of a material to absorb deformation energy elastically while the loss modulus ((G″)) denotes the energy dissipated when deformation forces are removed. While GAB hydrogels were observed to have a storage (G′) and loss (G″) moduli (Fig. 4.5.5a) order(s) of magnitude greater than the values recommended from previous reports [202, 209], it is still expected that GAB will be suitable as a bioink for 3D bioprinting given previous reports used an extruder temperature of 4ºC [202, 209, 297, 298] for bioprinting GelMA bioinks. Therefore, the storage (G′) and loss (G″) moduli could be mediated through increasing extruder temperatures. The viscosity of GAB hydrogels (Fig. 4.5.5b) was found to exhibit shear-thinning behavior, an attractive characteristic for bioinks given that self-healing abilities can be expressed with the removal of shear forces. Using equation 3.4.7, GAB hydrogels were found to have a flow consistency index (K) and flow index behavior of 417±10 (Pa·s^n) and 0.045±0.007 respectively, where a correlation coefficient of 0.98 was noted when computed using the region where a linear decrease in viscosity as a function of shear rate (i.e. 1-10 s^{-1}; Fig. 4.5.5b) was observed. Given the minimal flow index behavior elucidated for GAB using Equation 3.4.7 provides quantitative evidence to suggest that GAB hydrogels are non-Newtonian fluids exhibiting shear thinning behavior.

Table 4.5.1: Experimental and literature values for the rheological properties of GelMA-containing bioinks.

Property	GAB Bioink 10% (w/v) GelMA			GelMA Bioink 10% (w/v) Literature			Recommended Values from Literature
Viscosity (Pa·s)	40,000	~1,000	~50	~300 [299]	~170 [299]	~40 [299]	0.3-60,000 [202, 209]
Shear Rate (s^{-1})	0.1	1	10	0.1 [299]	1 [299]	10 [299]	
Storage Modulus (Pa)		~75,000			~800-1,000 [246, 300]		100-1,000[202, 209]
Loss Modulus (Pa)		~20,000			~5-40 [246, 300]		

4.5.3 Optimization of 3D printing parameters for hybrid scaffolds

Figure 4.5.5c shows a successful extrusion of GAB 3D printed into a single layer scaffold-like geometry. This successful printing was achieved when an extruder pressure and temperature of 15 psi and 27ºC respectively were used, where GAB hydrogels were extruded through a 27-gauge metal-tapered tip and print velocity set to 4 mm s^{-1}. Interestingly, the extruder temperature used for GAB bioinks was 23ºC greater than reported temperatures for GelMA bioinks [202, 209, 297, 298] and is 10ºC cooler than the ideal physiological temperature (i.e. 37ºC) used for the incubation of cell-containing materials. Therefore, it would be expected that cell viability will be greater for GAB bioinks compared to GelMA bioinks given the proximity of the required extruder temperature needed for successful 3D bioprinting. Furthermore, it should be noted that GAB hydrogels exhibit more attractive characteristics for 3D bioprinting compared to GelMA hydrogels. This work additionally demonstrates for the first time 3D bioprinting of class II hybrid hydrogels comprised of GelMA and a multi-component bioactive glass composition (i.e. Ag-BG), thus circumventing the need to incorporate a multi-component bioactive glass composition using nanoparticles that are known to inhibit cell viability when 3D bioprinting given the additional shear forces exhibited by the presence of nanoparticles during extrusion.

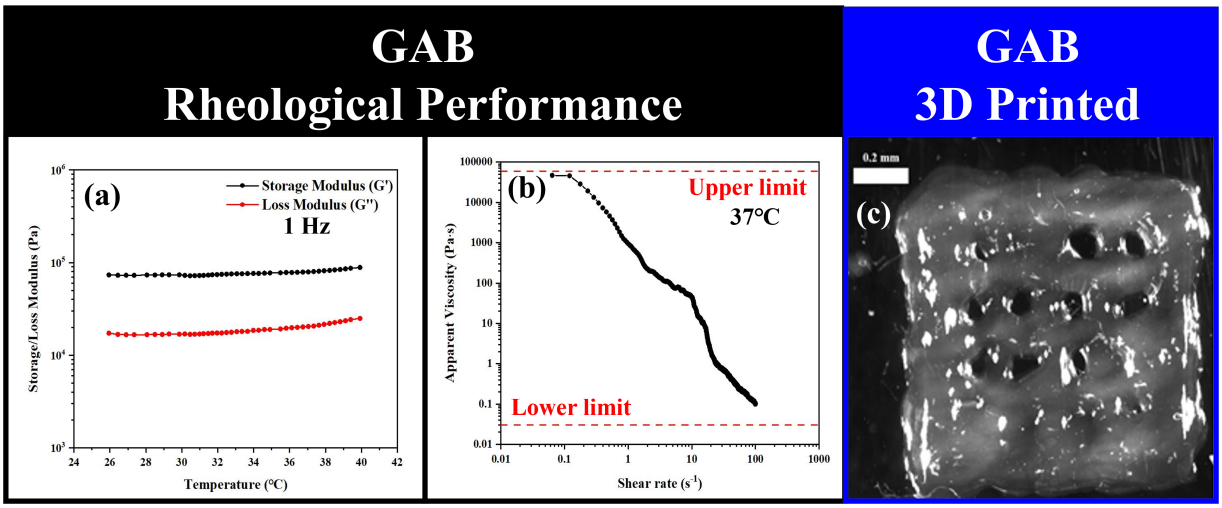

Figure 4.5.5: (a) The storage (G′) and loss (G″) moduli for GAB hydrogels as a function of temperature ranging from 25°C to 40°C oscillating at 1 Hz. (b) The apparent viscosity of GAB hydrogels as a function of shear rate showing GAB exhibits shear thinning behavior. (c) A single mesh layer successfully 3D printed using GAB hydrogels.

CHAPTER 5

DISCUSSION

5.1 Structural evolution of Ag-BG

5.1.1 Insights from thermal behavior characterization

Study of the thermal behavior of as-received Ag-BG micro-sized particles (Fig. 4.1.1) elucidated modest glass formability when computing the Hrubý coefficient (Eq. 4.1.1); however, this approach was unable to fully account for the observed thermal behavior of as-received Ag-BG micro-sized particles (Fig. 4.1.1). Illumination of the sintering characteristics was crucial for the identification of the sintering conditions that should be applied for the heat treatment of Ag-BG scaffolds to elicit preferential structural characteristics to deliver mechanically competent Ag-BG scaffolds whilst maintaining their advanced antibacterial and biological performances. Previous reports have demonstrated large variations exist for the sintering mechanisms for bioactive glass systems, where either viscous sintering or densification through crystallization had occurred during heat treatment.

For example, the most well-known bioactive glass composition (45S5; $45SiO_2$ – $24.5CaO$ – $24.5Na_2O$ – $6P_2O_5$ (wt%)) strongly exhibits crystallization behavior [257] transforming the initial amorphous structure to crystalline combeite ($Na_2Ca_2Si_3O_9$) achieving a maximum crystallinity of ~77% [25] during densification rather than displaying a viscous sintering mechanism whereas 13-93 bioactive glass ($53SiO_2$ – $20CaO$ – $12K_2O$ – $6Na_2O$ – $5MgO$ – $4P_2O_5$ (wt%)) undergoes viscous sintering [58] preserving the amorphous structure expected to enhanced biological performance given the lack of long-range order and increase in free volume compared to ceramics. 13-93 was able to maintain its amorphous structure during heat treatment due to an increase in glass formers (i.e. SiO_2) and the addition of K_2O known to inhibit crystallization tendencies of complex silicate-based compositions (i.e. bioactive glass) [29, 66, 301, 302].

It is “ideal”, therefore, given the previously described compositional dependencies for bioactive

glass systems for Ag-BG to form a glass-ceramic during sintering to deliver Ag-BG glass-ceramic scaffolds to improve mechanical performance [303–305] whilst preserving the biological and antibacterial performance characteristics previously reported for as-received Ag-BG micro-sized particles [31, 32, 34–37, 54, 55]. This, however, was not observed for Ag-BG (Fig. 4.1.1a), where even though the "ideal" processing window (i.e. T_g to $T_{c,\ onset}$) was identified between ~450°C to ~700°C, HSM (Fig. 4.1.1b-j) demonstrated Ag-BG cannot undergo the needed densification within this temperature range. This was corroborated with the unacceptable mechanical performance observed for Ag-BG solution scaffolds (Fig. 4.2.6a). When the thermal behavior of as-received Ag-BG micro-sized particles was described using the sinterability equation (Eq. 4.1.2), the large negative value observed after this computation suggested Ag-BG has a high viscosity and low surface tension leading to crystallization rather than viscous sintering agreeing with previously described experimental evidence herein. Given the unavoidability of incurring crystallization of Ag-BG during heat treatment of Ag-BG scaffolds, it was advantageous to explore the thermal behavior at high temperatures (i.e. T > 700°C) to identify what phases have formed or transformed to manipulate the crystalline phases produced to maximize antibacterial and biological performance.

5.1.2 Evolution of Ag-BG structure as a function of temperature

Herein, a mechanistic description is provided to describe the structural evolution of Ag-BG as a function of temperature to account for all elements present in Ag-BG given the absence of Al or Na containing phases.

To start, bioactive glasses such as Ag-BG synthesized by the sol-gel technique have a propensity to begin undergoing crystallization of hydroxyapatite beginning at ~500°C due to the effect processing parameters, such as stirring rate, that is known to increase the resulting crystallinity of such system [45, 49, 50, 257]. Melt-derived bioactive glasses do not exhibit such crystallization behavior as the quenching rate of the molten glass is sufficiently fast to avoid crystallization as there was insufficient time for atomic mobility within the cooling glass, thus delivering bioactive glasses having an amorphous structure [303]. Regardless, the crystallization of HA for sol-gel-derived

systems such as Ag-BG occurred as a result of phase separation between Si and P atoms when sintered in air at temperatures exceeding 500°C [306]. As this phase separation continues as a function of increasing temperature, local regions having sufficient concentrations of P to promote HA, or more precisely Ca-deficient HA crystallization [307]. The following equation (Eq. 5.1.1), generalizes the reactions between Ca and P atoms during crystallization, where all P atoms are assumed to have been consumed [307].

$$10CaO + 3P_2O_5 + H_2O \rightarrow Ca_{10}(PO_4)_6(OH)_2 \tag{5.1.1}$$

Interestingly, as temperatures continue to increase, $[AlO_4]^-$ molecules appear to become less effective at maintaining the stability of Ag^+ ions leading to the formation of AgNPs instead. The purpose of incorporating Al into Ag-BG was to preserve Ag^+ ions by $[AlO_4]^-$ molecules for enhanced antibacterial performance, and since this was not the case (Figs. 4.2.1a-b, 4.2.3a, 4.2.5, 4.3.4b, and 4.3.6e-f), an explanation was necessary.

Consider the ternary SiO_2 – Al_2O_3 – Ag_2O glass system, where Ag^+ ions were demonstrated to remain stable up to 1100°C behaving as a charge compensator for $[AlO_4]^-$ molecules to maintain electroneutrality before crystallization was observed [51–53, 308], where the release of Ag mechanistically switches from being predominantly Al-mediated to Si-mediated. Regardless, the presence of Si, Al, and Ag cannot be correlated to the observed disruption of Ag^+ ion stabilization by $[AlO_4]^-$ molecules, therefore it must be either Ca^{2+} and Na^+ cations present, creating a competition between cations for electrically neutralizing $[AlO_4]^-$ molecules. Examining this cation competition at sintering temperatures of 900°C and 1000°C respectively from a thermodynamical perspective, the Gibbs free energy of $Ca(AlO_4)_2$, $NaAlO_4$, and $AgAlO_4$ were computed and presented in Table 5.1 [223]. Based on the thermodynamic calculations presented in Table 5.1, it would be expected that all Ag^+ cations would be displaced by Ca^{2+} atoms forming AgNPs that should have accounted for all Ag present in Ag-BG when performing Rietveld analysis (Table 4.2.2). Since this was not the case for Ag-BG scaffolds, other explanations had to be investigated.

Considering the difference in atomic size between Ag^+ and Ca^{2+} cations, the size of Ca^{2+}

Table 5.1.1: The Gibbs free energy of $AgAlO_4$, $Ca(AlO_4)_2$, and $NaAlO_4$ molecules were computed at 900°C and 1000°C.

Temperature (°C)	$AgAlO_4$	$Ca(AlO_4)_2$	$NaAlO_4$
900	-686.0	-2049.9	-643.9
1000	-685.7	-2039.7	-637.5

cations (i.e. 1.14 Å) was found to be ~12% smaller than Ag^+ ions (i.e. 1.29 Å) [40]. It is plausible, therefore, that the smaller size of Ca^{2+} cations allows for greater atomic mobility at sufficiently high temperatures (i.e. T > 800°C), however, the size difference between Ca^{2+} and Ag^+ ions is thought to have a weak effect on disrupting the status of Ag. Examination of the field strengths of Ca^{2+} (i.e. 0.31 $Å^{-2}$) and Ag^+ (i.e. 0.14 $Å^{-2}$) cations found that the field strength of Ca^{2+}cations was ~55% stronger compared to Ag^+ cations [40], thus providing a stronger argument for justifying Ag^+ cation displacement by Ca^{2+} cations. Indeed, the 55% increase in field strength for Ca^{2+} cations comparatively presents an effective pathway for Ca^{2+} cation substitutions with Ag^+ cations in the presence of free electron sources (i.e. residual H_2O and residual Si-OH condensation reactions), as shown in Equation 5.1.2 [309].

$$AgAlO_4 + Ca(SiO_4)_2 + e^- \rightarrow Ca(AlO_4)(SiO_4) + Ag^0 + SiO_4 \quad (5.1.2)$$

Interestingly, equation 5.1.2 reports $Ca(AlO_4)(SiO_4)$ as a product of the substitution reaction rather than $Ca(AlO_4)_2$, as previously described by Table 5.1.1, when taking into consideration the L*ö*wenstein Al-avoidance principle [310, 311] stating that Al-O-Al linkages do not exist in aluminosilicates, but rather Al-O-Si linkages, demonstrating the avoidance behavior of Al atoms. It must be noted, however, that recent reports have shown that the L*ö*wenstein Al-avoidance principle can be violated when the Al/Si ratio exceeds 1 [310, 311]. Since Ag-BG has an Al/Si ratio of ~0.08, it was expected that the Löwenstein Al-avoidance principle would be followed, therefore accounting for the reaction product of $Ca(AlO_4)(SiO_4)$ over $Ca(AlO_4)_2$.

While the Ag^0 observed as a reaction product of equation 5.1.2 can account for the observed changes in chromaticity for Ag-BG solution scaffolds (Fig. 4.2.1a, b), it cannot describe the chro-

matic shift observed between Ag-BG solution (Fig. 4.2.1a, b) and slurry (Fig. 4.2.1c, d) scaffolds. Previous reports have shown that the presence of reduced Ag in a silica-rich matrix promotes the formation of AgNPs [309]. When AgNPs are surrounded by a silica-rich matrix, AgNPs perturb this silica-rich matrix by decreasing the energy required for oxygen vacancy formation [309]. Due to the local increase in oxygen vacancies, the system attempts to maintain its lowest energy state through crystallization leading to the AgNPs becoming embedded in crystalline silica. Regardless of the scaffold processing conditions applied to deliver Ag-BG scaffolds, all conditions produced cristobalite as the crystalline silica phase (Figs. 4.2.3b, 4.3.4b, and 4.4.3b).

The presence of reduced Ag promotes the formation of AgNPs, which then act to perturb the surrounding silica matrix through a decrease in the energy required for oxygen vacancy formation [309]. Because of this, the silica matrix begins to crystallize around the AgNPs to maintain its lowest energy state, causing AgNPs to become embedded within a crystalline silica matrix. The effect of this embedment was studied by Pegliara et al. who elucidated that the maximum thickness of the embedment cannot exceed 7 nm, as any thickness greater than this prevents the release of Ag [312], thus preventing the material from exhibiting antibacterial properties. Considering the Ag ion release profile for FFF printed Ag-BG scaffolds (Fig. 4.4.7f), it was hypothesized that the thickness of the embedded AgNPs is likely ~6 nm to ~7 nm.

Intriguingly, it should be noted that bulk Ag has a melting point of ~962ºC [56], which is below the sintering temperatures applied to deliver Ag-BG slurry and FFF printed Ag-BG scaffolds, so it would have been expected that Ag would melt during heat treatment. Furthermore, since Ag was identified as AgNPs, their melting point should be depressed. Mathematically, this was demonstrated to be true in the derivation of the Gibbs-Thompson equation (Eq. 5.1.5) [313, 314] using the Clausius-Clapeyron relation (Eq. 5.1.3) [314, 315] and Young-Laplace equation (Eq. 5.1.4) [314, 316]. In the Clausius-Clapeyron relation (Eq. 5.1.3), ΔS^* describes the difference in entropy between two phases (i.e. α and β), ΔV^* represents the difference in volume between α and β, T is the temperature in Kelvin, P^β describes the pressure being experienced by the β-phase, and γ^α , V^α, and k^α represent the surface tension, volume, and curvature of the α-phase respectively.

In the Young-Laplace equation (Eq. 5.1.4), γ^{α} and k^{α} describes the surface tension and curvature of the α-phase respectively, assuming the β-phase is infinitely large. In the Gibbs-Thompson equation (Eq. 5.1.5), ${T_m}^{nano}$, ${T_m}^{bulk}$, and ΔH^* represent the melting point of a nanoparticle, the bulk melting point of a material, and the difference in enthalpy respectively with all other variables being previously defined by equations 5.1.3 and 5.1.4. Therefore, according to the Gibbs-Thompson equation (Eq. 5.1.5), the AgNPs should have melted during sintering; however, experimentally, this was not observed given the detection of AgNPs in all Ag-BG scaffolds studied herein.

$$\Delta S^* dT - \Delta V^* dP^{\beta} + 2\gamma^{\alpha} V^{\alpha} k^{\alpha} = 0 \qquad \text{(5.1.3 [314, 315])}$$

$$\Delta P^* = 2\gamma^{\alpha} k^{\alpha} \qquad \text{(5.1.4 [314, 316])}$$

$$T_m^{nano} = T_m^{Bulk} - \frac{2T_m^{Bulk}\gamma^{\alpha} V^{\alpha} k^{\alpha}}{\Delta H^*} \qquad \text{(5.1.5 [313, 314])}$$

To reconcile the disagreement between the Gibbs-Thompson equation (Eq. 5.1.5) and the experimental evidence presented previously (Figs. 4.2.1a-b; 4.2.3a; 4.2.4g, m; 4.2.5a, e, c; 4.2.7; 4.3.3e; 4.3.4b; 4.3.5g; 4.3.6e-f; 4.3.8; 4.4.4h; 4.4.7f; 4.4.8; and Table 4.2.2) alternative explanations needed to be explored. Previous reports have demonstrated that the embedment of AgNPs in cristobalite only occurs when surface defects are present on the surface of an AgNP in proximity to an oxygen vacancy within cristobalite [288, 289]. The presence of such defects increases the local free energy that results in the breakage of a Si-O bond for an Ag-Si and Ag-O bond when the system attempts to return to its lowest energy configuration, thus creating a viable pathway for Ag to enter cristobalite [288, 289]. This interdiffusion mechanism, however, is slow given Ag diffusion is limited by oxygen vacancy diffusion within cristobalite, where the accumulation of Ag is proportional to the concentration of oxygen vacancies present [288, 289]. Through this process, AgNPs can form defect-free surfaces that result in a significant increase in thermal stability well beyond the expected melting points, thus accounting for the presence of Ag when sintering temperatures above the melting point of Ag are used.

While most of the phenomena observed during structural characterization of as-received Ag-BG and Ag-BG scaffolds have been accounted for, the appearance of cristobalite at temperatures as low as 700ºC remains elusive. According to the silica phase diagram presented in Figure 5.1.1 [317], cristobalite should not appear until temperatures exceed 1,500ºC, which was an impossibility for Ag-BG considering the melting point was experimentally observed to occur ~1450ºC (Fig. 4.1.1a, b). To explain this, consider a complex system such as Ag-BG whose complexity arises from its hepta-elemental composition (Table 3.1.2). Such complex systems are not well-described by classical nucleation theory (CNT) given CNT underestimates the nucleation rate by an order of over 1 nonillion (10^{30}) cm^{-3} s^{-1} to 10 septendecillion (10^{55}) cm^{-3} s^{-1} [303]. To provide some context to this underestimation, 30 orders of magnitude difference is equivalent to the difference between 10 μm and the Planck length, while 55 orders of magnitude difference is equivalent to the difference between 1 kg and the mass of the observable universe.

To address this absurd underestimation, Wilhelm Ostwald considered possible non-CNT pathways for nucleation observing that subcritical nuclei (i.e. embryos) will evolve during the crystallization process ephemerally forming metastable phases from the highest possible energy configuration until the system reaches its lowest energy configuration (i.e. Ostwald's step rule) [303, 318]. For crystalline silica, the Gibbs free energy of cristobalite, tridymite, and quartz are -854±1.92 kJ mol^{-1}, -854±2.43 kJ mol^{-1}, and -856±1.72 kJ mol^{-1} respectively [319]. Given that the error for all three crystalline phases is within the same range, energetically speaking there is no discernable difference between which crystalline phase forms, thus warranting an alternative approach. Examining the effect the elements present in Ag-BG have on stabilizing crystalline silica, previous reports have demonstrated that the presence of both Ag and Al are known to stabilizers cristobalite [33, 320, 321]. It should be noted, however, that Chatzistavrou et al. demonstrated that at a fixed concentration of Al, the absence of Ag led to no formation of cristobalite, whereas increasing concentrations of Ag led to increased formation of cristobalite, suggesting that Ag is the predominant stabilizer element for cristobalite [33].

If it is assumed that Al has a negligible stabilizing effect on cristobalite, as demonstrated

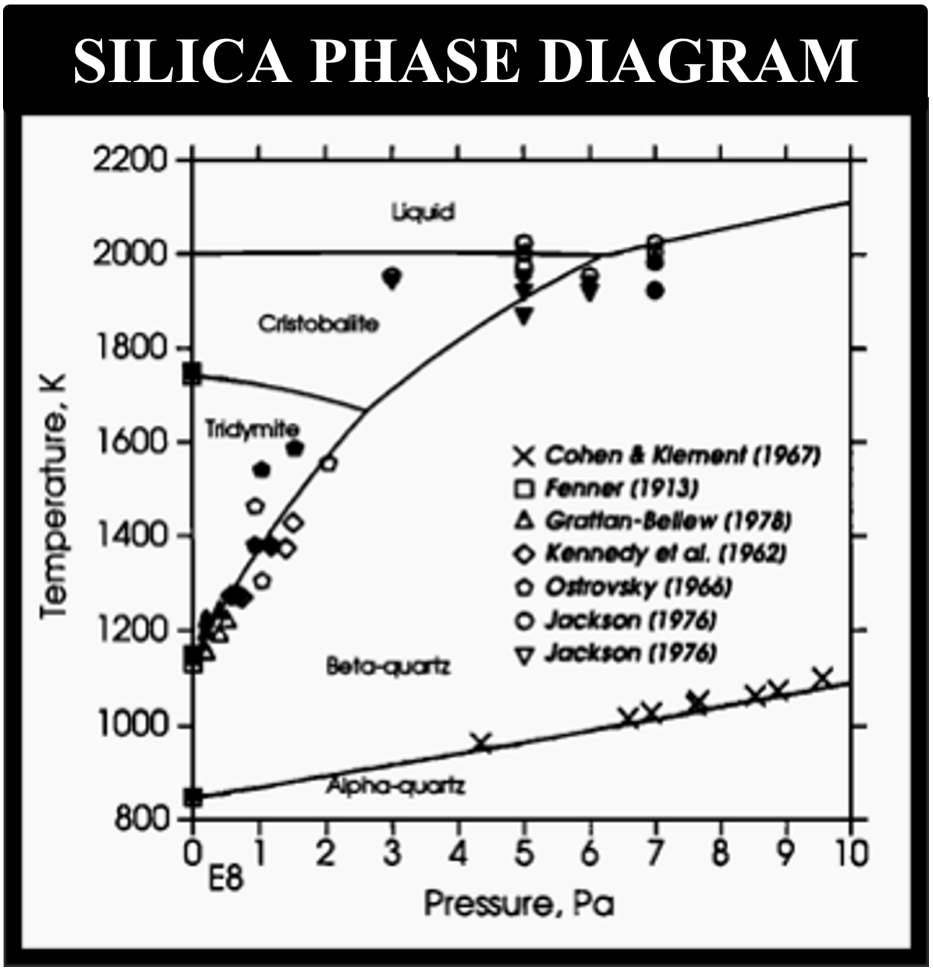

Figure 5.1.1: Phase diagram of silica as presented unaltered from Figure 4 published by Swamy et al. entitled "A thermodynamic assessment of silica phase diagram" [317]. The original figure caption is additionally presented for convenience: "Calculated phase equilibrium relations among α-quarts, β-quartz, tridymite, cristobalite, and liquid silica. The experimental data from Cohen and Klement [1967] represent α-quarts = β-quartz. Data from Jackson [1976] are on silica glass (open circles), β-quartz (solid circles), and cristobalite (solid triangles). The open and solid symbols from the other sources represent half-brackets on opposite sides of each equilibrium" [317].

by Chatzistavrou et al. [33], then both Al and Na remain unaccounted, therefore necessitating investigations into their whereabouts. Previous reports have shown that both Al and Na influence the formation of W. 2M [223, 322–324]. Indeed, Al and Na can substitute with Si and Ca atoms respectively in a W. 2M unit cell given the similarities between atomic radii [323]. Not only has Na been reported to act as a nucleating agent for W. 2M due to the ability of Na to decrease the energy required for W. 2M formation [322], while Al, in the concentrations used for Ag-BG scaffolds,

promotes W. 2M formation [223, 324], but also the presence of Ca-deficient HA in conjunction with a residual amorphous phase also act as W. 2M nucleating agents [223, 322, 324]. Therefore, there are multiple opportunities for Al and Na to be consumed during W. 2M formation. When computing theoretical phase concentrations to compare with Rietveld analysis (Table 4.4.1), the only way to reconcile the theoretical W. 2M concentration with the Rietveld analysis is to include both Al and Na into the calculation. It is important to note that when Ca-deficient HA transforms to β-TCP in the presence of excess silica, additional W. 2M can be formed, thus providing even more opportunities for Al and Na to be consumed during W. 2M formation [307, 325]. Considering all the different phenomena explored in Section 5.1.2, this allowed for a full description of the various thermally dependent events observed for both Ag-BG and Ag-BG scaffolds.

5.2 Process—Structure—Performance relationships

Ultimately, as previously described in Chapter 1, the delivery of Ag-BG scaffolds suitable for targeting bone tissue regeneration in load-bearing applications was approached in a multi-disciplinary manner aimed at elucidating process–performance relationships, utilizing structural characteristics to bridge this gap. The applied general scheme is shown in Figure 5.2.1, illustrating the relationships between process – structure – and performance to achieve the aforementioned aims.

5.2.1 Effects of Ag-BG scaffold processing on delivered structures

Two fundamentally different avenues for Ag-BG scaffold synthesis were explored in this dissertation: (1) polymer foam replication technique, and (2) fused filament fabrication for delivering scaffolds having competent mechanical, antibacterial, and biological performance for targeting bone tissue regeneration in load-bearing applications. The process–structure relationships illuminated shall be explored herein (Fig. 5.2.1).

Porosity on the macro, milli, micro, and meso scales all play a role in dictating the in vitro performance of 3D scaffolds targeting bone tissue regeneration, however, Section 5.2.1 will examine

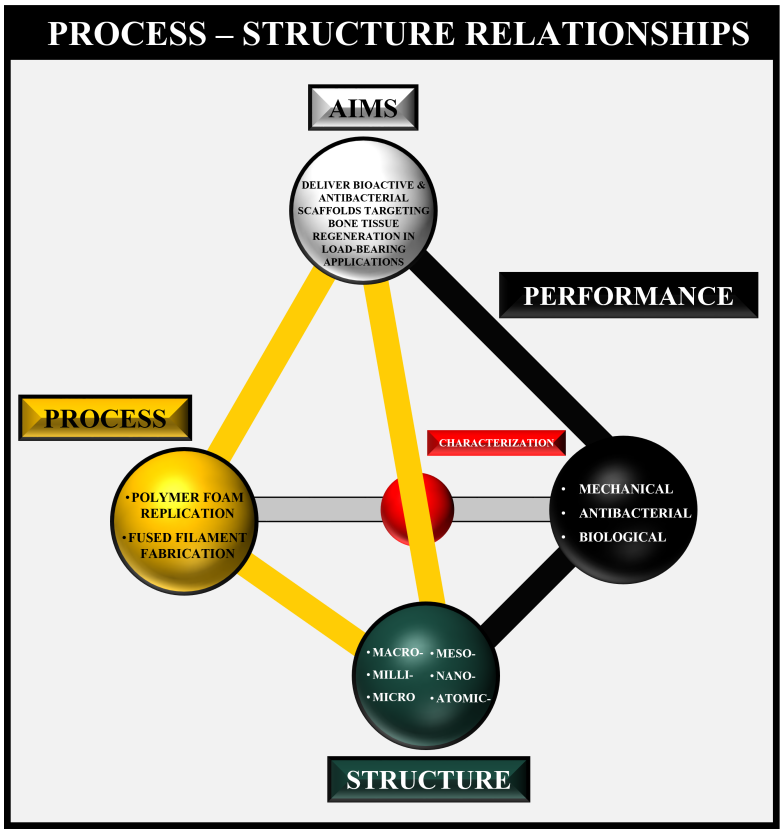

Figure 5.2.1: Figure highlighting the triangular aims – process – structure face of the tetrahedron being examined in Section 5.2.1.

the structural effects of the polymer foam replication and FFF processing techniques had on the delivered structures.

For the polymer foam replication technique, while both Ag-BG solution and slurry scaffolds exhibited high porosity (i.e. > 90%), the Ag-BG solution scaffolds presented the strongest evidence of having microporosity (Figs. 4.2.1f, 4.2.4a) as a result of synthesizing Ag-BG solution scaffolds using the sol-gel technique. The observed micro-porosity in Ag-BG solution scaffolds can be correlated to the aging and drying steps applied in the heat treatment described in Figure 3.1.1. While Ag-BG is still in the solution stage, hydrolysis produces ethanol as a byproduct of the hydrolysis reaction between TEOS and water in addition to the desired silanols (Eq. 2.1.1), while the condensation reaction (Eq. 2.1.2) sees the silanol groups condense into a silica network producing water as a byproduct. During the aging step of the applied heat treatment (Fig. 3.1.1), the ethanol groups congregate in the pores produced by the evaporation of volatile molecules present,

creating a pore liquor with the drying stage removing the remaining water present [75, 77, 78]. After drying, some of the micro-sized pores remain that are retained during the calcination and thermal stabilization processes (Fig. 3.1.1), delivering materials having a high degree of surface area (i.e. > 100 m^2 g^{-1} [50]) leading to higher dissolution rates as a result. Given this, only the process applied for the solution technique (Fig. 3.2.1) to deliver Ag-BG scaffolds was capable of maintaining the micro-sized pores developed using the sol-gel technique. The slurry technique nor the FFF technique was capable of maintaining the micro-sized pores as the sintering temperatures used to deliver mechanically competent Ag-BG scaffolds resulted in their destruction due to the densification processes that occurred during sintering. It is important to note that while micro-sized pores were observed in FFF printed Ag-BG scaffolds (Fig. 4.3.2, 4.3.3, 4.3.5, 4.4.1, and 4.4.4), this was found to be an effect of the particle size distribution used and not of the process used to synthesize the Ag-BG itself. Continued discussion of multiscale porosity will be explored further regarding their effect on performance in Section 5.2.2.

Comparing now the differences in the processes applied to deliver Ag-BG solution (Fig. 3.2.1) and slurry (Fig. 3.2.2) scaffolds, micro-CT investigations revealed (Fig. 4.2.2) more frequent breakages for Ag-BG solution scaffolds when studying their 1 mm thick 3D reconstructed cross-sections, suggesting that the slurry technique was more successful at loading Ag-BG onto the polyurethane foam template used. This claim was supported by the differences in porosity, pore size, strut thickness, and apparent density (Table 4.2.1), where Ag-BG slurry scaffolds had a ~3% decrease in porosity, ~17% reduction in pore size, ~37% increase in strut thickness, and a ~60% increase in apparent density comparatively. These differences were correlated to the greater viscosity the Ag-BG slurry had compared to the Ag-BG sol, thus allowing more mass to be loaded. All these factors played a role in the resulting mechanical performance of both Ag-BG solution and slurry scaffolds and will be explored further in Section 5.2.2.

Regarding the crystallinity of the Ag-BG scaffolds delivered, only Ag-BG solution scaffolds were capable of delivering a scaffold having a glass-ceramic structure. This was due to the use of Ag-BG in the solution stage, as the slurry and FFF techniques saw the Ag-BG particles used to

undergo a second heat treatment at significantly higher temperatures, providing ample opportunities for crystallization to occur. While it was demonstrated using Ag-BG slurry scaffolds that the phase concentrations could be manipulated to elicit phases more conducive to antibacterial and biological performance, this was demonstrated to not be the predominant structural factor dictating scaffold performance.

Further considering the effect of the applied processes on the delivered Ag-BG scaffold structures, the strongest correlation observed was the change from using a unimodal distribution of Ag-BG particles versus a bimodal distribution of Ag-BG particles. To start, the successful implementation of FFF for delivering pristine Ag-BG scaffolds demonstrated for the first time that silicate-based 3D scaffolds could be synthesized using FFF technology [221]. The demonstrated success, however, resulted from the proper application of the shaping, debinding, and sintering processes [185], where structural integrity was maintained. The desired 3D scaffold structure was able to be maintained due to the solvent debinding process applied before thermal debinding, engineering temporary micro-pores to create channels allowing for an escape route for the thermally decomposing polymeric components within brown body Ag-BG scaffolds. This was the first key to unlocking the full potential of FFF printing 3D scaffolds targeting bone tissue regeneration in load-bearing applications.

The second key was found to be the particle size distribution used during filament synthesis. Our initial work with synthesizing Ag-BG scaffolds using FFF, as previously described, used a unimodal distribution of Ag-BG particles, whose average size was ~29 μm. As observed in the optical and micro-CT images (Figs. 4.3.2, and 4.3.3), internal voids and defects were found to be plentiful. The amount of such porous defects was so great that they limited the sintering conditions that could be applied. Sintering these Ag-BG scaffolds using the unimodal distribution of Ag-BG particles previously described could only be performed up to 900ºC for 2 h, as any increase in temperature or time resulted in catastrophic structural collapse. Considering sintering mechanics, pores will either grow or shrink during the sintering process depending on the balance of forces described by the dihedral angle (ψ), specific grain boundary energy (γ_{gb}), and the specific surface

energy (γ_{sv}), as shown in equation 5.2.1 [286].

$$\cos(\frac{\psi}{2}) = \frac{\gamma_{gb}}{2\gamma_{sv}} \qquad \text{(5.1.4 [286])}$$

Qualitatively, based on experimental evidence, demonstrates that the pore surfaces are lively convex, having a positive curvature, thus increasing in size. This positive surface curvature results from the pores having a large pore coordination number resulting from a large number of surrounding grains. To reverse this trend, the FFF process required modifications so that the balance of forces favors pores having concavity, thus minimizing the number of internal porous defects during sintering.

To elicit the necessary conditions to deliver well-densified Ag-BG scaffolds, it was hypothesized that improvement in the packing efficiency of Ag-BG particles could produce the desired effects. The effect of packing efficiency achieved by exploring different particle size distributions has been well-documented in other fields of study such as its effect on resulting rheological properties [192–198], effects on optimizing pigment color in paint formation [326], and in the development of high-strength concrete [327]. In a consensus amongst the different fields of study previously mentioned, the use of a multimodal distribution of particles led to improvement in their packing efficiency, allowing for their aimed improvements to be achieved. Therefore, it was postulated that using a bimodal distribution of Ag-BG particles would deliver Ag-BG scaffolds minimizing the number of porous defects present in their internal structures.

This was indeed the case, as using a bimodal distribution of Ag-BG particles (Table 3.2.3) minimized the number of porous defects produced, as evidenced by micro-CT investigations (Fig. 4.4.2). This result was achieved, as the smaller sized Ag-BG particles were able to occupy the voids between the larger Ag-BG particles, thus decreasing the size of pores formed and preferentially changing the balance of forces to minimize the number of convex pores formed and allowing for greater sintering conditions to be applied while maintaining structural integrity that should translate to a significant increase in mechanical performance.

5.2.2 Effects of structure of Ag-BG scaffolds on performance

With the effects of each Ag-BG scaffold synthesis process applied herein elucidated, the structural–performance relationships could be identified and compared to the desired aims to determine the degree of success achieved.

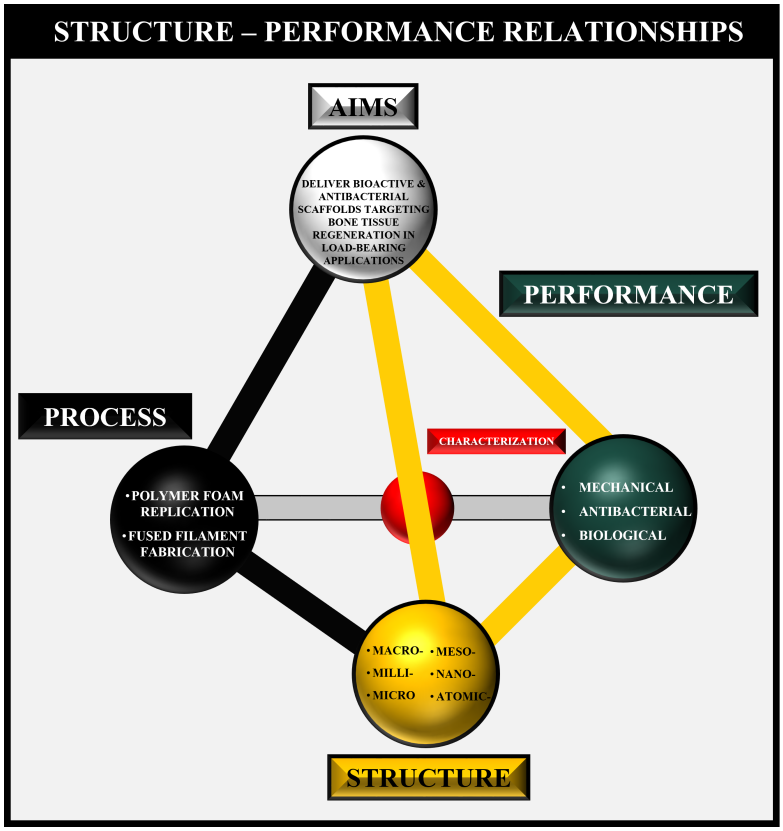

Figure 5.2.2: Figure highlighting the triangular aims – structure – performance face of the tetrahedron being examined in Section 5.2.2.

As previously described, the porosity of 3D scaffolds is known to have a strong effect on the resulting mechanical performance. This was no different for Ag-BG scaffolds explored herein. Starting with the compressive behavior of Ag-BG solution and slurry scaffolds (Fig. 4.2.6), both types of scaffolds demonstrated atypical compressive behavior for what is known for glasses and ceramics [56]. Typical compressive behavior of glasses and ceramics would elicit a linear increase in stress as a function of strain until catastrophic failure is achieved when the material changes from an elastic to a plastic deformation regime. Both glasses and ceramics are notorious for exhibiting no signs of plastic deformation before catastrophic failure, as energy cannot be dissipated through

atomic motion due to the presence of both anions and cations ionically bonded. For Ag-BG solution and slurry scaffolds, given that their internal structures are hollow, this could lead to atypical compressive behavior. Indeed, their compressive behavior was observed to be "noisy" where local fluctuations in stress as a function of strain are observed leading to the noted jagged behavior [25]. The hollow interior of the Ag-BG solution and slurry scaffolds coupled with the presence of defective/thin struts introduced by a heterogeneous distribution of Ag-BG during the soaking and squeezing processes applied. The defective/thin struts cannot support as much stress before fracture compared to thicker struts well-formed struts, thus each local decrease in stress as a function of strain is the result of a strut fracturing and releasing energy. This behavior continues until even the strongest struts can no longer bear the compressive forces being applied, thus leading to catastrophic failure.

Furthermore, the computation of the Hashin-Shtrikman bounds offered a method to compare the mechanical performance of all Ag-BG scaffolds explored herein to visualize how detrimental the internal porosity observed compared to the theoretical upper and lower bounds of elastic moduli that could be observed at a specific porosity. It was observed (Fig. 4.2.6) that both Ag-BG solution and slurry scaffolds had elastic moduli close to the lower bound of the predicted elastic modulus. This demonstrated that the high degree of internal porosity observed achieved near the maximum of how detrimental porosity can be towards mechanical performance.

Examining FFF printed Ag-BG scaffolds, those synthesized using a unimodal distribution of Ag-BG particles having large internal porous defects restricted the elastic modulus to be close to the theoretical lower limit (Fig. 4.3.7b). Even though the compressive strength of FFF printed Ag-BG scaffolds synthesized using a unimodal distribution of Ag-BG particles was improved compared to Ag-BG solution and slurry scaffolds and within the range required for targeting bone tissue regeneration in load-bearing applications, the improvement in compressive strength was correlated to the overall decrease in porosity of Ag-BG scaffolds and not towards the minimization of internal porous defects. While the porosity of FFF printed Ag-BG scaffolds was decreased by $\sim$10% when synthesized using a bimodal distribution of Ag-BG particles, the resulting elastic modulus was

found to have appreciably moved away from the lower Hashin-Shtrikman bound (Fig. 4.4.6i) suggesting that the minimization of internal porous defects observed had a greater contribution to the increase in elastic modulus than the decrease in overall porosity.

Further examination of the mechanical performance of FFF printed Ag-BG scaffolds synthesized using a bimodal distribution of Ag-BG particles reported that the overall bulk compressive strength of an Ag-BG scaffold having 0% porosity would surpass the lower limit (i.e. 100 MPa) of the mechanical performance requirements needed to target bone tissue regeneration in high load-bearing applications. This analysis, however only provided a lower limit of the required porosity of FFF printed Ag-BG scaffolds. To identify an upper limit, the porosity and compressive strengths were measured for two groups having a difference of approximately 10% in porosity (Fig. 5.2.3). Gibson and Ashby previously demonstrated that the relationship between porosity and compressive strength is well-described by a power-law fitting [57]. As observed in Figure 5.2.3, the model well-describes the relationship of the compressive strength of Ag-BG scaffolds to their porosity, where it was found that the predicted compressive strength is close to the 100 MPa lower limit previously described at a porosity of 40%. Assuming the compressive strength of Ag-BG scaffolds reaches 100 MPa at a porosity of ~35%, this would constitute the upper bound of porosity when targeting high load-bearing applications. Considering all observed evidence, the lower bound for porosity is hypothesized to exist at ~7%, as determined through image analysis of the cross-sections of FFF printed Ag-BG scaffolds synthesized using a bimodal distribution of Ag-BG particles, therefore it is predicted that the required porosity to target high load-bearing applications is between ~7% and ~35%.

While porosity has a strong effect on the resulting mechanical performance of Ag-BG scaffolds, porosity also exhibits strong effects on the resulting antibacterial and biological performance. Interestingly, using solely the effective porosity and pore morphology of a scaffold, or the porosity of open and interconnected pores, the tortuosity (i.e. the ratio between the length of a tortuous pore and the length of a permeable scaffold along a macroscopic pressure gradient) and permeability [328] can be computed giving insight into transport performance. For FFF printed Ag-BG scaffolds,

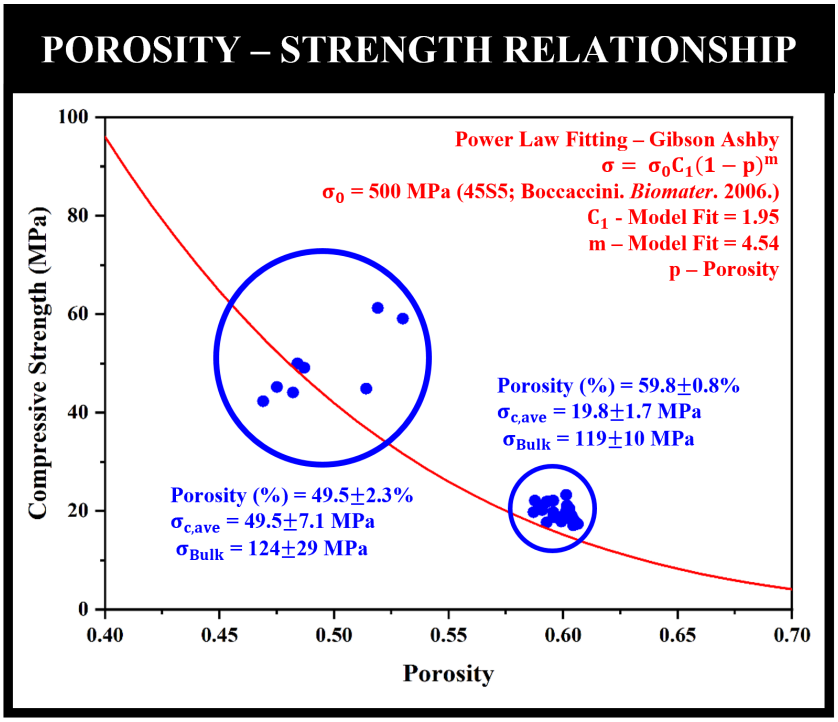

Figure 5.2.3: Power law fitting of the compressive strengths of FFF printed Ag-BG scaffolds synthesized using a bimodal distribution of Ag-BG particles, derived by Gibson and Ashby [57].

micro-CT investigations revealed no blocked (i.e. closed) pores (Figs. 4.3.3 and 4.4.2), so the effective porosity can be assumed to be equal to the total porosity. Equation 5.2.1 show how permeability (k) was computed, where ψ_p^2 describes pore sphericity, which for FFF printed Ag-BG scaffolds is assumed to be ~0.806 for pores having cubic geometry, d_p^2 represents the average pore diameter, and ϵ describes the effective porosity. For FFF printed Ag-BG scaffolds synthesized using a unimodal distribution of Ag-BG particles, their permeability was computed at $\sim 2 \cdot 10^{-12}$ m^2 while the FFF printed scaffolds synthesized using a bimodal distribution of Ag-BG particles had a computed permeability of $\sim 2 \cdot 10^{-13}$ m^2, essentially an order of magnitude decrease in permeability comparatively. For cancellous bone, the permeability is reported in the range of $1.21 \cdot 10^{-8}$ m^2 to $1.0 \cdot 10^{-11}$ m^2 [328–330]. At a minimum, FFF-printed Ag-BG scaffolds have a 1 to 2 order of magnitude decrease in permeability compared to the least permeable cancellous bone, therefore presenting FFF printed Ag-BG scaffolds exhibiting reduced mass transport comparatively leading to slower antibacterial and biological performance that is supported experimentally.

$$\frac{72k}{\psi_p^2 d_p^2} = \frac{\epsilon^2}{(1-\epsilon^2)}\left(\frac{1}{2}\left[1+\frac{1}{2}\sqrt{1-\epsilon}+\sqrt{1-\epsilon}\frac{\sqrt{\left(\frac{1}{\sqrt{1-\epsilon}}\right)^2+\frac{1}{4}}}{1-\sqrt{1-\epsilon}}\right]\right)^{-1} \quad \text{(5.2.1 [286])}$$

Regarding the effect of the delivered structures on the antibacterial performance of Ag-BG scaffolds, the reduced permeability previously described should translate to a slower antibacterial response. Ag-BG solution and slurry scaffolds synthesized by the polymer foam replication technique should have greater permeability given previous reports on 45S5 and calcium phosphate scaffolds demonstrating comparable permeability to cancellous bone [328], thus leading to improved transport properties that should allow for stronger antibacterial performance. Indeed, this was the case as Ag-BG scaffolds synthesized using the polymer foam replication technique displayed improved antibacterial performance compared to FFF printed Ag-BG scaffolds using a unimodal distribution of Ag-BG particles at the same mass to volume ratio, however, this difference was within an order of magnitude, thus demonstrating that permeability is not a strong indicator of antibacterial performance.

To identify the predominant structural factor dictating antibacterial performance, the effect of crystallinity and morphology was studied. When the anti-MRSA effect of Ag-BG solution versus slurry scaffolds was explored, an insignificant difference in MRSA inhibition was observed indicating that the difference in crystallinity (i.e. glass-ceramic nature of Ag-BG solution scaffolds versus the highly crystalline nature of Ag-BG slurry scaffolds) was found to have a minimal effect on antibacterial performance. Comparing instead the effect of morphology, Ag-BG slurry scaffolds were pulverized, and the powdered Ag-BG slurry scaffold used at the same mass to volume ratio as Ag-BG slurry scaffolds finding that pulverized Ag-BG slurry scaffolds displayed bactericidal behavior as a result of the ~3 orders of magnitude increase in surface area.

With the identification of morphology as the dominant factor dictating antibacterial performance, the mechanism of MRSA inhibition could be further elucidated. ^{27}Al NMR (Fig. 4.2.5g) in conjunction with XRD (Figs. 4.2.3a and 4.3.4b), TEM (Figs. 4.2.5a, e, and 4.3.6f)) and UV-Vis (Figs. 4.2.5c and 4.3.6e, f) found that Ag likely exists in both ionic form stabilized by $[AlO_4]^-$ and elemental Ag in the form of nanoparticles, therefore the mechanism of MRSA inhibition is likely

contributed by both forms of Ag. For AgNPs, they are known to attach to the cell wall of MRSA, disrupting cellular functions on the cell wall surface, leading to perforation of the cell wall allowing the AgNP to penetrate the cytoplasm of MRSA. The release of Ag^+ ions from the surface of the AgNPs after penetration will disrupt protein synthesis and induce DNA damage given the affinity of Ag^+ ions to complex with electron donor groups such as thiols or phosphates [331, 332]. The size of the AgNPs is additionally known to have a direct effect on their ability to inhibit bacteria such as MRSA, where increasing surface area to volume ratios correlated to stronger inhibitory responses.

As reported by Pajares-Chamorro et al., Ag-BG micro-sized particles possess the remarkable ability to reactivate antibiotics that MRSA is known to resist [37]. Pajares-Chamorro et al. elucidated the various MRSA inhibition mechanisms at work, finding ~52% of MRSA inhibition at the minimum inhibitory concentration (MIC) resulted from Ag^+ ions and resulting in oxidative stress [333]. Furthermore, it was demonstrated that in addition to Ag^+ ions, the presence of other mechanisms such as the osmotic effect, reactive oxygen species from Ag-BG, and nanosized debris allow for antibiotics MRSA is known to resist to be reactivated [333]. Damage to the cell was of MRSA was found to be imperative, as the damage allows the inactive antibiotic to penetrate the cell wall, bypassing the cell wall adaptations that allowed MRSA to resist antibiotics and interfere with the synthesis processes in an attempt to induce irreparable damage that competes with the ability of MRSA to repair its cell wall [333]. Under growth-arrested conditions, Ag-BG slurry scaffolds combined with fosfomycin (Fig. 4.2.7b) and vancomycin (Fig. 4.2.7c) elicited a significantly stronger inhibition of MRSA in both cases after 24 h compared to Ag-BG slurry scaffolds. After 48 h, however, this synergistic effect was no longer observed. As previously reported by Pajares-Chamorro et al., the antibiotics used begin to degrade after 24 h [333], which can explain why synergistic effects were not observed after 48 h.

For biological performance, structurally speaking, pore size on the multiscale serves various functions. For example, pores on the order of the macroscale assist with functionality and shape while pores on the milliscale affect bone in growth and cellular growth and infiltration [334].

It should be noted, however, that pores below 300 μm have been reported to exhibit inhibitory effects on the above processes previously mentioned [87]. Decreasing in scale, pores on the order of the micro-scale can dictate the types of cells attracted, cellular development, orientation, and directionality of in growth with meso-sized pores dictating interaction with proteins and bioactivity [87]. For all Ag-BG scaffolds reported herein, their pore sizes are expected to not have an inhibitory effect on cell infiltration and spreading given their pore sizes are essentially > 300 μm. Furthermore, the low permeability of FFF printed Ag-BG scaffolds synthesized using a bimodal distribution of Ag-BG particles suggests that biological performance would be inhibited when studied in vitro. Despite this, hMSCs were found to be more viable and prolific when indirectly exposed to FFF printed Ag-BG scaffolds synthesized using a bimodal distribution of Ag-BG particles resulting from the therapeutic ions released (Fig. 4.4.7) during degradation suggesting acceptable performance when studied *in vivo*.

Additionally, it was demonstrated using Ag-BG slurry scaffolds that the phases produced during heat treatment impact biological performance. Recalling Table 4.4.2, the phase concentrations of W. 2M and PsW were successfully modified while maintaining the approximate concentrations of all the other phases reported. Thermodynamically, PsW was found to be more soluble than W. 2M leading to an increased rate of formation of an apatite-like layer when immersed in SBF, as reported by Sainz et al. [284] and Magallenes-Perdomo et al. [285]. Exploring this, however, from a crystallographic perspective, both PsW and W. 2M contain the same number of atoms per unit cell, the unit cell volume of PsW is approximately 400% greater than the unit cell volume of W. 2M. This unit cell volume increase was thought to translate to greater internal lattice energy resulting in less cohesion and thus greater solubility of PsW compared to W. 2M [335]. Quantification of the internal lattice energies for both W. 2M and PsW was accomplished using the extended, generalized Kapustinskii equation [336], shown in equations 5.2.2 and 5.2.3, where A (121.39 kJ mol^{-1} nm) is based on the Madelung constant [336], I is a constant defined by equation 5.2.2, n_i is the number of ions with integer charge z_i, and V_m defines the ratio of the number of formula units per unit cell to unit cell volume (i.e. 0.0663 nm^{-3} for wollastonite [336]. The internal lattice energy for

W. 2M was calculated to be 15,234 kJ mol^{-1} and 32,959 kJ mol^{-1}, thus providing crystallographic evidence to further support the thermodynamic and experimental evidence previously presented by Sainz et al. [284] and Magallenes-Perdomo et al. [285].

$$UPOT = AI(\frac{2I}{V_m})^{\frac{1}{3}} \quad (5.2.2\ [336])$$

$$2I = \sum n_i z_i^2 \quad (5.2.3\ [336])$$

5.3 Hybrids

The synthesis of GelMA has traditionally been performed in aqueous environments such as PBS [296] using methacrylic anhydride (MAA) and the methacrylation agent to functionalize the lysine groups present in as-received gelatin. Exposing methacrylic anhydride to an aqueous environment induces hydrolysis transforming MAA into methacrylic acid, leading to a decrease in pH, reducing the effectiveness of the desired functionalization reaction, and increasing the rate of gelatin hydrolysis. All these factors in combination lead to maximum achievable degrees of substitution between 80% and 85% in addition to large batch-to-batch variations. It is important to note as well that the maximum values reported for the degree of substitution require a 10 to 32-fold molar excess of MAA compared to the lysine groups present in as-received gelatin to compensate for the hydrolysis reaction of MAA [337]. Not only this but also a lengthy dialysis process (i.e. > 7 days) is required to remove the excess MAA to ensure no cytotoxic effects are exhibited. With GelMA dissolved for such a lengthy period of time, this provides ample opportunities for hydrolysis that could lead to variations in the resulting molecular weight of the synthesized GelMA. Previous reports have demonstrated that the use of a carbonate-bicarbonate system tuned to have a pH of 9.0 found success in increasing the DS up to 97% while dramatically lowering the MAA required to a 2.2 molar excess [337]. This was possible due to the alkaline pH used, as a pH of 9 is above the isoelectric point of as-received gelatin, thus providing a stronger attractive driving force for

the desired methacrylation reaction [217]. Despite such improvements, however, a lengthy dialysis post-processing step was still required.

To further build upon such findings, removal of the adverse effects generated through the synthesis of GelMA in an aqueous environment could be achieved using an organic solvent. Here, DMSO was selected as all the required reagents for GelMA synthesis were soluble in DMSO, while removing the pH dependence previously described in addition to preventing the hydrolysis of MAA, allowing for a near 100% degree of substitution to be achieved. To bypass dialysis, it was hypothesized that a precipitation approach could be viable. Previous reports have investigated precipitation methods such as the use of NaCl at sufficient concentrations to induce protein agglomeration within GelMA, leading to precipitation, and the use of ethanol at cryogenic temperatures to induce precipitation [218]. Both precipitation approaches, however, fail to fully precipitate GelMA, leading to low reaction yields.

It was recently reported by Mohamed et al. that toluene could be an ideal solvent for precipitating GelMA. The low dielectric constant of toluene (i.e. ~2.4 [218]) coupled with its zero hydrophile-lipophile balance lowers solvent polarity increasing the attractive forces between the negative and positive charges present on dissolved GelMA. Furthermore, all reagents used during GelMA synthesis are soluble in toluene except for GelMA itself, allowing for maximum recovery of GelMA from solution. This, while allowing the dialysis process to be circumvented, is not the only attractive quality of toluene. Previous reports have demonstrated that toluene is a useful antimicrobial and sterilizing agent that when coupled with its high volatility means that sterilization can be incorporated into the synthesis process as residual toluene should evaporate quite quickly, leaving an aseptic hydrogel behind [218].

Here, we aimed to remove the adverse effects created by synthesizing GelMA in a non-aqueous environment through the use of an organic solvent, DMSO. It was hypothesized that the use of DMSO would prevent MAA hydrolysis and allow for ~100% DS to be achieved during synthesis. Furthermore, it was recently found that the dialysis step could be circumvented when using toluene as a precipitating agent [218]. The small dielectric constant for toluene (ϵ ~2.4), when exposed

to the GelMA solution, increases the attractive forces between the oppositely charged portions of the GelMA allowing for agglomerations to grow resulting in the precipitation of the GelMA. An additional benefit to using the toluene precipitation method is that the DMSO and MAA are soluble in toluene allowing for their removal without the need for a dialysis process [218]. This precipitation method was further found to additionally be compatible with GAB synthesis, highlighting the attractiveness of the toluene precipitation approach.

Regarding the performance aspects of GelMA and GAB, their pH evolution was studied for 7 days (Fig. 4.5.3) in addition to a GelMA-Ag-BG nanoparticle composite to demonstrate the advantages of forming a hybrid material as opposed to the use of a nanocomposite. It was found that molecular coupling between GelMA and Ag-BG mediated by GPTMS allowed for a pH evolution to be observed more in line with GelMA compared to the GelMA-Ag-BG nanocomposite. The covalent bonds formed between GelMA and Ag-BG likely allowed for greater homogenization of the degradation characteristics between GelMA and Ag-BG. Since Ag-BG was only incorporated at 3 wt%, the degradation of GelMA was able to mediate the degradation of the overall hydrogel. The GelMA-Ag-BG nanocomposite elicited a greater increase in pH that was observed to peak ~8.8 before dropping below 8 after 5 d of immersion. This was due to the burst release of ions from Ag-BG nanoparticles, or the osmotic effect exhibited by bioactive glasses at short time points [248].

The rheological performance of GAB elucidated both the storage (G′) and loss (G″) moduli finding values corresponding to approximately 2 orders of magnitude less for both GelMA and the values recommended by literature for successful 3D bioprinting (Table 4.5.1). It was hypothesized that the covalent bonds formed between GelMA and Ag-BG, as mediated by GPTMS, allowed for improvements in the amount of elastic deformation energy absorbed and dissipated due to bonds connecting the covalently bonded GelMA with the strong ionic bonds of Ag-BG. Given that ionically bonded materials such as Ag-BG, a glass-ceramic, possess a high degree of stiffness compared to soft polymers such as GelMA, it is unsurprising that incorporation of 3 wt% of Ag-BG would lead to such a significant increase in storage and loss moduli. While the storage and loss

moduli were greater than the values recommended from the literature, successful 3D bioprinting using GAB was still achieved (Fig. 4.5.5c).

CHAPTER 6

CONCLUDING REMARKS

6.1 Polymer foam replication

The delivery of Ag-BG solution and slurry scaffolds through the implementation of the polymer foam replication technique was successful at producing desirable antibacterial and biological performances at the expense of mechanical performance. The polymer foam replication process, while achieving high degrees of porosity (i.e. > 90%), created hollow internal structures that were identified as the main culprit in the unacceptable mechanical performances observed. Both Ag-BG solution and slurry scaffolds were useful in elucidating the strong relationship between gross morphology and antibacterial performance through surface area characterization. Ag-BG slurry scaffolds revealed the process – structure – biological performance relationship between the formed crystalline phases and their impact on dissolution. The ability of Ag-BG scaffolds to reactivate antibiotics MRSA is known to resist was found to be much weaker compared to previous reports using Ag-BG micro-sized particles that were predicted to be the result of the inability of Ag-BG scaffolds to sufficiently damage the cell walls of MRSA, allowing for biosynthesis to successfully repair the damaged cell walls and prevent further penetration of antibiotics into the cytoplasm. Overall, the structural and performance characteristics observed for Ag-BG scaffolds delivered using the polymer foam replication technique demonstrate these scaffolds would be suitable for targeting bone tissue regeneration in low to non-load-bearing applications.

6.2 Fused filament fabrication

The suboptimal mechanical performance characteristics observed for Ag-BG scaffolds synthesized using the polymer foam replication technique inspired the novel adaptation of FFF for the delivery of pristine Ag-BG scaffolds with improved mechanical performance. The shaping – debinding – sintering post-processing steps applied were found to be key in maintaining structural

integrity during post-processing, allowing the FFF technique to be successfully implemented in the synthesis of 3D silicate-based scaffolds for the first time. While the compressive strength of FFF printed Ag-BG scaffolds synthesized using a unimodal distribution of Ag-BG particles met the lower bound of the required mechanical performance for targeting bone tissue regeneration in load-bearing applications. It was elucidated that the generation of large internal porous defects during the applied processes severely compromised the full mechanical performance potential that could be achieved using FFF, as evidenced by the proximity of their elastic modulus to the lower Hashin-Shtrikman bound. Furthermore, the large internal porous defects were found to additionally compromise the sintering conditions that could be applied, further extubating the limited mechanical performance potential. The delivered FFF printed Ag-BG scaffolds produced using a unimodal distribution of Ag-BG particles were found to form an apatite-like layer when immersed in SBF in addition to time-dependent anti-MRSA capabilities. These Ag-BG scaffolds, while possessing more attractive performance characteristics compared to Ag-BG scaffolds delivered using the polymer foam replication technique, still failed to meet all the desired aims. As a result, improvements to the FFF process were required.

Moving from the use of a unimodal distribution of Ag-BG particles to a bimodal distribution of Ag-BG particles allowed for the optimal sintering conditions to be investigated and identified. The application of the optimal sintering conditions delivered FFF printed Ag-BG scaffolds that had robust and reliable mechanical performance and correlated to the increased packing efficiency of Ag-BG particles, minimizing the number of internal porous defects generated during sintering. The reduction in internal porous defects allowed for the reported elastic modulus to move appreciably away from the lower Hashin-Shtrikman bound to begin realizing the full mechanical performance potential of FFF technology. Additionally, it was predicted that the mechanical performance of FFF printed Ag-BG scaffolds using a bimodal distribution of Ag-BG particles could achieve the mechanical requirements needed for targeting bone tissue regeneration in high load-bearing applications having upper and lower porosity bounds of ~35% to ~7% respectively. Not only were the mechanical performance characteristics improved, but also these FFF printed Ag-BG scaffolds

displayed advanced anti-MRSA capabilities by their ability to successfully combat both planktonic MRSA and MRSA as a biofilm in addition to showing significant improvements in hMSC viability, proliferation, and mineralization. The overall structural and performance characteristics of the FFF printed Ag-BG scaffolds produced using a bimodal distribution of Ag-BG particles delivered scaffolds having exceedingly attractive characteristics for targeting bone tissue regeneration in load-bearing applications.

6.3 Hybrids

Using a novel synthesis approach to deliver GelMA and GAB hydrogels was successful at increasing the degree of methacrylation while preventing unwanted hydrolysis hypothesized to minimize the known batch-to-batch variability that exists with conventional synthesis approaches. Not only this but also the novel synthesis approach used herein delivered hydrogels capable of undergoing appreciable cross-linking, enabling their use as a compatible ink for 3D printing. The shear-thinning behavior observed for GAB during rheological investigations further supports the compatibility of GAB for 3D printing. The incorporation of Ag-BG was found to be successful given the increase in storage and loss moduli, the elemental homogeneity observed, and the display of anti-MRSA capabilities without evidence of cytotoxicity both during antibacterial and biological performance characterization. GAB, therefore, is expected to be suitable for extrusion-based 3D bioprinting technologies allowing for the delivery of ions to promote preferential cellular behaviors due to the successful incorporation of Ag-BG in the formation of class II hybrid hydrogels.

CHAPTER 7

FUTURE WORK

7.1 Identification and recommendations regarding the limitaitons on the scope of work

The work presented in this dissertation was aimed at delivering Ag-BG scaffolds capable of having the necessary mechanical, antibacterial, and biological performance characteristics for targeting bone tissue regeneration in load-bearing applications. To achieve these aims, the process – structure – performance relationships were investigated to elucidate a feedback loop capable of bridging the gap between process and performance through structural characterization to progressively work towards the desired aims.

One limitation of the work presented herein would be the mechanical performance characterization used. While FFF printed Ag-BG scaffolds synthesized using a bimodal distribution of Ag-BG particles displayed relatively comprehensive mechanical performance characterization, studying the compressive and flexural strengths in addition to elucidation of their fracture toughness, fatigue testing should also be performed given that the scaffolds will undergo cyclic loading and unloading of compressive forces during use. Overall, within the biomaterials field, however, fatigue testing is commonly neglected, thus minimal information is available within the literature. While valuable, the ideal setup for fatigue testing would require implementation under an aqueous environment to mimic the conditions the scaffolds would more closely face during application. Furthermore, such an aqueous environment should be set up under dynamic conditions to mimic the flow of fluids that occurs in the body.

Further extrapolation on the biological performance characterization limitations is found regarding the *in vitro* experiments performed. In this setup, hMSCs were indirectly exposed to FFF printed Ag-BG scaffolds synthesized using a bimodal distribution of Ag-BG particles, so only the effect of the ions released during degradation was observed. While preferential biological perfor-

mance characteristics were identified, direct exposure of cells to Ag-BG scaffolds would indicate how well cells would be able to move through the scaffolds in addition to characterization of the viability of cells that had migrated into the interior of the porous network created by the Ag-BG scaffolds. Additionally, *in vivo* studies should be conducted using a suitable animal model, so that the performance of Ag-BG scaffolds could be assessed under load-bearing conditions.

Regarding the generation of load-bearing conditions, it is expected that the application of cyclic compressive forces would increase the rate of degradation of Ag-BG scaffolds. While more potent antibacterial performance characteristics and improved biological performance characteristics would be expected from the increased rate of dissolution, the predicted time for complete degradation reported herein likely represents the upper limit considering the experiment was performed under static loading conditions. Furthermore, given the advanced antibacterial performance characteristics observed for FFF printed Ag-BG scaffolds synthesized using a bimodal distribution of Ag-BG particles, the next logical step in this characterization would be to examine their antibacterial performance *in vivo* using a suitable animal model generating load-bearing conditions.

The success demonstrated moving from a unimodal distribution of Ag-BG particles to a bimodal distribution of Ag-BG particles in mechanical performance characteristics of delivered Ag-BG scaffolds warrants further exploration. To this end, a trimodal distribution of Ag-BG particles should be explored, incorporating nano-sized Ag-BG particles and adjusting the ratios of all three particle size distributions to identify the proper conditions needed to eliminate the generation of internal porous defects, which should unlock the full mechanical performance potential of 3D scaffolds produced using FFF technology.

The work done into the development of class II GelMA-Ag-BG (GAB) hybrid hydrogels represents foundational investigations for future exploration. The main aim of this work was to identify a process capable of producing GAB having suitable mechanical, antibacterial, and biological performance requirements for future use as a bioink for 3D bioprinting. To demonstrate the full potential of GAB as an attractive bioink, studies on cell viability need to be conducted on cell-laden GAB after undergoing extrusion-based 3D bioprinting to observe the efficacy of GAB

on preserving cell viability. A more in-depth investigation is needed to elucidate both this and what effects GAB has on cell proliferation and differentiation. The degradation characteristics of 3D cell-laden GAB scaffolds additionally need exploration as the presence of cells will modify this behavior. It is likely as well that investigation into a method of delivering oxygen to cell-laden GAB scaffolds so that embedded cells receive sufficient oxygen for maximum survivability. The antibacterial performance of 3D cell-laden GAB scaffolds should also be assessed to observe their antibacterial characteristics in the presence of microbes. After successful 3D bioprinting, the mechanical performance aspects also need in-depth characterization. Ideally, enough samples would be produced to perform Weibull statistics on their mechanical performance characteristics to get an understanding of their reliability. There is enormous potential in 3D bioprinting cell-laden scaffolds for targeting more advanced and complex tissue regeneration with the work presented herein providing a foundational roadmap towards success.

APPENDIX

Bright-field TEM images are formed when the objective lens aperture is placed inside the back focal plane of the objective lens so that only the transmitted electrons are allowed to pass through to the image plane of the projector lens (Fig. S2). To form a bright-field image, the selected area diffraction aperture (SAD) is inserted into the back focal plane of the objective lens and the imaging mode on the instrument adjusted so that the back focal plane of the objective lens can act as the object plane of the intermediate lens [229]. The objective lens aperture is then inserted and aligned with the transmitted spot on the SAD pattern to prevent the scattered electrons from being imaged. The instrument is adjusted again so that the object plane of the intermediate lens is used for generating images. This generates an image having an illuminated background with the specimen appearing dark as a result of the scattered electrons not being allowed to pass through down to the image plane of the projector lens. Image contrast differences appear in bright-field images as a function of mass and thickness.

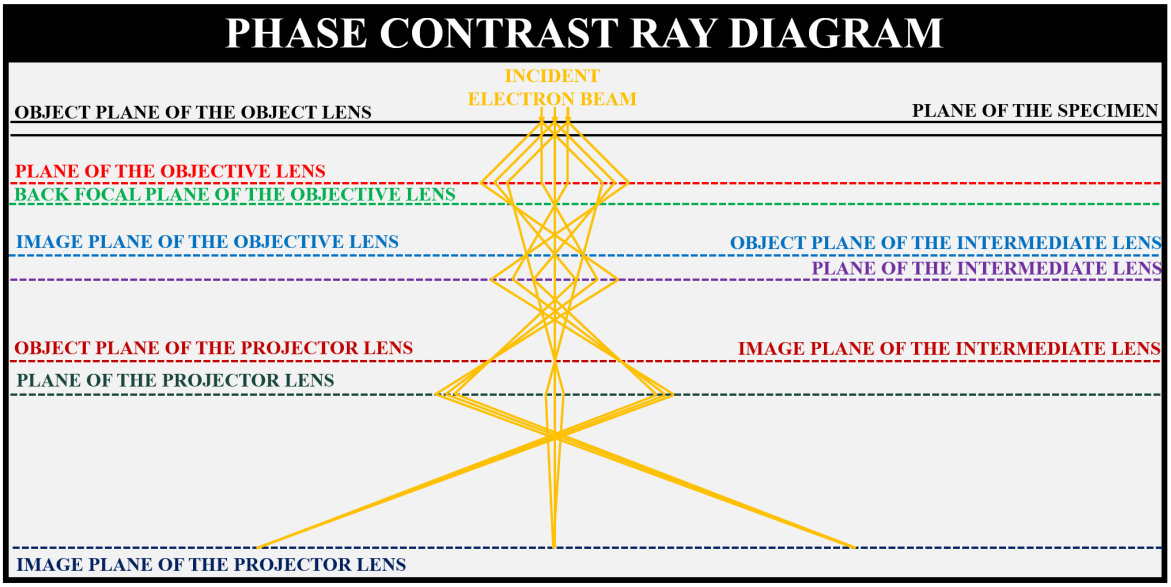

Figure S1: Ray diagram of the path of the electron beam as the electrons travel through the specimen forming a phase-contrast image on the image plane of the projector lens.

Bright-field TEM images are formed when the objective lens aperture is placed inside the back focal plane of the objective lens so that only the transmitted electrons are allowed to pass through to the image plane of the projector lens (Fig. S2). To form a bright-field image, the selected

area diffraction aperture (SAD) is inserted into the back focal plane of the objective lens and the imaging mode on the instrument adjusted so that the back focal plane of the objective lens can act as the object plane of the intermediate lens [229]. The objective lens aperture is then inserted and aligned with the transmitted spot on the SAD pattern to prevent the scattered electrons from being imaged. The instrument is adjusted again so that the object plane of the intermediate lens is used for generating images. This generates an image having an illuminated background with the specimen appearing dark as a result of the scattered electrons not being allowed to pass through down to the image plane of the projector lens. Image contrast differences appear in bright-field images as a function of mass and thickness.

Dark-field TEM images are formed when the selected area diffraction (SAD) aperture is placed inside the image plane of the objective lens, which is the same plane as the object plane of the intermediate lens (Fig. S3). To generate a dark-field image, the SAD aperture is first added while the instrument is in imaging mode (i.e. using the object plane of the intermediate lens to generate images). The instrument is then adjusted so that the back focal plane of the objective lens can act as the object plane of the intermediate lens, allowing for a SAD pattern to be imaged.

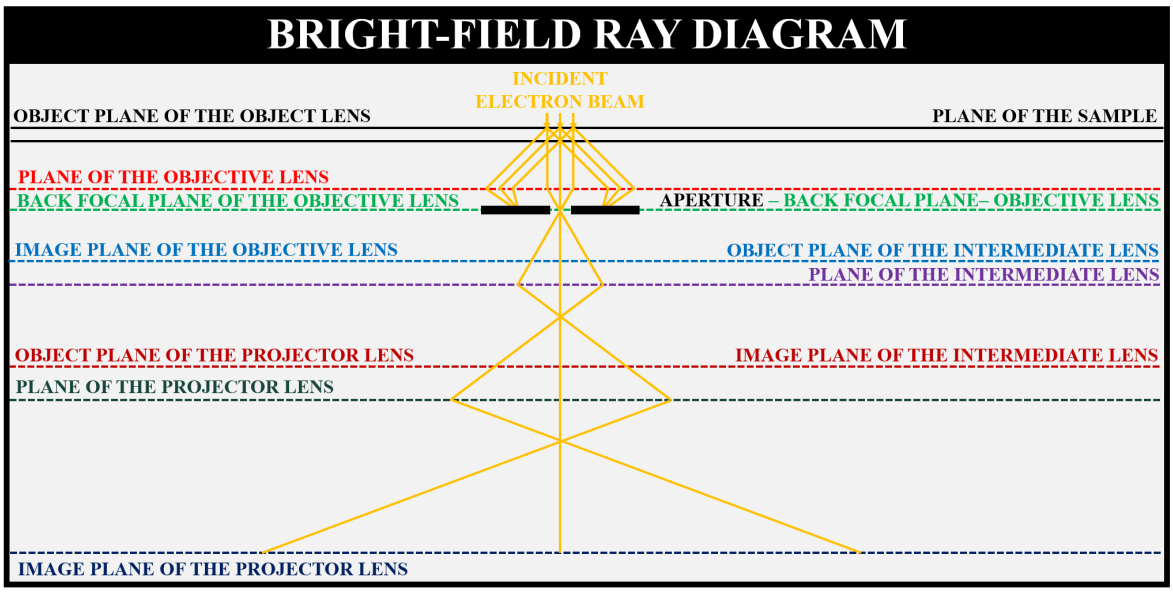

Figure S2: Ray diagram of the path of the electron beam as the electrons travel through the specimen forming a bright-field image on the image plane of the projector lens.

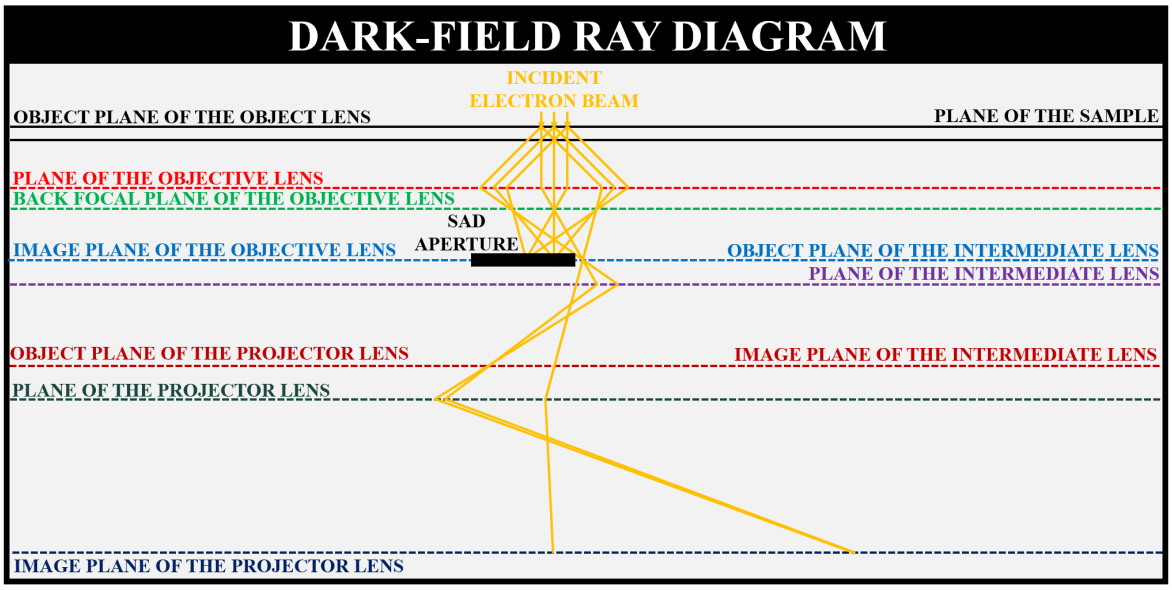

Figure S3: Ray diagram of the path of the electron beam as the electrons travel through the specimen forming a dark-field image on the image plane of the projector lens.

Histology was performed on the FFF printed Ag-BG scaffolds after 50 d of implantation into calvaria defects of mice with Goldner's trichrome (Fig. S4a-c) and Toluidine blue (Fig. S4d-f) stain on prepared cross-sections. In both cases, cell infiltration was found to be plentiful suggesting that the FFF printed Ag-BG scaffolds provided an attractive environment for cells. The small, dark oval-like features marked by the red-boxes in Figure S4c, f are suspected to be macrophages removing scaffold material, which is an expected event known to occur during the healing process. Furthermore, there was minimal evidence that a foreign-body reaction (i.e. white circles in Figure S4b-c) was taking place, suggesting that the body was able to tolerate the presence of the FFF printed Ag-BG scaffolds. These pieces of evidence together support that the FFF printed Ag-BG scaffolds are biocompatible and agree with the presented *in vitro* studies.

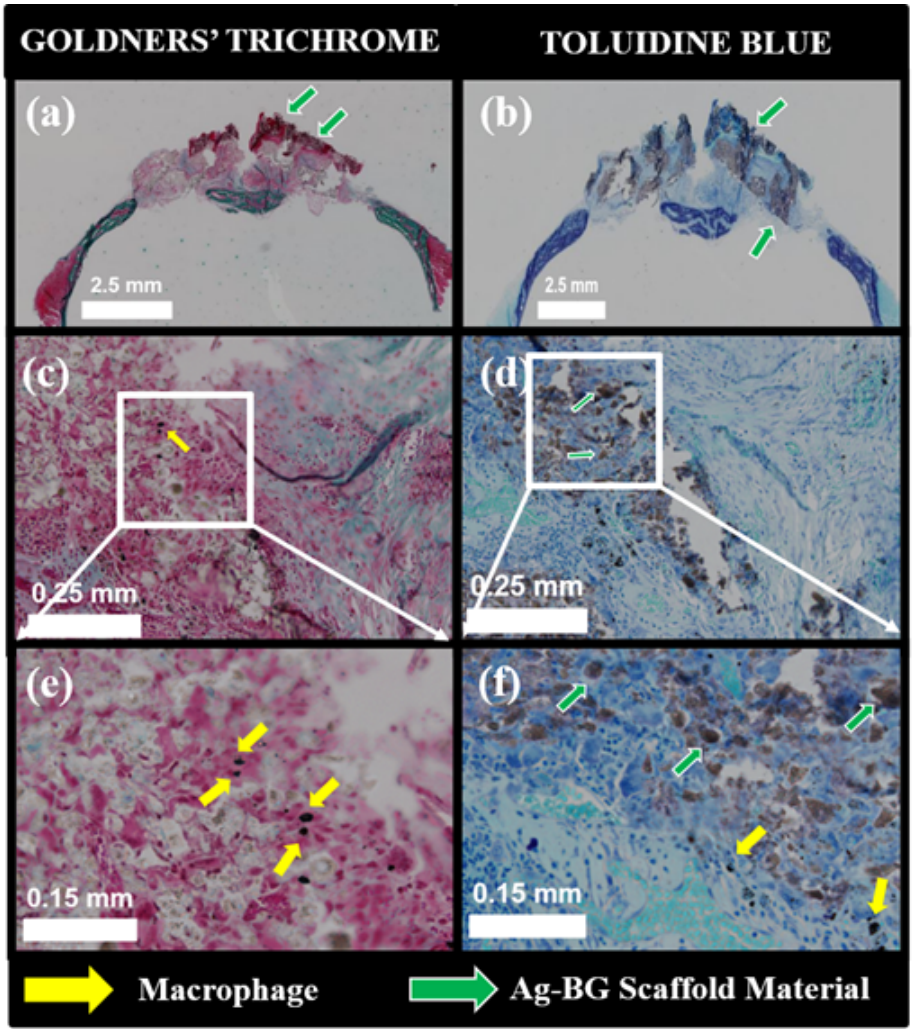

Figure S4: Histology of FFF printed Ag-BG scaffolds after 50d of implantation in calvaria defects. Goldner's Trichrome (a, c, e) and toluidine blue (b, d, f) were the histological stains applied presented at increasing magnifications. The yellow arrows denote features suspected to be macrophages up taking FFF printed Ag-BG scaffold material. The green arrows denote regions where FFF printed Ag-BG scaffold material is present.

BIBLIOGRAPHY

BIBLIOGRAPHY

[1] Adele L. Boskey. Bone composition: relationship to bone fragility and antiosteoporotic drug effects. *BoneKEy reports*, 2:447–447, 2013. ISSN 2047-6396. doi: 10.1038/bonekey.2013.181. URL https://pubmed.ncbi.nlm.nih.gov/24501681https://www.ncbi.nlm.nih.gov/pmc/articles/PMC3909232/.

[2] Maria P. Nikolova and Murthy S. Chavali. Recent advances in biomaterials for 3d scaffolds: A review. *Bioactive materials*, 4:271–292, 2019. ISSN 2452-199X. doi: 10.1016/j.bioactmat.2019.10.005. URL https://pubmed.ncbi.nlm.nih.gov/31709311https://www.ncbi.nlm.nih.gov/pmc/articles/PMC6829098/.

[3] U. H. Lerner. Bone remodeling in post-menopausal osteoporosis. *Journal of Dental Research*, 85(7):584–595, 2006. ISSN 0022-0345. doi: 10.1177/154405910608500703. URL https://doi.org/10.1177/154405910608500703.

[4] Yulin Li, Yin Xiao, and Changsheng Liu. The horizon of materiobiology: A perspective on material-guided cell behaviors and tissue engineering. *Chemical Reviews*, 117(5):4376–4421, 2017. ISSN 0009-2665. doi: 10.1021/acs.chemrev.6b00654. URL https://doi.org/10.1021/acs.chemrev.6b00654.

[5] Steffen Esslinger and Rainer Gadow. Additive manufacturing of bioceramic scaffolds by combination of fdm and slip casting. *Journal of the European Ceramic Society*, 2019. ISSN 0955-2219. doi: https://doi.org/10.1016/j.jeurceramsoc.2019.10.029. URL http://www.sciencedirect.com/science/article/pii/S0955221919307009.

[6] Erika Roddy, Malcolm R. DeBaun, Adam Daoud-Gray, Yunzhi P. Yang, and Michael J. Gardner. Treatment of critical-sized bone defects: clinical and tissue engineering perspectives. *European Journal of Orthopaedic Surgery & Traumatology*, 28(3):351–362, 2018. ISSN 1432-1068. doi: 10.1007/s00590-017-2063-0. URL https://doi.org/10.1007/s00590-017-2063-0.

[7] Emil H. Schemitsch. Size matters: Defining critical in bone defect size! *Journal of Orthopaedic Trauma*, 31, 2017. ISSN 0890-5339. URL https://journals.lww.com/jorthotrauma/Fulltext/2017/10005/Size_Matters__Defining_Critical_in_Bone_Defect.5.aspx.

[8] Xiaojian Wang, Shanqing Xu, Shiwei Zhou, Wei Xu, Martin Leary, Peter Choong, M. Qian, Milan Brandt, and Yi Min Xie. Topological design and additive manufacturing of porous metals for bone scaffolds and orthopaedic implants: A review. *Biomaterials*, 83:127–141, 2016. ISSN 0142-9612. doi: https://doi.org/10.1016/j.biomaterials.2016.01.012. URL http://www.sciencedirect.com/science/article/pii/S0142961216000144.

[9] Maximilien E. Launey, Markus J. Buehler, and Robert O. Ritchie. On the mechanistic origins of toughness in bone. *Annual Review of Materials Research*, 40(1):25–53, 2010.

ISSN 1531-7331. doi: 10.1146/annurev-matsci-070909-104427. URL https://doi.org/10.1146/annurev-matsci-070909-104427.

[10] Arun R. Shrivats, Michael C. McDermott, and Jeffrey O. Hollinger. Bone tissue engineering: state of the union. *Drug Discovery Today*, 19(6):781–786, 2014. ISSN 1359-6446. doi: https://doi.org/10.1016/j.drudis.2014.04.010. URL http://www.sciencedirect.com/science/article/pii/S1359644614001354.

[11] Ángel E. Mercado-Pagán, Alexander M. Stahl, Yaser Shanjani, and Yunzhi Yang. Vascularization in bone tissue engineering constructs. *Annals of Biomedical Engineering*, 43(3):718–729, 2015. ISSN 1573-9686. doi: 10.1007/s10439-015-1253-3. URL https://doi.org/10.1007/s10439-015-1253-3.

[12] Wenhao Wang and Kelvin W. K. Yeung. Bone grafts and biomaterials substitutes for bone defect repair: A review. *Bioactive Materials*, 2(4):224–247, 2017. ISSN 2452-199X. doi: https://doi.org/10.1016/j.bioactmat.2017.05.007. URL http://www.sciencedirect.com/science/article/pii/S2452199X17300464.

[13] Susmita Bose, Mangal Roy, and Amit Bandyopadhyay. Recent advances in bone tissue engineering scaffolds. *Trends in Biotechnology*, 30(10):546–554, 2012. ISSN 0167-7799. doi: https://doi.org/10.1016/j.tibtech.2012.07.005. URL http://www.sciencedirect.com/science/article/pii/S0167779912001151.

[14] Petra Chocholata, Vlastimil Kulda, and Vaclav Babuska. Fabrication of scaffolds for bone-tissue regeneration. *Materials*, 12(4), 2019. ISSN 1996-1944. doi: 10.3390/ma12040568.

[15] J. R. Jones. Review of bioactive glass: from hench to hybrids. *Acta Biomater*, 9(1):4457–86, 2013. ISSN 1878-7568 (Electronic) 1742-7061 (Linking). doi: 10.1016/j.actbio.2012.08.023. URL https://www.ncbi.nlm.nih.gov/pubmed/22922331.

[16] Qiang Fu, Eduardo Saiz, Mohamed N. Rahaman, and Antoni P. Tomsia. Bioactive glass scaffolds for bone tissue engineering: state of the art and future perspectives. *Materials Science and Engineering: C*, 31(7):1245–1256, 2011. ISSN 0928-4931. doi: https://doi.org/10.1016/j.msec.2011.04.022. URL http://www.sciencedirect.com/science/article/pii/S0928493111001275.

[17] Lutz-Christian Gerhardt and Aldo R. Boccaccini. Bioactive glass and glass-ceramic scaffolds for bone tissue engineering. *Materials*, 3(7), 2010. ISSN 1996-1944. doi: 10.3390/ma3073867.

[18] Elise F. Morgan, Ginu U. Unnikrisnan, and Amira I. Hussein. Bone mechanical properties in healthy and diseased states. *Annual Review of Biomedical Engineering*, 20(1):119–143, 2018. ISSN 1523-9829. doi: 10.1146/annurev-bioeng-062117-121139. URL https://doi.org/10.1146/annurev-bioeng-062117-121139.

[19] Irsalan Cockerill, Yingchao Su, Subhasis Sinha, Yi-Xian Qin, Yufeng Zheng, Marcus L. Young, and Donghui Zhu. Porous zinc scaffolds for bone tissue engineering applications: A novel additive manufacturing and casting approach. *Materials Science and Engineering: C*, 110:110738, 2020. ISSN 0928-4931. doi: https://doi.org/10.1016/j.msec.2020.110738. URL http://www.sciencedirect.com/science/article/pii/S0928493119347071.

[20] Toktam Ghassemi, Azadeh Shahroodi, Mohammad H. Ebrahimzadeh, Alireza Mousavian, Jebraeel Movaffagh, and Ali Moradi. Current concepts in scaffolding for bone tissue engineering. *The archives of bone and joint surgery*, 6(2):90–99, 2018. ISSN 2345-4644 2345-461X. URL https://pubmed.ncbi.nlm.nih.gov/29600260https://www.ncbi.nlm.nih.gov/pmc/articles/PMC5867363/.

[21] Elisa Fiume, Jacopo Barberi, Enrica Verné, and Francesco Baino. Bioactive glasses: From parent 45s5 composition to scaffold-assisted tissue-healing therapies. *Journal of Functional Biomaterials*, 9(1), 2018. ISSN 2079-4983. doi: 10.3390/jfb9010024.

[22] Alexander Hoppe, Viviana Mouriño, and Aldo R. Boccaccini. Therapeutic inorganic ions in bioactive glasses to enhance bone formation and beyond. *Biomater. Sci.*, 1:254–256, 2013. ISSN 2047-4830. doi: 10.1039/C2BM00116K.

[23] Marta Miola, Enrica Verné, Chiara Vitale-Brovarone, and Francesco Baino. Antibacterial bioglass-derived scaffolds: Innovative synthesis approach and characterization. *International Journal of Applied Glass Science*, 7(2):238–247, 2016. ISSN 2041-1286. doi: 10.1111/ijag.12209. URL https://doi.org/10.1111/ijag.12209.

[24] Di Zhang, Outi Leppäranta, Eveliina Munukka, Heimo Ylänen, Matti K. Viljanen, Erkki Eerola, Mikko Hupa, and Leena Hupa. Antibacterial effects and dissolution behavior of six bioactive glasses. *Journal of Biomedical Materials Research Part A*, 93A(2):475–483, 2010. ISSN 1549-3296. doi: 10.1002/jbm.a.32564. URL https://doi.org/10.1002/jbm.a.32564.

[25] Qizhi Z. Chen, Ian D. Thompson, and Aldo R. Boccaccini. 45s5 bioglass®-derived glass–ceramic scaffolds for bone tissue engineering. *Biomaterials*, 27(11):2414–2425, 2006. ISSN 0142-9612. doi: https://doi.org/10.1016/j.biomaterials.2005.11.025. URL http://www.sciencedirect.com/science/article/pii/S0142961205010422.

[26] Julian R. Jones, Lisa M. Ehrenfried, and Larry L. Hench. Optimising bioactive glass scaffolds for bone tissue engineering. *Biomaterials*, 27(7):964–973, 2006. ISSN 0142-9612. doi: https://doi.org/10.1016/j.biomaterials.2005.07.017. URL http://www.sciencedirect.com/science/article/pii/S0142961205006319.

[27] Larry L. Hench. The story of bioglass®. *Journal of Materials Science: Materials in Medicine*, 17(11):967–978, 2006. ISSN 1573-4838. doi: 10.1007/s10856-006-0432-z. URL https://doi.org/10.1007/s10856-006-0432-z.

[28] Julian R. Jones. Review of bioactive glass: From hench to hybrids. *Acta Biomaterialia*, 9

(1):4457–4486, 2013. ISSN 1742-7061. doi: https://doi.org/10.1016/j.actbio.2012.08.023. URL http://www.sciencedirect.com/science/article/pii/S1742706112003996.

[29] A. Hoppe, N. S. Guldal, and A. R. Boccaccini. A review of the biological response to ionic dissolution products from bioactive glasses and glass-ceramics. *Biomaterials*, 32(11):2757–74, 2011. ISSN 1878-5905 (Electronic) 0142-9612 (Linking). doi: 10.1016/j.biomaterials.2011.01.004. URL https://www.ncbi.nlm.nih.gov/pubmed/21292319.

[30] J. M. Oliveira, R. N. Correia, and M. H. Fernandes. Effects of si speciation on the in vitro bioactivity of glasses. *Biomaterials*, 23(2):371–379, 2002. ISSN 0142-9612. doi: https://doi.org/10.1016/S0142-9612(01)00115-6. URL https://www.sciencedirect.com/science/article/pii/S0142961201001156.

[31] X. Chatzistavrou, R. R. Rao, D. J. Caldwell, A. W. Peterson, B. McAlpin, Y. Y. Wang, L. Zheng, J. C. Fenno, J. P. Stegemann, and P. Papagerakis. Collagen/fibrin microbeads as a delivery system for ag-doped bioactive glass and dpscs for potential applications in dentistry. *Journal of Non-Crystalline Solids*, 432:143–149, 2016. ISSN 0022-3093. doi: 10.1016/j.jnoncrysol.2015.03.024. URL <GotoISI>://WOS:000367769100019.

[32] Xanthippi Chatzistavrou, J. Christopher Fenno, Denver Faulk, Stephen Badylak, Toshihiro Kasuga, Aldo R. Boccaccini, and Petros Papagerakis. Fabrication and characterization of bioactive and antibacterial composites for dental applications. *Acta Biomaterialia*, 10:3723–3732, 2014. doi: 10.1016/j.actbio.2014.04.030.

[33] Xanthippi Chatzistavrou, Eleana Kontonasaki, Athina Bakopoulou, Anna Theocharidou, Afroditi Sivropoulou, Konstantinos M. Paraskevopoulos, Petros Koidis, Aldo R. Boccaccini, and Toshihiro Kasuga. Development of new sol-gel derived ag-doped biomaterials for dental applications. *MRS Proceedings*, 1417, 2012. ISSN 1946-4274. doi: 10.1557/opl.2012.743.

[34] Xanthippi Chatzistavrou, Anna Lefkelidou, Lambrini Papadopoulou, Eleni Pavlidou, Konstantinos M. Paraskevopoulos, J. Christopher Fenno, Susan Flannagan, Carlos González-Cabezas, Nikos Kotsanos, and Petros Papagerakis. Bactericidal and bioactive dental composites. *Frontiers in Physiology*, 9:103, 2018. ISSN 1664-042X. URL https://www.frontiersin.org/article/10.3389/fphys.2018.00103.

[35] Xanthippi Chatzistavrou, Saalini Velamakanni, Kyle DiRenzo, Anna Lefkelidou, J. Christopher Fenno, Toshihiro Kasuga, Aldo R. Boccaccini, and Petros Papagerakis. Designing dental composites with bioactive and bactericidal properties. *Materials Science and Engineering: C*, 52:267–272, 2015. ISSN 0928-4931. doi: https://doi.org/10.1016/j.msec.2015.03.062. URL http://www.sciencedirect.com/science/article/pii/S0928493115002441.

[36] Hiba Kattan, Xanthippi Chatzistavrou, James Boynton, Joseph Dennison, Peter Yaman, and Petros Papagerakis. Physical properties of an ag-doped bioactive flowable composite resin. *Materials*, 8(8), 2015. ISSN 1996-1944. doi: 10.3390/ma8084668.

[37] Natalia Pajares-Chamorro, John Shook, Neal D. Hammer, and Xanthippi Chatzistavrou. Resurrection of antibiotics that methicillin-resistant staphylococcus aureus resists by silver-doped bioactive glass-ceramic microparticles. *Acta Biomaterialia*, 2019. ISSN 1742-7061. doi: https://doi.org/10.1016/j.actbio.2019.07.012. URL http://www.sciencedirect.com/science/article/pii/S1742706119304921.

[38] Natalia Pajares-Chamorro, Yadav Wagley, Neal Hammer, Kurt Hankenson, and Xanthippi Chatzistavrou. Bioactive glass particles as multi-functional therapeutic carriers against antibiotic-resistant bacteria. *Journal of the American Ceramic Society*, n/a(n/a), 2021. ISSN 0002-7820. doi: https://doi.org/10.1111/jace.17923. URL https://doi.org/10.1111/jace.17923.

[39] Natalia Pajares, Yadav Wagley, Chima V. Maduka, Daniel W. Youngstrom, Alyssa Yeger, Stephen F. Badylak, Neal D. Hammer, Kurt Hankenson, and Xanthippi Chatzistavrou. Silver-doped bioactive glass particles for in vivo bone tissue regeneration and enhanced methicillin-resistant staphylococcus aureus (mrsa) inhibition. *Materials Science and Engineering: C*, page 111693, 2020. ISSN 0928-4931. doi: https://doi.org/10.1016/j.msec.2020.111693. URL http://www.sciencedirect.com/science/article/pii/S0928493120336122.

[40] Logan D. Soule, Natalia Pajares Chomorro, Kayla Chuong, Nathan Mellott, Neal Hammer, Kurt D. Hankenson, and Xanthippi Chatzistavrou. Sol–gel-derived bioactive and antibacterial multi-component thin films by the spin-coating technique. *ACS Biomaterials Science & Engineering*, 2020. doi: 10.1021/acsbiomaterials.0c01140. URL https://doi.org/10.1021/acsbiomaterials.0c01140.

[41] Wang Y-Y, X. Chatzistavrou, D. Faulk, S. Badylak, L. Zheng, P. Papagerakis, L. Ge, H. Liu, and P. Papagerakis. Biological and bactericidal properties of ag-doped bioactive glass in a natural extracellular matrix hydrogel with potential application in dentistry. *European Cells and Materials*, 29:14, 2015. ISSN 1473-2262. doi: 10.22203/eCM.v029a26. URL https://www.ecmjournal.org/papers/vol029/pdf/v029a26.pdf.

[42] Robert C. Bielby, Ioannis S. Christodoulou, Russell S. Pryce, Warwick J. P. Radford, Larry L. Hench, and Julia M. Polak. Time- and concentration-dependent effects of dissolution products of 58s sol–gel bioactive glass on proliferation and differentiation of murine and human osteoblasts. *Tissue Engineering*, 10(7-8):1018–1026, 2004. ISSN 1076-3279. doi: 10.1089/ten.2004.10.1018. URL https://doi.org/10.1089/ten.2004.10.1018.

[43] Chengde Gao, Tingting Liu, Cijun Shuai, and Shuping Peng. Enhancement mechanisms of graphene in nano-58s bioactive glass scaffold: mechanical and biological performance. *Scientific Reports*, 4:4712, 2015. ISSN 2045-2322 (Electronic)2̊045-2322 (Linking). doi: 10.1038/srep04712.

[44] Ourania Menti Goudouri, Xanthippi Chatzistavrou, Eleana Kontonasaki, Nikolaos Kantiranis, Lambrini Papadopoulou, K. Chrissafis, and Konstantinos M. Paraskevopoulos. Study of the bioactive behavior of thermally treated modified 58s bioactive glass. *Key Engineer-*

ing Materials, 396-398:131–134, 2008. ISSN 978-0-87849-353-1. doi: 10.4028/www.scientific.net/kem.396-398.131. URL https://www.scientific.net/KEM.396-398.131.

[45] Ourania Menti Goudouri, Maria Perissi, Eleni Theodosoglou, Lambrini Papadopoulou, Xanthippi Chatzistavrou, Eleana Kontonasaki, Petros Koidis, and Konstantinos M. Paraskevopoulos. The impact of stirring rate on the crystallinity and bioactivity of 58s bioactive glass. *Key Engineering Materials*, 493-494:43–48, 2011. ISSN 1662-9795. doi: 10.4028/www.scientific.net/KEM.493-494.43. URL https://www.scientific.net/KEM.493-494.43.

[46] Julie Elizabeth Gough, Julian R. Jones, and Larry L. Hench. Nodule formation and mineralisation of human primary osteoblasts cultured on a porous bioactive glass scaffold. *Biomaterials*, 25(11):2039–2046, 2004. ISSN 0142-9612. doi: https://doi.org/10.1016/j.biomaterials.2003.07.001. URL http://www.sciencedirect.com/science/article/pii/S0142961203006276.

[47] M. Hamadouche, A. Meunier, D. C. Greenspan, C. Blanchat, J. P. Zhong, G. P. La Torre, and L. Sedel. Long-term in vivo bioactivity and degradability of bulk sol-gel bioactive glasses. *J Biomed Mater Res*, 54(4):560–6, 2001. ISSN 0021-9304 (Print) 0021-9304 (Linking). doi: 10.1002/1097-4636(20010315)54:4<560::AID-JBM130>3.0.CO;2-J. URL https://www.ncbi.nlm.nih.gov/pubmed/11426602.

[48] R. Li, A. E. Clark, and L. L. Hench. An investigation of bioactive glass powders by sol-gel processing. *Journal of Applied Biomaterials*, 2(4):231–239, 1991. ISSN 1045-4861. doi: 10.1002/jab.770020403. URL https://doi.org/10.1002/jab.770020403.

[49] P. Sepulveda, J. R. Jones, and L. L. Hench. In vitro dissolution of melt-derived 45s5 and sol-gel derived 58s bioactive glasses. *Journal of Biomedical Materials Research*, 61(2):301–311, 2002. ISSN 0021-9304. doi: 10.1002/jbm.10207. URL https://doi.org/10.1002/jbm.10207.

[50] Pilar Sepulveda, Julian R. Jones, and Larry L. Hench. Characterization of melt-derived 45s5 and sol-gel–derived 58s bioactive glasses. *Journal of Biomedical Materials Research*, 58(6):734–740, 2002. ISSN 0021-9304. doi: 10.1002/jbm.10026. URL https://doi.org/10.1002/jbm.10026.

[51] M. Kawashita, S. Tsuneyama, F. Miyaji, T. Kokubo, H. Kozuka, and K. Yamamoto. Antibacterial silver-containing silica glass prepared by sol-gel method. *Biomaterials*, 21(4):393–8, 2000. ISSN 0142-9612 (Print) 0142-9612 (Linking). doi: 10.1016/S0142-9612(99)00201-X. URL https://www.ncbi.nlm.nih.gov/pubmed/10656321.

[52] Masakazu Kawashita, Shogo Toda, Hyun-Min Kim, Tadashi Kokubo, and Noriaki Masuda. Preparation of antibacterial silver-doped silica glass microspheres. *Journal of Biomedical Materials Research Part A*, 66A(2):266–274, 2003. ISSN 1549-3296. doi: 10.1002/jbm.a.10547. URL https://doi.org/10.1002/jbm.a.10547.

[53] Noriaki Masuda, Masakazu Kawashita, and Tadashi Kokubo. Antibacterial activity of

silver-doped silica glass microspheres prepared by a sol-gel method. *Journal of Biomedical Materials Research Part B: Applied Biomaterials*, 83B(1):114–120, 2007. ISSN 1552-4973. doi: 10.1002/jbm.b.30773. URL https://doi.org/10.1002/jbm.b.30773.

[54] Y-Y. Wang, X. Chatzistavrou, D. Faulk, L. Zheng, S. Papagerakis, L. Ge, H. Liu, and P. Papagerakis. Biological and bactericidal properties of ag-doped bioactive glass in a natural extracellular matrix hydrogel with potential application in dentistry. *European Cells and Materials*, 29:342–355, 2015. ISSN 1473-2262. doi: 10.22203/eCM.v029a26. URL https://www.ecmjournal.org/papers/vol029/pdf/v029a26.pdf.

[55] R. Cunningham, A. Cockayne, and H. Humphreys. Clinical and molecular aspects of the pathogenesis of staphylococcus aureus bone and joint infections. *Journal of Medical Microbiology*, 44(3):157–164, 1996. ISSN 0022-2615. doi: https://doi.org/10.1099/00222615-44-3-157. URL https://www.microbiologyresearch.org/content/journal/jmm/10.1099/00222615-44-3-157.

[56] William C Callister and David G. Rethwisch. Materials science and engineering: An introduction. page 960, 2010. ISSN 0470419970.

[57] Lorna J. Gibson and Michael F. Ashby. *Cellular Solids: Structure and Properties*. Cambridge Solid State Science Series. Cambridge University Press, Cambridge, 2 edition, 1997. ISBN 9780521499118. doi: DOI:10.1017/CBO9781139878326. URL https://www.cambridge.org/core/books/cellular-solids/BC25789552BAA8E3CAD5E1D105612AB5.

[58] Q. Fu, M. N. Rahaman, B. S. Bal, R. F. Brown, and D. E. Day. Mechanical and in vitro performance of 13-93 bioactive glass scaffolds prepared by a polymer foam replication technique. *Acta Biomater*, 4(6):1854–64, 2008. ISSN 1878-7568 (Electronic) 1742-7061 (Linking). doi: 10.1016/j.actbio.2008.04.019. URL https://www.ncbi.nlm.nih.gov/pubmed/18519173.

[59] Qiang Fu, Eduardo Saiz, Mohamed N. Rahaman, and Antoni P. Tomsia. Toward strong and tough glass and ceramic scaffolds for bone repair. *Advanced Functional Materials*, 23(44):5461–5476, 2013. ISSN 1616-301X. doi: https://doi.org/10.1002/adfm.201301121. URL https://doi.org/10.1002/adfm.201301121.

[60] L. Lefebvre, L. Gremillard, J. Chevalier, R. Zenati, and D. Bernache-Assolant. Sintering behaviour of 45s5 bioactive glass. *Acta Biomaterialia*, 4(6):1894–1903, 2008. ISSN 1742-7061. doi: https://doi.org/10.1016/j.actbio.2008.05.019. URL https://www.sciencedirect.com/science/article/pii/S1742706108001633.

[61] Devis Bellucci and Valeria Cannillo. A novel bioactive glass containing strontium and magnesium with ultra-high crystallization temperature. *Materials Letters*, 213:67–70, 2018. ISSN 0167-577X. doi: https://doi.org/10.1016/j.matlet.2017.11.020. URL https://www.sciencedirect.com/science/article/pii/S0167577X17316397.

[62] Devis Bellucci, Valeria Cannillo, Gianluca Ciardelli, Piergiorgio Gentile, and Antonella Sola. Potassium based bioactive glass for bone tissue engineering. *Ceramics International*, 36(8): 2449–2453, 2010. ISSN 0272-8842. doi: https://doi.org/10.1016/j.ceramint.2010.07.009. URL https://www.sciencedirect.com/science/article/pii/S0272884210002610.

[63] Devis Bellucci, Valeria Cannillo, and Antonella Sola. A new potassium-based bioactive glass: Sintering behaviour and possible applications for bioceramic scaffolds. *Ceramics International*, 37(1):145–157, 2011. ISSN 0272-8842. doi: https://doi.org/10.1016/j.ceramint.2010.08.020. URL https://www.sciencedirect.com/science/article/pii/S0272884210003111.

[64] Devis Bellucci, Elena Veronesi, Massimo Dominici, and Valeria Cannillo. A new bioactive glass with extremely high crystallization temperature and outstanding biological performance. *Materials Science and Engineering: C*, 110:110699, 2020. ISSN 0928-4931. doi: https://doi.org/10.1016/j.msec.2020.110699. URL https://www.sciencedirect.com/science/article/pii/S0928493119338779.

[65] V. Cannillo and A. Sola. Potassium-based composition for a bioactive glass. *Ceramics International*, 35(8):3389–3393, 2009. ISSN 0272-8842. doi: https://doi.org/10.1016/j.ceramint.2009.06.011. URL https://www.sciencedirect.com/science/article/pii/S0272884209002508.

[66] Sayed Mahmood Rabiee, Neda Nazparvar, Misaq Azizian, Daryoosh Vashaee, and Lobat Tayebi. Effect of ion substitution on properties of bioactive glasses: A review. *Ceramics International*, 41(6):7241–7251, 2015. ISSN 0272-8842. doi: https://doi.org/10.1016/j.ceramint.2015.02.140. URL http://www.sciencedirect.com/science/article/pii/S0272884215003818.

[67] S. J. Watts, R. G. Hill, M. D. O'Donnell, and R. V. Law. Influence of magnesia on the structure and properties of bioactive glasses. *Journal of Non-Crystalline Solids*, 356(9): 517–524, 2010. ISSN 0022-3093. doi: https://doi.org/10.1016/j.jnoncrysol.2009.04.074. URL https://www.sciencedirect.com/science/article/pii/S0022309309007704.

[68] Francesco Baino, Monica Ferraris, Oana Bretcanu, Enrica Verné, and Chiara Vitale-Brovarone. Optimization of composition, structure and mechanical strength of bioactive 3-d glass-ceramic scaffolds for bone substitution. *Journal of Biomaterials Applications*, 27(7):872–890, 2011. ISSN 0885-3282. doi: 10.1177/0885328211429193. URL https://doi.org/10.1177/0885328211429193.

[69] Reinhard Conradt. *Thermodynamics and Kinetics of Glass*, pages 51–77. Springer International Publishing, Cham, 2019. ISBN 978-3-319-93728-1. doi: 10.1007/978-3-319-93728-1_2. URL https://doi.org/10.1007/978-3-319-93728-1_2.

[70] Lutgard C. De Jonghe and Mohamed N. Rahaman. *Chapter 4 - 4.1 Sintering of Ceramics*, pages 187–264. Academic Press, Oxford, 2003. ISBN 978-0-12-654640-8. doi: https://doi.org/10.1016/B978-012654640-8/50006-7. URL https://www.sciencedirect.com/science/article/pii/B9780126546408500067.

[71] C. Lara, M. J. Pascual, and A. Durán. Glass-forming ability, sinterability and thermal properties in the systems ro–bao–sio2 (r=mg, zn). *Journal of Non-Crystalline Solids*, 348: 149–155, 2004. ISSN 0022-3093. doi: https://doi.org/10.1016/j.jnoncrysol.2004.08.140. URL http://www.sciencedirect.com/science/article/pii/S0022309304007100.

[72] Satoshi Tanaka. *Solid State Reactions and Sintering*, pages 45–74. Springer Singapore, Singapore, 2019. ISBN 978-981-13-9935-0. doi: 10.1007/978-981-13-9935-0_3. URL https://doi.org/10.1007/978-981-13-9935-0_3.

[73] Marlin Magallanes-Perdomo, Antonio H. De Aza, Isabel Sobrados, Jesús Sanz, Zofia B. Luklinska, and Pilar Pena. Structural changes during crystallization of apatite and wollastonite in the eutectic glass of ca3(po4)2-casio3 system. *Journal of the American Ceramic Society*, 100(9):4288–4304, 2017. ISSN 0002-7820. doi: https://doi.org/10.1111/jace.14943. URL https://doi.org/10.1111/jace.14943.

[74] C. Jeffrey Brinker and George W. Scherer. *CHAPTER 4 - Particulate Sols and Gels*, pages 234–301. Academic Press, San Diego, 1990. ISBN 978-0-08-057103-4. doi: https://doi.org/10.1016/B978-0-08-057103-4.50009-X. URL http://www.sciencedirect.com/science/article/pii/B978008057103450009X.

[75] C. Jeffrey Brinker and George W. Scherer. *CHAPTER 3 - Hydrolysis and Condensation II: Silicates*, pages 96–233. Academic Press, San Diego, 1990. ISBN 978-0-08-057103-4. doi: https://doi.org/10.1016/B978-0-08-057103-4.50008-8. URL http://www.sciencedirect.com/science/article/pii/B9780080571034500088.

[76] C. Jeffrey Brinker and George W. Scherer. *CHAPTER 5 - Gelation*, pages 302–355. Academic Press, San Diego, 1990. ISBN 978-0-08-057103-4. doi: https://doi.org/10.1016/B978-0-08-057103-4.50010-6. URL http://www.sciencedirect.com/science/article/pii/B9780080571034500106.

[77] C. Jeffrey Brinker and George W. Scherer. *CHAPTER 6 - Aging of Gels*, pages 356–405. Academic Press, San Diego, 1990. ISBN 978-0-08-057103-4. doi: https://doi.org/10.1016/B978-0-08-057103-4.50011-8. URL http://www.sciencedirect.com/science/article/pii/B9780080571034500118.

[78] C. Jeffrey Brinker and George W. Scherer. *CHAPTER 8 - Drying*, pages 452–513. Academic Press, San Diego, 1990. ISBN 978-0-08-057103-4. doi: https://doi.org/10.1016/B978-0-08-057103-4.50013-1. URL http://www.sciencedirect.com/science/article/pii/B9780080571034500131.

[79] Priya Saravanapavan, Julian R. Jones, Russell S. Pryce, and Larry L. Hench. Bioactivity of gel–glass powders in the cao-sio2 system: A comparison with ternary (cao-p2p5-sio2) and quaternary glasses (sio2-cao-p2o5-na2o). *Journal of Biomedical Materials Research Part A*, 66A(1):110–119, 2003. ISSN 1549-3296. doi: 10.1002/jbm.a.10532. URL https://doi.org/10.1002/jbm.a.10532.

[80] Lakshmi M. Mukundan, Remya Nirmal, Dhanesh Vaikkath, and Prabha D. Nair. A new synthesis route to high surface area sol gel bioactive glass through alcohol washing: a preliminary study. *Biomatter*, 3(2):e24288, 2013. ISSN 2159-2535 2159-2527. doi: 10.4161/biom.24288. URL https://pubmed.ncbi.nlm.nih.gov/23512012https://www.ncbi.nlm.nih.gov/pmc/articles/PMC3749803/.

[81] L. L. Hench, G. P. LaTorre, and Ö H. Andersson. *The Kinetics of Bioactive Ceramics Part III: Surface Reactions for Bioactive Glasses compared with an Inactive Glass*, pages 155–162. Butterworth-Heinemann, 1991. ISBN 978-0-7506-0269-3. doi: https://doi.org/10.1016/B978-0-7506-0269-3.50025-6. URL http://www.sciencedirect.com/science/article/pii/B9780750602693500256.

[82] L. L. Hench and J. K. West. *Biological Applications of Bioactive Glasses*. Life chemistry reports. Harwood Academic Publishers, 1996. URL https://books.google.com/books?id=SU_njwEACAAJ.

[83] Larry L. Hench. Bioceramics: From concept to clinic. *Journal of the American Ceramic Society*, 74(7):1487–1510, 1991. ISSN 0002-7820. doi: 10.1111/j.1151-2916.1991.tb07132.x. URL https://doi.org/10.1111/j.1151-2916.1991.tb07132.x.

[84] Larry L. Hench and Örjan Andersson. *BIOACTIVE GLASSES*, volume Volume 1 of *Advanced Series in Ceramics*, pages 41–62. WORLD SCIENTIFIC, 1993. ISBN 978-981-02-1400-5. doi: doi:10.1142/9789814317351_000310.1142/9789814317351_0003. URL https://doi.org/10.1142/9789814317351_0003.

[85] Scott J. Hollister. Porous scaffold design for tissue engineering. *Nature Materials*, 4:518, 2005. doi: 10.1038/nmat1421. URL http://dx.doi.org/10.1038/nmat1421.

[86] J. R. Jones and L. L. Hench. Factors affecting the structure and properties of bioactive foam scaffolds for tissue engineering. *J Biomed Mater Res B Appl Biomater*, 68(1):36–44, 2004. ISSN 1552-4973 (Print) 1552-4973 (Linking). doi: 10.1002/jbm.b.10071. URL https://www.ncbi.nlm.nih.gov/pubmed/14689494.

[87] Vassilis Karageorgiou and David Kaplan. Porosity of 3d biomaterial scaffolds and osteogenesis. *Biomaterials*, 26(27):5474–5491, 2005. ISSN 0142-9612. doi: https://doi.org/10.1016/j.biomaterials.2005.02.002. URL http://www.sciencedirect.com/science/article/pii/S0142961205001511.

[88] Cuijun Deng, Jiang Chang, and Chengtie Wu. Bioactive scaffolds for osteochondral regeneration. *Journal of Orthopaedic Translation*, 17:15–25, 2019. ISSN 2214-031X. doi: https://doi.org/10.1016/j.jot.2018.11.006. URL http://www.sciencedirect.com/science/article/pii/S2214031X18301700.

[89] Nora T. Khanarian, Nora M. Haney, Rachel A. Burga, and Helen H. Lu. A functional agarose-hydroxyapatite scaffold for osteochondral interface regeneration. *Biomaterials*, 33(21):5247–

5258, 2012. ISSN 0142-9612. doi: https://doi.org/10.1016/j.biomaterials.2012.03.076. URL http://www.sciencedirect.com/science/article/pii/S0142961212003894.

[90] Tetsushi Taguchi, Yu Sawabe, Hisatoshi Kobayashi, Yusuke Moriyoshi, Kazunori Kataoka, and Junzo Tanaka. Preparation and characterization of osteochondral scaffold. *Materials Science and Engineering: C*, 24(6):881–885, 2004. ISSN 0928-4931. doi: https://doi.org/10.1016/j.msec.2004.08.033. URL http://www.sciencedirect.com/science/article/pii/S0928493104001122.

[91] Francesca Tallia, Laura Russo, Siwei Li, Alexandra L. H. Orrin, Xiaomeng Shi, Shu Chen, Joseph A. M. Steele, Sylvain Meille, Jérôme Chevalier, Peter D. Lee, Molly M. Stevens, Laura Cipolla, and Julian R. Jones. Bouncing and 3d printable hybrids with self-healing properties. *Materials Horizons*, 5(5):849–860, 2018. ISSN 2051-6347. doi: 10.1039/C8MH00027A. URL http://dx.doi.org/10.1039/C8MH00027A.

[92] Sunny A. Abbah, Christopher X. F. Lam, Kumarsing A. Ramruttun, James C. H. Goh, and Hee-Kit Wong. Autogenous bone marrow stromal cell sheets-loaded mpcl/tcp scaffolds induced osteogenesis in a porcine model of spinal interbody fusion. *Tissue Engineering Part A*, 17(5-6):809–817, 2010. ISSN 1937-3341. doi: 10.1089/ten.tea.2010.0255. URL https://doi.org/10.1089/ten.tea.2010.0255.

[93] Sunny A. Abbah, Christopher X. L. Lam, Dietmar W. Hutmacher, James C. H. Goh, and Hee-Kit Wong. Biological performance of a polycaprolactone-based scaffold used as fusion cage device in a large animal model of spinal reconstructive surgery. *Biomaterials*, 30(28):5086–5093, 2009. ISSN 0142-9612. doi: https://doi.org/10.1016/j.biomaterials.2009.05.067. URL http://www.sciencedirect.com/science/article/pii/S0142961209005973.

[94] Lucas D. Albrecht, Stephen W. Sawyer, and Pranav Soman. Developing 3d scaffolds in the field of tissue engineering to treat complex bone defects. *3D Printing and Additive Manufacturing*, 3(2):106–112, 2016. ISSN 2329-7662. doi: 10.1089/3dp.2016.0006. URL https://doi.org/10.1089/3dp.2016.0006.

[95] Milda Alksne, Migle Kalvaityte, Egidijus Simoliunas, Ieva Rinkunaite, Ieva Gendviliene, Janis Locs, Vygandas Rutkunas, and Virginija Bukelskiene. In vitro comparison of 3d printed polylactic acid/hydroxyapatite and polylactic acid/bioglass composite scaffolds: Insights into materials for bone regeneration. *Journal of the Mechanical Behavior of Biomedical Materials*, 104:103641, 2020. ISSN 1751-6161. doi: https://doi.org/10.1016/j.jmbbm.2020.103641. URL http://www.sciencedirect.com/science/article/pii/S1751616119316613.

[96] A. Berner, J. Henkel, M. A. Woodruff, S. Saifzadeh, G. Kirby, S. Zaiss, J. Gohlke, J. C. Reichert, M. Nerlich, M. A. Schuetz, and D. W. Hutmacher. Scaffold–cell bone engineering in a validated preclinical animal model: precursors vs differentiated cell source. *Journal of Tissue Engineering and Regenerative Medicine*, 11(7):2081–2089, 2017. ISSN 1932-6254. doi: 10.1002/term.2104. URL https://doi.org/10.1002/term.2104.

[97] Arne Berner, Jan Henkel, Maria A. Woodruff, Roland Steck, Michael Nerlich, Michael A. Schuetz, and Dietmar W. Hutmacher. Delayed minimally invasive injection of allogenic bone marrow stromal cell sheets regenerates large bone defects in an ovine preclinical animal model. *STEM CELLS Translational Medicine*, 4(5):503–512, 2015. ISSN 2157-6564. doi: 10.5966/sctm.2014-0244. URL https://doi.org/10.5966/sctm.2014-0244.

[98] Arnaud Bruyas, Frank Lou, Alexander M. Stahl, Michael Gardner, William Maloney, Stuart Goodman, and Yunzhi Peter Yang. Systematic characterization of 3d-printed pcl/β-tcp scaffolds for biomedical devices and bone tissue engineering: Influence of composition and porosity. *Journal of Materials Research*, 33(14):1948–1959, 2018. ISSN 0884-2914. doi: 10.1557/jmr.2018.112. URL https://rdcu.be/cFDpR.

[99] Gang Chen, Ning Chen, and Qi Wang. Fabrication and properties of poly(vinyl alcohol)/β-tricalcium phosphate composite scaffolds via fused deposition modeling for bone tissue engineering. *Composites Science and Technology*, 172:17–28, 2019. ISSN 0266-3538. doi: https://doi.org/10.1016/j.compscitech.2019.01.004. URL http://www.sciencedirect.com/science/article/pii/S0266353818328094.

[100] A. Cipitria, W. Wagermaier, P. Zaslansky, H. Schell, J. C. Reichert, P. Fratzl, D. W. Hutmacher, and G. N. Duda. Bmp delivery complements the guiding effect of scaffold architecture without altering bone microstructure in critical-sized long bone defects: A multiscale analysis. *Acta Biomaterialia*, 23:282–294, 2015. ISSN 1742-7061. doi: https://doi.org/10.1016/j.actbio.2015.05.015. URL http://www.sciencedirect.com/science/article/pii/S1742706115002391.

[101] Amaia Cipitria, Claudia Lange, Hanna Schell, Wolfgang Wagermaier, Johannes C. Reichert, Dietmar W. Hutmacher, Peter Fratzl, and Georg N. Duda. Porous scaffold architecture guides tissue formation. *Journal of Bone and Mineral Research*, 27(6):1275–1288, 2012. ISSN 0884-0431. doi: 10.1002/jbmr.1589. URL https://doi.org/10.1002/jbmr.1589.

[102] Chunming Ding, Zhiguang Qiao, Wenbo Jiang, Haowei Li, Jianhe Wei, Guangdong Zhou, and Kerong Dai. Regeneration of a goat femoral head using a tissue-specific, biphasic scaffold fabricated with cad/cam technology. *Biomaterials*, 34(28):6706–6716, 2013. ISSN 0142-9612. doi: https://doi.org/10.1016/j.biomaterials.2013.05.038. URL http://www.sciencedirect.com/science/article/pii/S0142961213006145.

[103] Marco Domingos, Antonio Gloria, Jorge Coelho, Paulo Bartolo, and Joaquim Ciurana. Three-dimensional printed bone scaffolds: The role of nano/micro-hydroxyapatite particles on the adhesion and differentiation of human mesenchymal stem cells. *Proceedings of the Institution of Mechanical Engineers, Part H: Journal of Engineering in Medicine*, 231 (6):555–564, 2017. ISSN 0954-4119. doi: 10.1177/0954411916680236. URL https://doi.org/10.1177/0954411916680236.

[104] Dietmar Drummer, Sandra Cifuentes-Cuéllar, and Dominik Rietzel. Suitability of pla/tcp for fused deposition modeling. *Rapid Prototyping Journal*, 18(6):500–507, 2012.

ISSN 1355-2546. doi: 10.1108/13552541211272045. URL https://doi.org/10.1108/13552541211272045.

[105] Gleb E. Dubinenko, Alexey L. Zinoviev, Evgeniy N. Bolbasov, Viktor T. Novikov, and Sergey I. Tverdokhlebov. Preparation of poly(l-lactic acid)/hydroxyapatite composite scaffolds by fused deposit modeling 3d printing. *Materials Today: Proceedings*, 22:228–234, 2020. ISSN 2214-7853. doi: https://doi.org/10.1016/j.matpr.2019.08.092. URL http://www.sciencedirect.com/science/article/pii/S221478531933069X.

[106] Saeid Esmaeili, Hossein Akbari Aghdam, Mehdi Motififard, Saeed Saber-Samandari, Amir Hussein Montazeran, Mohammad Bigonah, Erfan Sheikhbahaei, and Amirsalar Khandan. A porous polymeric–hydroxyapatite scaffold used for femur fractures treatment: fabrication, analysis, and simulation. *European Journal of Orthopaedic Surgery & Traumatology*, 30(1):123–131, 2020. ISSN 1432-1068. doi: 10.1007/s00590-019-02530-3. URL https://doi.org/10.1007/s00590-019-02530-3.

[107] Carola Esposito Corcione, Francesca Gervaso, Francesca Scalera, Sanosh Kunjalukkal Padmanabhan, Marta Madaghiele, Francesco Montagna, Alessandro Sannino, Antonio Licciulli, and Alfonso Maffezzoli. Highly loaded hydroxyapatite microsphere/ pla porous scaffolds obtained by fused deposition modelling. *Ceramics International*, 45(2, Part B): 2803–2810, 2019. ISSN 0272-8842. doi: https://doi.org/10.1016/j.ceramint.2018.07.297. URL http://www.sciencedirect.com/science/article/pii/S027288421832039X.

[108] Boyang Huang, Guilherme Caetano, Cian Vyas, J. Jonny Blaker, Carl Diver, and Paulo Bártolo. Polymer-ceramic composite scaffolds: The effect of hydroxyapatite and β-tricalcium phosphate. *Materials*, 11(1), 2018. ISSN 1996-1944. doi: 10.3390/ma11010129.

[109] Marian Janek, Veronika Žilinská, Vladimír Kovár, Zora Hajdúchová, Katarína Tomanová, Peter Peciar, Peter Veteška, Tatiana Gabošová, Roman Fialka, Jozef Feranc, Leona Omaníková, Roderik Plavec, and Ľuboš Bača. Mechanical testing of hydroxyapatite filaments for tissue scaffolds preparation by fused deposition of ceramics. *Journal of the European Ceramic Society*, 2020. ISSN 0955-2219. doi: https://doi.org/10.1016/j.jeurceramsoc.2020.01.061.

[110] Wenbo Jiang, Jun Shi, Wei Li, and Kang Sun. Three dimensional melt-deposition of polycaprolactone/bio-derived hydroxyapatite composite into scaffold for bone repair. *Journal of Biomaterials Science, Polymer Edition*, 24(5):539–550, 2013. ISSN 0920-5063. doi: 10.1080/09205063.2012.698894. URL https://doi.org/10.1080/09205063.2012.698894.

[111] Zhiwei Jiao, Bin Luo, Shengyi Xiang, Haopeng Ma, Yuan Yu, and Weimin Yang. 3d printing of ha / pcl composite tissue engineering scaffolds. *Advanced Industrial and Engineering Polymer Research*, 2(4):196–202, 2019. ISSN 2542-5048. doi: https://doi.org/10.1016/j.aiepr.2019.09.003. URL http://www.sciencedirect.com/science/article/pii/S2542504819300363.

[112] Jinku Kim, Sean McBride, Brandi Tellis, Pedro Alvarez-Urena, Young-Hye Song, David D. Dean, Victor L. Sylvia, Hoda Elgendy, Joo Ong, and Jeffrey O. Hollinger. Rapid-

prototyped plga/β-tcp/hydroxyapatite nanocomposite scaffolds in a rabbit femoral defect model. *Biofabrication*, 4(2):025003, 2012. ISSN 1758-5082 1758-5090. doi: 10.1088/1758-5082/4/2/025003. URL http://dx.doi.org/10.1088/1758-5082/4/2/025003.

[113] Sun-Jong Kim, Myung-Rae Kim, Jin-Sub Oh, Inho Han, and Sang-Wan Shin. Effects of polycaprolactone-tricalcium phosphate, recombinant human bone morphogenetic protein-2 and dog mesenchymal stem cells on bone formation: Pilot study in dogs. *Yonsei Med J*, 50 (6):825–831, 2009. ISSN 0513-5796. URL http://synapse.koreamed.org/DOIx.php?id=10.3349%2Fymj.2009.50.6.825.

[114] Jyrki Korpela, Anne Kokkari, Harri Korhonen, Minna Malin, Timo Närhi, and Jukka Seppälä. Biodegradable and bioactive porous scaffold structures prepared using fused deposition modeling. *Journal of Biomedical Materials Research Part B: Applied Biomaterials*, 101B(4):610–619, 2013. ISSN 1552-4973. doi: 10.1002/jbm.b.32863. URL https://doi.org/10.1002/jbm.b.32863.

[115] Artem B. Kutikov, Anvesh Gurijala, and Jie Song. Rapid prototyping amphiphilic polymer/hydroxyapatite composite scaffolds with hydration-induced self-fixation behavior. *Tissue Engineering Part C: Methods*, 21(3):229–241, 2014. ISSN 1937-3384. doi: 10.1089/ten.tec.2014.0213. URL https://doi.org/10.1089/ten.tec.2014.0213.

[116] Christopher X. F. Lam, Dietmar W. Hutmacher, Jan-Thorsten Schantz, Maria Ann Woodruff, and Swee Hin Teoh. Evaluation of polycaprolactone scaffold degradation for 6 months in vitro and in vivo. *Journal of Biomedical Materials Research Part A*, 90A(3):906–919, 2009. ISSN 1549-3296. doi: 10.1002/jbm.a.32052. URL https://doi.org/10.1002/jbm.a.32052.

[117] Yi Li, Zhi-gang Wu, Xiao-kang Li, Zheng Guo, Su-hua Wu, Yong-quan Zhang, Lei Shi, Swee-hin Teoh, Yu-chun Liu, and Zhi-yong Zhang. A polycaprolactone-tricalcium phosphate composite scaffold as an autograft-free spinal fusion cage in a sheep model. *Biomaterials*, 35 (22):5647–5659, 2014. ISSN 0142-9612. doi: https://doi.org/10.1016/j.biomaterials.2014.03.075. URL http://www.sciencedirect.com/science/article/pii/S0142961214003500.

[118] Daniel Muller, Harvey Chim, Augustinus Bader, Matthew Whiteman, and Jan-Thorsten Schantz. Vascular guidance: Microstructural scaffold patterning for inductive neovascularization. *Stem Cells International*, 2011:547247, 2011. ISSN 1687-966X. doi: 10.4061/2011/547247. URL https://doi.org/10.4061/2011/547247.

[119] P. Nevado, A. Lopera, V. Bezzon, M. R. Fulla, J. Palacio, M. A. Zaghete, G. Biasotto, A. Montoya, J. Rivera, S. M. Robledo, H. Estupiñan, C. Paucar, and C. Garcia. Preparation and in vitro evaluation of pla/biphasic calcium phosphate filaments used for fused deposition modelling of scaffolds. *Materials Science and Engineering: C*, 114: 111013, 2020. ISSN 0928-4931. doi: https://doi.org/10.1016/j.msec.2020.111013. URL http://www.sciencedirect.com/science/article/pii/S0928493119337129.

[120] Vincent Diong Weng Nga, Jing Lim, David Kim Seng Choy, Mya Aye Nyein, Jia Lu, Ning

Chou, Tseng Tsai Yeo, and Swee-Hin Teoh. Effects of polycaprolactone-based scaffolds on the blood–brain barrier and cerebral inflammation. *Tissue Engineering Part A*, 21(3-4): 647–653, 2014. ISSN 1937-3341. doi: 10.1089/ten.tea.2013.0779. URL https://doi.org/10.1089/ten.tea.2013.0779.

[121] Ethan Nyberg, Alexandra Rindone, Amir Dorafshar, and Warren L. Grayson. Comparison of 3d-printed poly-ϵ-caprolactone scaffolds functionalized with tricalcium phosphate, hydroxyapatite, bio-oss, or decellularized bone matrix. *Tissue Engineering Part A*, 23(11-12):503–514, 2016. ISSN 1937-3341. doi: 10.1089/ten.tea.2016.0418. URL https://doi.org/10.1089/ten.tea.2016.0418.

[122] Bankole I. Oladapo, S. A. Zahedi, and A. O. M. Adeoye. 3d printing of bone scaffolds with hybrid biomaterials. *Composites Part B: Engineering*, 158:428–436, 2019. ISSN 1359-8368. doi: https://doi.org/10.1016/j.compositesb.2018.09.065. URL http://www.sciencedirect.com/science/article/pii/S1359836818324004.

[123] T. S. Petrovskaya, N. E. Toropkov, E. G. Mironov, and F. Azarmi. 3d printed biocompatible polylactide-hydroxyapatite based material for bone implants. *Materials and Manufacturing Processes*, 33(16):1899–1904, 2018. ISSN 1042-6914. doi: 10.1080/10426914.2018.1476764. URL https://doi.org/10.1080/10426914.2018.1476764.

[124] Patrina S. P. Poh, Dietmar W. Hutmacher, Molly M. Stevens, and Maria A. Woodruff. Fabrication and in vitro characterization of bioactive glass composite scaffolds for bone regeneration. *Biofabrication*, 5(4):045005, 2013. ISSN 1758-5082 1758-5090. doi: 10.1088/1758-5082/5/4/045005. URL http://dx.doi.org/10.1088/1758-5082/5/4/045005.

[125] Bina Rai, Jane L. Lin, Zophia X. H. Lim, Robert E. Guldberg, Dietmar W. Hutmacher, and Simon M. Cool. Differences between in vitro viability and differentiation and in vivo bone-forming efficacy of human mesenchymal stem cells cultured on pcl–tcp scaffolds. *Biomaterials*, 31(31):7960–7970, 2010. ISSN 0142-9612. doi: https://doi.org/10.1016/j.biomaterials.2010.07.001. URL http://www.sciencedirect.com/science/article/pii/S0142961210008422.

[126] Bina Rai, Megan E. Oest, Ken M. Dupont, Kee H. Ho, Swee H. Teoh, and Robert E. Guldberg. Combination of platelet-rich plasma with polycaprolactone-tricalcium phosphate scaffolds for segmental bone defect repair. *Journal of Biomedical Materials Research Part A*, 81A(4):888–899, 2007. ISSN 1549-3296. doi: 10.1002/jbm.a.31142. URL https://doi.org/10.1002/jbm.a.31142.

[127] Nishant Ranjan, Rupinder Singh, and I. P. S. Ahuja. Development of pla-hap-cs-based biocompatible functional prototype: A case study. *Journal of Thermoplastic Composite Materials*, 33(3):305–323, 2018. ISSN 0892-7057. doi: 10.1177/0892705718805531. URL https://doi.org/10.1177/0892705718805531.

[128] Nishant Ranjan, Rupinder Singh, I. P. S. Ahuja, Ranvijay Kumar, Jatenderpal Singh, Anita K. Verma, and Ankita Leekha. On 3d printed scaffolds for orthopedic tissue engineering

applications. *SN Applied Sciences*, 2(2):192, 2020. ISSN 2523-3971. doi: 10.1007/s42452-020-1936-8. URL https://doi.org/10.1007/s42452-020-1936-8.

[129] Nishant Ranjan, Rupinder Singh, I. P. S. Ahuja, and Jatenderpal Singh. *Fabrication of PLA-HAp-CS Based Biocompatible and Biodegradable Feedstock Filament Using Twin Screw Extrusion*, pages 325–345. Springer International Publishing, Cham, 2019. ISBN 978-3-319-91713-9. doi: 10.1007/978-3-319-91713-9_11. URL https://doi.org/10.1007/978-3-319-91713-9_11.

[130] Johannes C. Reichert, Amaia Cipitria, Devakara R. Epari, Siamak Saifzadeh, Pushpanjali Krishnakanth, Arne Berner, Maria A. Woodruff, Hanna Schell, Manav Mehta, Michael A. Schuetz, Georg N. Duda, and Dietmar W. Hutmacher. A tissue engineering solution for segmental defect regeneration in load-bearing long bones. *Science Translational Medicine*, 4(141):141ra93, 2012. doi: 10.1126/scitranslmed.3003720. URL http://stm.sciencemag.org/content/4/141/141ra93.abstract.

[131] S. Sahmani, A. Khandan, S. Esmaeili, S. Saber-Samandari, M. Ghadiri Nejad, and M. M. Aghdam. Calcium phosphate-pla scaffolds fabricated by fused deposition modeling technique for bone tissue applications: Fabrication, characterization and simulation. *Ceramics International*, 46(2):2447–2456, 2020. ISSN 0272-8842. doi: https://doi.org/10.1016/j.ceramint.2019.09.238. URL http://www.sciencedirect.com/science/article/pii/S0272884219327750.

[132] A. A. Sawyer, S. J. Song, E. Susanto, P. Chuan, C. X. F. Lam, M. A. Woodruff, D. W. Hutmacher, and S. M. Cool. The stimulation of healing within a rat calvarial defect by mpcl–tcp/collagen scaffolds loaded with rhbmp-2. *Biomaterials*, 30(13):2479–2488, 2009. ISSN 0142-9612. doi: https://doi.org/10.1016/j.biomaterials.2008.12.055. URL http://www.sciencedirect.com/science/article/pii/S0142961208010582.

[133] Jan-Thorsten Schantz, Arthur Brandwood, Dietmar Werner Hutmacher, Hwei Ling Khor, and Katharina Bittner. Osteogenic differentiation of mesenchymal progenitor cells in computer designed fibrin-polymer-ceramic scaffolds manufactured by fused deposition modeling. *Journal of Materials Science: Materials in Medicine*, 16(9):807–819, 2005. ISSN 1573-4838. doi: 10.1007/s10856-005-3584-3. URL https://doi.org/10.1007/s10856-005-3584-3.

[134] F. S. Senatov, K. V. Niaza, A. A. Stepashkin, and S. D. Kaloshkin. Low-cycle fatigue behavior of 3d-printed pla-based porous scaffolds. *Composites Part B: Engineering*, 97:193–200, 2016. ISSN 1359-8368. doi: https://doi.org/10.1016/j.compositesb.2016.04.067. URL http://www.sciencedirect.com/science/article/pii/S1359836816305194.

[135] F. S. Senatov, K. V. Niaza, M. Yu Zadorozhnyy, A. V. Maksimkin, S. D. Kaloshkin, and Y. Z. Estrin. Mechanical properties and shape memory effect of 3d-printed pla-based porous scaffolds. *Journal of the Mechanical Behavior of Biomedical Materials*, 57:139–148, 2016. ISSN 1751-6161. doi: https://doi.org/10.1016/j.jmbbm.2015.11.036. URL http://www.sciencedirect.com/science/article/pii/S1751616115004543.

[136] Jong-Jae Sun, Chang-Jun Bae, Young-Hag Koh, Hyoun-Ee Kim, and Hae-Won Kim. Fabrication of hydroxyapatite-poly(ϵ-caprolactone) scaffolds by a combination of the extrusion and bi-axial lamination processes. *Journal of Materials Science: Materials in Medicine*, 18(6):1017–1023, 2007. ISSN 1573-4838. doi: 10.1007/s10856-007-0155-9. URL https://doi.org/10.1007/s10856-007-0155-9.

[137] Ghifari Syuhada, Ghiska Ramahdita, A. J. Rahyussalim, and Yudan Whulanza. Multimaterial poly(lactic acid) scaffold fabricated via fused deposition modeling and direct hydroxyapatite injection as spacers in laminoplasty. *AIP Conference Proceedings*, 1933(1): 020008, 2018. ISSN 0094-243X. doi: 10.1063/1.5023942. URL https://aip.scitation.org/doi/abs/10.1063/1.5023942.

[138] Erin Yiling Teo, Shin-Yeu Ong, Mark Seow Khoon Chong, Zhiyong Zhang, Jia Lu, Shabbir Moochhala, Bow Ho, and Swee-Hin Teoh. Polycaprolactone-based fused deposition modeled mesh for delivery of antibacterial agents to infected wounds. *Biomaterials*, 32(1):279–287, 2011. ISSN 0142-9612. doi: https://doi.org/10.1016/j.biomaterials.2010.08.089. URL http://www.sciencedirect.com/science/article/pii/S0142961210011270.

[139] Nuttawut Thuaksuban, Rungrot Pannak, Pleumjit Boonyaphiphat, and Naruporn Monmaturapoj. In vivo biocompatibility and degradation of novel polycaprolactone-biphasic calcium phosphate scaffolds used as a bone substitute. *Bio-Medical Materials and Engineering*, 29: 253–267, 2018. ISSN 1878-3619. doi: 10.3233/BME-171727.

[140] Ning Xu, Xiaojian Ye, Daixu Wei, Jian Zhong, Yuyun Chen, Guohua Xu, and Dannong He. 3d artificial bones for bone repair prepared by computed tomography-guided fused deposition modeling for bone repair. *ACS Applied Materials & Interfaces*, 6(17):14952–14963, 2014. ISSN 1944-8244. doi: 10.1021/am502716t. URL https://doi.org/10.1021/am502716t.

[141] Yiwen Xuan, Hua Tang, Bin Wu, Xinyu Ding, Zhongyuan Lu, Wei Li, and Zhifei Xu. A specific groove design for individualized healing in a canine partial sternal defect model by a polycaprolactone/hydroxyapatite scaffold coated with bone marrow stromal cells. *Journal of Biomedical Materials Research Part A*, 102(10):3401–3408, 2014. ISSN 1549-3296. doi: 10.1002/jbm.a.35012. URL https://doi.org/10.1002/jbm.a.35012.

[142] A. Yeo, C. Cheok, S. H. Teoh, Z. Y. Zhang, D. Buser, and D. D. Bosshardt. Lateral ridge augmentation using a pcl-tcp scaffold in a clinically relevant but challenging micropig model. *Clinical Oral Implants Research*, 23(12):1322–1332, 2012. ISSN 0905-7161. doi: 10.1111/j.1600-0501.2011.02366.x. URL https://doi.org/10.1111/j.1600-0501.2011.02366.x.

[143] Alvin Yeo, Wah Jie Wong, and Swee-Hin Teoh. Surface modification of pcl-tcp scaffolds in rabbit calvaria defects: Evaluation of scaffold degradation profile, biomechanical properties and bone healing patterns. *Journal of Biomedical Materials Research Part A*, 93A(4):1358–1367, 2010. ISSN 1549-3296. doi: 10.1002/jbm.a.32633. URL https://doi.org/10.1002/jbm.a.32633.

[144] Iwan Zein, Dietmar W. Hutmacher, Kim Cheng Tan, and Swee Hin Teoh. Fused deposition modeling of novel scaffold architectures for tissue engineering applications. *Biomaterials*, 23(4):1169–1185, 2002. ISSN 0142-9612. doi: https://doi.org/10.1016/S0142-9612(01)00232-0. URL http://www.sciencedirect.com/science/article/pii/S0142961201002320.

[145] Yefang Zhou, Fulin Chen, Saey Tuan Ho, Maria Ann Woodruff, Tit Meng Lim, and Dietmar W. Hutmacher. Combined marrow stromal cell-sheet techniques and high-strength biodegradable composite scaffolds for engineered functional bone grafts. *Biomaterials*, 28(5):814–824, 2007. ISSN 0142-9612. doi: https://doi.org/10.1016/j.biomaterials.2006.09.032. URL http://www.sciencedirect.com/science/article/pii/S0142961206008374.

[146] Patrick Judeinstein and Clément Sanchez. Hybrid organic–inorganic materials: a land of multidisciplinarity. *Journal of Materials Chemistry*, 6(4):511–525, 1996. ISSN 0959-9428. doi: 10.1039/JM9960600511. URL http://dx.doi.org/10.1039/JM9960600511.

[147] Bruce M. Novak. Hybrid nanocomposite materials—between inorganic glasses and organic polymers. *Advanced Materials*, 5(6):422–433, 1993. ISSN 0935-9648. doi: 10.1002/adma.19930050603. URL https://doi.org/10.1002/adma.19930050603.

[148] Cédric Bossard, Henri Granel, Édouard Jallot, Valérie Montouillout, Franck Fayon, Jérémy Soulié, Christophe Drouet, Yohann Wittrant, and Jonathan Lao. Mechanism of calcium incorporation inside sol–gel silicate bioactive glass and the advantage of using ca(oh)2 over other calcium sources. *ACS Biomaterials Science & Engineering*, 5(11):5906–5915, 2019. doi: 10.1021/acsbiomaterials.9b01245. URL https://doi.org/10.1021/acsbiomaterials.9b01245.

[149] A. Rámila, F. Balas, and M. Vallet-Regí. Synthesis routes for bioactive sol-gel glasses: Alkoxides versus nitrates. *Chemistry of Materials*, 14(2):542–548, 2002. ISSN 0897-4756. doi: 10.1021/cm0110876. URL https://doi.org/10.1021/cm0110876.

[150] M.M. Pereira, J.R. Jones, and L.L. Hench. Bioactive glass and hybrid scaffolds prepared by sol–gel method for bone tissue engineering. *Advances in Applied Ceramics*, 104:35–42, 2005. doi: 10.1179/174367605225011034.

[151] Tobias Fey, Ulf Betke, Stefan Rannabauer, and Michael Scheffler. Reticulated replica ceramic foams: Processing, functionalization, and characterization. *Advanced Engineering Materials*, 19(10):1700369, 2017. ISSN 1438-1656. doi: https://doi.org/10.1002/adem.201700369. URL https://doi.org/10.1002/adem.201700369.

[152] Prakash Jayabalan, Andrea R. Tan, Mohammed N. Rahaman, B. Sonny Bal, Clark T. Hung, and James L. Cook. Bioactive glass 13-93 as a subchondral substrate for tissue-engineered osteochondral constructs: A pilot study. *Clinical Orthopaedics and Related Research®*, 469(10):2754–2763, 2011. ISSN 1528-1132. doi: 10.1007/s11999-011-1818-x. URL https://doi.org/10.1007/s11999-011-1818-x.

[153] T Mantsos, X Chatzistavrou, J A Roether, L Hupa, H Arstila, and A R Boccaccini. Non-crystalline composite tissue engineering scaffolds using boron-containing bioactive glass and poly(d,l-lactic acid) coatings. *Biomedical Materials*, 4:055002, 2009. ISSN 1748-6041. doi: 10.1088/1748-6041/4/5/055002.

[154] C. Wu, W. Fan, Y. Zhu, M. Gelinsky, J. Chang, G. Cuniberti, V. Albrecht, T. Friis, and Y. Xiao. Multifunctional magnetic mesoporous bioactive glass scaffolds with a hierarchical pore structure. *Acta Biomater*, 7(10):3563–72, 2011. ISSN 1878-7568 (Electronic) 1742-7061 (Linking). doi: 10.1016/j.actbio.2011.06.028. URL https://www.ncbi.nlm.nih.gov/pubmed/21745610.

[155] Chengtie Wu, Richard Miron, Anton Sculean, Stefan Kaskel, Thomas Doert, Renate Schulze, and Yufeng Zhang. Proliferation, differentiation and gene expression of osteoblasts in boron-containing associated with dexamethasone deliver from mesoporous bioactive glass scaffolds. *Biomaterials*, 32:7068–7078, 2011. ISSN 1878-5905. doi: 10.1016/j.biomaterials.2011.06.009.

[156] Chengtie Wu, Yinghong Zhou, Wei Fan, Pingping Han, Jiang Chang, Jones Yuen, Meili Zhang, and Yin Xiao. Hypoxia-mimicking mesoporous bioactive glass scaffolds with controllable cobalt ion release for bone tissue engineering. *Biomaterials*, 33:2076–2085, 2012. ISSN 8621524139. doi: 10.1016/j.biomaterials.2011.11.042.

[157] Y. F. Zhu, F. J. Shang, B. Li, Y. Dong, Y. F. Liu, M. R. Lohe, N. Hanagata, and S. Kaskel. Magnetic mesoporous bioactive glass scaffolds: preparation, physicochemistry and biological properties. *Journal of Materials Chemistry B*, 1(9):1279–1288, 2013. ISSN 2050-750x. doi: 10.1039/c2tb00262k. URL <GotoISI>://WOS:000314801900011.

[158] Y. F. Zhu, C. T. Wu, Y. Ramaswamy, E. Kockrick, P. Simon, S. Kaskel, and H. Zrelqat. Preparation, characterization and in vitro bioactivity of mesoporous bioactive glasses (mbgs) scaffolds for bone tissue engineering. *Microporous and Mesoporous Materials*, 112(1-3):494–503, 2008. ISSN 1387-1811. doi: 10.1016/j.micromeso.2007.10.029. URL <GotoISI>://WOS:000256713300055.

[159] Y. F. Zhu, Y. F. Zhang, C. T. Wu, Y. Fang, J. H. Yang, and S. L. Wang. The effect of zirconium incorporation on the physiochemical and biological properties of mesoporous bioactive glasses scaffolds. *Microporous and Mesoporous Materials*, 143(2-3):311–319, 2011. ISSN 1387-1811. doi: 10.1016/j.micromeso.2011.03.007. URL <GotoISI>://WOS:000292227300008.

[160] Francesco Baino, Elisa Fiume, Jacopo Barberi, Saeid Kargozar, Juliana Marchi, Jonathan Massera, and Enrica Verné. Processing methods for making porous bioactive glass-based scaffolds—a state-of-the-art review. *International Journal of Applied Ceramic Technology*, 16(5):1762–1796, 2019. ISSN 1546-542X. doi: 10.1111/ijac.13195. URL https://doi.org/10.1111/ijac.13195.

[161] Paulo J. Bártolo, Henrique A. Almeida, Rodrigo A. Rezende, Tahar Laoui, and Bopaya Bidanda. *Advanced Processes to Fabricate Scaffolds for Tissue Engineering*, pages 149–170. Springer US, Boston, MA, 2008. ISBN 978-0-387-68831-2. doi: 10.1007/978-0-387-68831-2_8. URL https://doi.org/10.1007/978-0-387-68831-2_8.

[162] Zhangwei Chen, Ziyong Li, Junjie Li, Chengbo Liu, Changshi Lao, Yuelong Fu, Changyong Liu, Yang Li, Pei Wang, and Yi He. 3d printing of ceramics: A review. *Journal of the European Ceramic Society*, 39(4):661–687, 2019. ISSN 0955-2219. doi: https://doi.org/10.1016/j.jeurceramsoc.2018.11.013. URL http://www.sciencedirect.com/science/article/pii/S0955221918306782.

[163] Anh-Vu Do, Behnoush Khorsand, Sean M. Geary, and Aliasger K. Salem. 3d printing of scaffolds for tissue regeneration applications. *Advanced Healthcare Materials*, 4(12):1742–1762, 2015. ISSN 2192-2640. doi: 10.1002/adhm.201500168. URL https://doi.org/10.1002/adhm.201500168.

[164] Farnaz Ghorbani, Dejian Li, Shuo Ni, Ying Zhou, and Baoqing Yu. 3d printing of acellular scaffolds for bone defect regeneration: A review. *Materials Today Communications*, 22:100979, 2020. ISSN 2352-4928. doi: https://doi.org/10.1016/j.mtcomm.2020.100979. URL http://www.sciencedirect.com/science/article/pii/S2352492819306245.

[165] R. Gmeiner, U. Deisinger, J. Schonherr, B. Lechner, R. Detsch, A. R. Boccaccini, and J. Stampfl. Additive manufacturing of bioactive glasses and silicate bioceramics. *Journal of Ceramic Science and Technology*, 6(2):75–86, 2015. ISSN 2190-9385. doi: 10.4416/Jcst2015-00001. URL <GotoISI>://WOS:000356565300001.

[166] Siamak Eqtesadi, Azadeh Motealleh, Pedro Miranda, Antonia Pajares, Alexandra Lemos, and José M. F. Ferreira. Robocasting of 45s5 bioactive glass scaffolds for bone tissue engineering. *Journal of the European Ceramic Society*, 34(1):107–118, 2014. ISSN 0955-2219. doi: https://doi.org/10.1016/j.jeurceramsoc.2013.08.003. URL http://www.sciencedirect.com/science/article/pii/S0955221913003610.

[167] Basam A. E. Ben-Arfa, Ana S. Neto, Ilaria E. Palamá, Isabel M. Miranda Salvado, Robert C. Pullar, and José M. F. Ferreira. Robocasting of ceramic glass scaffolds: Sol–gel glass, new horizons. *Journal of the European Ceramic Society*, 39(4):1625–1634, 2019. ISSN 0955-2219. doi: https://doi.org/10.1016/j.jeurceramsoc.2018.11.019. URL http://www.sciencedirect.com/science/article/pii/S0955221918306848.

[168] Qiang Fu, Eduardo Saiz, and Antoni P. Tomsia. Bioinspired strong and highly porous glass scaffolds. *Advanced Functional Materials*, 21(6):1058–1063, 2011. ISSN 1616-301X. doi: 10.1002/adfm.201002030. URL https://doi.org/10.1002/adfm.201002030.

[169] Xin Liu, Mohamed N. Rahaman, Gregory E. Hilmas, and B. Sonny Bal. Mechanical properties of bioactive glass (13-93) scaffolds fabricated by robotic deposition for structural bone repair. *Acta Biomaterialia*, 9(6):7025–7034, 2013. ISSN 1742-7061. doi: https:

//doi.org/10.1016/j.actbio.2013.02.026. URL http://www.sciencedirect.com/science/article/pii/S1742706113000901.

[170] Elena Mancuso, Naif Alharbi, Oana A. Bretcanu, Martyn Marshall, Mark A. Birch, Andrew W. McCaskie, and Kenneth W. Dalgarno. Three-dimensional printing of porous load-bearing bioceramic scaffolds. *Proceedings of the Institution of Mechanical Engineers, Part H: Journal of Engineering in Medicine*, 231(6):575–585, 2017. ISSN 0954-4119. doi: 10.1177/0954411916682984. URL https://doi.org/10.1177/0954411916682984.

[171] Susmita Bose, Sahar Vahabzadeh, and Amit Bandyopadhyay. Bone tissue engineering using 3d printing. *Materials Today*, 16(12):496–504, 2013. ISSN 1369-7021. doi: https://doi.org/10.1016/j.mattod.2013.11.017. URL http://www.sciencedirect.com/science/article/pii/S136970211300401X.

[172] Andrea Zocca, Paolo Colombo, Cynthia M. Gomes, and Jens Günster. Additive manufacturing of ceramics: Issues, potentialities, and opportunities. *Journal of the American Ceramic Society*, 98(7):1983–2001, 2015. ISSN 0002-7820. doi: 10.1111/jace.13700. URL https://doi.org/10.1111/jace.13700.

[173] Shailly H. Jariwala, Gregory S. Lewis, Zachary J. Bushman, James H. Adair, and Henry J. Donahue. 3d printing of personalized artificial bone scaffolds. *3D Printing and Additive Manufacturing*, 2(2):56–64, 2015. ISSN 2329-7662. doi: 10.1089/3dp.2015.0001. URL https://doi.org/10.1089/3dp.2015.0001.

[174] Johan Van der Stok, Esther M. M. Van Lieshout, Youssef El-Massoudi, Gerdine H. Van Kralingen, and Peter Patka. Bone substitutes in the netherlands – a systematic literature review. *Acta Biomaterialia*, 7(2):739–750, 2011. ISSN 1742-7061. doi: https://doi.org/10.1016/j.actbio.2010.07.035. URL https://www.sciencedirect.com/science/article/pii/S1742706110003557.

[175] Matteo Chiapasco, Paolo Casentini, and Marco Zaniboni. Bone augmentation procedures in implant dentistry. *The International journal of oral & maxillofacial implants*, 24 Suppl: 237–259, 2009. ISSN 0882-2786. URL http://europepmc.org/abstract/MED/19885448.

[176] Judith Baumhauer, Michael S. Pinzur, Rafe Donahue, William Beasley, and Christopher DiGiovanni. Site selection and pain outcome after autologous bone graft harvest. *Foot & Ankle International*, 35(2):104–107, 2013. ISSN 1071-1007. doi: 10.1177/1071100713511434. URL https://doi.org/10.1177/1071100713511434.

[177] Vincent Y. Ng. Risk of disease transmission with bone allograft. *Orthopedics*, 35(8):679–681, 2012. doi: doi:10.3928/01477447-20120725-04. URL https://journals.healio.com/doi/abs/10.3928/01477447-20120725-04.

[178] Kokkari A. Korhonen H. Malin M. NÃ¤rhi T. Korpela J and J. SeppÃ¤lÃ¤. Biodegradable and bioactive porous scaffold structures prepared using fused deposition modeling. *J.*

Biomed. Mater. Res., 101:610, 2012. ISSN 1552-4973. URL http://dx.doi.org/10.1002/jbm.b.32863.

[179] O. N. Musskaya, V. K. Krut'ko, A. I. Kulak, S. A. Filatov, E. V. Batyrev, and T. V. Safronova. Calcium phosphate compositions with polyvinyl alcohol for 3d printing. *Inorganic Materials: Applied Research*, 11(1):192–197, 2020. ISSN 2075-115X. doi: 10.1134/S2075113320010268. URL https://doi.org/10.1134/S2075113320010268.

[180] Almoatazbellah Youssef, Scott J. Hollister, and Paul D. Dalton. Additive manufacturing of polymer melts for implantable medical devices and scaffolds. *Biofabrication*, 9(1):012002, 2017. ISSN 1758-5090. doi: 10.1088/1758-5090/aa5766. URL http://dx.doi.org/10.1088/1758-5090/aa5766.

[181] C. K. Chua, K. F. Leong, and C. S. Lim. *Rapid Prototyping*. WORLD SCIENTIFIC, 2003. ISBN 978-981-238-117-0. doi: doi:10.1142/5064. URL https://doi.org/10.1142/5064.

[182] S. Scott Crump. Apparatus and method for creating three-dimensional objects, 1992.

[183] Johannes Au Abel, Uwe Au Scheithauer, Thomas Au Janics, Stefan Au Hampel, Santiago Au Cano, Axel Au Müller-Köhn, Anne Au Günther, Christian Au Kukla, and Tassilo Au Moritz. Fused filament fabrication (fff) of metal-ceramic components. *JoVE*, (143): e57693, 2019. ISSN 1940-087X. doi: doi:10.3791/57693. URL https://www.jove.com/video/57693.

[184] Omar A. Mohamed, Syed H. Masood, and Jahar L. Bhowmik. Optimization of fused deposition modeling process parameters: a review of current research and future prospects. *Advances in Manufacturing*, 3(1):42–53, 2015. ISSN 2195-3597. doi: 10.1007/s40436-014-0097-7. URL https://doi.org/10.1007/s40436-014-0097-7.

[185] Joamin Gonzalez-Gutierrez, Santiago Cano, Stephan Schuschnigg, Christian Kukla, Janak Sapkota, and Clemens Holzer. Additive manufacturing of metallic and ceramic components by the material extrusion of highly-filled polymers: A review and future perspectives. *Materials*, 11(5), 2018. ISSN 1996-1944. doi: 10.3390/ma11050840.

[186] Xin Wang, Man Jiang, Zuowan Zhou, Jihua Gou, and David Hui. 3d printing of polymer matrix composites: A review and prospective. *Composites Part B: Engineering*, 110:442–458, 2017. ISSN 1359-8368. doi: https://doi.org/10.1016/j.compositesb.2016.11.034. URL http://www.sciencedirect.com/science/article/pii/S1359836816321230.

[187] N. Venkataraman, S. Rangarajan, M. J. Matthewson, B. Harper, A. Safari, S. C. Danforth, G. Wu, N. Langrana, S. Guceri, and A. Yardimci. Feedstock material property – process relationships in fused deposition of ceramics (fdc). *Rapid Prototyping Journal*, 6(4):244–253, 2000. ISSN 1355-2546. doi: 10.1108/13552540010373344. URL https://doi.org/10.1108/13552540010373344.

[188] Natesan Venkataraman. *The process-property-performance relationships of feedstock materials used for fused deposition of ceramics (FDC)*. Thesis, 2000. URL https://ui.adsabs.harvard.edu/abs/2000PhDT.....83V.

[189] Jintian Wu, Ning Chen, Feng Bai, and Qi Wang. Preparation of poly(vinyl alcohol)/poly(lactic acid)/hydroxyapatite bioactive nanocomposites for fused deposition modeling. *Polymer Composites*, 39(S1):E508–E518, 2018. ISSN 0272-8397. doi: 10.1002/pc.24642.

[190] N. Turner Brian, Robert Strong, and A. Gold Scott. A review of melt extrusion additive manufacturing processes: I. process design and modeling. *Rapid Prototyping Journal*, 20(3):192–204, 2014. ISSN 1355-2546. doi: 10.1108/RPJ-01-2013-0012. URL https://doi.org/10.1108/RPJ-01-2013-0012.

[191] Jian-Lin Shi and J. D. Zhang. Compaction and sintering behavior of bimodal alumina powder suspensions by pressure filtration. *Journal of the American Ceramic Society*, 83(4):737–742, 2000. ISSN 0002-7820. doi: https://doi.org/10.1111/j.1151-2916.2000.tb01267.x. URL https://doi.org/10.1111/j.1151-2916.2000.tb01267.x.

[192] R. J. Farris. Prediction of the viscosity of multimodal suspensions from unimodal viscosity data. *Transactions of the Society of Rheology*, 12(2):281–301, 1968. ISSN 0038-0032. doi: 10.1122/1.549109. URL https://doi.org/10.1122/1.549109.

[193] Chang-Jun Bae and John W. Halloran. Concentrated suspension-based additive manufacturing – viscosity, packing density, and segregation. *Journal of the European Ceramic Society*, 39(14):4299–4306, 2019. ISSN 0955-2219. doi: https://doi.org/10.1016/j.jeurceramsoc.2019.05.034. URL http://www.sciencedirect.com/science/article/pii/S095522191930353X.

[194] Aaron Dörr, Amsini Sadiki, and Amirfarhang Mehdizadeh. A discrete model for the apparent viscosity of polydisperse suspensions including maximum packing fraction. *Journal of Rheology*, 57(3):743–765, 2013. ISSN 0148-6055. doi: 10.1122/1.4795746. URL https://doi.org/10.1122/1.4795746.

[195] S. Mueller, E. W. Llewellin, and H. M. Mader. The rheology of suspensions of solid particles. *Proceedings of the Royal Society A: Mathematical, Physical and Engineering Sciences*, 466 (2116):1201–1228, 2010. doi: 10.1098/rspa.2009.0445. URL https://doi.org/10.1098/rspa.2009.0445.

[196] M. Pishvaei, C. Graillat, P. Cassagnau, and T. F. McKenna. Modelling the zero shear viscosity of bimodal high solid content latex: Calculation of the maximum packing fraction. *Chemical Engineering Science*, 61(17):5768–5780, 2006. ISSN 0009-2509. doi: https://doi.org/10.1016/j.ces.2006.04.024. URL http://www.sciencedirect.com/science/article/pii/S0009250906002582.

[197] Fuzhong Qi and Roger I. Tanner. Relative viscosity of bimodal suspensions. *Korea-*

Australia Rheology Journal, 23(2):105–111, 2011. ISSN 1226-119X. doi: 10.1007/s13367-011-0013-7. URL https://doi.org/10.1007/s13367-011-0013-7.

[198] Fuzhong Qi and Roger I. Tanner. Random close packing and relative viscosity of multimodal suspensions. *Rheologica Acta*, 51(4):289–302, 2012. ISSN 1435-1528. doi: 10.1007/s00397-011-0597-3. URL https://doi.org/10.1007/s00397-011-0597-3.

[199] N. Ashammakhi, A. Hasan, O. Kaarela, B. Byambaa, A. Sheikhi, A. K. Gaharwar, and A. Khademhosseini. Advancing frontiers in bone bioprinting. *Adv Healthc Mater*, 8(7):e1801048, 2019. ISSN 2192-2640. doi: 10.1002/adhm.201801048.

[200] R. Masaeli, K. Zandsalimi, M. Rasoulianboroujeni, and L. Tayebi. Challenges in three-dimensional printing of bone substitutes. *Tissue Eng Part B Rev*, 25(5):387–397, 2019. ISSN 1937-3368. doi: 10.1089/ten.TEB.2018.0381.

[201] N. Tellisi, N. A. Ashammakhi, F. Billi, and O. Kaarela. Three dimensional printed bone implants in the clinic. *J Craniofac Surg*, 29(8):2363–2367, 2018. ISSN 1049-2275. doi: 10.1097/scs.0000000000004829.

[202] N. Ashammakhi, S. Ahadian, C. Xu, H. Montazerian, H. Ko, R. Nasiri, N. Barros, and A. Khademhosseini. Bioinks and bioprinting technologies to make heterogeneous and biomimetic tissue constructs. *Materials Today Bio*, 1:100008, 2019. ISSN 2590-0064. doi: https://doi.org/10.1016/j.mtbio.2019.100008. URL http://www.sciencedirect.com/science/article/pii/S2590006419300146.

[203] Murat Guvendiren, Joseph Molde, Rosane M. D. Soares, and Joachim Kohn. Designing biomaterials for 3d printing. *ACS Biomaterials Science & Engineering*, 2(10):1679–1693, 2016. doi: 10.1021/acsbiomaterials.6b00121. URL https://doi.org/10.1021/acsbiomaterials.6b00121.

[204] Susanne Heid and Aldo R. Boccaccini. Advancing bioinks for 3d bioprinting using reactive fillers: A review. *Acta Biomaterialia*, 113:1–22, 2020. ISSN 1742-7061. doi: https://doi.org/10.1016/j.actbio.2020.06.040. URL http://www.sciencedirect.com/science/article/pii/S1742706120303706.

[205] Tuğrul Tolga Demirtaş, Gülseren Irmak, and Menemşe Gümüşderelioğlu. A bioprintable form of chitosan hydrogel for bone tissue engineering. *Biofabrication*, 9(3):035003, 2017. ISSN 1758-5090. doi: 10.1088/1758-5090/aa7b1d. URL http://dx.doi.org/10.1088/1758-5090/aa7b1d.

[206] S. Midha, S. Murab, and S. Ghosh. Osteogenic signaling on silk-based matrices. *Biomaterials*, 97:133–53, 2016. ISSN 0142-9612. doi: 10.1016/j.biomaterials.2016.04.020.

[207] Batzaya Byambaa, Nasim Annabi, Kan Yue, Grissel Trujillo-de Santiago, Mario Moisés Alvarez, Weitao Jia, Mehdi Kazemzadeh-Narbat, Su Ryon Shin, Ali Tamayol, and Ali

Khademhosseini. Bioprinted osteogenic and vasculogenic patterns for engineering 3d bone tissue. *Advanced Healthcare Materials*, 6(16):1700015, 2017. ISSN 2192-2640. doi: https://doi.org/10.1002/adhm.201700015. URL https://onlinelibrary.wiley.com/doi/abs/10.1002/adhm.201700015.

[208] Xiaohong Wang, Emad Tolba, Heinz C. Schröder, Meik Neufurth, Qingling Feng, Bärbel Diehl-Seifert, and Werner E. G. Müller. Effect of bioglass on growth and biomineralization of saos-2 cells in hydrogel after 3d cell bioprinting. *PLOS ONE*, 9(11):e112497, 2014. doi: 10.1371/journal.pone.0112497. URL https://doi.org/10.1371/journal.pone.0112497.

[209] Nureddin Ashammakhi, Anwarul Hasan, Outi Kaarela, Batzaya Byambaa, Amir Sheikhi, Akhilesh K. Gaharwar, and Ali Khademhosseini. Advancing frontiers in bone bioprinting. *Advanced Healthcare Materials*, 8(7):1801048, 2019. ISSN 2192-2640. doi: 10.1002/adhm.201801048. URL https://doi.org/10.1002/adhm.201801048.

[210] Tyler Potyondy, Jorge Alfredo Uquillas, Peyton J. Tebon, Batzaya Byambaa, Anwarul Hasan, Maryam Tavafoghi, Heloise Mary, George E. Aninwene, Ippokratis Pountos, Ali Khademhosseini, and Nureddin Ashammakhi. Recent advances in 3d bioprinting of musculoskeletal tissues. *Biofabrication*, 13(2):022001, 2021. ISSN 1758-5082 1758-5090. doi: 10.1088/1758-5090/abc8de. URL http://dx.doi.org/10.1088/1758-5090/abc8de.

[211] Caroline Murphy, Krishna Kolan, Wenbin Li, Julie Semon, Delbert Day, and Ming Leu. 3d bioprinting of stem cells and polymer/bioactive glass composite scaffolds for bone tissue engineering. *2017*, 3(1):11, 2017. ISSN 2424-8002. doi: 10.18063/ijb.2017.01.005. URL http://ijb.whioce.com/index.php/int-j-bioprinting/article/view/92.

[212] Márcia T. Tavares, Vítor M. Gaspar, Maria V. Monteiro, José Paulo S Farinha, Carlos Baleizão, and João F. Mano. Gelma/bioactive silica nanocomposite bioinks for stem cell osteogenic differentiation. *Biofabrication*, 13(3):035012, 2021. ISSN 1758-5082 1758-5090. doi: 10.1088/1758-5090/abdc86. URL http://dx.doi.org/10.1088/1758-5090/abdc86.

[213] Mahbub Hassan, Khyati Dave, Rona Chandrawati, Fariba Dehghani, and Vincent G. Gomes. 3d printing of biopolymer nanocomposites for tissue engineering: Nanomaterials, processing and structure-function relation. *European Polymer Journal*, 121:109340, 2019. ISSN 0014-3057. doi: https://doi.org/10.1016/j.eurpolymj.2019.109340. URL https://www.sciencedirect.com/science/article/pii/S001430571931122X.

[214] Chengtie Wu, Richard Miron, Anton Sculean, Stefan Kaskel, Thomas Doert, Renate Schulze, and Yufeng Zhang. Proliferation, differentiation and gene expression of osteoblasts in boron-containing associated with dexamethasone deliver from mesoporous bioactive glass scaffolds. *Biomaterials*, 32(29):7068–7078, 2011. ISSN 0142-9612. doi: https://doi.org/10.1016/j.biomaterials.2011.06.009. URL http://www.sciencedirect.com/science/article/pii/S0142961211006740.

[215] Chengtie Wu, Yinghong Zhou, Wei Fan, Pingping Han, Jiang Chang, Jones Yuen, Meili

Zhang, and Yin Xiao. Hypoxia-mimicking mesoporous bioactive glass scaffolds with controllable cobalt ion release for bone tissue engineering. *Biomaterials*, 33(7):2076–2085, 2012. ISSN 1878-5905 (Electronic) 0142-9612 (Linking). doi: 10.1016/j.biomaterials.2011.11.042. URL https://www.ncbi.nlm.nih.gov/pubmed/22177618.

[216] Gelatin Manufacturers Institute of America. *Gelatin Handbook*. Gelatin Manufactuers Institute of America, 2019. URL http://www.gelatin-gmia.com/uploads/1/1/8/4/118450438/gmia_gelatin_manual_2019.pdf.

[217] Bae Hoon Lee, Hitomi Shirahama, Nam-Joon Cho, and Lay Poh Tan. Efficient and controllable synthesis of highly substituted gelatin methacrylamide for mechanically stiff hydrogels. *RSC Advances*, 5(128):106094–106097, 2015. doi: 10.1039/C5RA22028A. URL http://dx.doi.org/10.1039/C5RA22028A.

[218] Mohamed Gamaleldin Abdelkhalek Mohamed. *High-efficiency biofabrication of cell-laden gelatin methacryloyl hydrogels*. Text, 2020. URL http://hdl.handle.net/2429/73819.

[219] N. Pajares-Chamorro and X. Chatzistavrou. Bioactive glass nanoparticles for tissue regeneration. *ACS Omega*, 5(22):12716–12726, 2020. ISSN 2470-1343. doi: 10.1021/acsomega.0c00180.

[220] Matthias Wagner. *10 - Thermogravimetric Analysis*, pages 162–186. Hanser, 2018. ISBN 978-1-56990-643-9. doi: https://doi.org/10.3139/9781569906446.010. URL https://www.sciencedirect.com/science/article/pii/B9781569906439500117.

[221] Adam C. Marsh, Yaozhong Zhang, Lucrezia Poli, Neal Hammer, Aljoscha Roch, Martin Crimp, and Xanthippi Chatzistavrou. 3d printed bioactive and antibacterial silicate glass-ceramic scaffold by fused filament fabrication. *Materials Science and Engineering: C*, 118:111516, 2021. ISSN 0928-4931. doi: https://doi.org/10.1016/j.msec.2020.111516. URL https://www.sciencedirect.com/science/article/pii/S0928493120334342.

[222] Matthias Wagner. *9 - Differential Thermal Analysis*, pages 158–161. Hanser, 2018. ISBN 978-1-56990-643-9. doi: https://doi.org/10.3139/9781569906446.009. URL https://www.sciencedirect.com/science/article/pii/B9781569906439500105.

[223] Adam C. Marsh, Nathan P. Mellott, Martin Crimp, Anthony Wren, Neal Hammer, and Xanthippi Chatzistavrou. Ag-doped bioactive glass-ceramic 3d scaffolds: Microstructural, antibacterial, and biological properties. *Journal of the European Ceramic Society*, 2021. ISSN 0955-2219. doi: https://doi.org/10.1016/j.jeurceramsoc.2021.01.011. URL https://www.sciencedirect.com/science/article/pii/S0955221921000133.

[224] Arun Kumar, Pritam Singh, and Arun Nanda. Hot stage microscopy and its applications in pharmaceutical characterization. *Applied Microscopy*, 50(1):12, 2020. ISSN 2287-4445. doi: 10.1186/s42649-020-00032-9. URL https://doi.org/10.1186/s42649-020-00032-9.

[225] Adam C. Marsh, Nathan P. Mellott, Natalia Pajares-Chamorro, Martin Crimp, Anthony Wren, Neal D. Hammer, and Xanthippi Chatzistavrou. Fabrication and multiscale characterization of 3d silver containing bioactive glass-ceramic scaffolds. *Bioactive Materials*, 4:215–223, 2019. ISSN 2452-199X. doi: https://doi.org/10.1016/j.bioactmat.2019.05.003. URL http://www.sciencedirect.com/science/article/pii/S2452199X1930026X.

[226] David B. Williams and C. Barry Carter. *The Transmission Electron Microscope*, pages 3–22. Springer US, Boston, MA, 2009. ISBN 978-0-387-76501-3. doi: 10.1007/978-0-387-76501-3_1. URL https://doi.org/10.1007/978-0-387-76501-3_1.

[227] Stanley L. Flegler, John W. Heckman Jr., and Karen L. Klomparens. *Scanning and Transmission Electron Microscopy: An Introduction*. Oxford University Press, 1993. ISBN 9780195107517. URL https://global.oup.com/ushe/product/scanning-and-transmission-electron-microscopy-9780195107517?cc=us&lang=en&.

[228] Joseph I. Goldstein, Dale E. Newbury, Joseph R. Michael, Nicholas W.M. Ritchie, John Henry J. Scott, and David C. Joy. *Scanning Electron Microscopy and X-Ray Microanalysis*. Springer, fourth edition, 2018. ISBN 978-1-4939-6674-5. doi: https://doi.org/10.1007/978-1-4939-6676-9.

[229] David B. Williams and C. Barry Carter. *Transmission electron microscopy: A textbook for materials science*. Springer US, Boston, MA, 2009. ISBN 9780387765006. doi: 10.1007/978-0-387-76501-3. URL http://link.springer.com/10.1007/978-0-387-76501-3.

[230] Shinya Inoué. *Foundations of Confocal Scanned Imaging in Light Microscopy*, pages 1–19. Springer US, Boston, MA, 2006. ISBN 978-0-387-45524-2. doi: 10.1007/978-0-387-45524-2_1. URL https://doi.org/10.1007/978-0-387-45524-2_1.

[231] C. N. McCash Elaine M. Banwell. *Fundamentals of molecular spectroscopy*. McGraw-Hill, London; New York, 1994. ISBN 0077079760 9780077079765.

[232] Roger S. Macomber. *A Complete Introduction to Modern NMR Spectroscopy*. Wiley, New York, 1998. ISBN 0-471-15736-8.

[233] Christiane Claaßen, Marc H. Claaßen, Vincent Truffault, Lisa Sewald, Günter E. M. Tovar, Kirsten Borchers, and Alexander Southan. Quantification of substitution of gelatin methacryloyl: Best practice and current pitfalls. *Biomacromolecules*, 19(1):42–52, 2018. ISSN 1525-7797. doi: 10.1021/acs.biomac.7b01221. URL https://doi.org/10.1021/acs.biomac.7b01221.

[234] Eva Hoch, Christian Schuh, Thomas Hirth, Günter E. M. Tovar, and Kirsten Borchers. Stiff gelatin hydrogels can be photo-chemically synthesized from low viscous gelatin solutions using molecularly functionalized gelatin with a high degree of methacrylation. *Journal of Materials Science: Materials in Medicine*, 23(11):2607–2617, 2012. ISSN 1573-4838. doi: 10.1007/s10856-012-4731-2. URL https://doi.org/10.1007/s10856-012-4731-2.

[235] V.C. Farmer. *The Infrared Spectra of Minerals*. Mineralogical Society of Great Britain and Ireland, London, 1974. ISBN 9780903056052. URL https://doi.org/10.1180/mono-4.

[236] A. L. Gonzalez and C. Noguez. Optical properties of silver nanoparticles. *Physica Status Solidi C - Current Topics in Solid State Physics, Vol 4, No 11*, 4(11):4118–4126, 2007. ISSN 1862-6351. doi: 10.1002/pssc.200675903. URL <GotoISI>://WOS:000252428100011.

[237] B.D. Cullity and S.R. Stock. Elements of x-ray diffraction, third edition, 2001.

[238] R. J. Hill and C. J. Howard. Peak shape variation in fixed-wavelength neutron powder diffraction and its effect on structural parameters obtained by rietveld analysis. *Journal of Applied Crystallography*, 18(3):173–180, 1985. ISSN 0021-8898. doi: 10.1107/S0021889885010068. URL https://doi.org/10.1107/S0021889885010068.

[239] W. Dollase. Correction of intensities for preferred orientation in powder diffractometry: application of the march model. *Journal of Applied Crystallography*, 19(4): 267–272, 1986. ISSN 0021-8898. doi: 10.1107/S0021889886089458. URL https://doi.org/10.1107/S0021889886089458.

[240] Kaan Orhan and Arda Büyüksungur. *Fundamentals of Micro-CT Imaging*, pages 27–33. Springer International Publishing, Cham, 2020. ISBN 978-3-030-16641-0. doi: 10.1007/978-3-030-16641-0_3. URL https://doi.org/10.1007/978-3-030-16641-0_3.

[241] Stephen Brunauer, P. H. Emmett, and Edward Teller. Adsorption of gases in multimolecular layers. *Journal of the American Chemical Society*, 60(2):309–319, 1938. ISSN 0002-7863. doi: 10.1021/ja01269a023. URL https://doi.org/10.1021/ja01269a023.

[242] Zeid Alothman. A review: Fundamental aspects of silicate mesoporous materials. *Materials*, 5:2874–2902, 2012. doi: 10.3390/ma5122874.

[243] R. E. Link, Serge Tamari, and Ariosto Aguilar Chavez. Optimum design of gas pycnometers for determining the volume of solid particles. *Journal of Testing and Evaluation - J TEST EVAL*, 33, 2005. doi: 10.1520/JTE12674.

[244] Astm c1674-16, 2016. URL http://www.astm.org/cgi-bin/resolver.cgi?C1674-16.

[245] Astm c1421-18, 2018. URL http://www.astm.org/cgi-bin/resolver.cgi?C1421-18.

[246] Miaomiao Zhou, Bae Hoon Lee, Yu Jun Tan, and Lay Poh Tan. Microbial transglutaminase induced controlled crosslinking of gelatin methacryloyl to tailor rheological properties for 3d printing. *Biofabrication*, 11(2):025011, 2019. ISSN 1758-5090. doi: 10.1088/1758-5090/ab063f. URL http://dx.doi.org/10.1088/1758-5090/ab063f.

[247] Paul D. Fey, Jennifer L. Endres, Vijaya Kumar Yajjala, Todd J. Widhelm, Robert J. Boissy, Jeffrey L. Bose, and Kenneth W. Bayles. A genetic resource for rapid and compre-

hensive phenotype screening of nonessential staphylococcus aureus genes. *mBio*, 4(1):e00537–12, 2013. doi: 10.1128/mBio.00537-12. URL http://mbio.asm.org/content/4/1/e00537-12.abstract.

[248] Francesca E. Ciraldo, Elena Boccardi, Virginia Melli, Fabian Westhauser, and Aldo R. Boccaccini. Tackling bioactive glass excessive in vitro bioreactivity: Preconditioning approaches for cell culture tests. *Acta Biomaterialia*, 75:3–10, 2018. ISSN 1742-7061. doi: https://doi.org/10.1016/j.actbio.2018.05.019. URL https://www.sciencedirect.com/science/article/pii/S1742706118302885.

[249] Frederike Hohenbild, Marcela Arango-Ospina, Arash Moghaddam, Aldo R. Boccaccini, and Fabian Westhauser. Preconditioning of bioactive glasses before introduction to static cell culture: What is really necessary? *Methods and Protocols*, 3(2), 2020. ISSN 2409-9279. doi: 10.3390/mps3020038.

[250] Sumiko Shiota, Masato Shimizu, Tohru Mizushima, Hideyuki Ito, Tsutomu Hatano, Takashi Yoshida, and Tomofusa Tsuchiya. Marked reduction in the minimum inhibitory concentration (mic) of β-lactams in methicillin-resistant staphylococcus aureus produced by epicatechin gallate, an ingredient of green tea (camellia sinensis). *Biological & Pharmaceutical Bulletin*, 22(12):1388–1390, 1999. doi: 10.1248/bpb.22.1388.

[251] Johannes Schindelin, Ignacio Arganda-Carreras, Erwin Frise, Verena Kaynig, Mark Longair, Tobias Pietzsch, Stephan Preibisch, Curtis Rueden, Stephan Saalfeld, Benjamin Schmid, Jean-Yves Tinevez, Daniel James White, Volker Hartenstein, Kevin Eliceiri, Pavel Tomancak, and Albert Cardona. Fiji: an open-source platform for biological-image analysis. *Nature Methods*, 9:676, 2012. doi: 10.1038/nmeth.2019https://www.nature.com/articles/nmeth.2019#supplementary-information. URL https://doi.org/10.1038/nmeth.2019.

[252] T. Kokubo, S. Ito, Z. T. Huang, T. Hayashi, S. Sakka, T. Kitsugi, and T. Yamamuro. Ca, p-rich layer formed on high-strength bioactive glass-ceramic a-w. *Journal of Biomedical Materials Research*, 24(3):331–343, 1990. ISSN 0021-9304. doi: 10.1002/jbm.820240306. URL https://doi.org/10.1002/jbm.820240306.

[253] T. Kokubo, H. Kushitani, S. Sakka, T. Kitsugi, and T. Yamamuro. Solutions able to reproduce in vivo surface-structure changes in bioactive glass-ceramic a-w. *J Biomed Mater Res*, 24(6):721–34, 1990. ISSN 0021-9304 (Print) 0021-9304 (Linking). doi: 10.1002/jbm.820240607. URL https://www.ncbi.nlm.nih.gov/pubmed/2361964.

[254] Alessandra Chesi, Yadav Wagley, Matthew E. Johnson, Elisabetta Manduchi, Chun Su, Sumei Lu, Michelle E. Leonard, Kenyaita M. Hodge, James A. Pippin, Kurt D. Hankenson, Andrew D. Wells, and Struan F. A. Grant. Genome-scale capture c promoter interactions implicate effector genes at gwas loci for bone mineral density. *Nature Communications*, 10(1):1260, 2019. ISSN 2041-1723. doi: 10.1038/s41467-019-09302-x. URL https://doi.org/10.1038/s41467-019-09302-x.

[255] Astm c1239-13(2018), 2018. URL http://www.astm.org/cgi-bin/resolver.cgi?C1239-13(2018).

[256] Francesco Baino and Elisa Fiume. Quantifying the effect of particle size on the crystallization of 45s5 bioactive glass. *Materials Letters*, 224:54–58, 2018. ISSN 0167-577X. doi: https://doi.org/10.1016/j.matlet.2018.04.073. URL http://www.sciencedirect.com/science/article/pii/S0167577X18306670.

[257] Oana Bretcanu, Xanthippi Chatzistavrou, Konstantinos Paraskevopoulos, Reinhard Conradt, Ian Thompson, and Aldo R. Boccaccini. Sintering and crystallisation of 45s5 bioglass® powder. *Journal of the European Ceramic Society*, 29(16):3299–3306, 2009. ISSN 0955-2219. doi: https://doi.org/10.1016/j.jeurceramsoc.2009.06.035. URL http://www.sciencedirect.com/science/article/pii/S0955221909003525.

[258] A. Hrubý. Evaluation of glass-forming tendency by means of dta. *Czechoslovak Journal of Physics B*, 22(11):1187–1193, 1972. ISSN 1572-9486. doi: 10.1007/BF01690134. URL https://doi.org/10.1007/BF01690134.

[259] Oscar Peitl, Edgar D. Zanotto, Francisco C. Serbena, and Larry L. Hench. Compositional and microstructural design of highly bioactive p2o5–na2o–cao–sio2 glass-ceramics. *Acta Biomaterialia*, 8(1):321–332, 2012. ISSN 1742-7061. doi: https://doi.org/10.1016/j.actbio.2011.10.014. URL http://www.sciencedirect.com/science/article/pii/S1742706111004454.

[260] Devis Bellucci, Antonella Sola, and Valeria Cannillo. Hydroxyapatite and tricalcium phosphate composites with bioactive glass as second phase: State of the art and current applications. *Journal of Biomedical Materials Research Part A*, 104(4):1030–1056, 2016. ISSN 1549-3296. doi: 10.1002/jbm.a.35619. URL https://doi.org/10.1002/jbm.a.35619.

[261] Marc Bohner, Bastien Le Gars Santoni, and Nicola Döbelin. β-tricalcium phosphate for bone substitution: Synthesis and properties. *Acta Biomaterialia*, 113:23–41, 2020. ISSN 1742-7061. doi: https://doi.org/10.1016/j.actbio.2020.06.022. URL http://www.sciencedirect.com/science/article/pii/S1742706120303524.

[262] Pierre Hudon and In-ho Jung. Critical evaluation and thermodynamic optimization of the cao-p^{s}ub 2^{o}^{s}ub 5^{s}ystem. *Metallurgical and Materials Transactions*, 46(1):494–522, 2015. ISSN 10735615. doi: http://dx.doi.org/10.1007/s11663-014-0193-x. URL http://ezproxy.msu.edu/login?url=https://www.proquest.com/docview/1647736392?accountid=12598http://za2uf4ps7f.search.serialssolution.com/?ctx_ver=Z39.88-2004&ctx_enc=info:ofi/enc:UTF-8&rfr_id=info:sid/ProQ%3Amaterialsscijournals:1647736392&rft_val_fmt=info:ofi/fmt:kev:mtx:journal&rft.genre=article&rft.jtitle=Metallurgical+and+Materials+Transactions&rft.atitle=Critical+Evaluation+and+Thermodynamic+Optimization+of+the+CaO-P%5Esub+2%5EO%5Esub+5%5E+System&rft.au=Hudon%2C+Pierre%3BJung%2C+In-ho&rft.aulast=Hudon&rft.aufirst=Pierre&rft.date=2015-02-01&rft.volume=46&rft.issue=1&rft.spage=494&rft.isbn=&rft.btitle=&rft.title=Metallurgical+and+Materials+Transactions&rft.issn=10735615&rft_id=info:doi/10.1007%2Fs11663-014-0193-x&

ProQDocID=1647736392.

[263] R. G. Carrodeguas and S. De Aza. α-tricalcium phosphate: Synthesis, properties and biomedical applications. *Acta Biomaterialia*, 7(10):3536–3546, 2011. ISSN 1742-7061. doi: https://doi.org/10.1016/j.actbio.2011.06.019. URL http://www.sciencedirect.com/science/article/pii/S174270611100256X.

[264] Daniel Moreno, Fabio Vargas, Jeisson Ruiz, and María Esperanza López. Solid-state synthesis of alpha tricalcium phosphate for cements used in biomedical applications. *Boletín de la Sociedad Española de Cerámica y Vidrio*, 2019. ISSN 0366-3175. doi: https://doi.org/10.1016/j.bsecv.2019.11.004. URL http://www.sciencedirect.com/science/article/pii/S0366317519300986.

[265] Oscar Peitl Filho, Guy P. La Torre, and Larry L. Hench. Effect of crystallization on apatite-layer formation of bioactive glass 45s5. *Journal of Biomedical Materials Research*, 30(4):509–514, 1996. ISSN 0021-9304. doi: 10.1002/(SICI)1097-4636(199604)30:4<509::AID-JBM9>3.0.CO;2-T. URL https://doi.org/10.1002/(SICI)1097-4636(199604)30:4<509::AID-JBM9>3.0.CO;2-T.

[266] Isabelle Denry and Liisa T. Kuhn. Design and characterization of calcium phosphate ceramic scaffolds for bone tissue engineering. *Dental Materials*, 32(1):43–53, 2016. ISSN 0109-5641. doi: https://doi.org/10.1016/j.dental.2015.09.008. URL http://www.sciencedirect.com/science/article/pii/S0109564115004042.

[267] Alireza Charmforoushan, Mahmood Rezaee Roknabadi, Nasser Shahtahmassebi, and Bizhan Malaekeh-Nikouei. Low temperature facile synthesis of pseudowollastonite nanoparticles by the surfactant-assisted sol-gel method. *Materials Chemistry and Physics*, 243:122629, 2020. ISSN 0254-0584. doi: https://doi.org/10.1016/j.matchemphys.2020.122629. URL http://www.sciencedirect.com/science/article/pii/S0254058420300110.

[268] C. Paluszkiewicz, M. Blażewicz, J. Podporska, and T. Gumuła. Nucleation of hydroxyapatite layer on wollastonite material surface: Ftir studies. *Vibrational Spectroscopy*, 48(2):263–268, 2008. ISSN 0924-2031. doi: https://doi.org/10.1016/j.vibspec.2008.02.020. URL http://www.sciencedirect.com/science/article/pii/S0924203108000544.

[269] Srinath Palakurthy, Venu Gopal Reddy K, Raj Kumar Samudrala, and Abdul Azeem P. In vitro bioactivity and degradation behaviour of β-wollastonite derived from natural waste. *Materials Science and Engineering: C*, 98:109–117, 2019. ISSN 0928-4931. doi: https://doi.org/10.1016/j.msec.2018.12.101. URL http://www.sciencedirect.com/science/article/pii/S0928493118312967.

[270] Ildikó Kotsis and Agnes Balogh. Synthesis of wollastonite. *Ceramics International*, 15(2):79–85, 1989. ISSN 0272-8842. doi: https://doi.org/10.1016/0272-8842(89)90018-7. URL http://www.sciencedirect.com/science/article/pii/0272884289900187.

[271] D. Fornasiero and F. Grieser. Analysis of the visible absorption and sers excitation-spectra of silver sols. *Journal of Chemical Physics*, 87(5):3213–3217, 1987. ISSN 0021-9606. doi: Doi10.1063/1.453009. URL <GotoISI>://WOS:A1987J808000094.

[272] K. Lance Kelly, Eduardo Coronado, Lin Lin Zhao, and George C. Schatz. The optical properties of metal nanoparticles: The influence of size, shape, and dielectric environment. *The Journal of Physical Chemistry B*, 107(3):668–677, 2003. ISSN 1520-6106. doi: 10.1021/jp026731y. URL https://doi.org/10.1021/jp026731y.

[273] A. Panacek, L. Kvitek, R. Prucek, M. Kolar, R. Vecerova, N. Pizurova, V. K. Sharma, T. Nevecna, and R. Zboril. Silver colloid nanoparticles: synthesis, characterization, and their antibacterial activity. *J Phys Chem B*, 110(33):16248–53, 2006. ISSN 1520-6106 (Print) 1520-5207 (Linking). doi: 10.1021/jp063826h. URL https://www.ncbi.nlm.nih.gov/pubmed/16913750.

[274] David Williams and Barry Carter C. Transmission electron microscopy a textbook for materials science, 2009. URL https://link-springer-com.proxy1.cl.msu.edu/book/10.1007%2F978-0-387-76501-3#toc.

[275] Jonathan F. Stebbins, Emily V. Dubinsky, Koji Kanehashi, and Kimberly E. Kelsey. Temperature effects on non-bridging oxygen and aluminum coordination number in calcium aluminosilicate glasses and melts. *Geochimica et Cosmochimica Acta*, 72(3):910–925, 2008. ISSN 0016-7037. doi: https://doi.org/10.1016/j.gca.2007.11.018. URL http://www.sciencedirect.com/science/article/pii/S0016703707006795.

[276] Jonathan F. Stebbins, Scott Kroeker, Sung Keun Lee, and T. J. Kiczenski. Quantification of five- and six-coordinated aluminum ions in aluminosilicate and fluoride-containing glasses by high-field, high-resolution 27al nmr. *Journal of Non-Crystalline Solids*, 275(1):1–6, 2000. ISSN 0022-3093. doi: https://doi.org/10.1016/S0022-3093(00)00270-2. URL http://www.sciencedirect.com/science/article/pii/S0022309300002702.

[277] Z. Hashin and S. Shtrikman. A variational approach to the theory of the elastic behaviour of multiphase materials. *Journal of the Mechanics and Physics of Solids*, 11(2):127–140, 1963. ISSN 0022-5096. doi: https://doi.org/10.1016/0022-5096(63)90060-7. URL http://www.sciencedirect.com/science/article/pii/0022509663900607.

[278] Fridtjov Irgens. *Theory of Elasticity*, pages 199–302. Springer Berlin Heidelberg, Berlin, Heidelberg, 2008. ISBN 978-3-540-74298-2. doi: 10.1007/978-3-540-74298-2_7. URL https://doi.org/10.1007/978-3-540-74298-2_7.

[279] Sebastian C. Kapfer, Stephen T. Hyde, Klaus Mecke, Christoph H. Arns, and Gerd E. Schröder-Turk. Minimal surface scaffold designs for tissue engineering. *Biomaterials*, 32(29):6875–6882, 2011. ISSN 0142-9612. doi: https://doi.org/10.1016/j.biomaterials.2011.06.012. URL http://www.sciencedirect.com/science/article/pii/S0142961211006776.

[280] K. K. Phani and Dipayan Sanyal. The relations between the shear modulus, the bulk modulus and young's modulus for porous isotropic ceramic materials. *Materials Science and Engineering: A*, 490(1):305–312, 2008. ISSN 0921-5093. doi: https://doi.org/10.1016/j.msea.2008.01.030. URL http://www.sciencedirect.com/science/article/pii/S0921509308000622.

[281] O. Zerhouni, M. G. Tarantino, and K. Danas. Numerically-aided 3d printed random isotropic porous materials approaching the hashin-shtrikman bounds. *Composites Part B: Engineering*, 156:344–354, 2019. ISSN 1359-8368. doi: https://doi.org/10.1016/j.compositesb.2018.08.032. URL http://www.sciencedirect.com/science/article/pii/S1359836818310710.

[282] Daina Zeng, Dmitri Debabov, Theresa L. Hartsell, Raul J. Cano, Stacy Adams, Jessica A. Schuyler, Ronald McMillan, and John L. Pace. Approved glycopeptide antibacterial drugs: Mechanism of action and resistance. *Cold Spring Harbor Perspectives in Medicine*, 6(12), 2016. URL http://perspectivesinmedicine.cshlp.org/content/6/12/a026989.abstract.

[283] Tadashi Kokubo and Hiroaki Takadama. How useful is sbf in predicting in vivo bone bioactivity? *Biomaterials*, 27(15):2907–2915, 2006. ISSN 0142-9612. doi: https://doi.org/10.1016/j.biomaterials.2006.01.017. URL http://www.sciencedirect.com/science/article/pii/S0142961206000457.

[284] M. A. Sainz, P. Pena, S. Serena, and A. Caballero. Influence of design on bioactivity of novel casio3–camg(sio3)2 bioceramics: In vitro simulated body fluid test and thermodynamic simulation. *Acta Biomaterialia*, 6(7):2797–2807, 2010. ISSN 1742-7061. doi: https://doi.org/10.1016/j.actbio.2010.01.003. URL http://www.sciencedirect.com/science/article/pii/S1742706110000073.

[285] M. Magallanes-Perdomo, Z. B. Luklinska, A. H. De Aza, R. G. Carrodeguas, S. De Aza, and P. Pena. Bone-like forming ability of apatite–wollastonite glass ceramic. *Journal of the European Ceramic Society*, 31(9):1549–1561, 2011. ISSN 0955-2219. doi: https://doi.org/10.1016/j.jeurceramsoc.2011.03.007. URL http://www.sciencedirect.com/science/article/pii/S0955221911001063.

[286] M. N. Rahaman. *Sintering of ceramics*. CRC Press, first edition, 2008. ISBN 9780849372865.

[287] Adam C. Marsh, Yaozhong Zhang, Yadav Wagley, Kurt Hankenson, Martin A. Crimp, Aldo R. Boccaccini, Neal D. Hammer, Aljoscha Roch, and Xanthippi Chatzistavrou. 3d printing ag-doped bioceramic scaffolds for bone tissue engineering using fused filament fabrication (fff) technology, 2021.

[288] Hilal Balout, Nathalie Tarrat, Joël Puibasset, Simona Ispas, Caroline Bonafos, and Magali Benoit. Density functional theory study of the spontaneous formation of covalent bonds at the silver/silica interface in silver nanoparticles embedded in sio2: Implications for ag+ release. *ACS Applied Nano Materials*, 2(8):5179–5189, 2019. doi: 10.1021/acsanm.9b01049. URL https://doi.org/10.1021/acsanm.9b01049.

[289] Anna L. Gould, Shima Kadkhodazadeh, Jakob B. Wagner, C. Richard A. Catlow, Andrew J. Logsdail, and Marcel Di Vece. Understanding the thermal stability of silver nanoparticles embedded in a-si. *The Journal of Physical Chemistry C*, 119(41):23767–23773, 2015. ISSN 1932-7447. doi: 10.1021/acs.jpcc.5b07324. URL https://doi.org/10.1021/acs.jpcc.5b07324.

[290] V. P. Galván-Chacón, S. Eqtesadi, A. Pajares, P. Miranda, and F. Guiberteau. Elucidating the role of 45s5 bioglass content in the density and flexural strength of robocast β-tcp/45s5 composites. *Ceramics International*, 44(11):12717–12722, 2018. ISSN 0272-8842. doi: https://doi.org/10.1016/j.ceramint.2018.04.074. URL https://www.sciencedirect.com/science/article/pii/S0272884218309428.

[291] Gurbinder Kaur, Vishal Kumar, Francesco Baino, John C. Mauro, Gary Pickrell, Iain Evans, and Oana Bretcanu. Mechanical properties of bioactive glasses, ceramics, glass-ceramics and composites: State-of-the-art review and future challenges. *Materials Science and Engineering: C*, 104:109895, 2019. ISSN 0928-4931. doi: https://doi.org/10.1016/j.msec.2019.109895. URL https://www.sciencedirect.com/science/article/pii/S092849311833964X.

[292] P. Habibovic and J. Barralet. Bioinorganics and biomaterials: bone repair. *Acta Biomater.*, 7:3013, 2011. URL http://dx.doi.org/10.1016/j.actbio.2011.03.027.

[293] S. Murphy, A. W. Wren, M. R. Towler, and D. Boyd. The effect of ionic dissolution products of ca–sr–na–zn–si bioactive glass on in vitro cytocompatibility. *Journal of Materials Science: Materials in Medicine*, 21(10):2827–2834, 2010. ISSN 1573-4838. doi: 10.1007/s10856-010-4139-9. URL https://doi.org/10.1007/s10856-010-4139-9.

[294] Adam C. Marsh, Natalia Pajares Chamorro, and Xanthippi Chatzistavrou. *15 - Long-term performance and failure of orthopedic devices*, pages 379–410. Woodhead Publishing, 2019. ISBN 978-0-08-102451-5. doi: https://doi.org/10.1016/B978-0-08-102451-5.00015-9. URL http://www.sciencedirect.com/science/article/pii/B9780081024515000159.

[295] Adam C. Marsh, Ehsanul Hoque Apu, Marcus Bunn, Christopher H. Contag, Nureddin Ashammakhi, and Xanthippi Chatzistavrou. A new bioink for improved 3d bioprinting of bone-like constructs. *bioRxiv*, page 2021.11.04.467312, 2021. doi: 10.1101/2021.11.04.467312. URL http://biorxiv.org/content/early/2021/11/05/2021.11.04.467312.abstract.

[296] An I. Van Den Bulcke, Bogdan Bogdanov, Nadine De Rooze, Etienne H. Schacht, Maria Cornelissen, and Hugo Berghmans. Structural and rheological properties of methacrylamide modified gelatin hydrogels. *Biomacromolecules*, 1(1):31–38, 2000. ISSN 1525-7797. doi: 10.1021/bm990017d. URL https://doi.org/10.1021/bm990017d.

[297] N. Ashammakhi, S. Ahadian, Z. J. Fan, K. Suthiwanich, F. Lorestani, G. Orive, S. Ostrovidov, and A. Khademhosseini. Advances and future perspectives in 4d bioprinting. *Biotechnology Journal*, 13(12), 2018. ISSN 1860-6768. doi: ARTN180014810.1002/biot.201800148. URL <GotoISI>://WOS:000453233800013.

[298] Nureddin Ashammakhi, Samad Ahadian, Ippokratis Pountos, Shu-Kai Hu, Nazzar Tellisi, Praveen Bandaru, Serge Ostrovidov, Mehmet Remzi Dokmeci, and Ali Khademhosseini. In situ three-dimensional printing for reparative and regenerative therapy. *Biomedical Microdevices*, 21(2):42, 2019. ISSN 1572-8781. doi: 10.1007/s10544-019-0372-2. URL https://doi.org/10.1007/s10544-019-0372-2.

[299] C. D. O'Connell and Others. Tailoring the mechanical properties of gelatin methacryloyl hydrogels through manipulation of the photocrosslinking conditions. *Soft Matter*, 14:2142–2151, 2018. doi: 10.1039/C7SM02187A. URL https://doi.org/10.1039/C7SM02187A.

[300] Muhammad Rizwan, Sarah W. Chan, Patricia A. Comeau, Thomas L. Willett, and Evelyn K. F. Yim. Effect of sterilization treatment on mechanical properties, biodegradation, bioactivity and printability of gelma hydrogels. *Biomedical Materials*, 15(6):065017, 2020. ISSN 1748-605X. doi: 10.1088/1748-605x/aba40c. URL http://dx.doi.org/10.1088/1748-605X/aba40c.

[301] Gurbinder Kaur, O. P. Pandey, K. Singh, Dan Homa, Brian Scott, and Gary Pickrell. A review of bioactive glasses: Their structure, properties, fabrication and apatite formation. *Journal of Biomedical Materials Research Part A*, 102(1):254–274, 2014. ISSN 1549-3296. doi: https://doi.org/10.1002/jbm.a.34690. URL https://doi.org/10.1002/jbm.a.34690.

[302] K. E. Wallace, R. G. Hill, J. T. Pembroke, C. J. Brown, and P. V. Hatton. Influence of sodium oxide content on bioactive glass properties. *Journal of Materials Science: Materials in Medicine*, 10(12):697–701, 1999. ISSN 1573-4838. doi: 10.1023/A:1008910718446. URL https://doi.org/10.1023/A:1008910718446.

[303] Mathieu Allix and Laurent Cormier. *Crystallization and Glass-Ceramics*, pages 113–167. Springer International Publishing, Cham, 2019. ISBN 978-3-319-93728-1. doi: 10.1007/978-3-319-93728-1_4. URL https://doi.org/10.1007/978-3-319-93728-1_4.

[304] Jean-Pierre Guin and Yann Gueguen. *Mechanical Properties of Glass*, pages 227–271. Springer International Publishing, Cham, 2019. ISBN 978-3-319-93728-1. doi: 10.1007/978-3-319-93728-1_7. URL https://doi.org/10.1007/978-3-319-93728-1_7.

[305] Junichi Matsushita. *Mechanical Properties of Ceramics*, pages 133–152. Springer Singapore, Singapore, 2019. ISBN 978-981-13-9935-0. doi: 10.1007/978-981-13-9935-0_7. URL https://doi.org/10.1007/978-981-13-9935-0_7.

[306] Qaisar Nawaz, Araceli de Pablos-Martín, Juliana Martins de Souza e Silva, Katrin Hurle, Altair T. Contreras Jaimes, Delia S. Brauer, and Aldo R. Boccaccini. New insights into the crystallization process of sol-gel–derived 45s5 bioactive glass. *Journal of the American Ceramic Society*, 103(8):4234–4247, 2020. ISSN 0002-7820. doi: 10.1111/jace.17124. URL https://doi.org/10.1111/jace.17124.

[307] M. Magallanes-Perdomo, P. Pena, P. N. De Aza, R. G. Carrodeguas, M. A. Rodríguez,

X. Turrillas, S. De Aza, and A. H. De Aza. Devitrification studies of wollastonite–tricalcium phosphate eutectic glass. *Acta Biomaterialia*, 5(8):3057–3066, 2009. ISSN 1742-7061. doi: https://doi.org/10.1016/j.actbio.2009.04.026. URL https://www.sciencedirect.com/science/article/pii/S1742706109001780.

[308] Wei-Lin Dai, Yong Cao, Li-Ping Ren, Xin-Li Yang, Jian-Hua Xu, He-Xing Li, He-Yong He, and Kang-Nian Fan. Ag–sio2–al2o3 composite as highly active catalyst for the formation of formaldehyde from the partial oxidation of methanol. *Journal of Catalysis*, 228(1): 80–91, 2004. ISSN 0021-9517. doi: https://doi.org/10.1016/j.jcat.2004.08.035. URL https://www.sciencedirect.com/science/article/pii/S0021951704004208.

[309] Anastasiia V. Shabalina, Tatyana I. Izaak, Tamara S. Kharlamova, Darya O. Martynova, Ivan N. Lapin, and Valery A. Svetlichnyi. Ag/siox nanocomposite powders synthesized from colloids obtained by pulsed laser ablation. *Colloids and Surfaces A: Physicochemical and Engineering Aspects*, 553:80–88, 2018. ISSN 0927-7757. doi: https://doi.org/10.1016/j.colsurfa.2018.05.047. URL https://www.sciencedirect.com/science/article/pii/S0927775718304096.

[310] Amarnath R. Allu, Anuraag Gaddam, Sudheer Ganisetti, Sathravada Balaji, Renée Siegel, Glenn C. Mather, Margit Fabian, Maria J. Pascual, Nicoletta Ditaranto, Wolfgang Milius, Jürgen Senker, Dmitrii A. Agarkov, Vladislav V. Kharton, and José M. F. Ferreira. Structure and crystallization of alkaline-earth aluminosilicate glasses: Prevention of the alumina-avoidance principle. *The Journal of Physical Chemistry B*, 122(17):4737–4747, 2018. ISSN 1520-6106. doi: 10.1021/acs.jpcb.8b01811. URL https://doi.org/10.1021/acs.jpcb.8b01811.

[311] Walter Löewenstein. The distribution of aluminum in the tetrahedra of silicates and aluminates. *American Mineralogist*, pages 92–96, 1954.

[312] Alessandro Pugliara, Kremena Makasheva, Bernard Despax, Maxime Bayle, Robert Carles, Patrizio Benzo, Gérard BenAssayag, Béatrice Pécassou, Maria Carmen Sancho, Enrique Navarro, Yolanda Echegoyen, and Caroline Bonafos. Assessing bio-available silver released from silver nanoparticles embedded in silica layers using the green algae chlamydomonas reinhardtii as bio-sensors. *Science of The Total Environment*, 565:863–871, 2016. ISSN 0048-9697. doi: https://doi.org/10.1016/j.scitotenv.2016.02.141. URL https://www.sciencedirect.com/science/article/pii/S0048969716303527.

[313] James E. McDonald. Homogeneous nucleation of supercooled water drops. *Journal of Atmospheric Sciences*, 10(6):416–433, 1953. doi: 10.1175/1520-0469(1953)010<0416:HNOSWD>2.0.CO;2. URL https://journals.ametsoc.org/view/journals/atsc/10/6/1520-0469_1953_010_0416_hnoswd_2_0_co_2.xml.

[314] Jason D. Nicholas. Lecture 10- nano-particle phase equilibria, 09/25/2015 2015.

[315] R. Clausius. Ueber die bewegende kraft der wärme und die gesetze, welche sich daraus für die wärmelehre selbst ableiten lassen. *Annalen der Physik*, 155(4):500–524, 1850. ISSN

0003-3804. doi: https://doi.org/10.1002/andp.18501550403. URL https://doi.org/10.1002/andp.18501550403.

[316] Carl Friedrich Gauss. *Principia generalia Theoriae Figurae Fluidorum in statu Aequilibrii*. Gottingae, Dieterichs, 1830. URL https://hdl.handle.net/2027/nyp.33433069098576.

[317] V. Swamy, Surendra K. Saxena, Bo Sundman, and J. Zhang. A thermodynamic assessment of silica phase diagram. *Journal of Geophysical Research: Solid Earth*, 99(B6):11787–11794, 1994. ISSN 0148-0227. doi: 10.1029/93JB02968. URL https://doi.org/10.1029/93JB02968.

[318] W. Ostwald. Studien über die bildung und umwandlung fester körper: 1. abhandlung: Übersättigung und Überkaltung. *Zeitschrift für Physikalische Chemie*, 22U(1):289–330, 1897. doi: doi:10.1515/zpch-1897-2233. URL https://doi.org/10.1515/zpch-1897-2233.

[319] Richard A. Robie and David R. Waldbaum. Thermodynamic properties of minerals and related substances at 298.15 k (25.0 c) and one atmosphere (1.013 bars) pressure and at higher temperatures. Report 1259, 1968. URL http://pubs.er.usgs.gov/publication/b1259.

[320] M. G. Garníca-Romo, J. González-Hernández, M. A. Hernández-Landaverde, Y. V. Vorobiev, F. Ruiz, and J. R. Martínez. Structure of heat-treated sol-gel sio2 glasses containing silver. *Journal of Materials Research*, 16(07):2007–2012, 2011. ISSN 0884-2914 2044-5326. doi: 10.1557/jmr.2001.0275. URL https://www.cambridge.org/core/article/structure-of-heattreated-solgel-sio2-glasses-containing-silver/5E27F859DEDBF2ADE2423CB797E1544D.

[321] M. F. Zawrah and E. M. A. Hamzawy. Effect of cristobalite formation on sinterability, microstructure and properties of glass/ceramic composites. *Ceramics International*, 28(2): 123–130, 2002. ISSN 0272-8842. doi: https://doi.org/10.1016/S0272-8842(01)00067-0. URL http://www.sciencedirect.com/science/article/pii/S0272884201000670.

[322] E. Mazzucato and A. F. Gualtieri. Wollastonite polytypes in the cao-sio2 system. *Physics and Chemistry of Minerals*, 27(8):565–574, 2000. ISSN 1432-2021. doi: 10.1007/s002690000095. URL https://doi.org/10.1007/s002690000095.

[323] Sumudu Nimasha, Sashikesh Ganeshalingam, Navaratnarajah Kuganathan, Konstantinos Davazoglou, and Alexander Chroneos. Defects and calcium diffusion in wollastonite. *Chemistry*, 2(4), 2020. ISSN 2624-8549. doi: 10.3390/chemistry2040059.

[324] Weiyi Zhang and He Liu. A low cost route for fabrication of wollastonite glass–ceramics directly using soda-lime waste glass by reactive crystallization–sintering. *Ceramics International*, 39(2):1943–1949, 2013. ISSN 0272-8842. doi: https://doi.org/10.1016/j.ceramint.2012.08.044. URL https://www.sciencedirect.com/science/article/pii/S0272884212007912.

[325] Kavish Sudan, Paramjot Singh, Azim Gökçe, Vamsi Krishna Balla, and Kunal H. Kate. Processing of hydroxyapatite and its composites using ceramic fused filament fabrication

(cf3). *Ceramics International*, 2020. ISSN 0272-8842. URL 10.1016/j.ceramint.2020.06.168.

[326] G. P. Bierwagen and T. E. Sanders. Studies of the effects of particle size distribution on the packing efficiency of particles. *Powder Technology*, 10(3):111–119, 1974. ISSN 0032-5910. doi: https://doi.org/10.1016/0032-5910(74)80036-7. URL https://www.sciencedirect.com/science/article/pii/0032591074800367.

[327] P. Wriggers and S. O. Moftah. Mesoscale models for concrete: Homogenisation and damage behaviour. *Finite Elements in Analysis and Design*, 42(7):623–636, 2006. ISSN 0168-874X. doi: https://doi.org/10.1016/j.finel.2005.11.008. URL https://www.sciencedirect.com/science/article/pii/S0168874X05001563.

[328] Elisa Fiume, Alessandro Schiavi, Gissur Orlygsson, Cristina Bignardi, Enrica Verné, and Francesco Baino. Comprehensive assessment of bioactive glass and glass-ceramic scaffold permeability: experimental measurements by pressure wave drop, modelling and computed tomography-based analysis. *Acta Biomaterialia*, 119:405–418, 2021. ISSN 1742-7061. doi: https://doi.org/10.1016/j.actbio.2020.10.027. URL https://www.sciencedirect.com/science/article/pii/S1742706120306164.

[329] Michcle J. Grimm and John L. Williams. Measurements of permeability in human calcaneal trabecular bone. *Journal of Biomechanics*, 30(7):743–745, 1997. ISSN 0021-9290. doi: https://doi.org/10.1016/S0021-9290(97)00016-X. URL https://www.sciencedirect.com/science/article/pii/S002192909700016X.

[330] E. A. Nauman, K. E. Fong, and T. M. Keaveny. Dependence of intertrabecular permeability on flow direction and anatomic site. *Annals of Biomedical Engineering*, 27(4):517–524, 1999. ISSN 1573-9686. doi: 10.1114/1.195. URL https://doi.org/10.1114/1.195.

[331] Nilda Vanesa Ayala-Núñez, Humberto H. Lara Villegas, Liliana del Carmen Ixtepan Turrent, and Cristina Rodríguez Padilla. Silver nanoparticles toxicity and bactericidal effect against methicillin-resistant staphylococcus aureus: Nanoscale does matter. *NanoBiotechnology*, 5 (1):2–9, 2009. ISSN 1551-1294. doi: 10.1007/s12030-009-9029-1. URL https://doi.org/10.1007/s12030-009-9029-1.

[332] Humberto H. Lara, Nilda V. Ayala-Núñez, Liliana del Carmen Ixtepan Turrent, and Cristina Rodríguez Padilla. Bactericidal effect of silver nanoparticles against multidrug-resistant bacteria. *World Journal of Microbiology and Biotechnology*, 26(4):615–621, 2010. ISSN 1573-0972. doi: 10.1007/s11274-009-0211-3. URL https://doi.org/10.1007/s11274-009-0211-3.

[333] Natalia Pajares Chamorro. *Synthesis and Characterization of Bioactive Glass-Ceramic Particles with Advanced Antibacterial Properties for Applications in Bone Regeneration*. Ph.d., 2021. URL http://ezproxy.msu.edu/login?url=https://www.proquest.com/dissertations-theses/synthesis-characterization-bioactive-glass/docview/2529374890/se-2?accountid=12598https://ezproxy.msu.edu/login?url=https:

//resolver.ebscohost.com/openurl?sid=&genre=dissertations+%26+theses&issn=&ISBN=9798728244875&volume=&issue=&date=2021&spage=&pages=&title=&atitle=Synthesis+and+Characterization+of+Bioactive+Glass-Ceramic+Particles+with+Advanced+Antibacterial+Properties+for+Applications+in+Bone+Regeneration&aulast=Pajares+Chamorro%2C+Natalia&id=DOI:.

[334] Sandra Sánchez-Salcedo, Daniel Arcos, and Maria Vallet-Regí. Upgrading calcium phosphate scaffolds for tissue engineering applications. *Key Engineering Materials - KEY ENG MAT*, 377:19–42, 2008. doi: 10.4028/www.scientific.net/KEM.377.19.

[335] S. Sureshbabu, Manoj Komath, and H. K. Varma. In situ formation of hydroxyapatite-αtricalcium phosphate biphasic ceramics with higher strength and bioactivity. *Journal of the American Ceramic Society*, 95(3):915–924, 2012. ISSN 0002-7820. doi: 10.1111/j.1551-2916.2011.04987.x. URL https://doi.org/10.1111/j.1551-2916.2011.04987.x.

[336] Leslie Glasser and H. Donald Brooke Jenkins. Lattice energies and unit cell volumes of complex ionic solids. *Journal of the American Chemical Society*, 122(4):632–638, 2000. ISSN 0002-7863. doi: 10.1021/ja992375u. URL https://doi.org/10.1021/ja992375u.

[337] Hitomi Shirahama, Bae Hoon Lee, Lay Poh Tan, and Nam-Joon Cho. Precise tuning of facile one-pot gelatin methacryloyl (gelma) synthesis. *Scientific Reports*, 6(1):31036, 2016. ISSN 2045-2322. doi: 10.1038/srep31036. URL https://doi.org/10.1038/srep31036.